Delft University of Technology

Document Version
Final published version

Citation (APA)
Bol, R. J. M. (2026). *Squeezing Concrete: A Numerical and Experimental Study on the Mechanisms within Auxetic Cementitious Composites.* [Dissertation (TU Delft), Delft University of Technology].
https://doi.org/10.4233/uuid:a4434796-2dc9-4f55-a934-bd930ed6d087

Important note
To cite this publication, please use the final published version (if applicable).
Please check the document version above.

Copyright
In case the licence states “Dutch Copyright Act (Article 25fa)”, this publication was made available Green Open Access via the TU Delft Institutional Repository pursuant to Dutch Copyright Act (Article 25fa, the Taverne amendment). This provision does not affect copyright ownership.
Unless copyright is transferred by contract or statute, it remains with the copyright holder.

Sharing and reuse
Other than for strictly personal use, it is not permitted to download, forward or distribute the text or part of it, without the consent of the author(s) and/or copyright holder(s), unless the work is under an open content license such as Creative Commons.

Takedown policy
Please contact us and provide details if you believe this document breaches copyrights.
We will remove access to the work immediately and investigate your claim.

This work is downloaded from Delft University of Technology.

Delft University of Technology

SQUEEZING CONCRETE

A NUMERICAL AND EXPERIMENTAL STUDY ON THE MECHANISMS WITHIN AUXETIC CEMENTITIOUS COMPOSITES

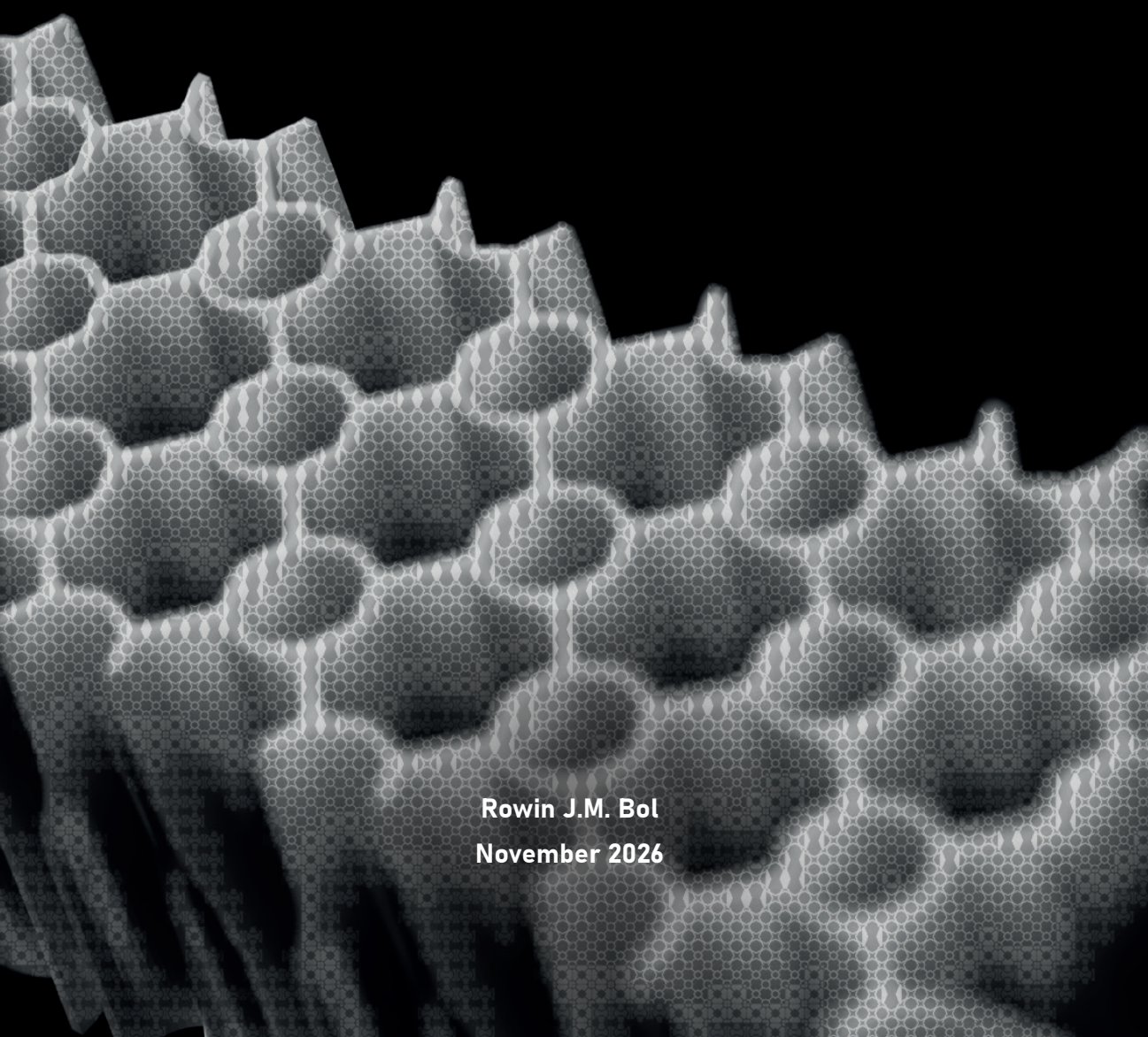

Rowin J.M. Bol

November 2026

SQUEEZING CONCRETE

A NUMERICAL AND EXPERIMENTAL STUDY ON THE MECHANISMS WITHIN AUXETIC CEMENTITIOUS COMPOSITES

SQUEEZING CONCRETE

A NUMERICAL AND EXPERIMENTAL STUDY ON THE MECHANISMS WITHIN AUXETIC CEMENTITIOUS COMPOSITES

Dissertation

for the purpose of obtaining the degree of doctor
at Delft University of Technology
by the authority of the Rector Magnificus,
Prof. dr. ir. H. Bijl,
chair of the Board for Doctorates
to be defended publicly on
Friday 6 November 2026 at 15:00

by

Rowin Johannes Marinus BOL

This dissertation has been approved by the promotors.

Composition of the doctoral committee:

Rector Magnificus,	chairperson
Dr. B. Šavija,	Delft University of Technology, promotor
Prof. dr. ir. E. Schlangen,	Delft University of Technology, promotor

Independent members:

Em. prof. dr. ir. J.G. Rots,	Delft University of Technology
Prof. dr. K. Masania,	Delft University of Technology
Dr. S.C. Barbosa Nunes,	Delft University of Technology
Dr. R. Moini,	Princeton University, USA
Dr. R. Vinai,	University of Exeter, UK

TU Delft Delft University of Technology

erc European Research Council
Established by the European Commission

Keywords: Additive Manufacturing (AM); Lattice Beam Model (LBM); mechanical anisotropy; architected materials; cementitious composites; auxetics
Printed by: Ipskamp printing
Cover by: Ir. L. van den Wildenberg
Copyright: © 2026 by R.J.M. Bol
ISBN: 978-94-6563-000-7

An electronic version of this dissertation is available at:
http://repository.tudelft.nl/

Education Enriches Your Life -
It Always Adds, It Never Subtracts.

Walter Lewin

CONTENTS

Summary xi

Samenvatting xiii

1 Introduction 1
- 1.1 Introduction & background . . . 2
- 1.2 Research scope & objectives . . . 4
- 1.3 Thesis outline . . . 5

2 Searching for micromechanical models to represent 3D printed polymers 9
- 2.1 Introduction . . . 10
- 2.2 Identification of printing process parameters . . . 12
- 2.3 Characteristic mechanical properties . . . 17
- 2.4 Available characterization techniques and models . . . 18
  - 2.4.1 Experimental analysis . . . 19
  - 2.4.2 Finite element analysis . . . 21
  - 2.4.3 Analytical and theoretical models . . . 27
  - 2.4.4 Microstructural and fractographic analyses . . . 29
  - 2.4.5 Geometrical analysis . . . 30
- 2.5 Conclusions . . . 33

3 Developing models for 3D printed reinforcements 37
- 3.1 Introduction . . . 38
- 3.2 Modelling of deformation & fracture . . . 40
  - 3.2.1 Lattice beam model . . . 41
  - 3.2.2 Lattice generation . . . 42
  - 3.2.3 Failure analysis . . . 43
- 3.3 Methodology . . . 44
  - 3.3.1 Microstructural experimental analysis . . . 45
  - 3.3.2 Printing path-dependent two-scale models . . . 51
  - 3.3.3 Calibration procedures . . . 53
  - 3.3.4 Experimental analysis of planar auxetics . . . 54
- 3.4 Results . . . 59
  - 3.4.1 Microstructural constitutive relationships . . . 59
  - 3.4.2 Two-scale models for planar auxetic designs . . . 60
  - 3.4.3 Output analysis . . . 68
- 3.5 Summary & conclusions . . . 71

4 Understanding the bond between 3D printed reinforcement and cementitious matrix **73**
4.1 Introduction . . . 74
4.2 Literature . . . 75
4.2.1 Reinforcement-matrix bond behaviour . . . 75
4.2.2 Experimental contributions . . . 76
4.2.3 Analytical models . . . 78
4.3 Methodology . . . 78
4.3.1 Experimental analysis . . . 79
4.3.2 Numerical simulations on two length scales . . . 83
4.4 Results . . . 87
4.4.1 Meso-scale bond stress-slip relationship . . . 87
4.4.2 Micro-scale bond stress-slip analysis . . . 89
4.5 Discussion . . . 92
4.6 Summary and conclusions . . . 94

5 Multi-scale modelling of auxetic cementitious composites **95**
5.1 Introduction . . . 96
5.2 Experimental . . . 99
5.2.1 Specimen design . . . 99
5.2.2 Mix design and specimen preparation . . . 99
5.2.3 Test setup . . . 100
5.3 Numerical . . . 101
5.3.1 Multi-scale modelling of deformation and fracture . . . 101
5.4 Results . . . 107
5.4.1 Plain reference mortar . . . 107
5.4.2 Auxetic Cementitious Composites (ACCs) . . . 107
5.5 Conclusions . . . 119

6 Tailoring the Poisson's ratio of 3D printed reinforcement for flexural applications **121**
6.1 Introduction . . . 122
6.2 Experimental Details . . . 125
6.2.1 Tailored Poisson's Ratio-reinforcement (TPR) . . . 125
6.2.2 Four-point bending tests of TPR . . . 126
6.2.3 Four-point bending tests of TPRCC . . . 128
6.3 Results and discussion . . . 132
6.3.1 Flexural behaviour of TPR . . . 132
6.3.2 Flexural behaviour of TPRCC . . . 137
6.4 Conclusions . . . 148

7 Revealing flexural lateral confinement mechanisms **151**
7.1 Introduction . . . 152
7.2 Numerical . . . 153
7.2.1 Model calibration . . . 154
7.2.2 TPR simulation results . . . 155
7.2.3 TPRCC simulation results . . . 156

7.2.4 Internal stress analysis . . . 160
7.2.5 Internal fracture analysis . . . 165
7.3 Conclusions . . . 166

8 Conclusions, recommendations, and limitations 169
8.1 Research Achievements . . . 170
8.2 Recommendations . . . 172
8.2.1 3D concrete printing . . . 173
8.2.2 Micromechanical characterization of ABS-mortar bond . . . 173
8.2.3 Tailored Poisson's ratio-Reinforcement . . . 175
8.2.4 Prestressing lattice metamaterials . . . 178
8.3 Limitations . . . 179

Bibliography 183

Acknowledgements 201

A Appendices 209
A.1 Variability influence on numerical output . . . 210
A.2 2D finite element method simulations of ACCs . . . 211
A.3 LBM simulations of TPR and TPRCC using isotropic properties . . . 214

Curriculum Vitæ 221

List of Publications 223

SUMMARY

Concrete is the most widely used construction material in the world, but it has a fundamental weakness: it is brittle in tension. Conventional steel reinforcement solves this by bridging cracks once they form, but it remains largely passive until the matrix has already failed. This is particularly problematic in situations demanding high ductility and energy absorption, such as impacts or earthquakes. This dissertation departs from an entirely different idea: what if the reinforcement could *actively* prevent crack formation in the first place?

The answer lies in *auxetic materials*, a class of mechanical metamaterials with a negative Poisson's ratio. Unlike conventional materials that expand laterally when compressed, auxetic structures contract inward. When used as reinforcement embedded in a cementitious matrix, compressive loading causes the reinforcement to squeeze the surrounded mortar laterally, placing it in a state of multi-axial compression. This *lateral confinement mechanism* actively restrains crack localization, turning what would be a sudden brittle failure into a slow, distributed process with far greater energy absorption. The auxetic reinforcements studied here are fabricated using 3D-printing, which enables the geometrically complex lattice designs that auxetic structures require, but also introduces significant complications through porosity and weakened intra- and inter-layer bonds. Models that ignore these printing-induced imperfections consistently overestimate strength and predict entirely wrong failure modes. This motivates the development of *printing path-dependent* numerical models based on the Lattice Beam Model (LBM), which form the numerical backbone of the entire thesis.

Before the reinforcement's interaction with the cementitious matrix can be modelled, the bond between the two must be understood. The filament extrusion process leaves the edges of printed parts with an elliptical cross-sectional profile, and the cementitious mortar fills these elliptical grooves completely, creating mechanical interlocking. The bond behaviour is found to be strongly direction-dependent: the inter-layer orientation shows a 56% increase in bond strength relative to a plain interface, while the intra-layer direction increases by only around 15%. Overall, bond strengths remain below 1 MPa due to the hydrophobic nature of the printed material (Acrylonitrile Butadiene Styrene (ABS)), meaning chemical adhesion is minimal and friction dominates, but the geometrically enhanced interlocking still proves significant for the composite behaviour.

With these models established, the dissertation turns to the full Auxetic Cementitious Composite (ACC) under uniaxial compression. The LBM-based multi-scale framework is extended to the specimen scale, successfully reproducing the experimentally observed behaviour: when compressed, the auxetic reinforcement contracts laterally and confines the surrounded mortar, shifting its stress state into multi-axial compression. The result is a drastic improvement in post-peak performance: instead of the sudden splitting failure of plain mortar, the composite displays a long, gradual softening response with multiple fine distributed cracks.

The second half of the dissertation asks whether the same lateral confinement mechanism can be exploited in *bending*, where the stress distribution is fundamentally more complex. The solution proposed here is *Tailored Poisson's Ratio-reinforcement* (TPR): a 3D-printed lattice with a through-height gradient of Poisson's ratio that mirrors the bending stress profile. The top chord is auxetic and contracts laterally under compression, confining the mortar above the neutral axis, while the bottom chord has a positive Poisson's ratio and also contracts laterally under tension. Four-point bending tests confirm that this concept works: composites having the reinforcement aligned with the bending stress profile (upright) show up to double the load capacity and toughness (104 % and 99.6 % higher, respectively) than those tested upside down, where the confinement mechanism is absent or reversed.

To prove that this improvement is truly caused by lateral confinement, the LBM framework is extended to full Tailored Poisson's Ratio-reinforced Cementitious Composite (TPRCC) simulations. Internal stress and fracture analyses provide the clearest evidence yet: in the upright configuration, compressive lateral stress concentrations develop within the mortar of the tensioned chord, confirming active confinement. μ-CT scanning independently validates the numerical predictions: upright specimens retain most of their matrix intact with only a single localized final crack, while upside down specimens display widespread matrix damage throughout. The models capture these contrasting fracture patterns with striking accuracy, including fine features such as horizontal crack deflections and diagonal branching. Taken together, the dissertation delivers a complete multi-scale modelling framework, from printing path to specimen failure, and uses it to establish, explain, and validate a new reinforcement concept for cementitious composites. The lateral confinement mechanism, first hypothesized for compression, is shown to be transferable to bending through intelligent tailoring of the Poisson's ratio gradient, with future directions including up-scaling using steel reinforcement and exploring prestressing of lattice metamaterials as a further means of enhancing lateral confinement in structural applications.

SAMENVATTING

Beton is het meest gebruikte bouwmateriaal ter wereld, maar het heeft een fundamentele zwakte: het is bros onder trekspanning. Conventionele staalwapening lost dit op door scheuren te overbruggen zodra ze ontstaan, maar blijft grotendeels passief totdat de matrix al bezweken is. Dit is vooral problematisch in situaties die een hoge ductiliteit en energieabsorptie vereisen, zoals bij impactbelastingen of aardbevingen. Dit proefschrift vertrekt vanuit een heel ander idee: wat als de wapening *actief* scheurvorming zou kunnen voorkomen?

Het antwoord ligt in *auxetische materialen*, een klasse mechanische metamaterialen met een negatieve Poisson-verhouding. In tegenstelling tot conventionele materialen die lateraal uitzetten bij samendrukking, vervormen auxetische structuren juist naar binnen samen. Wanneer deze als wapening in een cementgebonden matrix worden toegepast, zorgt drukbelasting ervoor dat de wapening de omliggende mortel lateraal samendrukt en deze in een toestand van meervoudige drukspanning brengt. Dit *laterale opsluitmechanisme* remt actief de lokalisatie van scheuren, waardoor wat anders een plotseling bros bezwijken zou zijn, verandert in een langzaam, gespreid proces met een veel grotere energieabsorptie. De auxetische wapeningselementen die in dit onderzoek worden bestudeerd, zijn vervaardigd met behulp van 3D-printen, wat de geometrisch complexe roosterontwerpen mogelijk maakt die auxetische structuren vereisen, maar ook aanzienlijke complicaties introduceert door porositeit en verzwakte intra- en inter-laagverbindingen. Modellen die deze printgeïnduceerde onvolkomenheden negeren, overschatten de sterkte consequent en voorspellen volledig verkeerde bezwijkmechanismen. Dit motiveert de ontwikkeling van *printpad-afhankelijke* numerieke modellen gebaseerd op het Lattice Beam Model (LBM), die de numerieke ruggengraat van het gehele proefschrift vormen.

Voordat de interactie tussen de wapening en de cementgebonden matrix gemodelleerd kan worden, moet de hechting tussen beide worden begrepen. Het filamentextrusieproces laat de randen van geprinte onderdelen achter met een elliptisch dwarsdoorsnedeprofiel, en de cementgebonden mortel vult deze elliptische groeven volledig op, waardoor mechanische inklemming ontstaat. Het hechtgedrag blijkt sterk richtingsafhankelijk te zijn: de inter-laagoriëntatie vertoont een 56% hogere hechtsterkte ten opzichte van een vlak grensvlak, terwijl de intra-laagrichting met slechts circa 15% toeneemt. De hechtsterkte blijft over het algemeen onder de 1 MPa vanwege de hydrofobe aard van het geprinte materiaal (Acrylonitril Butadieen Styreen (ABS)), wat betekent dat chemische adhesie minimaal is en wrijving domineert, maar de geometrisch verbeterde inklemming blijkt toch significant voor het composietgedrag.

Met deze modellen vastgesteld, richt het proefschrift zich op het volledige Auxetisch Cementgebonden Composiet (ACC) onder eenassige druk. Het LBM-gebaseerde meerschalige raamwerk wordt uitgebreid naar de proefstukschaal en reproduceert met succes het experimenteel waargenomen gedrag: bij samendrukking trekt de auxetische wape-

ning lateraal samen en sluit de omliggende mortel op, waardoor de spanningstoestand verschuift naar meervoudige drukspanning. Het resultaat is een drastische verbetering van het gedrag na de pieklast: in plaats van het plotselinge splijten van gewone mortel vertoont het composiet een lange, geleidelijke verzwakkingsrespons met meerdere fijn verdeelde scheuren.

De tweede helft van het proefschrift onderzoekt of hetzelfde laterale opsluitmechanisme benut kan worden in *buiging*, waar de spanningsverdeling fundamenteel complexer is. De hier voorgestelde oplossing is *Tailored Poisson's Ratio-wapening* (TPR): een 3D-geprint rooster met een over de hoogte verlopende gradiënt van de Poissonverhouding die het buigspanningsprofiel weerspiegelt. De bovenste koord is auxetisch en trekt lateraal samen onder druk, waarmee de mortel boven de neutrale lijn wordt opgesloten, terwijl de onderste koord een positieve Poisson-verhouding heeft en eveneens lateraal samentrekt onder trek. Vierpuntsbuigproeven bevestigen dat dit concept werkt: composieten waarbij de wapening uitgelijnd is met het buigspanningsprofiel (rechtop) vertonen tot wel dubbel de draagkracht en taaiheid (respectievelijk 104 % en 99.6 % hoger) dan omgekeerd geteste proefstukken, waarbij het opsluitmechanisme afwezig of omgekeerd is.

Om aan te tonen dat deze verbetering werkelijk wordt veroorzaakt door laterale opsluiting, wordt het LBM-raamwerk uitgebreid naar volledige *Tailored Poisson's Ratio-reinforced Cementitious Composite*, oftewel TPRCC-simulaties. Interne spannings- en scheuranalyses leveren het overtuigendste bewijs: in de rechtopstaande configuratie ontwikkelen zich druklaterale spanningsconcentraties in de mortel van de getrokken koord, wat actieve opsluiting bevestigt. µ-CT-scanning valideert de numerieke voorspellingen onafhankelijk: rechtopstaande proefstukken behouden het grootste deel van hun matrix intact met slechts één gelokaliseerde eindscheur, terwijl omgekeerde proefstukken wijdverspreide matrixschade vertonen. De modellen leggen deze contrasterende scheurpatronen met opvallende nauwkeurigheid vast, inclusief fijne kenmerken zoals horizontale scheurafbuigingen en diagonale vertakkingen. Samenvattend levert het proefschrift een volledig meerschalig modelleringskader op, van printpad tot proefstukbezwijken, en gebruikt dit om een nieuw wapeningsconcept voor cementgebonden composieten te onderbouwen, te verklaren en te valideren. Het laterale opsluitmechanisme, aanvankelijk gehypothetiseerd voor druk, blijkt overdraagbaar naar buiging door een intelligente aanpassing van de Poisson-verhoudingsgradiënt, met toekomstige richtingen waaronder opschaling met behulp van stalen wapening en het verkennen van voorspanning van roostermetamaterialen als verdere manier om laterale opsluiting in constructieve toepassingen te versterken.

1

INTRODUCTION

This chapter introduces the research background, outlines the research scope, main objective, activities, and structure of the thesis.

1

1.1. INTRODUCTION & BACKGROUND

Concrete is globally the most used construction material since its raw production materials are inexpensive and directly available in the biggest part of the planet [1, 2]. It has a high compressive strength in combination with durability, fire resistance and a large flexibility in shape because it is a liquid when casting before hardening [2]. It's tensile strength, however, is much lower which results in a brittle response in tension and early crack development at low tensile stresses [3]. Conventional methods solve this deficiency by strengthening the concrete through the use of continuous steel reinforcement bars (rebars), which prevent mass separation of the cementitious matrix (i.e., crack propagation) in order to keep structures intact and maintain their structural integrity [4]. Although this current approach is appropriate for most loading scenarios, it has been demonstrated to be ineffective for situations that require (high) ductility (i.e., deformation capacity) and energy dissipation or absorption, such as incidental loads (e.g., impacts [4] or earthquakes [3]).

Currently, two approaches can be distinguished that are both based on energy dissipation [3–5]. The first one considers continuous reinforcement [6] using densely spaced conventional rebars [3], providing confinement in compression which results in high ductility [7]. However, the ductility entirely depends on complicated details [3] that may suffer from poor construction practices [8]. The second approach concerns discrete reinforcement [6], and aims to accomplish energy dissipation through multiple, evenly spaced fine micro-cracks in structural elements experiencing tensile loads [3, 5, 9–11]. Such composites consist of cementitious matrix mixed with short synthetic polymer [12] or steel fibers [3, 13, 14] that can absorb great amounts of (fracture) energy during cracking of the matrix and pull-out of the fibers [4]. This is accomplished through crack bridging of the fibers [15]. Moreover, supplementary nanofibers have been found to bridge nano- and micro-scale cracks [16]. Nevertheless, the manually mixed fibers are often assumed to have a uniform distribution which can never be assured on-site, plus the casting procedure may encounter fiber clustering or poor flowability [17] and workability [18] of the mix, thereby worsening its mechanical properties [19–21]. As a result of these casting effects, Fiber Reinforced Concrete (FRC) is generally highly anisotropic causing a high scatter in both strength and ductility which makes it unreliable in terms of structural robustness [5, 22–24]. In both cases, the existence of cracks (i.e., damage) is required to improve ductility and energy absorption capacity. The latter is usually measured by the area under the stress-strain curve [4].

Meanwhile, the construction industry is well-known to be conservative in terms of innovation as most projects remain using traditional methods and working practices to this day. Other industries have already embraced newly developed methods, such as Additive Manufacturing (AM) [25]. However, the use of large-scale AM in construction using a variety of resources like polymers, metals and cementitious materials has gained more attention [26]. Regarding AM applications in civil engineering, 3D Concrete Printing (3DCP) is further developed and more often used than both metal or polymer printing techniques. Examples of 3DCP projects so far are limited to complete structures [25] such as residential and office buildings, and several pedestrian bridges [1]. Nonetheless, Buchanan and Gardner [1] expect 'hybrid solutions' to be more likely in the construction sector, in which traditional approaches and AM components are combined. Therefore,

the industry might shift towards the development of novel materials with improved properties instead of focusing on changing construction methods.

In view of advances in AM techniques, mechanical metamaterials have emerged [27] that exhibit extraordinary properties because of their rational designs [28]. Metamaterials can be defined as man-made, artificially-designed materials [29] whose unique physical properties arise from their deliberately designed internal geometry rather than their chemical composition. One particularly interesting class of mechanical metamaterials are those having a negative Poisson's ratio, which are referred to as 'auxetic materials' [30–43]. Auxetic materials are known to have a variety of mechanical properties that are scarce in common natural (non-auxetic) materials: synclastic curvature in bending, variable permeability, high shear stiffness, high specific strength, enhanced indentation resistance, high fracture toughness, impact resistance, fatigue toughness, improved damping, sound and energy absorption properties, and being lightweight [29, 33–35, 37, 40–47]. Because of their geometrical complexity, auxetic designs cannot always be easily created [32]. However, AM methods like 3D printing present the opportunity to construct auxetic structures, as suggested in the latter reference. Nevertheless, AM techniques are prone to several issues that affect the auxetic behaviour. For example, 3D printed material can be highly anisotropic [34]. AM parts can also contain various geometrical imperfections [39], while it is important to have sufficient printing accuracy in relation to mechanical properties of auxetic designs [32, 48].

Although the enhanced mechanical properties listed before sound promising, auxetic materials often possess a relatively low overall stiffness which makes their applicability questionable when multiple of these characteristics (e.g., high shear stiffness, strength and energy absorption) are required at the same time [41]. However, it is believed that auxetic composite materials can overcome this limitation. The combination of auxetic materials and conventional (non-auxetic) materials could lead towards material characteristics that are unseen in both conventional as well as auxetic materials alone [37]. Auxetic composites are most often composite materials that show auxeticity because of their constituent material's structure [34]. Nevertheless, each constituent material of a composite has the possibility to contribute their individual properties independently to enhance its general performance [41]: The use of auxetic lattice structures as reinforcement (fabricated with a glassy polymer) in composite materials that have nearly incompressible soft matrix material (a highly flexible rubber-like material that easily changes shape but resists changing its overall volume when loading is applied) suggests great possibilities in terms of material characteristics. One particular example of an auxetic composite is described in several works (e.g., [37, 41, 46]), which concerns fiber-reinforced composites. If auxetic fibers are embedded in a cementitious matrix, these will expand under tension when the matrix fails. As a result, the pull-out resistance increases [37], thereby improving its energy absorption capacity [46]. Conversely, the auxeticity of auxetic reinforcement could also be utilized when compressed, where the matrix would experience a state of biaxial or triaxial compression as a result [41]. As argued by Edmund et al. [49], contemporary literature suggests that cementitious composites with 3D printed auxetic reinforcements are viable to be applied in civil engineering, 'specially as protective rendering on vulnerable structures for disaster resilience'.

1

1.2. RESEARCH SCOPE & OBJECTIVES

The current research is embedded within a larger project called 'Auxetic Cementitious Composites by 3D Printing' or 'ACC-3D' in short. Whereas conventional reinforcement, like steel rebars or fibers, only becomes active once the matrix has cracked (i.e., it prevents existing cracks from growing), it is hypothesized that auxetic reinforcement will actively restrain crack localization within the cementitious matrix, thereby limiting crack widths: compressive loads will make the reinforcement provide active local confinement to the cementitious matrix, leading to a state of multi-axial compression. However, the mechanism of interaction between deformable auxetic reinforcement and the stiff cementitious matrix is unknown. The main objective of this thesis therefore is to understand these mechanisms through modelling the material at multiple length scales, from the micro-scale to the specimen (laboratory) scale. To this end, a multi-scale modelling framework for reliably simulating deformation and fracture of cementitious composites with auxetic reinforcement is developed. The main objective has been subdivided into several activities:

- Developing a model for simulating mechanical behaviour of 3D printed auxetic cellular reinforcement.
- Developing a two-scale model for simulating the bond between cementitious matrix and 3D printed reinforcement.
- Developing a specimen-scale model for simulating deformation and fracture of auxetic cementitious composites.

The aforementioned activities are accompanied by the following research questions:

- What impact have 3D printing techniques and their resulting imperfections on the mechanical response of (auxetic) reinforcement?
- What is the relationship between cementitious matrix and interface microstructure of 3D printed reinforcement?
- What is the interfacial strength between cementitious matrix and 3D printed reinforcement?
- What are the underlying mechanisms of interaction between auxetic reinforcement and cementitious matrix that result in composite action?

In the present study, these research questions have been answered through the development of numerical models using the Lattice Beam Model (LBM) and the implementation of a parameter-passing multi-scale modelling scheme, combined with experimental tests for collecting input parameters and validations.

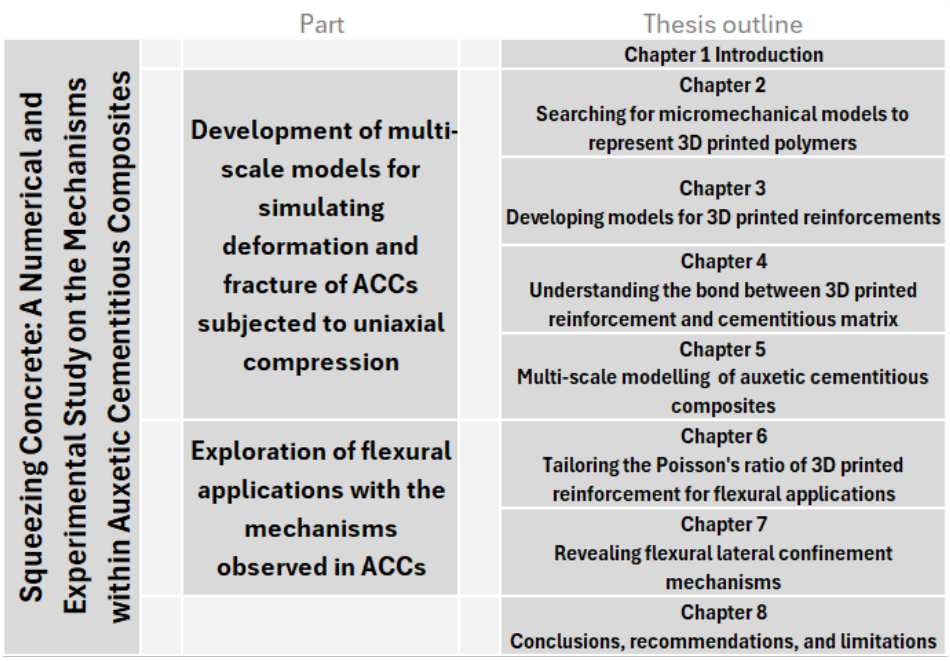

Figure 1.1: Thesis outline

1.3. THESIS OUTLINE

This thesis comprises the development of a multi-scale modelling framework for simulating deformation and fracture of cementitious composites with auxetic reinforcement. It is organized into two parts: (i) Development of multi-scale models for simulating deformation and fracture of ACCs subjected to uniaxial compression, and (ii) Exploration of flexural applications with the mechanisms observed in ACCs. These are subdivided into eight chapters, starting with an introduction (Chapter 1) and ending with conclusions, recommendations, and limitations (Chapter 8). An overview of all chapters and their relations can be found in Figure 1.1.

Chapter 1 Introduction
This chapter introduces the research background, outlines the research scope, main objective, activities, and structure of the thesis.

Chapter 2 Searching for micromechanical models to represent 3D printed polymers
This chapter presents a literature review of micromechanical models for Fused Deposition Modelling (FDM) 3D-printed polymers. Printing process parameters that are considered to affect the micromechanical composition of FDM 3D-printed polymers are identified, and their (negative) influence on characteristic mechanical properties is discussed. Conclusions are drawn based on geometrical, numerical, and experimental analyses of FDM-printed parts in view of microstructural modelling. The geometrical models explored therein are used in Chapter 3 to represent the 3D printed material.

1

Chapter 3 Developing models for 3D printed reinforcements
This chapter proposes printing path-dependent models based on an experimentally-validated multi-scale modelling scheme using the Lattice Beam Model (LBM). This is done by first representing idealized microstructures of extruded 3D printed polymers through the geometric models discussed in Chapter 2 and simulating these on the material scale. The aim is to explicitly model the inter-layer and intra-layer bonds that exist in material extruded 3D printed parts by assigning experimentally obtained interface properties that significantly differ from the bulk material. On the auxetic structure scale, two planar auxetic designs are modelled using the determined material scale relationships as input.

Chapter 4 Understanding the bond between 3D printed reinforcement and cementitious matrix
This chapter focuses on the bond between 3D printed reinforcement and cementitious matrix. Because of the layer-by-layer filament extrusion process of the 3D printing technique, the edges of FDM 3D printed polymers are typically composed of ellipses. Based on this, it is hypothesized that morphological effects as a result of the 3D printing technique enhance the reinforcement-matrix bond: The elliptic geometry potentially facilitates interlocking with the cementitious mortar, thereby possibly enhancing the bond behaviour in certain directions. To investigate the geometrical directional-dependent features at the edges of 3D printed polymers in more detail, micro-scale models are developed.

Chapter 5 Multi-scale modelling of auxetic cementitious composites
This chapter aims to develop a better understanding of Auxetic Cementitious Composites (ACCs) using numerical models. To date, ACCs reinforced with 3D printed polymeric auxetic structures are typically modelled by means of Finite Element Methods (FEM). Therein, polymers usually receive a plastic material description, whilst the cementitious matrix gets generally described by a Concrete Damaged Plasticity Model (CDPM). However, these methods fail to capture the (large) anisotropy exhibited by the polymeric lattice reinforcement which is caused by popular 3D printing techniques like FDM. In the light of these previous attempts to model ACCs, a modelling approach based on LBM is proposed here.

Chapter 6 Tailoring the Poisson's ratio of 3D printed reinforcement for flexural applications
This chapter explores the opportunity to tailor the Poisson's ratio of 3D printed reinforcements to align with local stress distributions in bending. Tailored Poisson's Ratio-reinforcements (TPR) were proposed, characterized by a linear gradient of Poisson's ratio along the height of the reinforcement to accommodate varying stress profiles within beams. Specifically, the top chords of TPR exhibit negative Poisson's ratios (auxetic), undergoing lateral contraction under compression, and providing confinement to the surrounded matrix. Conversely, the bottom chords possess positive Poisson's ratios, contributing to lateral contraction under tension.

Chapter 7 Revealing flexural lateral confinement mechanisms
This chapter expands and substantially elaborates lattice modelling of Tailored Poisson's Ratio-reinforced Cementitious Composites (TPRCCs) to confirm the lateral confinement hypothesis posted in the previous chapter. Therefore, LBM simulations are used to perform internal stress and fracture analysis. The stress states in the cementitious matrix phase at the bottom chords of the TPRCC specimens are visualized to prove the presence of lateral contraction before reinforcement failure, and experimental X-ray Computed Tomography (XCT) images are compared to numerical crack widths for validation.

Chapter 8 Conclusions, recommendations, and limitations
This chapter presents conclusions, recommendations, and limitations.

2

SEARCHING FOR MICROMECHANICAL MODELS TO REPRESENT 3D PRINTED POLYMERS

Among the most common AM techniques is fused filament fabrication (FFF), usually referred to by its trademarked name: fused deposition modeling (FDM). This is the most efficient technique for manufacturing physical three-dimensional thermoplastics, such that FDM machines are nowadays the most common. Regardless of the 3D-printing methodology, AM techniques involve layer-by-layer deposition. Generally, this layer-wise process introduces anisotropy into the produced parts. The manufacturing procedure creates parts possessing heterogeneities at the micro (usually up to 1 mm) and meso (mm to cm) length scales, such as voids and pores, whose size, shape, and spatial distribution are mainly influenced by the so-called printing process parameters. Therefore, it is crucial to investigate their influence on the mechanical properties of FDM 3D-printed parts. This review starts with the identification of the printing process parameters that are considered to affect the micromechanical composition of FDM 3D-printed polymers. In what follows, their (negative) influence is attributed to characteristic mechanical properties. The remainder of this work reviews the state of the art in geometrical, numerical, and experimental analyses of FDM-printed parts. Finally, conclusions are drawn for each of the aforementioned analyses in view of microstructural modeling.

With the exception of minor textual adjustments, this chapter is reproduced from: R.J.M. Bol, B. Šavija, *Micromechanical Models for FDM 3D-Printed Polymers: A Review*, *Polymers* **2023**, 15(23), 4497.

2.1. INTRODUCTION

Additive manufacturing (AM) and rapid prototyping (RP) are popular names associated with 3D-printing techniques [50]. The principle behind the fabrication of these 3D-printing methods is to slice three-dimensional objects from virtual models, obtained through computer-aided design (CAD) software [51], and build them layer by layer [52]. Due to its large number of advantages compared to traditional subtractive manufacturing techniques [53], such as its cost-efficiency [50, 54, 55], prototyping speed [50, 56–59], high flexibility in producing complex geometries [50, 53–56, 58, 60, 61], reduced material waste [50, 54, 59], decreased time and labour costs [62], and facilitation of product customization [52, 59, 61], this process has gained increasing attention [60] and popularity [63]. Therefore, 3D-printing technology applications can be found in a large variety of sectors, not limited to the automotive [58], aerospace engineering [54, 58, 64], medical application [58], biomedical engineering, civil engineering [64], marine engineering [65], clothes, and music [66] industries. However, the disadvantages are that these processes are subject to problems of accuracy [59, 67]; difficulty in performance tailoring [59] (defects, durability, and anisotropy in particular [52, 57, 59, 63, 68]); poor surface quality [69, 70] and roughness [59, 71, 72]; low production rates; a lack of regulation and standards; and the limited size of parts [59]. Hence, it is important to develop a profound understanding of 3D-printed polymers' microstructural mechanical characteristics before these materials are allowed to be used in final consumer products [73, 74].

Compared to metal and metallic material printing, the 3D printing of polymers is much more accessible and economical considering the printing equipment requirements, raw material production, and printing costs [75]. Among the most common AM techniques is material extrusion [76], also known as fused filament fabrication (FFF), the generic name for extrusion-based processes in which molten extrudate is deposited through a nozzle with a small diameter ranging from about 0.1 mm to 1 mm [77], usually referred to by its trademarked name: fused deposition modeling™ (FDM) [68]. Stratasys Inc., USA, developed FDM [57] in 1990 [50, 62]. The FDM technique essentially consists of three stages: (i) design generation, (ii) machine code (G-code) generation, and (iii) fabrication [58]. The process is initiated through the creation of a three-dimensional solid model, which can be carried out with many sophisticated CAD software options [62, 67]; this is stage (i). In stage (ii), the model is converted into 3D stereolithography format, i.e., standard triangulation language (STL) file format [50, 62, 67, 71]. This format tessellates the model into a set of triangles, after which it is sliced horizontally into a large number of thin sections [67]. These slices depict two-dimensional contours, which altogether form the tool paths for each layer to be deposited. This set of instructions is called the G-code, which is produced by devoted software, usually referred to as *slicer* or *slicing software* [51], and contains all information about the filament supply, nozzle and base plate temperatures, and extrusion head and platform motions for extruding the fused filament. Finally, in step (iii), the specific printing instructions in the form of the G-code are sent to the FDM machine for fabrication [58].

Besides being one of the most widely adopted AM and RP technologies [50, 55, 68, 70, 73], FDM is the most efficient [71] technique for manufacturing physical three-dimensional thermoplastics [56]. As a result, FDM machines are nowadays the most common [70]. During the FDM process, a thermoplastic filament is heated and extruded

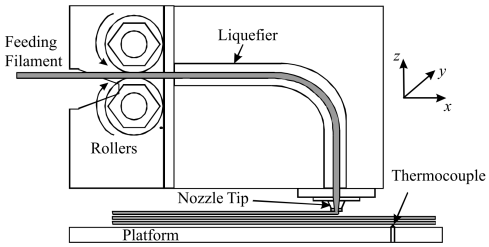

Figure 2.1: FDM 3D-printing technique [61].

in a prescribed layer-by-layer pattern onto a platform [51, 56, 61, 71]; see Figure 2.1. Each printed layer is composed of filaments, also known as fibers, beads, or roads [51]. Since the thermoplastic filament is extruded and deposited in a semi-molten state, the added material fuses with the already deposited neighboring filaments, after which it cools down, solidifies, and bonds with the adjoining material [57, 67]. In the case of traditional Cartesian 3D printers, after finishing a layer, the platform (see Figure 2.1) moves downwards by the height of one filament and continues with the deposition of the next layer. On the other hand, more modern Delta 3D printers rely on a fixed platform, whilst the extrusion head changes height.

In general, various types of thermoplastics can be used in the FDM process [50, 76]. The material most commonly used is acrylonitrile butadiene styrene (ABS) [51, 52, 54, 55, 57–62, 67, 68, 73, 77–85], followed by poly-lactic acid (PLA) [53, 56, 58, 63, 64, 73, 74, 86–90]. Other than these, widely used FDM filaments include thermoplastic polyurethane (TPU) [50, 59]; polycarbonate (PC) [50, 58]; polyetherimide (PEI) [58]; polyaryletherketone (PAEK) [77]; and polyetheretherketone (PEEK) [58], which has particularly high strength and thermal resistance. The micromechanical models for FDM 3D-printed polymers covered in this review mainly relate to ABS and PLA in view of their regular application [76].

Most of the existing reviews available in the literature mainly focused on a single material or only addressed one of the many aspects of 3D-printed polymers. For example, a review by Khan and Kumar [85] was limited to the printing process parameters in relation to the mechanical characteristics of ABS. Another review by Paul [50] concentrated on finite element analyses (FEA) with only brief descriptions of experimental validation strategies. Other reviews, such as that by Zohdi and Yang [91], discussed a large variety of (pre-)treatments and post-processing techniques with the aim of intercepting the cause of mechanical anisotropy. In view of this, the scope of the present review is to provide an overview applicable to different types of thermoplastics that can be used in the FDM process while dealing with multiple 3D-printing aspects in more depth. This will be accomplished by explaining and emphasizing the significance of the aforementioned printing process parameters, after which the review will delve into their intricate influence on the micromechanical composition of FDM 3D-printed polymers and investigate their subsequent impact on the mechanical properties. A thorough exploration follows, encompassing geometrical, numerical, and experimental analyses related to material extrusion, culminating in insightful conclusions for each of these analytical approaches in the context of microstructural modeling.

2.2. IDENTIFICATION OF PRINTING PROCESS PARAMETERS

Regardless of the 3D-printing methodology, AM techniques involve layer-by-layer deposition [53, 58, 70, 73, 74, 76]. Generally, this layer-wise process introduces anisotropy in the produced parts [52, 55, 58, 62, 63, 67, 68, 78, 86]. The manufacturing procedure creates parts with heterogeneities at the micro (usually up to 1 mm) and meso (mm to cm) length scales, such as voids and pores, whose size, shape, and spatial distribution are mainly influenced by the so-called *printing process parameters* [56, 73] or *build parameters* [58]. These geometrical variations result in parts having the same net shape at the macroscale, while their mesostructures can be very different [78]. Most studies have shown that mechanical properties are negatively affected by these parameters [50, 53, 55–57, 60–64, 71, 73, 77, 78, 86, 87]. Since FDM is a complex process that involves many process parameters [87], the resulting mechanical properties are often uncertain [57] and can be greatly influenced by small changes in any parameter. The internal composition at the sub-millimeter scale, i.e., the *mesostructure* [51], thus depends on the printing process parameters. Therefore, it is crucial to investigate their influence on the mechanical properties of FDM 3D-printed parts [73, 87]. In what follows, the parameters affecting the (mechanical) properties of FDM parts are identified.

A vast amount of research has been performed on the subject of 3D-printing process parameters for FDM, describing their effect on material characteristics and behavior [87]. The studied FDM process parameters include: porosity or solidity [50, 56, 68, 77, 87], printing path [50–55, 57, 58, 60, 62, 67, 69, 71, 87], infill degree or air gap [50–52, 54, 55, 57, 58, 60, 62, 67, 71, 87, 91], feed rate or infill speed [54, 58, 60, 71, 87, 91], raster orientation [50–53, 55, 57, 58, 60, 63, 67, 68, 71, 78, 87, 91], bead width [51–55, 57, 60, 62, 67, 71, 87, 91], model temperature [50, 51, 53, 54, 58, 60, 62, 67, 77, 91], nozzle size [60, 67], surface roughness and quality [50, 60, 62, 69–71], color [62, 67], build direction [53–55, 57, 68, 70, 71, 77, 87, 91], number of contours [51, 55, 57, 58, 71], and inclination angle [50, 69]. Since the above list of parameters is quite extensive, it can be concluded that it is difficult to study and include all of them in a model. Furthermore, it is not always possible to have complete control over all printing process parameters, e.g., when closed-control FFF printers are used, with which the access to most parameters is restricted [68]. This review only includes process parameters that are considered to affect the micromechanical composition of 3D-printed polymers.

Figure 2.2 depicts a magnified cross-section of an FDM part in which the shape of the deposited filaments resemble elliptic curves [72]. The cross-sectional shape parameters of these filaments, often referred to as beads, are therefore considered to have a major effect on the micromechanical characteristics of the 3D-printed material. The cross-sectional printing process parameters taken into account in this study are the *bead width* and *layer thickness*. The bead width is defined as the width of one filament extruded by the FDM nozzle [57]. This parameter usually varies between 0.3 mm and 1 mm [57, 67], depending on the material, FDM printer, and settings. Layer thickness is usually described as the thickness of a deposited bead, which is equivalent to the thickness of one layer [57]. Values are commonly taken as one half of the bead width. To avoid ambiguities, it can be helpful to distinguish the terms *layer thickness* and *bead height*, which are generally used interchangeably. To clarify: in this review, *bead height* refers to the height of the ellipse, while *layer thickness* refers to the actual height of one layer, that is, with the subtraction of

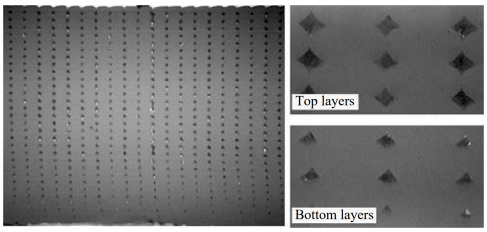

(a)

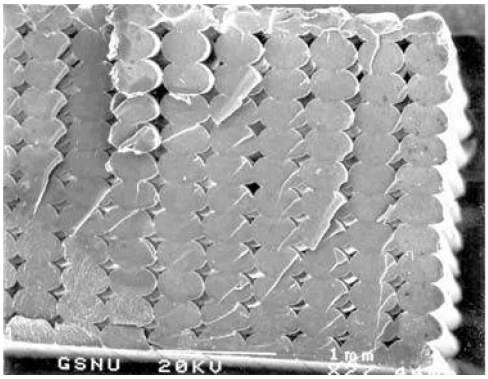

(b)

Figure 2.2: Enlarged section of an FDM-printed part [72]. (**a**) Side view of extruded polymer [61]. (**b**) Shape of deposited filaments [67].

the overlap between layers above and below, as can be seen in Figure 2.3.

This subtraction of the overlap between layers is usually referred to as the *overlap interval*, *hatching distance*, or *air gap*. Nevertheless, it is debatable whether one should differentiate between these terms. The *overlap interval* is often used to define the vertical overlap between layers above and below, not between beads. The *air gap* or *hatching distance* is commonly used to describe the horizontal distance or overlap between adjacent beads. The available literature lacks a clear definition, since all terms are used interchangeably. Most works use the aforementioned terms to describe the horizontal distance or overlap between adjacent beads. However, in [70–72], these terms were used for the vertical overlap between layers above and below. The most common terminology will be used here, that is, the *overlap interval* defines the vertical overlap, while the *air gap* describes the horizontal distance or overlap (see Figure 2.3). Regarding the horizontal distance between the beads (air gap), the standard value is mostly set to zero, such that the beads just touch [57, 72] and thus do not intersect. Alternative settings are either a positive air gap, meaning that the beads do not touch and therefore leave an actual air gap, or a negative air gap, resulting in overlapping bead tracks where adjacent beads intersect (this is the case in Figure 2.3).

Related to the latter parameter(s) are the heterogeneities introduced by the FDM process at the micro and meso length scales, i.e., voids and pores [56], or *porosity*; see Figures 2.2 and 2.3. As stated previously, these geometrical variations result in parts having

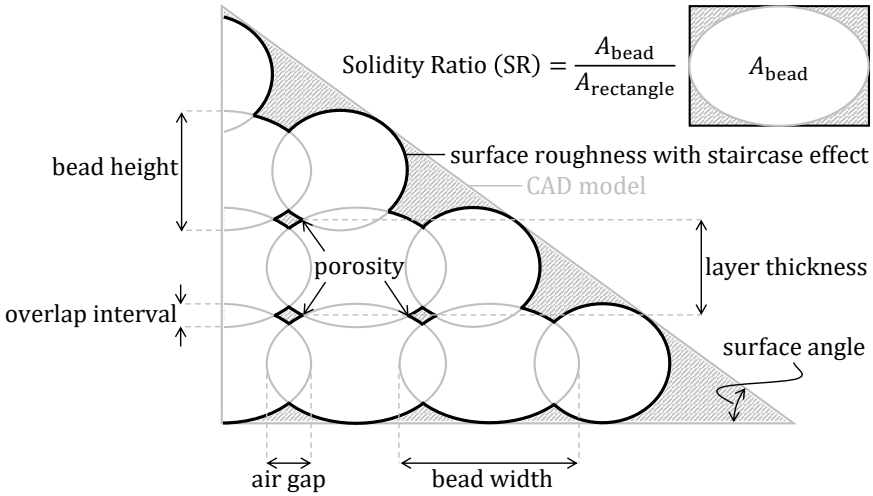

Figure 2.3: Schematic cross-section explaining several printing process parameters.

the same net shape at the macroscale, while their mesostructures can be very different [73, 78]. A related term is *solidity*, which is defined by the voids between neighboring beads [68] and can be used to express the so-called solidity ratio (SR). This ratio is in fact a normalization of the density, which varies depending on the bead shape and has a maximum value of 1.0, meaning a fully solid part. Porosity is therefore considered to be an important parameter that requires significant investigation with respect to the mechanical properties of FDM-produced parts [50].

Similar to the porosity, the *surface roughness* or *surface quality* is inherent to the layer-by-layer deposition of the AM process; see Figures 2.2(b) and 2.3. The resulting surface texture can be seen as a superficial defect in FDM-manufactured parts, since the three-dimensional solid CAD model does not include this detail [70]. Because the cross-sectional shape of the beads resembles elliptic curves, variations in the surface occur [72]. In fact, these can be regarded as the 'porosity of the edges'.

The *inclination angle* or *surface angle* is connected to the surface roughness in the sense that it influences the effective roughness, particularly when inclined surfaces are involved (see Figure 2.3). This parameter is known to cause and influence the stair stepping effect [72], staircasing [69], or the *staircase effect* [70] and is also a result of the layer-wise printing procedure. It is considered to be an extreme defect of the surface, which occurs when surfaces are printed under an angle (defined by this parameter) such that successive layers cannot be stacked directly on top of each other. Consequently, relatively large stair-step-shaped defects exist on inclined surfaces of 3D-printed parts, as illustrated in Figure 2.3.

The *build direction* or *part orientation* is the direction along which the consecutive layers are stacked during the FDM process. By definition, this direction is orthogonal to the platform of the FDM printer (see Figure 2.1) and thus also orthogonal to each

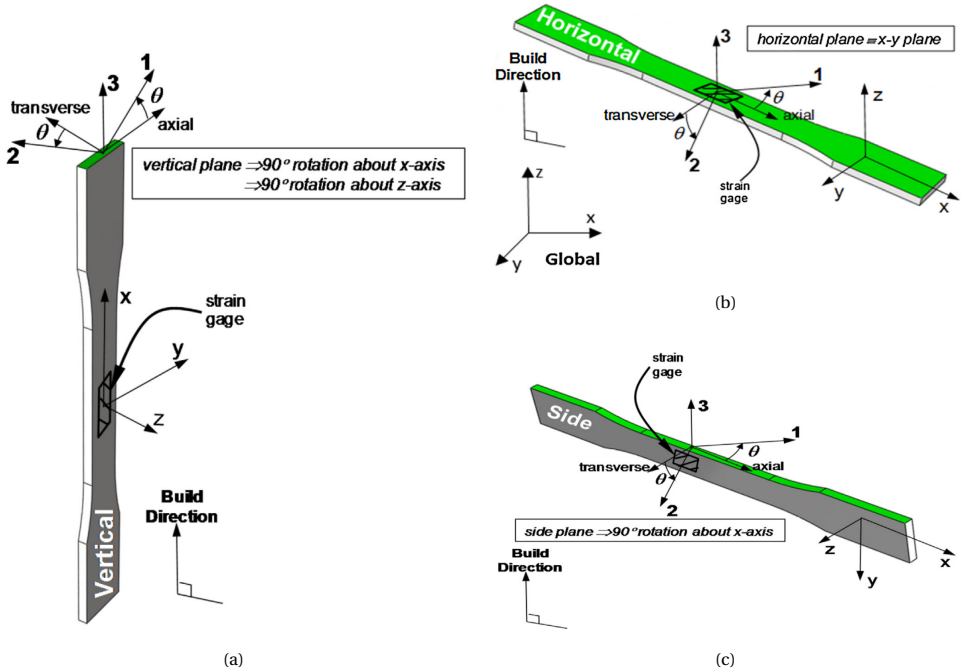

Figure 2.4: Vertical (V), horizontal (H), and side (S) build directions [62]. (**a**) Vertical build direction (V). (**b**) Horizontal build direction (H). (**c**) Side build direction (S).

layer's surface [57]. Parts built in different build directions may have deviating numbers of layers and volumetric errors (e.g., porosity or surface roughness). Three different build directions (V–H–S) of a part with respect to the Cartesian coordinate system ($x-y-z$) are depicted in Figure 2.4.

In addition to the build direction, the *raster orientation* or *hatching angle* is known as a significant process parameter affecting the mechanical characteristics of 3D-printed parts [56]. The raster orientation is defined as the slope of the extruded filaments, usually compared to the loading direction [57, 67]. Typical raster orientations are 0°, 90°, 0°/90°, and ±45° (Figure 2.5).

Besides the internal raster discussed and depicted above, which is the infill, it is customary for an FDM 3D-printed part to have yet another component, namely the *outer shell*, composed of the *contours* and solid/bottom layers [51]. Usually, the manufacturing process starts with depositing filaments along a part's edge [57]. After completing an entire contour, one more additional filament is often deposited inside. Depending on the defined *number of contours*, one of the printing process parameters considered here, new contours are added on the inner side of the previous contour. Afterwards, the remainder of the internal portion of the part is filled according to the raster orientation described earlier [68]. Depending on the slicing software, the outer shells of parts are usually printed in a so-called SOLID fashion [54] by default, while the internal raster may have a larger air gap to save material or reduce weight.

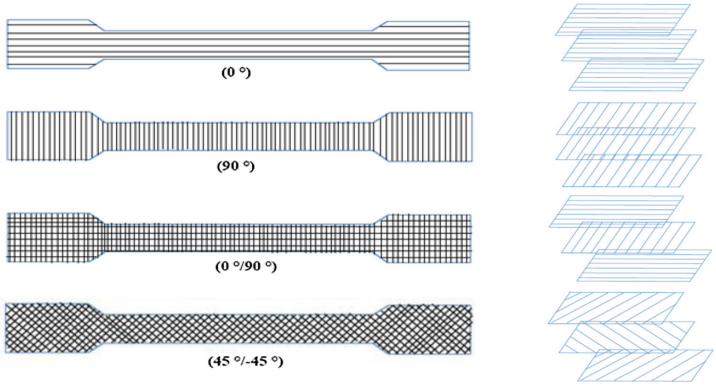

Figure 2.5: Illustration of the raster orientations for a part loaded in the horizontal direction [60].

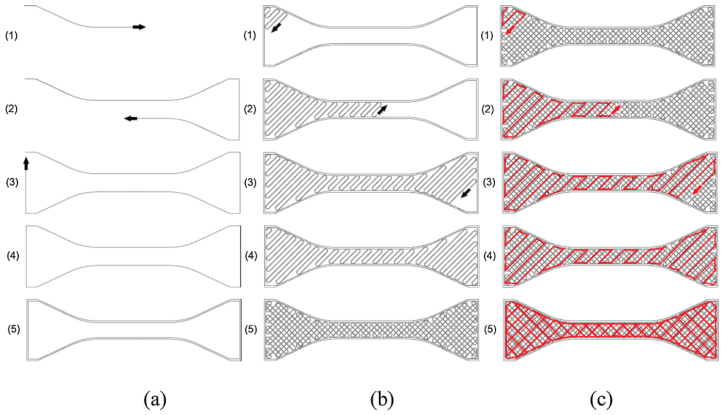

Figure 2.6: Schematic representation of printing path for the (**a**) outer shell, (**b**) bottom layer, and (**c**) infill [54].

All the consecutive motions of the nozzle for extruding the fused filament together, as part of the G-code, constitute the so-called *printing path*, the last parameter considered here. A schematic representation of the complete printing process of an FDM part is visualized in Figure 2.6, where the number of contours is two (Figure 2.6(a)) and the raster orientation is set as $\pm 45^{\circ}$ (Figure 2.6(b)). Figure 2.6(c) illustrates an infill with a larger air gap compared to the bottom layer of the part. For two-dimensional representations of 3D-printed polymers, as displayed in Figure 2.2, the printing path mostly influences the cross-sectional shape parameters of the beads. However, when looking at three-dimensional representations, more printing process parameters become important, like the build direction and raster orientation.

Other parameters, such as nozzle size and temperature, have an influence on the properties of FDM-printed parts. Nevertheless, parameters other than those listed in this section are either difficult to control or assumed to be related to those already considered. For example, nozzle size mainly affects the cross-sectional parameters of the beads, while temperature (e.g., thermal history) is very difficult to control as it is a function of both

location and time [84]. Several publications have aimed to either optimize the printing process parameters or apply external modifications to the 3D-printing process. According to [88], these can be subdivided into (i) pre-process, (ii) in-process, and (iii) post-process methods. An example of this first strategy is to modify the material prior to printing by adding a low-molecular-weight (LMW) additive [90]. In-process technique examples can be found in the form of nozzle modifications, like adding hot air nozzles [92] or a pre-heater [93], or using a laser system [94] to locally heat the previously deposited layer. Post-process methods often include treatments of various kinds, such as acetone vapor [55].

2.3. CHARACTERISTIC MECHANICAL PROPERTIES

As described in the previous sections, 3D-printed polymers contain heterogeneities at the micro and meso length scales, causing anisotropy in the produced parts [52, 55, 58, 62, 63, 67, 68, 78, 86]. The resulting mechanical properties are often uncertain [57] and can be greatly influenced by small changes in any of the previously discussed printing process parameters. Most studies have shown that the mechanical properties are negatively affected. In this section, the characteristic mechanical properties of 3D FDM-manufactured parts are listed, including (some of) their most influential parameters.

The most studied mechanical property is *strength*, specifically *tensile strength*, since it is most influenced by the printing process parameters. According to Ahn et al. [67], the raster orientation and air gap have a large effect on the tensile strength, while the bead width was found to have only a small influence. A recent study using machine learning (ML) models to predict relationships between printing process parameters and mechanical properties [95] found that larger infill densities (related to the air gap) have a positive effect on tensile strength, while higher printing speeds negatively affect this mechanical property. *Compressive strength* was found to be unaffected. Generally, studies on compressive strength are very rare, and the only examples found were [67] and [53], in which the tension/compression asymmetry and direction-dependent response of the material were discussed.

Related to strength are two other characteristic mechanical properties found in literature by which FDM parts are deeply affected: the *inter-layer* and *intra-layer bonding* between the beads [58, 74]; see Figure 2.7. Together with the heterogeneities resulting from FDM (i.e., air voids), weak inter-layer adhesion is one of the most significant problems of this process [91]. The results in [79] indicate that the average strength of intra-layer bonds is higher compared to that of inter-layer bonds. The failure of FDM-manufactured parts was found to mainly occur along layer interfaces [55], mostly related to the level of adhesion between different layers, and it is clear that raster orientation has a great influence. Additionally, this level of adhesion was found to be dependent on various printing process parameters, with temperature (i.e., thermal history), which is very difficult to control, being the most influential [84]. As defined by Yao et al. [64], inter-layer failure occurs at the interface of two neighboring layers, meaning that the material layers remain undamaged afterwards. To approximate this interface strength, the tensile strength of vertically built parts is sometimes used [77]. However, in general, the adhesive strength between layers cannot be obtained directly from stress–strain-based methods [81, 82], nor do these methods have predictive capabilities [81]. Inter-layer failure is known to

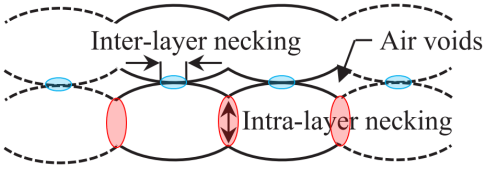

Figure 2.7: Inter-layer and intra-layer necking [55].

negatively affect the *tensile failure strength* (TFS) [64], which is defined as the strength perpendicular to the boundary between two layers. Monaldo and Marfia [74] explained the inter-layer bond as *cohesion* between neighboring layers (i.e., vertically) and the intra-layer bond as *cohesion* between neighboring beads inside the same layer (i.e., horizontally), rather than using the more common description involving *adhesion*. They attributed the early failure of 3D-printed parts to de-cohesion between deposited beads, where the inter-facial bond strengths are governed by the printing process parameters.

Stiffness is also significantly affected by the printing process parameters. For instance, Croccolo et al. [57] observed that a larger number of contours yielded higher stiffness. Furthermore, the results obtained in [60] illustrate that it is inadequate to use the volume fraction of pores to extrapolate the stiffness of printed parts from the stiffness of injection-molded samples and the porosity volume fraction.

Another typical property that characterizes the mechanical response of FDM-printed parts is the *modulus of toughness*, which was found to increase under higher infill densities [54] and could be related to a greater elongation at break [62]. Additionally, build direction and raster orientation were found to have a significant impact [78]. Toughness is usually measured as the area underneath the stress–strain curve [87].

Other mechanical properties include the *Poisson's ratio*, which is often found to be approximately equal to 1/3 [56]; the *shear strength* or *shear failure strength* (SFS) [64], defined as the strength at the boundary between two layers of material; and the *deflection at failure*, which was found to be correlated with infill density and directional parameters [77]. Table 2.1 summarizes the characteristic mechanical properties described in this section with the influencing printing process parameters, including literature references.

2.4. AVAILABLE CHARACTERIZATION TECHNIQUES AND MODELS

An extensive literature review on modeling strategies for FDM-printed parts was performed by Paul [50]. In this work, the author concluded that existing (finite element) models for FDM research are far from realistic and not computationally efficient. According to Paul [50], available (numerical) models can be partitioned as follows: (i) thermal analysis, (ii) geometrical analysis, and (iii) mechanical characterization. Sharafi et al. [77] categorized the available literature as: (i) exploratory experimental studies on the relation between the printing process parameters and mechanical characteristics of 3D prints, (ii) numerical investigations and simulations that consider the macroscopic behavior in relation to a restricted number of printing process parameters, and (iii) extensive finite element analyses of mechanical behavior without considering the direct effects of printing. Finally, the review presented here considers geometrical analyses, numerical analyses, and experimental analyses. The latter is included for completeness and because most

Table 2.1: Summary of printing process parameters affecting characteristic mechanical properties

Characteristic Mechanical Property	Printing Process Parameter
Tensile failure strength (TFS)	Raster orientation [67] Infill density [67] Bead width [95] Printing speed [95]
Inter-layer and intra-layer bonding	Raster orientation [55] Temperature (thermal history) [84]
Stiffness	Number of contours [57] Porosity [60]
Modulus of toughness	Infill density [54] Build direction [78] Raster orientation [78]
Deflection at failure	Infill density [77] Build direction [77]

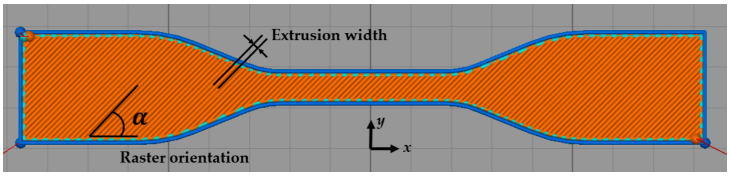

Figure 2.8: Tensile test specimen including printing path, raster orientation, and extrusion width [56].

(numerical) studies are accompanied by experimental validations. Thermal analyses are beyond the scope of this review. Table 2.2, at the end of this section, summarizes for each characteristic mechanical property which printing process parameter negatively affects the mesostructure characteristics of 3D-printed polymers.

2.4.1. EXPERIMENTAL ANALYSIS

Almost all experimental analyses performed on 3D-printed FDM parts are tensile tests, e.g., [51–57, 60, 62, 64, 67, 68, 76, 77, 83, 87]. These experiments are conducted on the specimen scale, specifically with ASTM dog bones in accordance with the testing guidelines ASTM D638 [96] (ASTM D638-14, Standard Test Method for Tensile Properties of Plastic, ASTM International, West Conshohocken, 2014). Usually, the raster orientation is considered to be a major influential process parameter. An illustration of such a tensile test specimen, including a printing path with indications of raster orientation ($\pm 45^\circ$) and extrusion width (bead width), is shown in Figure 2.8. Other common test methods for 3D-printed polymer structures include (three-point) bending (and impact) tests [83].

Other experiments are often performed alongside tensile tests. Only two reports of compressive tests performed alongside tensile tests were found, i.e., [67] and [53]. In the compressive experiments performed in [67], cylindrical specimens were tested, only

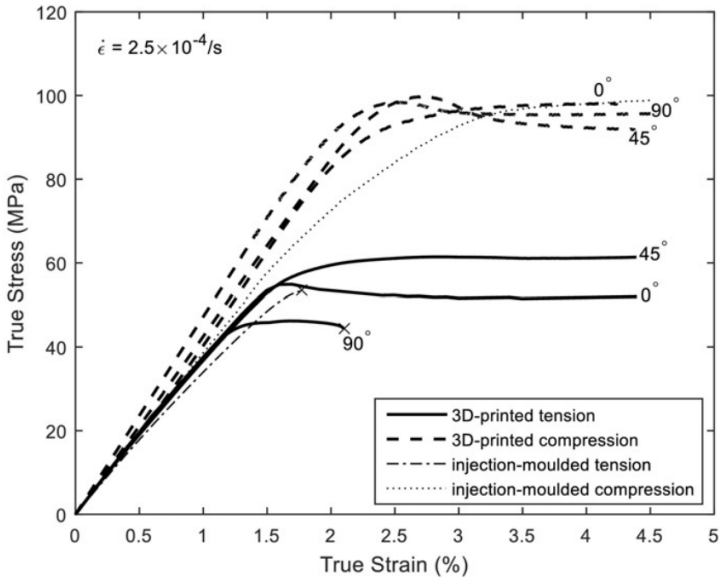

Figure 2.9: Tensile and compressive response of test specimens for various build directions [53].

examining the build direction. The results showed higher compressive strength compared to the tensile strength obtained in the same work. In the other study [53], compression tests were conducted by loading cuboidal specimens. Similarly, the response of the material exhibited tension/compression asymmetry and direction-dependency. The authors concluded that the elastic response (i.e., stiffness) was approximately the same in terms of tension and compression, regardless of the test direction. All tests showed ductile elasto-plastic behavior in both tension and compression; see Figure 2.9.

Different experimental studies have analyzed fracture toughness for different mesostructures, e.g., three build directions and two raster orientations [78], or between two materials, e.g., with different degrees of stiffness [89]. Compact tension specimens, according to ASTM D5045 [97] (ASTM D5045-14, Standard Test Methods for Plane-Strain Fracture Toughness and Strain Energy Release Rate of Plastic Materials, ASTM International, West Conshohocken, 2014), are used to realize Mode I crack opening for the determination of fracture toughness. Representative load versus crack opening curves have been obtained, from which it could be concluded that build direction and raster orientation have a great influence on fracture toughness. Similar experiments were reported in [81, 82] using double-cantilever beam (DCB) fracture specimens whose raster orientation was in the same direction as the crack growth to enable the measurement of the (adhesive) bond strength between layers. To achieve this, the real load-bearing cross-section was measured by optical microscopy, referred to as the surface intact ratio, which is the ratio between this real cross-sectional portion and the nominal fracture surface area (based on the bulk geometrical dimensions). Representative load–displacement curves have been obtained for various printing temperatures; see Figure 2.10.

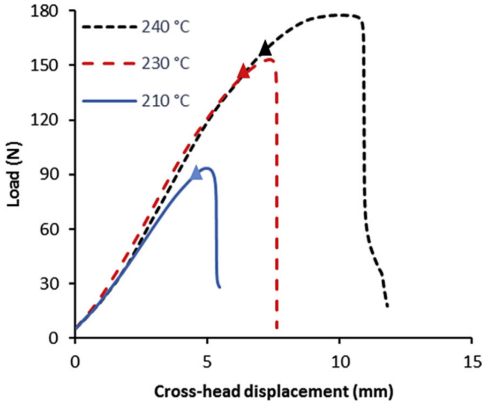

Figure 2.10: Load versus cross−head displacement results for a variety of extrusion head temperatures (cracks started to occur at the triangular indicators) [81].

One particular Mode III 'trouser tear' fracture experiment, modified from the ASTM D1938-14 [98] (ASTM D1938-14, Standard Test Method for Tear-Propagation Resistance (Trouser Tear) of Plastic Film and Thin Sheeting by a Single-Tear Method, ASTM International, West Conshohocken, 2014) test method, was used to determine the strength and fracture toughness of a single bond (referred to as a 'weld') [80]. Similar to the DCB specimen studies above ([81, 82], this experimental study also used optical microscopy for cross-sectional characterization, i.e., obtaining the actual weld dimensions. Figure 2.11 shows a schematic of the sample preparation process as well as the experimental testing setup. Representative force versus cross-head displacement curves were obtained for the different printing temperatures and printing velocities and were used to determine an average tearing force. Furthermore, another self-developed test setup for the determination of the inter-layer shear bond strength was reported in [88], in which a sharp tip was used to tear the top layer from a substrate while the tearing force, representing the inter-layer bond strength, was measured.

2.4.2. FINITE ELEMENT ANALYSIS

The influences of numerous printing process parameters on the characteristic properties of FDM parts, such as those discussed in the previous section, govern the finite element analysis (FEA) in this area [50]. In this portion of the literature review, special attention is paid to FEA that specifically considers the microstructural effects resulting from the process parameters to model the material as a continuum, either through the use of a representative volume element (RVE) or by modeling the specimen completely.

Until recently no FEA studies *explicitly* modeled the inter-layer or intra-layer bonds. Rather, they considered the geometry resulting from the FDM process, meaning that the main focus was on modeling the characteristic cross-sectional shape (see Figure 2.2), including its related heterogeneities, i.e., voids and pores. Thus, the aim was to indirectly incorporate the effects caused by the different layer bonds. To this end, either porosity was included in the geometrical representation of the material to obtain the so-called 'bonded regions' [55], or the bonded dimensions between the filaments in the RVE were

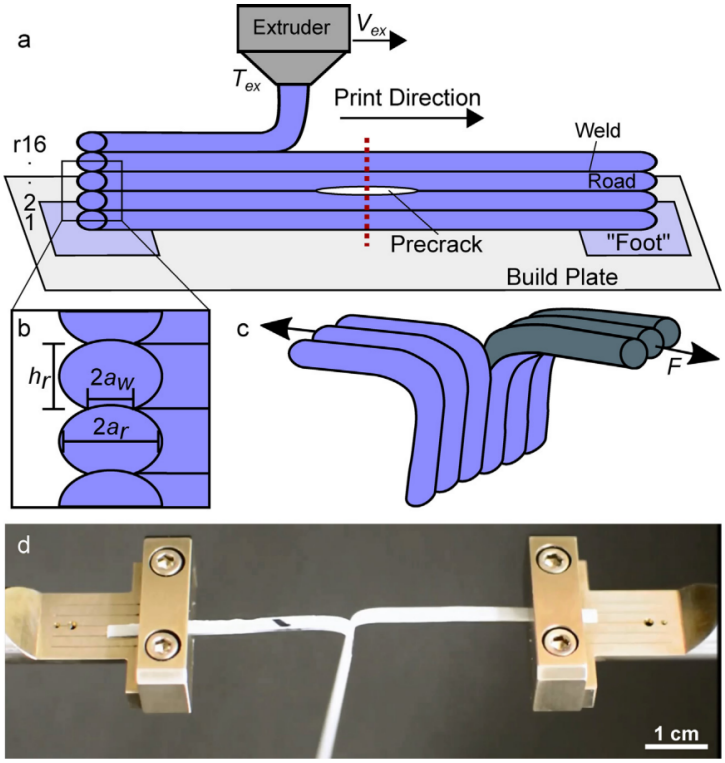

Figure 2.11: Schematic of sample preparation and experimental setup [80]. (**a**) Specimens of one single bead in thickness, including layer indications (r1-r16) and dashed cutting line. (**b**) Close up of specimen section with symbolic indications for bead height, h_r, bead width, $2a_r$, and weld width, $2a_w$. (**c**) Test setup. (**b**) Picture taken during experiment.

modified according to the experimental results [77], but inter-layer and intra-layer bond properties (e.g., strength) were never considered simultaneously. Instead, the material was generally considered to have the same properties in these 'bonded regions'. Only some recently published FEA studies using phase-field models for 3D-printed materials actually distinguished between cross-layer or bulk layer failure (i.e., filament or bead failure) and inter-layer or inter-phase failure [99, 100] in their formulations. Similar observations were made in a very recent publication by Monaldo and Marfia [74], who, to the best of the author's knowledge, were the first to *explicitly* incorporate both the porosity and inter-facial bond properties (i.e., inter-layer and intra-layer bond strengths) simultaneously in numerical (microstructural) models for 3D-printed polymers produced by material extrusion.

REPRESENTATIVE VOLUME ELEMENTS

Three different approaches are distinguished in the literature when it comes to FEA using RVEs based on (i) quantitative characterization by X-ray computed tomography (XCT); (ii) microstructural images and cross-sectional morphology (e.g., actual versus idealized RVE); and (iii) homogenization approaches (e.g., Mori–Tanaka).

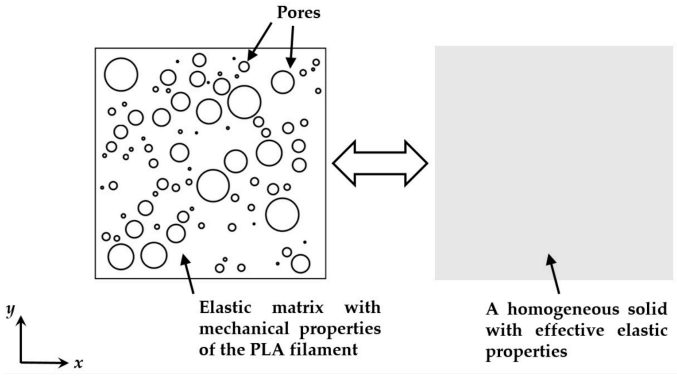

Figure 2.12: Representative volume element and equivalent homogeneous solid [56].

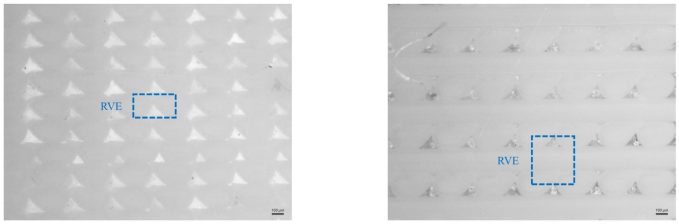

Figure 2.13: Microstructural images of different layups including actual RVEs [63].

Quantitative characterization by X-ray computed tomography In this case, a micromechanical FEA was used for the prediction of elastic properties based on the microscopic details of an actual 3D-printed specimen that was characterized by XCT [56]. This model estimated the macroscopic response of the material via the two-dimensional analysis of a periodic RVE. The internal structure was envisioned as a square elastic matrix, where the pore size and distribution were determined from the actual pore sizes obtained by XCT, and the pores were assumed to be circular in shape; see Figure 2.12. In the end, predicted Young's modulus versus porosity curves were obtained that were generally close to those of other models.

Microstructural images and cross-sectional morphology Most FEA studies belong to this category, in which microscopic images are usually employed to acquire RVEs. Images obtained in [63] clearly showed inter-bead voids that were inherent to the printing process; see Figure 2.13. Two separate RVEs were selected for two different raster orientations, namely (a) a unidirectional (UD) layup, and (b) a 0/90 layup. In addition to the actual RVEs shown here, ideal RVEs were also directly obtained from the slicer software to study the influence of the microstructure. It was found that the use of actual RVEs had no advantages compared to using ideal RVEs for the 0/90 case. Similar to the model using quantitative characterization by XCT (i.e., [56]), Young's modulus versus air gap (related to porosity) curves were constructed using the models in [63]. However, only two raster orientations were investigated in [63], while [56] considered four variations in raster orientation.

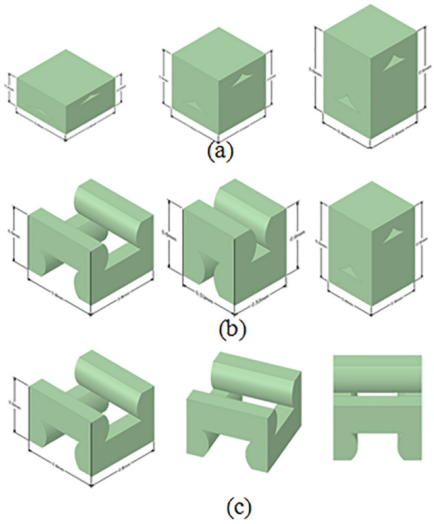

Figure 2.14: Idealized RVEs for (**a**) negative air gap and different layer heights, (**b**) constant layer height and different air gap values, and (**c**) positive air gap and different raster orientations [58].

Other studies started directly from an idealized RVE, in which the cross-sectional morphological characteristics of FDM parts (such as voids) were observed to occur in a repetitive pattern [58]. In [58], the effect of a variety of printing parameters on the mechanical properties were investigated by altering the layer thickness, raster orientation, and air gap. The RVE was modeled assuming that the inter-layer boundaries were completely fused with adjacent material, which is arguably an overestimation of the inter-layer bond strength. The considered ideal RVEs are depicted in Figure 2.14. Again, the results suggested a relationship between the elastic modulus and air gap (i.e., porosity). Additionally, relationships for both the elastic and shear moduli were obtained with respect to all the considered printing parameters.

Homogenization approaches For this purpose, a phenomenological numerical model is used to compute local stiffness matrices from an RVE [77]. In this specific study, raster orientation, build direction, and inter-facial bond dimensions (which are related to layer thickness, bead width, overlap interval, and air gap) were taken into account at the microscale. To characterize the material at the macroscale by making use of the Mori–Tanaka homogenization framework, the model considered the RVE as springs and dashpots to include both elastic and plastic responses. The effect of porosity (i.e., voids) was included by reducing the RVE's stiffness for larger porosities. Figure 2.15 presents a schematic representation of the load transfer between the macro- and microscale for three different build directions. The results of the experiments were used to model the geometry of the RVE. As shown in Figure 2.15, the material response was elastic until yielding occurred, i.e., $x \leq x_A$, after which plastic deformation occurred, i.e., $x > x_A$.

More recent developments by Monaldo et al. [73, 74, 76] included multi-scale approaches that considered the cross-sectional shape of the microstructure using a reduced-

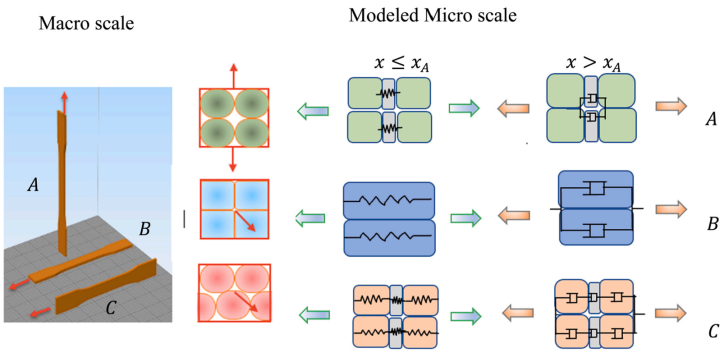

Figure 2.15: Schematic representation of the load transfer between the macro- and microscale for three different build directions [77].

order model (ROM) while performing macroscopic homogenization by means of first-order shear deformation laminate theory (FSDT). To represent the microstructure of 3D-printed polymers, these models considered pseudo-elliptical bead shapes including porosity (referred to as unit cell (UC)); see Figure 2.16. Initially, the authors used geometrical data from Alaimo et al. [51] and Garg and Bhattacharya [55] in [73], while microscopic images were used in [76]. Previous modeling attempts assumed a constant layer height and perfect inter-layer bonding, although changes in raster orientation were permitted in each layer [73]. Further assumptions in these two-level multi-scale models included that the bead phase (i.e., material parallel to the printing path) behaved elasto-plastically and exhibited locally homogeneous and isotropic behavior [76]. A major drawback in the earlier multi-scale models proposed by Monaldo et al. [73, 76] was that they did not consider damage phenomena like inter-layer and intra-layer bond failure, which were identified from the plastic deformation results in [76].

Nevertheless, Monaldo and Marfia [74] realized the importance of capturing the inter-layer and intra-layer (de-)cohesion when simulating the strength of 3D-printed polymers produced by material extrusion. To this end, they extended their former multi-scale models by introducing a cohesive damage interface model using a cohesive constitutive relationship through transformation field analysis (TFA). In this case, the UC (or RVE) was described by a parallelepiped including four quarters of the previous pseudo-elliptical bead shapes with a void at its center (see Figure 2.17). Similar to other works, the bead phase was described by elasto-plastic behavior (e.g., [51, 73]). The cohesive damage interface model enabled the inclusion of de-bonding and cohesive cracking among neighboring beads by means of zero-thickness interfaces. Monaldo and Marfia [74] also addressed the limited availability of inter-facial properties, which is duly noted by the author. Therefore, they assigned inter-facial stiffness and strength properties based on assumptions. The results indicated intra-layer de-cohesion, with most damage occurring near the void. Contrary to most reports in the literature, inter-layer damage did not appear. Furthermore, it is worth mentioning that all models proposed by Monaldo et al. [73, 74, 76] achieved significant savings in computational demand (i.e., internal or historic variables) compared to non-linear FEA (e.g., FE^2). To the best of the author's knowledge, the multi-scale technique proposed by Monaldo and Marfia in [74] was the

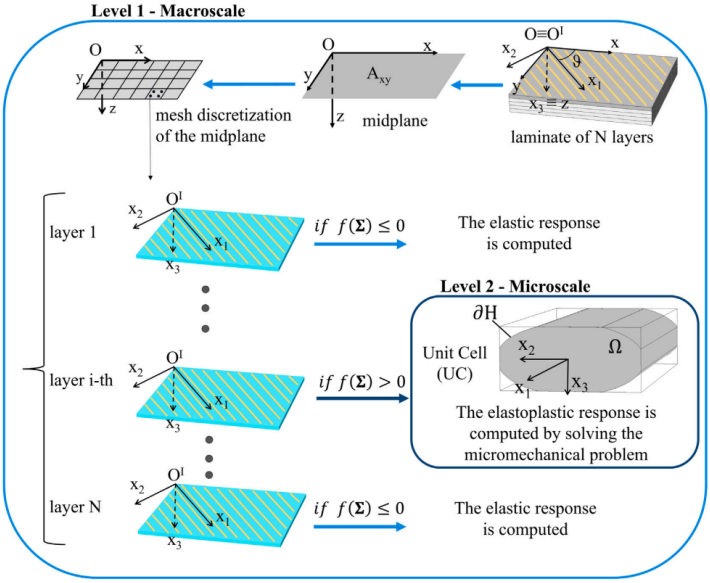

Figure 2.16: Schematic description of the two-level strategy for multi-scale analysis [76].

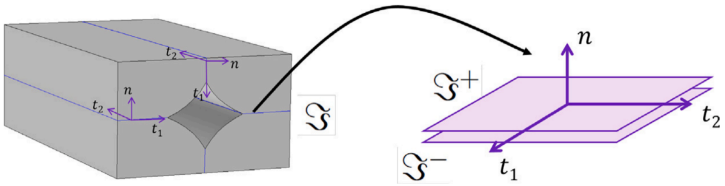

Figure 2.17: Schematic representation of the interface and its local coordinate system [74].

first to *explicitly* incorporate both the porosity and inter-facial bond properties (i.e., inter-layer and intra-layer bond strengths) simultaneously in a numerical (microstructural) model for 3D-printed polymers produced by material extrusion.

SPECIMEN-LEVEL MODELS

Several studies have focused on modeling a complete 3D-printed specimen with FEA [54, 55, 77]. However, only Garg and Bhattacharya [55] have reported a realistic geometrical representation of an FDM tensile test specimen (ASTM D638), which was created in accordance with microscopic images. The entire specimen was modeled in 3D, only excluding the regions under the grip in the tensile testing machine to reduce computational costs. As a result, various printing process parameters had to be included in the model, such as raster orientation, layer thickness, overlap interval, and air gap. Isotropic and homogeneous material behavior was assumed, based on experimental data for solid samples. The entire three-dimensional tensile specimen model can be seen in Figure 2.18. It was observed that necking occurred for raster orientations parallel to the loading direction, and inferior strength was obtained for specimens with a build direction parallel to the direction of loading.

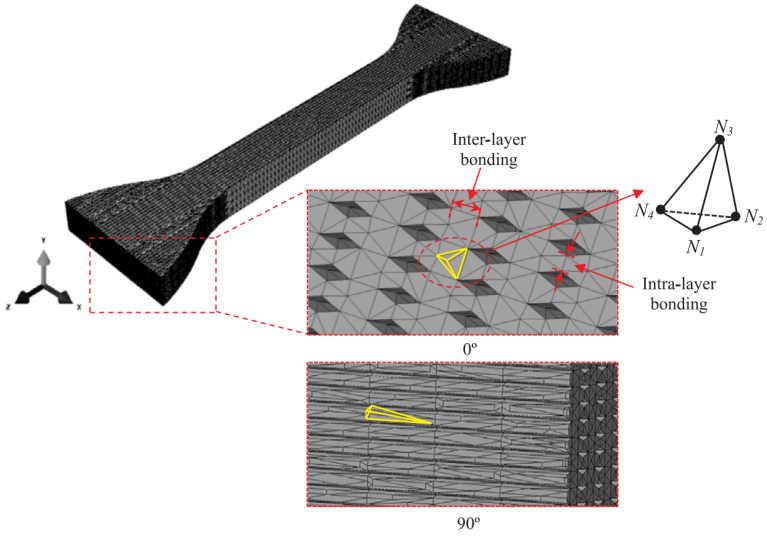

Figure 2.18: Three-dimensional tensile test specimen model, including mesh and elements [55].

FEA studies using phase-field models for 3D-printed parts also considered complete specimens [99–102]. The printing process parameter investigated in these studies was raster orientation. Most of these studies were limited to two-dimensional representations, but Khosravani et al. simulated both 2D [101] and 3D specimens [102]. Li et al. [100] presented an elasto-plastic phase-field model that incorporated anisotropy through damage variables for the bulk material (i.e., filament or bead failure) and inter-layer direction, while Khosravahni et al. [101, 102] utilized anisotropic cohesive phase-field models. The publication by Lampron et al. [99] proposed a combination of the former two phase-field models, resulting in an anisotropic fracture model comprising cross-layer fracture (i.e., filament or bead failure) and inter-layer fracture (similar to Li et al. [100]) without an explicit consideration of interfaces. The quantitative and qualitative experimental findings from three-point bending specimens agreed well with the numerical results for different raster orientations; see Figure 2.19.

2.4.3. ANALYTICAL AND THEORETICAL MODELS

Two types of analytical and theoretical models are distinguished for 3D-printed materials in this study, namely yield criteria and plasticity models and predictive and generalized strength models. In what follows, some notable models found in the literature will be discussed.

YIELD CRITERIA AND PLASTICITY MODELS

Three-dimensionally printed materials have already been modeled using classical lamination theory (CLT) and the Tsai–Hill yield criterion in several studies [51, 64], where layers of parallel beads are considered as lamina. The material strength of AM parts is incorporated through the Tsai–Hill yield criterion for the multi-axial loading of composites. The resulting expression can be used to compute the material's yield strength with

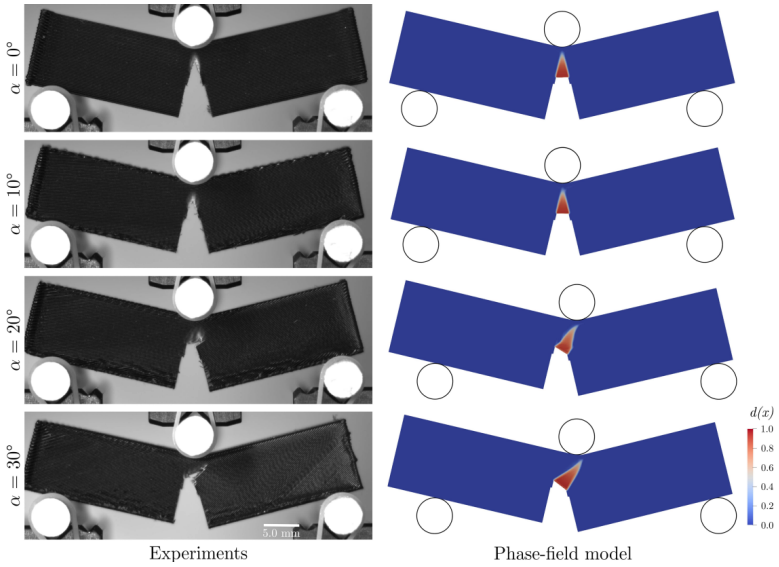

Figure 2.19: Experimental and phase-field model crack paths from 3-point bending specimens [99].

respect to raster orientation. Furthermore, an equation for obtaining the elastic modulus with respect to raster orientation for unidirectional printed parts is derived, as well as insight into strain at failure, shear modulus, and shear strength [51]. Another strategy for modeling the plastic and damage behavior of 3D-printed parts was presented by Kerekes et al. [54], using a Gurson–Tvergaard (GT) yield function for porous plastic materials and inverse analysis. This yield function decreased with increasing pore volume fractions, enabling the inclusion of softening behavior.

PREDICTIVE AND GENERALIZED STRENGTH MODELS

Croccolo et al. [57] addressed the availability of *predictive models* that account for important printing process parameters and are capable of predicting the mechanical properties of 3D-printed parts, specifically referring to strength and stiffness. To this end, an analytical model was developed to match experimental findings by incorporating influential parameters like part dimensions, build direction, bead width, raster orientation, layer thickness, and the number of contours. These types of models can be particularly useful in the design of FDM-printed components to avoid the extensive tuning of printing parameters like the air gap and raster orientation, which are usually set to default values in the production process. The model considered here could provide strength and stiffness characteristics given the aforementioned parameters. This is shown in Figure 2.20, where it can be seen that the predictive analytical model corresponded particularly well in the initial stage to the experimental results.

Another approach is represented by generalized strength models for predicting the tensile failure strength resulting from inter-layer failure in 3D-printed parts [64]. Previously, it was concluded that the failure of FDM-manufactured parts mainly occurred along layer interfaces (see Section 2.3). Therefore, the strength model developed in [64] was based on this characteristic of 3D-printed polymers and included TFS (as defined in

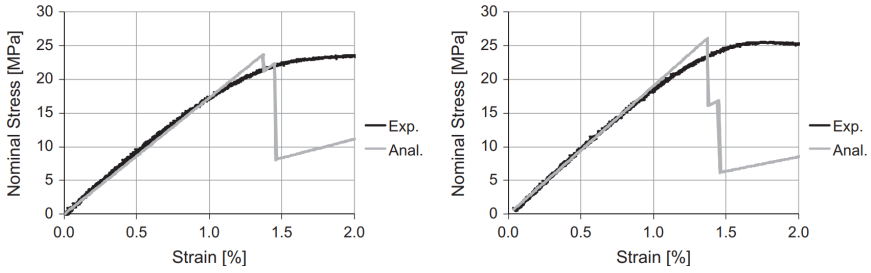

Figure 2.20: Predictive analytical model compared to numerical and experimental results [57].

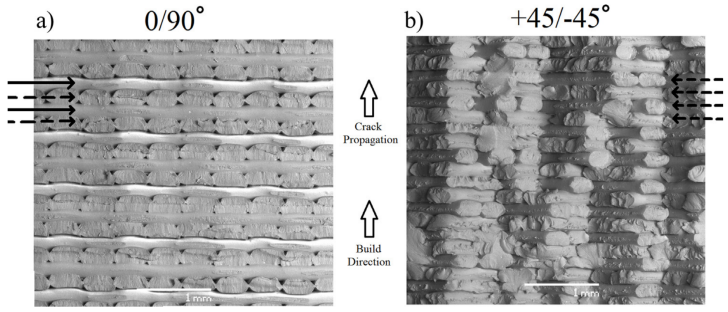

Figure 2.21: SEM fracture surfaces for two different raster orientations: (**a**) 0°/90° and (**b**) ±45° [78].

Section 2.3) as well as *shear failure strength* (SFS). TFS and SFS can be determined from experiments to obtain expressions for failure, equivalent to an inter-layer failure-informed failure criterion. Similar to the yield criteria and plasticity models discussed above, a generalized strength model can predict the inter-layer failure of FFF 3D-printed materials as a function of raster orientation.

2.4.4. MICROSTRUCTURAL AND FRACTOGRAPHIC ANALYSES

In order to gain more insight into the printing process parameters affecting the failure mechanisms of 3D prints and the geometric characteristics of their microstructures, a variety of microstructural and fractographic analysis techniques are available. A vast majority of this information is acquired through scanning electron microscope (SEM) pictures, e.g., [53, 55, 60, 67, 78, 87], of which an example has already been shown in Figure 2.2 from [67]. For instance, by considering the fracture surfaces obtained in [78] (see Figure 2.21) it was concluded that 0°/90° specimens failed in a brittle manner, presenting a planar fracture surface (Figure 2.21(a)), while the ±45° specimens showed a more jagged saw-toothed topography, resulting in more energy dissipation, which increased the fracture toughness (Figure 2.21(b)). In Figure 2.21, dashed arrows indicate shear failure and solid arrows illustrate inter-filament failure.

Other types of resources include microphotographs [61] or optical microscopy images [63], photographic images [62], and XCT [56, 59]. A microphotograph taken from [61] was shown earlier in Figure 2.2(a). These resources can be used for fractographic analysis, but their primary use is in determining the effect of process parameters like cross-sectional shape parameters.

2.4.5. GEOMETRICAL ANALYSIS

Geometrical analysis is considered to be the most important characterization and modeling strategy for representing and idealizing the microstructural geometries of 3D-printed polymers. However, Paul [50] concluded in his extensive literature review that surface quality and geometry defects in FDM-printed parts are the least researched aspects in available publications and that only a few defects have been identified. Furthermore, no finite element models exist that consider defects in the geometry and surface finish of FDM-manufactured samples. According to Paul [50], various geometrical models have been suggested in the existing literature concerning the evaluation of edge quality and surface quality. This section reviews two specific types of geometrical analysis found in the literature, namely edge profile simulations and surface roughness and quality models.

EDGE PROFILE SIMULATIONS

Edge profiles can be described as surface errors along the edges of 3D-printed parts resulting from the printing technique. These usually comprise geometric effects that cause differences compared to the intended CAD model, such as the staircase effect discussed above. Based on earlier work, Armilotta [69] presented a graphic and numerical approach for edge profiles in FDM prints in order to simulate position and form errors [50]. In this method, the edge profile was modeled based on layer thickness and three characteristic angles (inclination angle α, included angle β, and incidence angle γ). To illustrate the exactness of the simulation with respect to the shape and size of the edge profiles, Figure 2.22 compares experimentally measured profiles with simulated profiles for several different combinations of characteristic angles. Figure 2.22(a) depicts a horizontal edge, Figure 2.22(b) shows a stair-stepped edge with partial drag, Figure 2.22(c) displays a stair-stepped edge with complete drag, and a side-facing edge can be seen in Figure 2.22(d). It was concluded that the shape of all edge profiles was simulated with sufficient correctness, except for the side-facing edge in Figure 2.22(d). The term *drag* refers to the so-called drag effect that is assumed to be caused by the extruded bead sticking more strongly to the underlying deposited layer than to the metal printer nozzle. Stair stepping has already been discussed in Section 2.2.

SURFACE ROUGHNESS AND QUALITY MODELS

According to [70], the elliptic cross-sectional shape of deposited beads suggested by Ahn et al. [72] is the most realistic approximation. This model approached the surface profile shape as a series of elliptic curves that overlap each other when stacked in the vertical direction, representing the deposited layers [70], as observed in Figure 2.2 in Section 2.2. First, an expression for the surface profile was defined through the schematic representation in Figure 2.23(a). From this figure, it can be observed that the surface profile depends on a variety of printing process parameters, namely the surface angle (θ), cross-sectional shape (a, b), layer thickness (t), overlap interval (c), and bead width ($2a$). Eventually, these process parameters were used to model the surface roughness. However, at some point the elliptic curves only have a single point of contact for a specific surface angle [72]; see Figure 2.23(b). This surface angle value is defined as the critical angle (θ_c) and relies on the previously listed parameters. If this angle is below the critical angle value, neighboring beads do not cross or touch, as illustrated in Figure 2.23(c), and the surface roughness cannot be established. Ahn et al. [72] referred to this region, where the

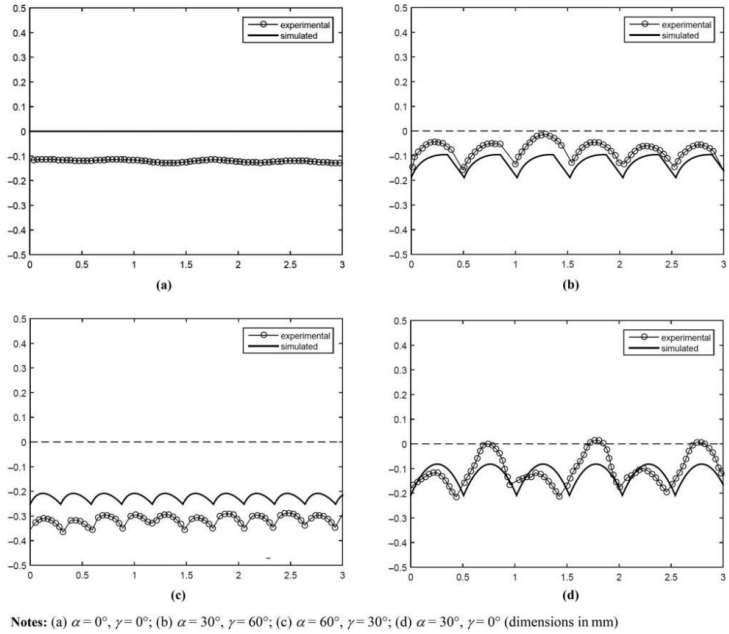

Notes: (a) $\alpha = 0°$, $\gamma = 0°$; (b) $\alpha = 30°$, $\gamma = 60°$; (c) $\alpha = 60°$, $\gamma = 30°$; (d) $\alpha = 30°$, $\gamma = 0°$ (dimensions in mm)

Figure 2.22: Comparison of measured and simulated profiles for constant layer thickness and β [69].

surface angle is smaller than θ_c, as the 'indeterminate region'. In the end, the simulated surface roughness values were compared with experimental data, which confirmed the validity of the obtained expression, proving its remarkably realistic approximation of the cross-sectional shape of FDM-printed parts. Haque et al. [71] used this model to show that the surface roughness is mostly affected in a negative way by the layer thickness, while other printing parameters were found to have a weaker effect.

However, as mentioned above, this geometric model is not defined if adjacent ellipses do not intersect [70] (see Figure 2.23(c)). In other words, the model works for surface angles $\theta \geq \theta_s$. Based on the same concept as the model of Ahn et al. [72] using elliptic curves to approximate the surface profile, an extension of this model was proposed in [70] that was also defined for surface angles smaller than the critical surface angle value, i.e., $\theta < \theta_s$. Similarly, the evaluation of the surface profile was performed in a normal section that was orthogonal to the contours. Figure 2.24 illustrates this for (a) $\theta > \theta_s$, which is similar to the model in Figure 2.22, and (b) $\theta < \theta_s$, where the stair-stepping is included.

For $\theta < \theta_s$, the surface profile is defined by steps that are composed of several ellipses, depending on the surface angle (θ), layer thickness (L), overlap interval (c), air gap (H), raster orientation (β), and cross-sectional shape parameters (a, b) or the ratio between the bead's long and short axes ($r = a/b$). The resulting expression of the surface profile is defined by the schematic model shown in Figure 2.25. However, it should be noted that the model works under the assumption that a negative air gap is used, meaning that the hatching part of the layers intersects with adjacent beads. This is not always the case in practice, but it can be defined in the printing process parameters. Concerning the input parameters, layer thickness, air gap, and raster orientation can be directly obtained

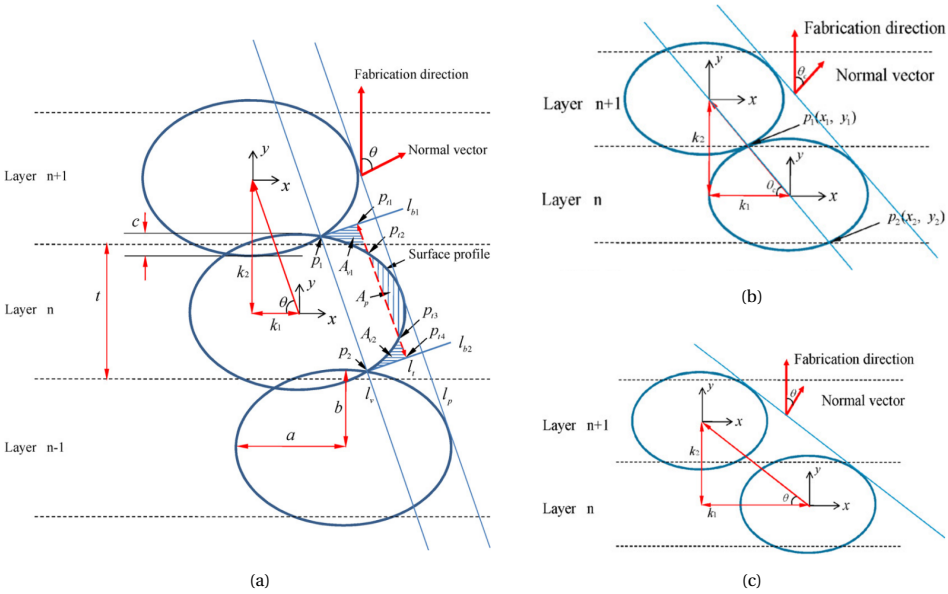

Figure 2.23: Representation of the geometric model by Ahn et al. [72]. (**a**) Representation of geometric model. (**b**) In the case of a single point of contact (θ_c). (**c**) In the case of no intersection or contact.

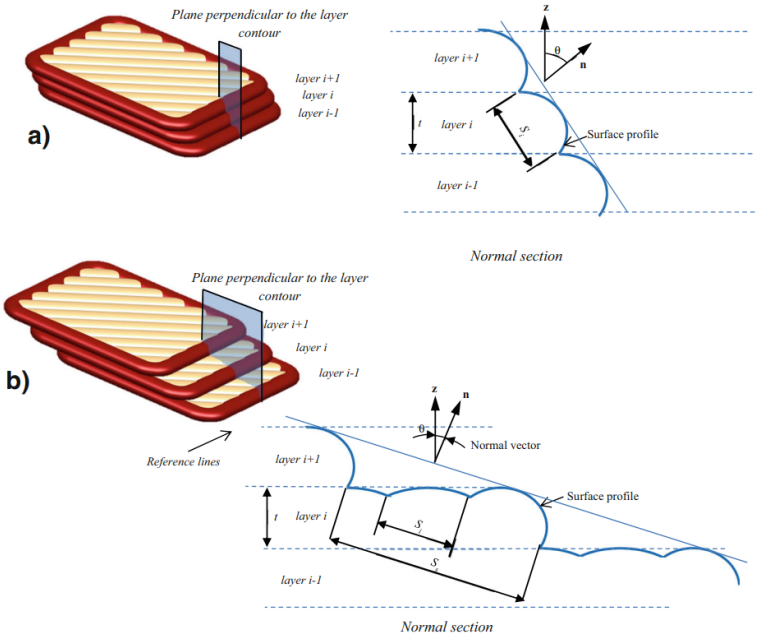

Figure 2.24: Surface profile contours for (**a**) $\theta > \theta_s$ and (**b**) $\theta < \theta_s$ [70].

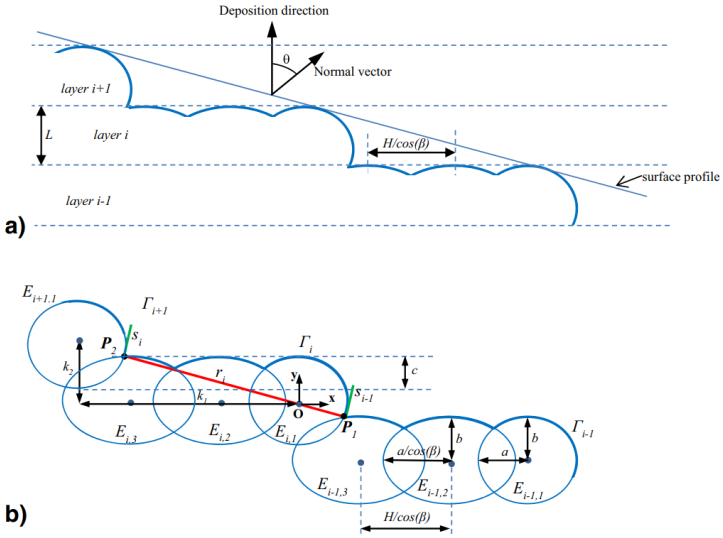

Figure 2.25: Representation of the extended geometric model by Angelo et al. [70]. (**a**) Approximation of surface profile with ellipses. (**b**) Theoretical model definition of surface profile.

from the machine data. On the other hand, the overlap interval and cross-sectional shape parameters should be measured from available microstructural analysis, e.g., SEM pictures (Figure 2.2) or other methods discussed in Section 2.4.4, as these are affected by other process parameters.

The geometric model depicted in Figure 2.25 and proposed by Angelo et al. [70], which is an extended version of that presented by Ahn et al. [72], works for any surface angle θ with only very minor deviations for $\theta \leq \theta_s$ as well as $\theta > \theta_s$. A comparison between the surface roughness obtained from the model and experiments showed good agreement, once more proving the model's ability to realistically represent the cross-sectional shapes of FDM-printed parts.

2.5. CONCLUSIONS

Several conclusions can be drawn from this review of the microstructural modeling of 3D-printed polymers. To begin with, the vast majority of experimental analyses of 3D-printed FDM parts are tensile tests performed on the specimen scale (ASTM dog bones). These experimental results are therefore not informative for smaller-scale (numerical) analyses, such as microstructural analysis. Furthermore, existing FEM analyses have mostly neglected the effects of internal bonds, i.e., the intra-layer and inter-layer bonds, with only a few recent exceptions. Rather, they have focused on the incorporation of porosity in geometrical representations of the material, but inter-layer and intra-layer bond properties like strength have rarely been considered. Only some recently published FEA studies using phase-field models for 3D-printed materials have actually distinguished between cross-layer or bulk layer failure (i.e., filament or bead failure) and inter-layer or inter-phase failure in their formulations. To the best of the author's knowledge, only one very recent multi-scale technique *explicitly* incorporated both the porosity and inter-

Table 2.2: Printing process parameters negatively affecting the mesostructure characteristics

Characteristic Mechanical Property	**Printing Process Parameter**
Strength	Raster orientation [51, 55–57, 64, 83, 99–102] Cross-sectional shape [55, 57] Layer thickness [55, 57] Overlap interval [55] Air gap [55, 57] Porosity [54] Build direction [57] Bead width [57] Number of contours [57]
Fracture toughness	Build direction [78] Raster orientation [78, 81, 82]
Inter-layer bond strength	Cross-sectional shape [51, 55, 73, 74, 76, 77, 80–82] Printing temperature [80–82] Printing speed [80–82] Porosity [55] Raster orientation [64, 99–102]
Stiffness	Porosity [56, 58, 77] Air gap [57, 58, 63, 77] Raster orientation [51, 56, 57, 63, 77] Build direction [57, 77] Cross-sectional shape [77] Layer thickness [57, 77] Bead width [57, 77] Overlap interval [77] Number of contours [57]

facial bond properties (i.e., inter-layer and intra-layer bond strengths) simultaneously in a numerical (microstructural) model for 3D-printed polymers produced by material extrusion. Analytical models may be helpful in illustrating tensile failure strength and stiffness in the linear-elastic regime, but these are highly dependent on the numerous printing process parameters. On the other hand, microstructural and fractographic analyses can provide useful geometrical input. Resources like SEM pictures, microphotographs, optical microscopy images, and XCT can be used for determining cross-sectional shape parameters. Finally, geometrical analyses can be used to realistically represent and idealize the microstructural geometries of 3D-printed polymers.

From the conclusions above, it can be said that smaller-scale experiments are required to obtain appropriate input parameters, i.e., cross-sectional shape parameters, surface intact ratios, and intra-layer and inter-layer bond strengths. This allows for the explicit incorporation of internal bonds by not only considering porosity, but also including the (adhesive) bond strength between layers. Considering the significant influence of

(small changes in) the printing process parameters on the characteristic mechanical properties of 3D-printed polymers, it is important to conduct tests with consistent printer settings at all length scales. When using consistent printing settings for all 3D-printed polymers, the geometrical input can be measured via microstructural analysis (e.g., XCT) to geometrically represent and idealize the respective microstructures using geometrical models.

However, capturing the (highly) anisotropic nature of FDM 3D-printed parts in numerical models still requires additional attention. Before polymeric parts created through material extrusion are allowed to be used in final consumer products, it is important to develop robust numerical models that can adequately describe and predict their mechanical properties regardless of their shape and complexity. Besides the locally inherent anisotropy caused by the spatial arrangement of porosity and weaker inter-facial bonds (i.e., the inter-layer and intra-layer bonds) that align with the printing path orientation at the material level, these printing path orientations can also change throughout 3D-printed parts at the global level. For instance, printing paths can be rather straightforward and parallel or significantly more complex when constantly changing direction within the same layer. Particularly in the latter case anisotropy cannot be introduced globally, meaning it is important that constitutive relationships are assigned locally in accordance with the changing printing path orientations. Even though recent studies proposed for the first time promising multi-scale approaches that consider the cross-sectional shape of the microstructure including both the porosity and the inter-facial bond properties (i.e., inter-layer and intra-layer bond strengths) in numerical models for 3D-printed polymers produced by material extrusion, which is a major contribution to the field, these are still limited to globally imposed parallel printing paths in each layer. When the printing paths are locally changing direction (even within a single layer), the interface directions are also constantly changing, such that the inherent anisotropy becomes dependent on the printing path orientation. Globally, this introduces an additional level of directional-dependency which is referred to here as *printing path-dependent anisotropy*.

In other words, there is a need for printing path-dependent models that locally take microstructural information into consideration for the inherent anisotropy and impose this globally based on changing printing path orientations. The printing path orientations can be directly adopted from the (CAD) model's G-code, while the assignment of printing path-dependent properties can be achieved using a local coordinate system in which one of the axes is oriented in the direction of the printing path and the others correspond to the inter-layer and intra-layer bond phases, respectively. Such models will provide a more robust, realistic, and reliable simulation approach for 3D-printed polymers produced by material extrusion since they can locally capture the effects of both the inter-layer and intra-layer bonds in relation to the globally changing printing path directions as a result of this AM technique.

3

DEVELOPING MODELS FOR 3D PRINTED REINFORCEMENTS

Additive Manufacturing (AM) methods like material extrusion in 3D printing present the opportunity to construct auxetic structures. Nevertheless, extruded 3D printed material can be highly anisotropic. Before 3D printed auxetics manufactured through material extrusion can be used in engineering applications, it is important to generate powerful simulation tools that can reliably reproduce and predict their mechanical characteristics irrespective of their form and intricacy. In view of this, the current work proposes printing path-dependent models based on an experimentally validated multi-scale modelling scheme using the Lattice Beam Model (LBM). This is done by first representing idealized microstructures of extruded 3D printed polymers through geometric models and simulating these on the material scale. The aim is to explicitly model the inter-layer and intra-layer bonds that exist in material extruded 3D printed parts by assigning experimentally obtained interface properties that significantly differ from the bulk material. On the auxetic structure scale, two planar auxetic designs are modelled using the determined material scale relationships as input: Re-Entrant (RE) and Rotating Square (RS). In terms of mechanical response, the experimentally and numerically obtained force displacement curves agree reasonably well: the stiffness of the modelled auxetic designs fit well with the experimentally measured ones while the LBM simulations generally provide a good estimation in strength. Finally, it has been shown on both the material and auxetic structure scales that incorporation of the interfacial bond strengths in simulations of extruded 3D printed polymers is important, because neglecting these results in significant overestimation of the strength.

With the exception of minor textual adjustments, this chapter is reproduced from: R.J.M. Bol, Y. Xu, B. Šavija, *Printing path-dependent two-scale models for 3D printed planar auxetics by material extrusion*, Additive Manufacturing **89**, 104293 (2024).

3.1. INTRODUCTION

In view of advances in Additive Manufacturing (AM) techniques, mechanical metamaterials have emerged [27] that exhibit extraordinary properties because of their rational designs [28]. Metamaterials can be defined as man-made, artificially-designed materials [29] whose unique physical properties arise from their deliberately designed internal geometry rather than their chemical composition. One particularly interesting class of mechanical metamaterials are those having a negative Poisson's ratio, which are referred to as 'auxetic materials' [30–43]. Auxetic materials are known to have a variety of mechanical properties that are scarce in common natural (non-auxetic) materials: synclastic curvature in bending, variable permeability, high shear stiffness, high specific strength, enhanced indentation resistance, high fracture toughness, impact resistance, fatigue toughness, improved damping, sound and energy absorption properties, and being lightweight [29, 33–35, 37, 40–47]. Because of their geometrical complexity, auxetic designs cannot always be easily created [32]. However, AM methods like 3D printing present the opportunity to construct auxetic structures, as suggested in the latter reference. Nevertheless, AM techniques are prone to several issues that affect the auxetic behaviour. For example, 3D printed material can be highly anisotropic [34]. AM parts can also contain various geometrical imperfections [39], while it is important to have sufficient printing accuracy in relation to mechanical properties of auxetic designs [32, 48].

It is known that a material's auxetic response and its related mechanical characteristics strongly depend on the deformation mechanism [37]. Based on these deformation mechanisms, auxetic materials can be classified. Numerous designs exist that (potentially) possess auxetic behaviour of which the most common and important classes are honeycomb arrangements of re-entrant models [29–34, 37–40, 48, 103–106], rotation unit mechanisms [29, 30, 34, 37, 38, 41, 48] and chiral mechanisms [29, 34, 37, 38, 41, 48, 105, 106]. Some auxetic designs may have a varying Poisson's ratio under deformation as a result of their structural motif, like re-entrant mechanisms. Other classes may only exhibit auxetic behaviour under compression, such as buckling induced mechanisms, while different ones only work in tension, which is the case for fibril/nodule mechanisms [37]. It is therefore essential to gain a thorough comprehension of the different deformation mechanisms involved in auxetic structures when selecting, designing and using auxetic materials for engineering applications.

Because of their enhanced mechanical characteristics, auxetic materials already have applications in numerous fields, such as automotive [32–34, 41, 107], aerospace [32, 34, 40, 41], military [32, 33, 41], (bio)medical [32, 33, 37–41, 46, 107], textile industry [33, 37], construction industry [37, 41, 46, 47], and protection [32, 37, 40]. Some examples of applications in the aforementioned fields are biomedical stents [38, 105], military and protection knee caps, safety jackets and helmets [32, 37], fastener, rivets and sandwich panels in construction [37, 46, 47], and fiber-reinforced composites [37, 46]. Future extensions may include specific engineering applications, like impact resistance structures and vibration mitigation structures [42], for instance in barriers for offshore break-waters and earthquakes in extreme conditions [43], respectively.

Recently, several studies have demonstrated that the use of 3D printed polymeric lattice reinforcement can improve the properties of cementitious composites [75, 108, 109]. Among these, auxetic designs have shown the best performance when the composite is

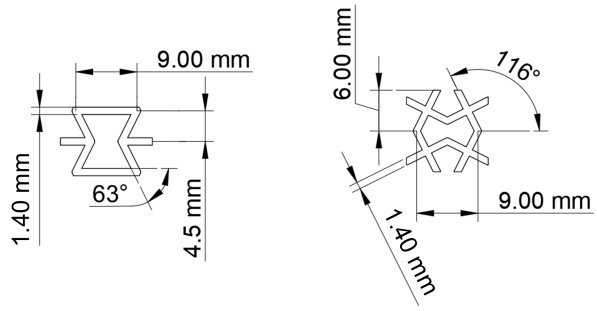

a) Re − Entrant (RE) b) Rotating Square (RS)

Figure 3.1: Design parameters for a) Re-Entrant (RE) and b) Rotating Square (RS) auxetic structures (unit cells)

subjected to uniaxial compression [110]. Nevertheless, the fabrication procedure of these reinforcements has a great influence on their mechanical behaviour, which is strongly dependent on the printing and loading directions [111]. In this study, therefore, it was chosen to focus on print-path dependent modelling of the two auxetic designs that showed the best performance in a previous study, namely Re-Entrant (RE) and Rotating Square (RS) [110]. Specifically, the compressive strength, ductility and crack-arresting effect of cementitious composites having 3D printed reinforcements considering four auxetic designs based on different deformation mechanisms (i.e., re-entrant mechanism, rotation unit mechanism, and chiral mechanism) were evaluated. The conclusions showed that both RE and RS auxetic reinforcements exhibited stronger crack-arresting effects under uniaxial compressive loading, thereby achieving comparable compressive strengths with plain mortar despite the inclusion of a softer polymeric phase, which was considerably higher than the other designs.

RE is the most basic and widely studied class of auxetic materials [29–34, 37–40, 48, 103–106]. These auxetic structures typically consist of thin ribs or trusses that are connected by hinges. The result is a polygonal truss having a repetitive pattern, usually referred to as a unit cell [37]. The term refers to one polygon angle being larger than 180° or negative [33]. One famous design is the RE bowtie honeycomb structure, whose unit cell is shown in Figure 3.1(a). RS is sometimes distinguished as another auxetic model in literature (e.g., [30]), referred to as a type of missing rib mechanism. Figure 3.1(b) depicts its unit cell. This specific auxetic design gets classified under most deformation mechanisms in various other literature (e.g., [30, 38, 48]). However, because of its rotational deformation mechanism, in this work it will be referred to as RS, similar to the former study by Xu & Šavija [110].

A review on micromechanical models for extruded 3D printed polymers, specifically Fused Deposition Modelling (FDM), is provided in Chapter 2. Therein, it is concluded that incorporating the (large) anisotropy present within microstructures of 3D printed parts manufactured through FDM needs more dedication to this day. Before 3D printed auxetics manufactured through material extrusion can be used in engineering applications, it is important to generate powerful simulation tools that can reliably reproduce and predict their mechanical characteristics irrespective of their form and intricacy. One example are the printing paths, which can be straight but frequently alternate their course already in

one layer. Especially for these deviating instances, it is important that material properties get allotted corresponding to all different printing path directions. Albeit Monaldo & Marfia [74] were the first to suggest a two-scale methodology for extruded 3D printed polymers which models microstructural geometries that consider both the voids and pores as well as the inter-layer and intra-layer bond strengths, an important development in this research area, it remains limited to constant printing paths within one layer. If printing paths are frequently alternating (already in the same layer), so is the directionality of the interfacial bonds which imposes supplementary directional-dependent anisotropy or *printing path-dependent anisotropy*. Put differently, printing path-dependent models are required that incorporate the characteristic features of extruded 3D printed polymers' microstructures.

In view of this, the current work proposes printing path-dependent models based on an experimentally validated two-scale modelling scheme using the Lattice Beam Model (LBM). This is done by first representing idealized microstructures of 3D printed polymers through geometric models described in Chapter 2 and simulating these on the material scale. The aim here is to explicitly model the inter-layer and intra-layer bonds by assigning experimentally obtained interface properties that significantly differ from the bulk material. To the author's knowledge, this is the first time experimentally obtained inter-layer bond and intra-layer bond properties are explicitly considered in numerical simulations of 3D printed parts by material extrusion. On the auxetic structure scale, planar auxetic designs are modelled using the determined material scale relationships as input. In this approach, printing path directions can be straightforwardly received through the 3D printer's G-code containing all information about printing temperature, printing speed, nozzle size, layer thickness and motions for extruding the polymer material. The allocation of printing path-dependent material characteristics is executed by coupling the printing path directions to a locally introduced coordinate system wherein the main axis follows the printing path while the other two reflect the interfacial bond properties. The resulting simulation tools present a powerful, factual and trustworthy numerical methodology for extruded 3D printed polymers as these incorporate the mechanical characteristics of both interfacial bond strengths due to the AM technique of material extrusion.

3.2. MODELLING OF DEFORMATION & FRACTURE

Schlangen and van Mier suggested a numerical approach for simulating fracture in concrete in the 1990s, known as lattice modelling [112, 113]. The lattice concept was adopted from the field of theoretical physics [112, 114] and was first used to study elasticity problems of continua by Hrennikoff [115] in the 1940s. In this discrete approach the material is discretized into a lattice of two-node elements that transfer the forces [116]. These can be springs [117, 118], but usually trusses or beams are used as it has been shown that the latter provides more accuracy on fracture patterns [119]. Lattice models enable to study and take the material's microstructure into consideration [120] through superimposing the lattice network over original (micro)structures [113]. Heterogeneity can be incorporated by implementing an irregular mesh or assigning different material characteristics to each element [121] and fracture is included through element removal, sometimes preceded by (gradual [122]) stiffness deterioration [123].

LBM has proved to be successful in simulating fracture for various types of material besides concrete, e.g., cement-paste, porous reactor core graphite and wood, as addressed in [111, 116, 124–127]. It has also been applied to simulate fiber pull-out behaviour at the microscale [128] and structural behaviour of reinforced concrete at the macroscale [129, 130], including interface modelling of ribbed re-bars [127]. So, the approach has been used to model concrete at various length-scales (micro-, meso- and macro-scale) [129]. Furthermore, the model has also been used for purposes other than fracture, such as moisture transport and chloride diffusion in cement-based systems [131, 132]. More recent applications of LBM can be found in the field of AM for 3D Concrete Printing (3DCP) by Chang [133–136].

In terms of models for FDM 3D printed plastics, numerous efforts have been made through a variety of (microstructural) modelling strategies in literature, see Chapter 2. Given the promising implementations of LBM for multi-phase particulate materials, like concrete [113, 118] with its different phases (e.g., aggregates, cementitious matrix and interface [120] or ITZ [137]), it is believed that the inter-layer and intra-layer bonds that exist in FDM 3D printed parts can be modelled explicitly using LBM. Variations in element properties as a result of processing techniques like FDM can be simply incorporated through assigning different input properties to each lattice element [29]. The model has already been used for FDM 3D printed lattice materials by Xu et al. [111] in which the anisotropy as a result of the FDM method was only *implicitly* incorporated in the model, i.e., by adjusting the constitutive law of beam elements, resulting in accurate predictions of the material's fracture behaviour and mechanical response in uniaxial tensile tests. Additionally, imperfections (caused by the FDM process) can be easily incorporated in the LBM [133] by means of superimposing.

3.2.1. LATTICE BEAM MODEL

The basis of LBM is to discretize a material into a network of beam elements that are connected at their ends [122, 130]. Since in this case the ratio between the length and cross-sectional dimensions of these beam elements is small, Timoshenko beam elements are used to account for shear deformation [125, 136, 138]. These elements are assigned certain material properties [130], which are generally linear-elastic (e.g., [122, 127, 139]) but can also be non-linear (e.g., [116, 129, 140]). Although the locally assigned behaviour of an element may be brittle, a global quasi-brittle or ductile response can be obtained [122, 126, 127]. Fracture is simulated through loading the lattice by a prescribed deformation or an imposed load, followed by carrying out a linear elastic analysis. Subsequently, the stresses occurring in each element are compared to a prescribed failure criterion (e.g., strength, strain, or energy criteria can be used [127]). An element that exceeds this criterion is removed from the mesh, thereby representing a micro-crack (i.e., fracture) in the material. The reaction forces and displacement field are stored in each analysis step and the procedure is repeated: the damaged lattice is reloaded, discarding one element at a time until the network of beam elements ultimately fails. This stepwise removal procedure basically mimics crack initiation and propagation. In this way, all performed linear-elastic analyses form one non-linear analysis by which realistic crack patterns can be obtained [122, 127]. For details of the method, e.g., its solution procedure or stiffness matrix assemblies, the reader is referred to the works of Qian [112, 113].

3.2.2. LATTICE GENERATION

The method for lattice generation presented here generally follows the procedure as described in [29, 111, 122, 139]. The part to be modelled is discretized into a grid of cubic cells (3D lattice) or square cells (2D lattice [122]), as shown in Figure 3.2 for simplicity. Within every cell, having length A, sub-cells are generated with length s such that $0 \leq s \leq A$. Inside these sub-cells, lattice nodes are randomly positioned. This randomness is defined as the ratio between the sub-cell size s and cell length A:

$$R = \frac{s}{A}. \tag{3.1}$$

Disorder in the lattice mesh is introduced through population of a single lattice node inside each sub-cell based on random seeds obtained from a list of generated pseudo random numbers. Therefore, heterogeneity is already built-in. R is set to 0.5 in this study. In the case of a 3D analysis, all nodes have six degrees of freedom (three translations and three rotations) [122]. The method for lattice network generation will be explained next. The starting point is similar to the heterogeneous rectangular or quadrangular lattice network constructions used in e.g., [113, 139], where quadrangular meshes are used that simply connect the lattice nodes parallel to the three main directions (i.e., along the X, Y and Z axes) without any diagonals. However, the lattice network generation method adopted here considers all adjacent directional connectivity possibilities. Besides the three main directions (XX, YY and ZZ), it also considers planar diagonals (XY, YZ and XZ) and spatial diagonals (XYZ). It should be noted that this holds for any lattice node, meaning that duplicate and intersecting beam elements are unavoidable without any measures. To this end, certain criteria are enforced during the lattice network construction. Planar diagonals in each direction (XY, YZ and XZ) have two possible orthogonal configurations. Without any criterion, both orthogonal configurations would be generated causing intersections. This is avoided by measuring the length of both elements and only selecting the shortest one for all neighboring lattice nodes in each planar diagonal direction. The same procedure is adopted for the spatial diagonals (XYZ) having four possible mutually orthogonal configurations.

The phase to which each beam element belongs is identified through superimposing the lattice onto a geometrical representation of the part to be modelled, including its material composition. For instance, the domain in Figure 3.2 represents the microstructure of an FDM 3D printed polymer and contains four quarters of elliptical filaments, referred to as bead regions (the bulk material), and a central void region. If the two end nodes of a beam element are both located in the same bead region (i.e., one of the four quarters), it is defined as an element belonging to the bead phase and assigned its corresponding material properties. In the case of Figure 3.2, when the two end nodes are located in different vertically adjoining bead regions, the element is considered as an inter-layer element. Similarly, if the two end nodes are positioned in different horizontally neighboring bead regions, the beam element receives intra-layer properties (see Figure 3.2). Lattice nodes that appear inside a void region are excluded from the mesh, including the elements that would be connected these nodes (indicated by the grey dashed lines in Figure 3.2).

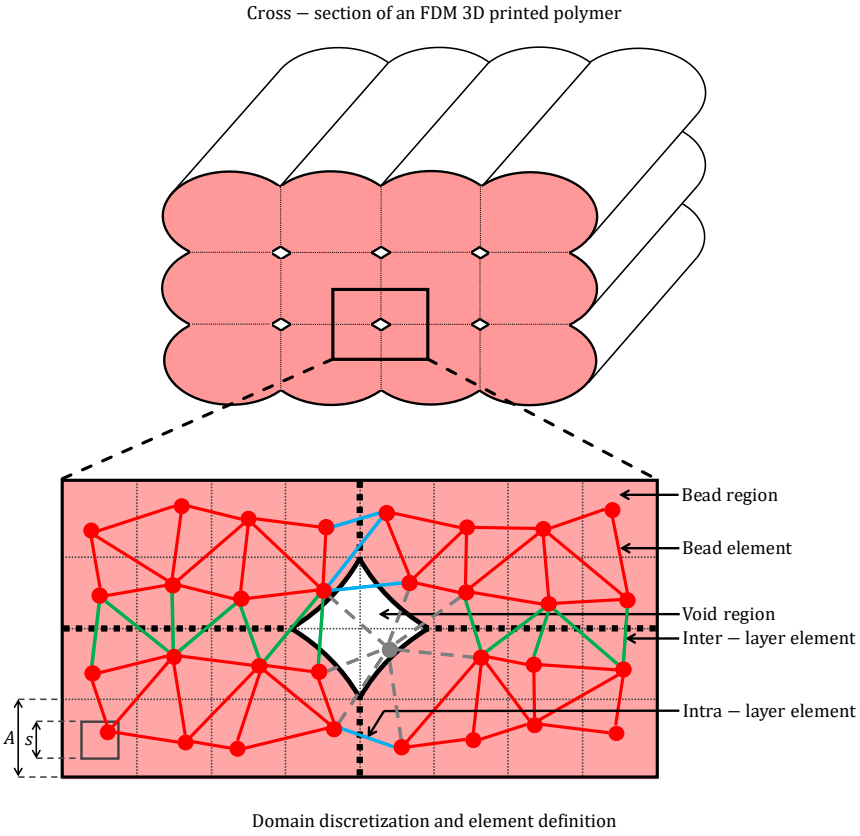

Figure 3.2: Schematics of domain discretization and element definition (shown in 2D for simplicity)

3.2.3. FAILURE ANALYSIS

The stresses occurring in each beam element are determined as follows [29, 111, 127, 133, 136, 138, 141]:

$$\sigma = \alpha_{\mathrm{N}} \frac{N}{A} + \alpha_{\mathrm{M}} \frac{\max\left(|M_i|, |M_j|\right)}{W}, \quad \text{with} \quad W = \frac{\pi D^3}{32}, \tag{3.2}$$

where N is the normal force, A the cross-sectional area, M_i and M_j are the maximum pure bending moments (in the plane with the longitudinal axis of the element) at both end nodes i and j, α_{N} and α_{M} are the normal force and bending moment influence factors, respectively, W is the section modulus of a circular cross-section and D the diameter of the lattice element. Torsional moments about the longitudinal axis are not included. Based on the aforementioned studies, α_{N} and α_{M} are taken as 1.0 and 0.05, respectively. The failure criterion used in the simulations presented here is based on strength, i.e., stress ($\mathbb{F}(\sigma)$):

$$\mathbb{F}(\sigma) = \frac{\sigma}{f_{\mathrm{y}}} \leq 1, \tag{3.3}$$

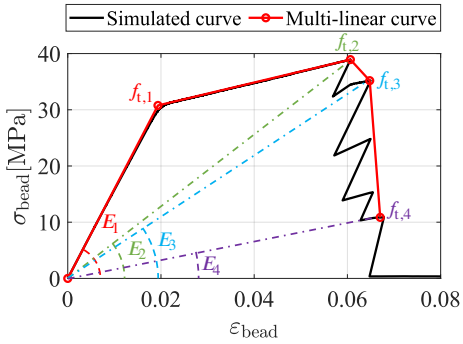

Figure 3.3: Example of a multi-linear constitutive relationship obtained at the material scale

where σ is the stress computed using Equation (3.2) and f_y the material's strength. If exactly one element reaches this failure criterion, i.e., $\mathbb{F}(\sigma) = 1$, the element is considered to have failed which results in removal from the mesh as stressed before.

3.3. METHODOLOGY

In the experimentally validated two-scale modelling scheme proposed here, constitutive relationships of lattice beam elements are derived from material scale (i.e., microstructural) simulations, providing input for local lattice elements in auxetic structure scale models [138]. Similar approaches using LBM have been previously described and found to be successful in various literature [113, 116, 126, 140, 142]. Numerical simulations of deformation and fracture using fine meshes for the microstructural model are computationally expensive [116], especially when a single length-scale approach is used this could be even impossible [126, 140]. To this end, the auxetic structure scale is discretized into smaller cubic cells. Subsequently, numerical simulations of tensile tests are performed on these smaller cubic cells, so-called material scale simulations. As a result of the material scale simulations, load-displacement and stress-strain curves are obtained that are schematized as multi-linear constitutive relationships to be used for the beam elements in the auxetic structure scale simulations. The beam elements are assigned with multi-linear relations obtained at the material scale, see Figure 3.3. Therefore, elements are not immediately removed in each analysis step, but their stiffness and strength change according to the implemented constitutive relationship. Once the element reaches its initial maximum stress, this element will adopt the stiffness and strength of the following point on the multi-linear curve. The element is only considered to have fully failed past the final point, which results in removal from the mesh as explained previously.

The first step in the two-scale modelling strategy is to geometrically describe and idealize the microstructures of extruded 3D printed material using the microstructural models established in Chapter 2. The resulting geometric model will be used as input for the LBM simulations as discussed in Section 3.2.1. Similar to what is often done in Finite Element Analysis (FEA), the general aim here is to determine a Representative Volume Element (RVE). However, besides the general approach to represent the microstructural morphology with the internal porosity, which is already often done in literature, this

study aims to explicitly model the interfacial bonds by assigning experimentally obtained interface properties that significantly differ from the bulk material.

To incorporate the effects of both porosity and internal bonds, the following methodology is proposed here. Initially, constitutive relationships shall be determined experimentally for three distinguished phases, namely: i) the bead or filament phase (i.e., the 'bulk material' without interfaces), ii) the inter-layer bond phase, and iii) the intra-layer bond phase. Their respective relationships will be obtained from material scale uniaxial tensile tests on dog bone shaped specimens. Seeing the significant consequences of (minor deviations in) printing settings on the material behaviour of 3D printed polymers in Chapter 2, these are kept constant throughout all length scales. Afterwards, the RVE will be modelled by means of LBM simulations using the measured geometrical input and constitutive relationships, thereby explicitly incorporating the effects of both porosity and internal bonds. Finally, the approach will be validated by means of auxetic structure scale LBM analyses of the planar auxetic designs using the determined material scale relationships as input.

3.3.1. MICROSTRUCTURAL EXPERIMENTAL ANALYSIS

Failure of extruded 3D printed polymers mainly occurs along layer interfaces [55], which is mainly due to poor attachment among layers, and must therefore be explicitly modelled. Occasionally, the tensile strength of parts that are printed in the vertical direction is utilized to estimate this interfacial strength [77]. Nonetheless, oftentimes it is not possible to acquire the interfacial strength among layers straightforwardly through stress and strain data [81, 82]. Therefore, this study will use material scale dog bone shaped specimens to obtain interface strengths to be used as input for the LBM simulations. Three different kinds of specimens have been designed to experimentally determine the constitutive relationships for the bead, inter-layer bond and intra-layer bond phases of the RVE, respectively. Acrylonitrile Butadiene Styrene (ABS) is used as polymer filament, similar to [75]. Starting with the bead phase, which can be regarded as the 'bulk material' without interfaces, material scale dog bone shaped ABS bars (see Figures 3.4(a), 3.5(a), and 3.6(a)) were printed in horizontal direction using an Ultimaker 2+ commercial FDM 3D printer and subjected to uniaxial tensile tests, similar to previous studies by Xu et al. [75, 110]. The interface specimens are manufactured in the same manner but required somewhat larger dog bone shaped specimens in order to ensure proper and consistent printing quality, and make them manageable for testing. The intra-layer bond specimens (depicted in Figures 3.4(b), 3.5(b), and 3.6(b)) were printed in horizontal direction. Lastly, the inter-layer bond specimens (shown in Figures 3.4(c), 3.5(c), and 3.6(c)) were printed in vertical direction. Seeing the considerable consequences of (minor deviations in) printing settings on the material behaviour of extruded 3D printed polymers in Chapter 2, these are kept constant throughout all length scales and are displayed in Table 3.1.

All three specimens were subjected to uniaxial tensile tests with an elongation speed of 5×10^{-3} mm s^{-1} by a Micro Tension-Compression Testing device. The resulting stress and displacement graphs are shown in Figure 3.7(a-c). The determination of the constitutive relationships for each of the three phases is straightforward and follows directly from the nominal cross-sectional area of the ABS dog bones. From these figures, it can be seen that four bead phase specimens, three intra-layer bond specimens and three inter-layer bond

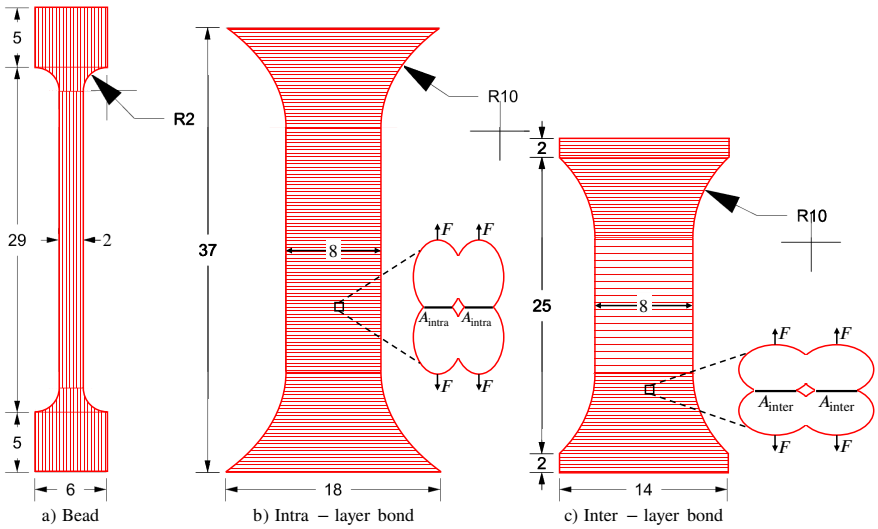

a) Bead b) Intra – layer bond c) Inter – layer bond

Figure 3.4: Schematics of material scale dog bone shaped specimens for a) bead, b) intra-layer bond, and c) inter-layer bond property determination (dimensions in mm)

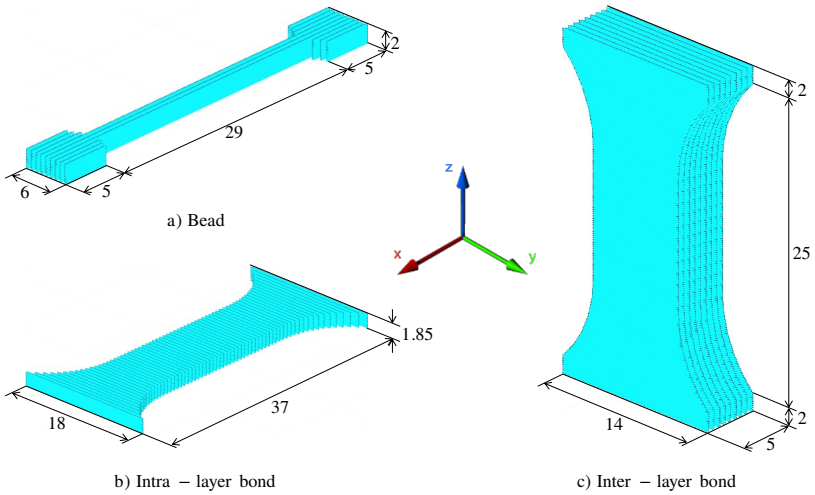

a) Bead b) Intra – layer bond c) Inter – layer bond

Figure 3.5: G-codes of material scale dog bone shaped specimens for a) bead, b) intra-layer bond, and c) inter-layer bond property determination (dimensions in mm)

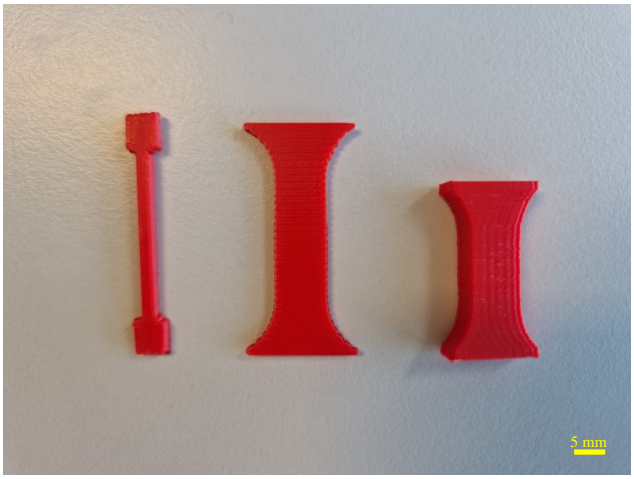

Figure 3.6: Manufactured material scale dog bone shaped specimens for a) bead, b) intra-layer bond, and c) inter-layer bond property determination

Table 3.1: Configurations of printing parameters

Printing parameters	**Configurations**
Printing temperature (°C)	260
Printing speed (mm s^{-1})	53
Nozzle size (mm)	0.6
Layer thickness (mm)	0.15

specimens were tested successfully. Although the loads are recorded accurately, the specimens were too small for using Linear Variable Differential Transformers (LVDTs) such that the displacements are only measured from the testing device itself. The recorded displacements are therefore much larger compared to reality as the measurements include significant deformation as a result of load transmission mechanisms within the test setup. Hence, similar to Xu et al. [111], only the measured strengths (i.e., peak loads) have been taken from the experiments. The average tensile strength of the three phases are computed to be 39.8 MPa for the bead material, 21.9 MPa for the intra-layer bond, and 4.58 MPa for the inter-layer bond. These average strengths and their corresponding standard deviations (±3.78 MPa, ±1.41 MPa, and ±0.760 MPa, respectively) are depicted in Figure 3.7(d). Young's modulus was assumed to be equal to its value provided by the manufacturer (E = 1590 MPa). Poisson's ratio was taken as 0.5 based on identical assumptions. Similar to Xu et al. [111], the shear modulus, G, is computed through Equation (3.4) for isotropic materials. According to the aforementioned study and references therein, even though anisotropic behaviour should be accounted for when exceeding the elastic regime (e.g., strength), the shear modulus of printed material can be assumed isotropic since printing direction has limited effect on the elastic properties:

$$G = \frac{E}{2(1+\nu)}. \tag{3.4}$$

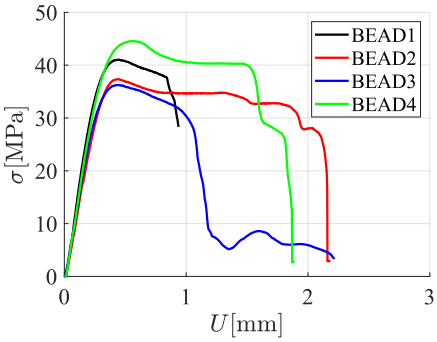

(a) Stress displacement curves of bead specimens

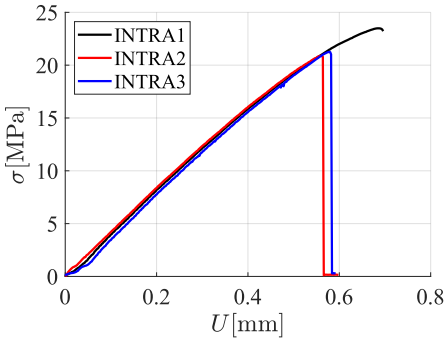

(b) Stress displacement curves of intra-layer bond specimens

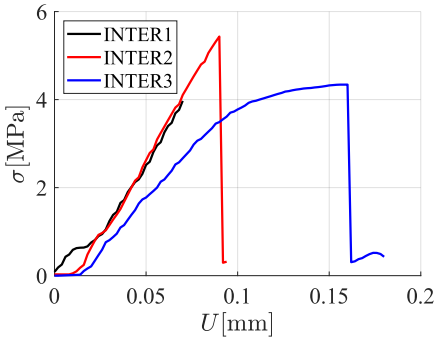

(c) Stress displacement curves of inter-layer bond specimens

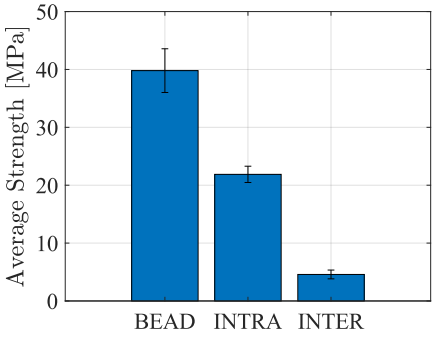

(d) Average strength values with standard deviation

Figure 3.7: Representative stress displacement curves for material scale dog bone specimens

It should be emphasized that the isotropic relation in Equation (3.4) is applied at the *local* scale, i.e., to individual lattice beam elements representing the extruded polymer within a single bead, and not to the printed material as a whole. In the present two-scale scheme, the elastic constants taken from the filament manufacturer characterize the raw ABS, whereas the directional dependence of the printed material emerges at the meso-scale from the idealized microstructural geometry (cross-sectional shape, overlap intervals and porosity; 3.8 and Table 3.2) together with the explicitly modelled inter-layer and intra-layer bond phases. Anisotropy is therefore an outcome of the RVE simulations rather than an input assumption: the effective moduli obtained for the seven directional element domains (Table 3.6) differ from one another and from the local input value, which is precisely the mechanism by which the raw material properties are translated to the meso-scale. Moreover, as noted before, the material scale specimens were too small for LVDT instrumentation, so only peak loads could be extracted reliably without available stiffness data. Assigning direction-dependent local values of E and G would have relied on fitting rather than measurement, and potentially risk accounting twice for the anisotropy that the microstructural RVE already reproduces explicitly through its geometry and interface phases. Therefore, the consequences of the isotropic assumption are considered to be limited for the presented model.

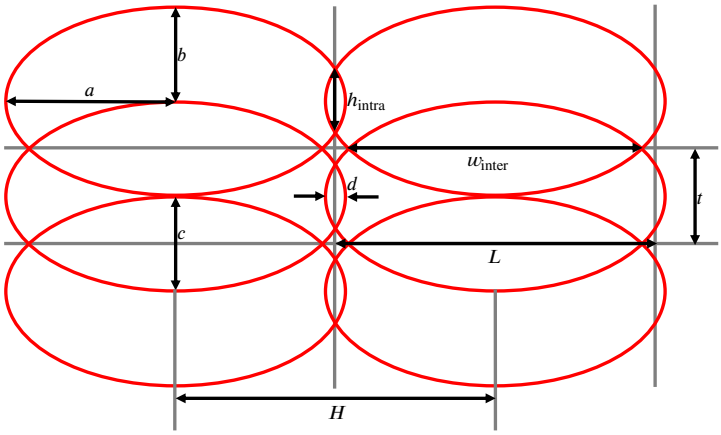

Figure 3.8: Further expansion of the geometrical models by Ahn et al. [72] & [70]

From all the reviewed characterizations and models in Chapter 2, the most important ones are considered to be the geometrical analyses, since these provide valuable insights for geometrical descriptions and idealizations of 3D printed microstructures using the FDM technique. The best model for representing the microstructural morphology of FDM 3D printed polymers was found in the geometrical models by Ahn et al. [72] and its extension in [70]. Therefore, it was chosen to model the microstructures of FDM printed parts using the extended model in [70]. This model requires five input parameters: the layer thickness (t), vertical overlap interval (c), air gap (H), raster orientation (β), and cross-sectional shape parameters (a, b) or the ratio between the bead's long and short axes ($r = a/b$). However, the model has been modified and extended here by adding the layer width (L), horizontal overlap interval (d), inter-layer bond width (w_{inter}), and intra-layer bond height (h_{intra}) in view of measurements as shown in Figure 3.8.

Figure 3.9 depicts a sideways section of a CT scan from an ABS FDM 3D printed cubic specimen ($8 \times 8 \times 13$ mm) at a resolution of 6 µm with the same printer settings as listed in Table 3.1. Similar to [82], the layer thickness is controlled by squeezing the extruded filament, which is done here to enhance strength. Several measurements of the vertical and horizontal overlap intervals as well as the layer thickness and width were performed for two random locations across the scanned areas at three different specimen depths. Overall, the considered microstructures show consistent average dimensions and correspond well with the configured printer parameters in Table 3.1. Because the overall dimensions were found to be consistent along the depth of the part, it is assumed that the cross-sectional dimensions are constant over the entire depth. The average input parameters for the extended geometrical model shown in Figure 3.8 as obtained from CT scans (Figure 3.9) and calculated are listed in Table 3.2.

Figure 3.9 and Table 3.2 illustrate that the printing parameters listed in Table 3.1 in combination with squeezing the filaments results in a very low porosity. Hence, the significant difference in (average) tensile strength in each of the three phases (i.e., bead, inter-layer bond and intra-layer bond) cannot be merely contributed to this phenomenon. The exact bond strengths as a result of this porosity can be determined using microstruc-

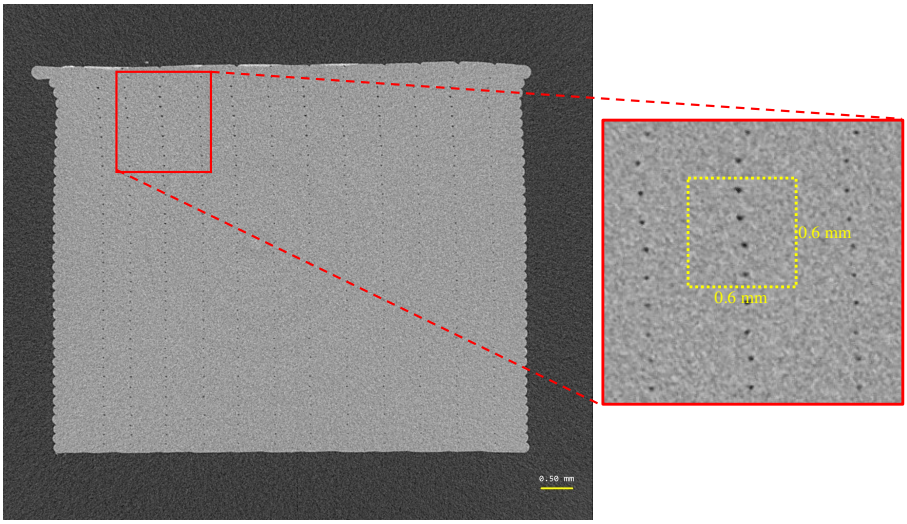

Figure 3.9: Sideways section of a CT scan from an ABS FDM 3D printed part

Table 3.2: Average input measurements from CT scan for extended geometrical model

Input parameters	**Dimensions** (mm)	**Standard deviation** (mm)
a	0.3864	
b	0.1111	
c	0.0722	
d	0.1728	
h_{intra}	0.14	0.006
w_{inter}	0.57	0.027
t	0.15	0.006
L	0.6	0.027
H	0.6	0.027

tural analyses in the form of the CT scan in Figure 3.9. Consequently, the data in Table 3.2 can be used to determine the actual load-bearing surface area, referred to as surface intact ratio [81, 82], which is the ratio between the actual surface area of the interface (A_i) and the nominal surface area based on the bulk geometrical dimensions (A_0):

$$r_{\text{A},i} = \frac{A_i}{A_0}. \tag{3.5}$$

In Equation (3.5), A_i can be regarded as A_{intra} and A_{inter} as shown in Figures 3.4(b) and (c), respectively. The above expression can be simplified for both interfaces using Figure 3.8, such that $r_{\text{A,inter}} = w_{\text{inter}}/L$ and $r_{\text{A,intra}} = h_{\text{intra}}/t$. Using the average input measurements in Table 3.2 yields surface intact ratios equal to 0.95 and 0.93 for the inter-layer and intra-layer bonds, respectively. These reductions in cross-sectional area of the FDM 3D printed parts are much smaller compared to the actual reductions in strength measured in the experiments mentioned earlier. It can thus be concluded that only

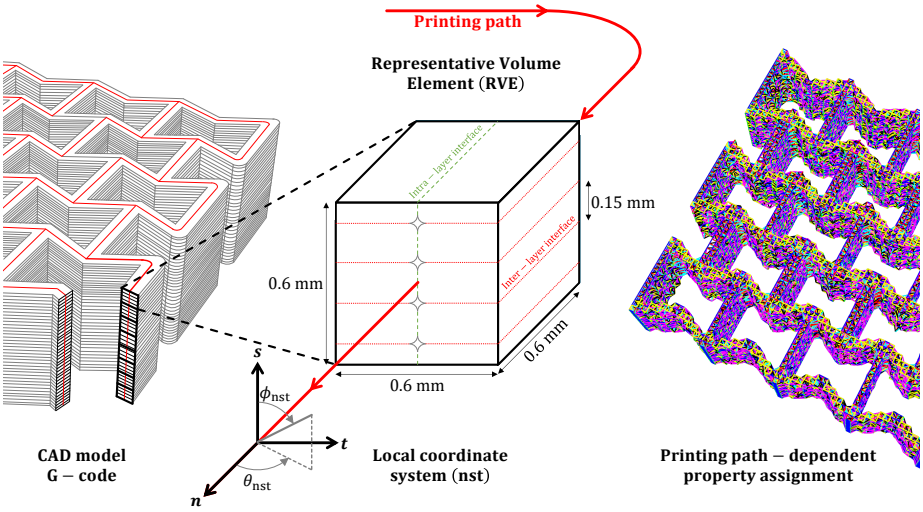

Figure 3.10: Printing path-dependent two-scale model for re-entrant bowtie honeycomb structure

including the porosity in numerical simulations of FDM printed parts is not sufficient and that it is therefore important to *explicitly* incorporate the inter-layer and intra-layer bond properties into the numerical models developed here.

3.3.2. PRINTING PATH-DEPENDENT TWO-SCALE MODELS

The experimental data in Figure 3.7 clearly indicate the large anisotropy present within 3D printed parts manufactured through FDM as a result of the interfaces present in the material. Although these effects will be explicitly incorporated into the idealized microstructural RVE, their translation towards auxetic structure scale LBM analyses of the auxetic designs requires special attention. Whereas the material scale dog bone shaped specimens in Figure 3.4 have straightforward and parallel printing paths, this printing process parameter becomes significantly more complex for the previously discussed planar auxetic architectures. In these more sophisticated geometries, the printing path typically follows the shape's outlines, thereby constantly changing its direction. This is illustrated in the left of Figure 3.10 for the re-entrant bowtie honeycomb structure.

To explicitly incorporate the effects of both porosity and experimentally obtained interface properties into LBM simulations, the RVE will be modelled using the measured geometrical input (Table 3.2) and recorded constitutive relationships (Figure 3.7). Because the beads are deposited in parallel, a 3D cubical RVE can be generated by extruding the cross-sectional shape of the four stacked layers with a value equal to $L = 4t = 0.6\,\text{mm}$, see the center of Figure 3.10. The constitutive relationships following from the material scale LBM simulations of this microstructural RVE should be assigned to the lattice beam elements of the FDM 3D printed auxetic structure scale models corresponding to all different printing path directions. As shown in Figure 3.10, printing path directions can be straightforwardly received through the 3D printer's G-code, but the corresponding element property allocation involves additional definitions.

Table 3.3: Directional element domains for printing path-dependent property assignment

Directions	θ_{nst} **(rad)**	ϕ_{nst} **(rad)**
n	$[0, \frac{1}{8}\pi] \cup [\frac{7}{8}\pi, \frac{9}{8}\pi] \cup [\frac{15}{8}\pi, 2\pi)$	$[\frac{3}{8}\pi, \frac{5}{8}\pi]$
s	$[0, 2\pi)$	$[0, \frac{1}{8}\pi] \cup [\frac{7}{8}\pi, \pi]$
t	$[\frac{3}{8}\pi, \frac{5}{8}\pi] \cup [\frac{11}{8}\pi, \frac{13}{8}\pi]$	$[\frac{3}{8}\pi, \frac{5}{8}\pi]$
ns	$(0, \frac{1}{8}\pi) \cup (\frac{7}{8}\pi, \frac{9}{8}\pi) \cup (\frac{15}{8}\pi, 2\pi)$	$(\frac{1}{8}\pi, \frac{3}{8}\pi) \cup (\frac{5}{8}\pi, \frac{7}{8}\pi)$
st	$(\frac{3}{8}\pi, \frac{5}{8}\pi) \cup (\frac{11}{8}\pi, \frac{13}{8}\pi)$	$(\frac{1}{8}\pi, \frac{3}{8}\pi) \cup (\frac{5}{8}\pi, \frac{7}{8}\pi)$
nt	$(\frac{1}{8}\pi, \frac{3}{8}\pi) \cup (\frac{5}{8}\pi, \frac{7}{8}\pi) \cup (\frac{9}{8}\pi, \frac{11}{8}\pi) \cup (\frac{13}{8}\pi, \frac{15}{8}\pi)$	$(\frac{3}{8}\pi, \frac{5}{8}\pi)$
nst	$(\frac{1}{8}\pi, \frac{3}{8}\pi) \cup (\frac{5}{8}\pi, \frac{7}{8}\pi) \cup (\frac{9}{8}\pi, \frac{11}{8}\pi) \cup (\frac{13}{8}\pi, \frac{15}{8}\pi)$	$(\frac{1}{8}\pi, \frac{3}{8}\pi) \cup (\frac{5}{8}\pi, \frac{7}{8}\pi)$

To facilitate the assignment of printing path-dependent properties, a local coordinate system is introduced. This coordinate system is composed of three mutually orthogonal unit vectors, n_i, s_i and t_i. The unit vector n_i is in the direction of the printing path, meaning that these are parallel (straight printing paths) or tangentially (curved printing paths) aligned. The two other unit vectors, s_i and t_i, are orthogonal and lie in the plane whose normal vector is n_i. The idealized microstructural cubical RVE of FDM 3D printed material with its direction of local coordinate axes is depicted in Figure 3.10. From this convention, it can be concluded that vector s_i is always perpendicular to the platform of the FDM printer such that vector t_i, together with vector n_i, constitutes a plane that is parallel to the platform. In other words: unit vector n_i corresponds to the bead phase, vector s_i matches the inter-layer bond phase, and vector t_i reflects the intra-layer bond phase.

The printing path-dependent property assignment matches the mechanical properties for all seven adjacent directional connectivity possibilities that exist within LBM simulations. These are imposed in every local coordinate system by means of spherical angles as shown in Figure 3.10. Based on this, the directional element categories are decomposed into domains within the local coordinate system and are listed in Table 3.3. The implementation of the printing path-dependent property assignment is depicted in the right of Figure 3.10 for the re-entrant bowtie honeycomb structure. Each colour of the lattice beam elements in Figure 3.10 corresponds to a different constitutive relationship. Using the idealized microstructural RVE, a more robust and computationally affordable two-scale modelling scheme has been established for FDM 3D printed planar auxetic models which still captures the mechanical characteristics of both interfacial bond strengths due to the AM technique of material extrusion. Nevertheless, a more simplified approach has been accommodated in parallel that only considers the three main directions (n_i, s_i and t_i). The three main directions are imposed using the same local coordinate system. This coarser decomposition of directional element domains is contained in Table 3.4.

Table 3.4: Directional element domains for simplified printing path-dependent property assignment

Directions	θ_{nst} **(rad)**	ϕ_{nst} **(rad)**
n	$[0, \frac{1}{4}\pi] \cup [\frac{3}{4}\pi, \frac{5}{4}\pi] \cup [\frac{7}{4}\pi, 2\pi)$	$[\frac{1}{4}\pi, \frac{3}{4}\pi]$
s	$[0, 2\pi)$	$[0, \frac{1}{4}\pi] \cup [\frac{3}{4}\pi, \pi]$
t	$[\frac{1}{4}\pi, \frac{3}{4}\pi] \cup [\frac{5}{4}\pi, \frac{7}{4}\pi]$	$[\frac{1}{4}\pi, \frac{3}{4}\pi]$

Table 3.5: Input parameters for LBM simulations of idealized cubical RVE

Properties (MPa)	**Bead**	**Inter-layer**	**Intra-layer**
E_1	1590	1590	1590
G_1	530	530	530
$f_{t,1}$	40	6.6	29
$f_{c,1}$	-50	-8.25	-36.25
E_2	343		
G_2	114.33		
$f_{t,2}$	38		
$f_{c,2}$	-47.5		

3.3.3. CALIBRATION PROCEDURES

Simulations using LBM require calibration in terms of both the radii of the circular beam elements, as well as their strength. The beam elements' radii are iteratively determined such that the global Young's modulus of the lattice mesh is equal to the locally assigned Young's modulus for a beam element in a tensile test [129, 130]. Local strength inputs are calibrated in a similar manner to ensure that the global strength matches experimental measurements. As a result, local strength inputs of LBM simulations may be somewhat different from experimentally obtained strengths, because the radii of the beam elements affect the global response. Studies on the compressive strength of 3D printed polymers are very rare, see Chapter 2. Nevertheless, Vukasovic et al. [143] characterized, among others, the tensile and compressive strength of 3D printed ABS (and PLA) in two perpendicular manufacturing directions: Upright (U) where layers were extruded orthogonally to the base plate, and Flat (F) having the layers parallel to the building platform. Their results for ABS filament indicate that the strength ratio between compression and tension is affected by printing orientation. In the U direction this strength ratio equals 2, while it has a value of about 1.25 in the F direction. Because the specimens in this study are subjected to loading parallel to the building platform, the local compressive strengths in the lattice meshes representing ABS filament are assumed to be a factor 1.25 larger than the local tensile strengths calibrated from experiments. The input parameters for LBM simulations of the microstructural 3D RVE (Figure 3.10) are provided in Table 3.5, where the subscripts correspond to the segment number of a (multi-)linear curve (see Figure 3.3).

After calibration of the microstructural RVE of FDM 3D printed material in Figure 3.10, its constitutive relationships can be determined to be used in the auxetic structure scale LBM analyses of the planar auxetic designs. This will be done through the use of the two-scale modelling scheme described before and the seven adjacent directional connectivity

possibilities present in LBM meshes. As discussed previously, to match the mechanical properties in the planar auxetic LBM simulations with the microstructural RVE, each of the seven directions require separate constitutive relationships. The acquisition of these relationships for the three main directions is straightforward and can be obtained directly from uniaxial tensile tests along the three local coordinate axes. However, the remaining four directions need more complicated biaxial or triaxial tensile tests.

To find the combined effect of the stress strain responses in the multi-axial tensile tests that correspond to their respective directions, stress and strain transformations are performed. The biaxial and triaxial LBM simulations only yield stresses and strains along the three main directions of the microstructural RVE, so these must be transformed in order to recompute their joint response. This will be done using *Cauchy's transformation law (principle)* [144]. Provided that θ_x, θ_y and θ_z are measured directly to the vector normal to the cut plane from their respective axes (x, y and z), the resulting normal stress may be transformed in 3D with respect to the original coordinate system as [145]:

$$\sigma_n = \sigma_x \lambda_x^2 + \sigma_y \lambda_y^2 + \sigma_z \lambda_z^2 + 2(\tau_{xy}\lambda_x\lambda_y + \tau_{yz}\lambda_y\lambda_z + \tau_{xz}\lambda_x\lambda_z), \tag{3.6}$$

where $\lambda_x = \cos(\theta_x)$, $\lambda_y = \cos(\theta_y)$ and $\lambda_z = \cos(\theta_z)$. Strain can be transformed in a similar fashion since stress and strain tensors have identical structures [144]. Therefore, using the same approach, σ can be simply replaced with ε and τ with $\gamma/2$ to express the general strain transformation. Hence, computing the resulting normal strain in terms of the non-transformed strain components in the original coordinate system as:

$$\varepsilon_n = \varepsilon_x \lambda_x^2 + \varepsilon_y \lambda_y^2 + \varepsilon_z \lambda_z^2 + \gamma_{xy}\lambda_x\lambda_y + \gamma_{yz}\lambda_y\lambda_z + \gamma_{xz}\lambda_x\lambda_z. \tag{3.7}$$

Finally, the implementation of the printing path-dependent two-scale models presented in this work is provided in Figure 3.11. Starting with the microstructural experimental analysis elaborated in Section 3.3.1, followed by the two-scale modelling scheme described in Section 3.3.2 including calibration procedures for the LBM simulations in Section 3.3.3. It is noted once more that the given procedure requires printer settings to be kept constant throughout all length scales.

3.3.4. EXPERIMENTAL ANALYSIS OF PLANAR AUXETICS

To validate the two-scale approach, the auxetic structure scale LBM analyses are accompanied by experiments on planar auxetics. In view of their favorable characteristics discovered in a previous study by Xu & Šavija [110], two auxetic designs are tested in uniaxial compression: Re-Entrant (RE) and Rotating Square (RS) architectures, see Figure 3.12. Both auxetic structures have similar dimensions of 37.4 × 37.4 × 10 mm and are printed in the out-of-plane direction as shown in Figure 3.12, which corresponds to the inter-layer direction. Identical to the microsctructural experimental analysis in Section 3.3.1, the RE and RS architectures were printed with the exact same ABS polymer filament and printing process parameters as listed in Table 3.1 to eliminate any possible influence on the results. The experimental setups for both auxetic designs are shown in Figure 3.13. To reduce friction between the specimens and loading plates, a thin transparent cling film was inserted in between. In the LBM simulations of the auxetic structures, the boundary conditions are therefore assumed to be frictionless.

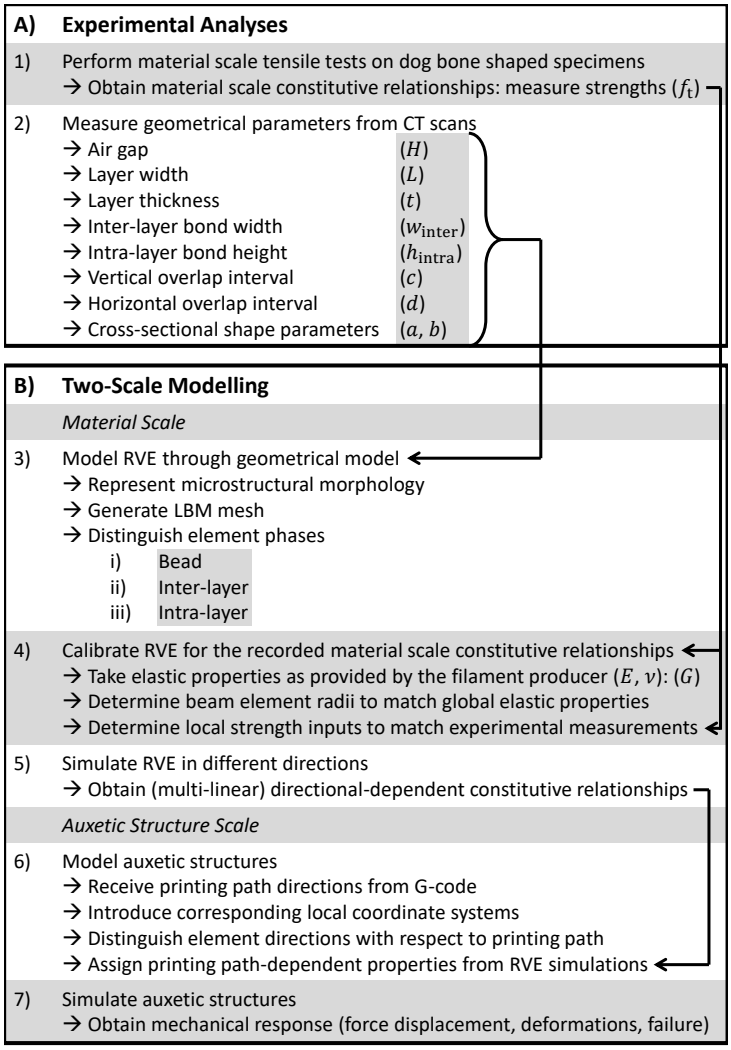

Figure 3.11: Procedure for calibrating the printing path-dependent two-scale models

For each design, two specimens were subjected to uniaxial compression under displacement control with a displacement rate of $0.01\,\mathrm{mm\,s^{-1}}$. The resulting load and displacement graphs are shown in Figure 3.14. However, the LBM described in Section 3.2.1 is unable to capture self-contact or contact of initially unloaded elements with the loading plates from the experimental setup. As a result, the LBM simulations of the planar auxetic architectures are only valid up to the point where either self-contact or contact of initially unloaded elements with loading plates occurs. This will be referred to as 'validity limit' for which the comparison between the experimental results and LBM simulations holds.

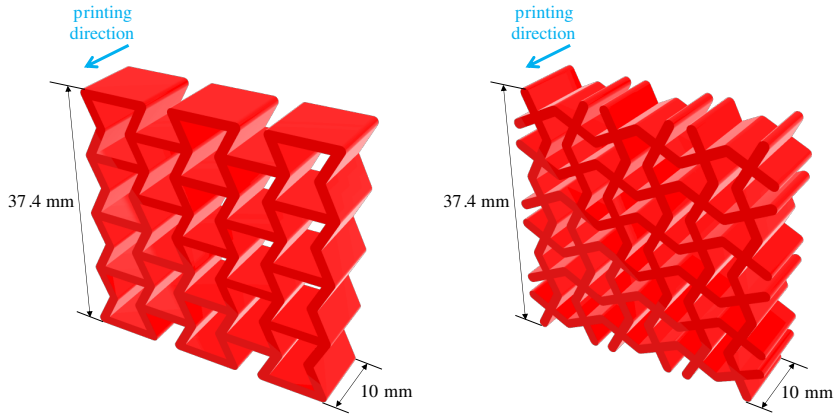

(a) Re − Entrant (RE) (b) Rotating Square (RS)

Figure 3.12: Schematics of the auxetic (a) Re-Entrant (RE) and (b) Rotating Square (RS) architectures

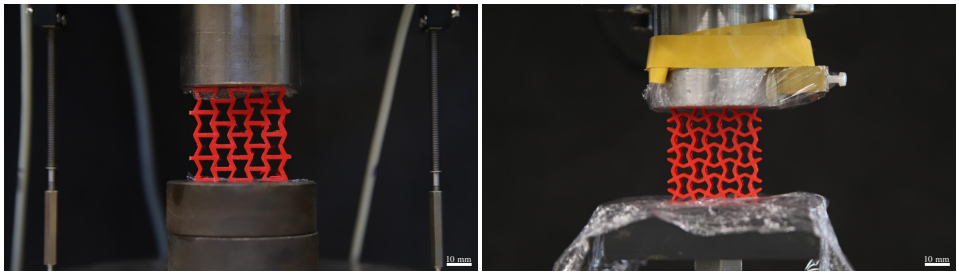

(a) Re-Entrant (RE) (b) Rotating Square (RS)

Figure 3.13: Experimental setups for uniaxial compression tests of (a) Re-Entrant (RE), and (b) Rotating Square (RS) architectures

The failure process of the RE specimens will be discussed first. At $u = 1.30$ mm in Figure 3.15, it can be seen that failure initiates in the diagonally opposing lower left and upper right joints between the inward-facing vertical struts (circled in cyan). This event corresponds with the maximal load prior to self-contact, such that afterwards the curve starts to descend under increasing deformation. Once the aforementioned joints have failed, the RE specimen exhibits diagonal shear failure from the bottom left to the upper right corner (see cyan dashed lines at $u = 2.10$ mm in Figure 3.15). Nevertheless, near a displacement of approximately 2.25 mm the diagonal pattern gets interrupted by one joint that is facing in the opposite direction (indicated by the cyan ellipse in Figure 3.15). Ultimately, the RE specimens make self-contact around a displacement of 3.00 mm between the upper right struts, see the cyan ellipse in Figure 3.15. This value of displacement marks the 'validity limit' of the RE design. Although friction between the specimens and loading plates was reduced by inserting a thin transparent cling film,

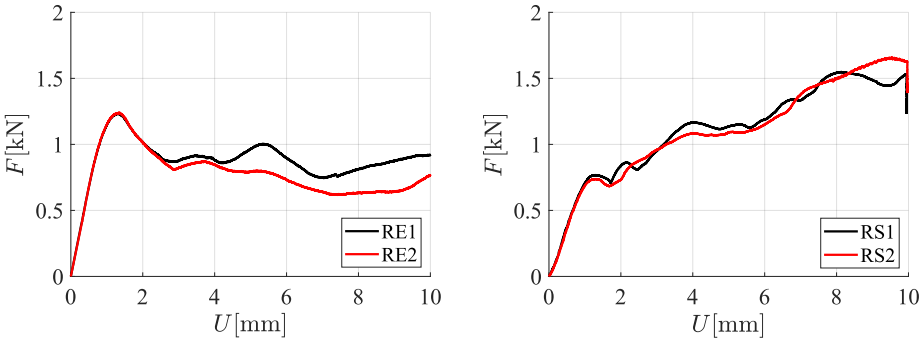

(a) Re-Entrant (RE)

(b) Rotating Square (RS)

Figure 3.14: Force displacement curves for uniaxial compression tests of (a) Re-Entrant (RE), and (b) Rotating Square (RS) architectures

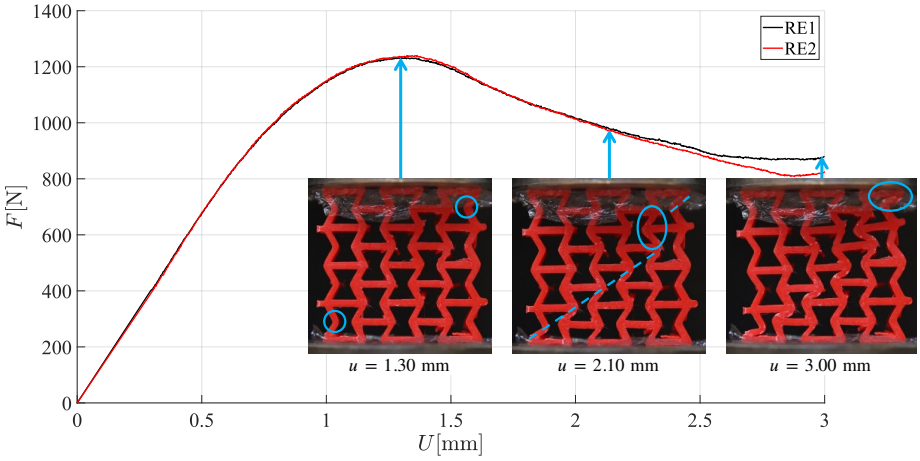

Figure 3.15: Illustration of RE specimens deformation and self-contact

it is inevitable that a certain amount of friction remained during testing. This could have hindered the auxetic deformation and caused the localized instability aligned on the diagonal direction. Because the RE specimens have a relatively large contact area with the loading plates (see Figure 3.13(a)), frictional contributions may have been more pronounced for RE than for RS specimens having a significantly smaller contact area with the loading plates (see Figure 3.13(b)).

The RS specimens undergo more complicated deformations that arguably affect their 'validity limit'. At the onset of non-linearity (near 1 mm in Figure 3.16) at least one of the exterior struts starts to fail as a result of plastic yielding, such that the specimen shows non-linear response. However, arguably the non-linearity partially comes from yielding

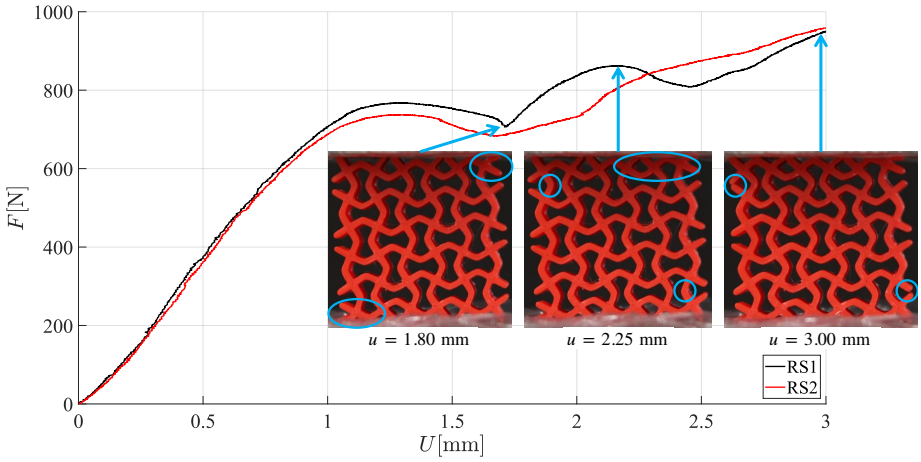

Figure 3.16: Illustration of RS specimens deformation and self-contact

of the ABS material itself as well. The two diagonally opposing lower left and upper right struts fail almost simultaneously before the inner structure makes contact with the bottom loading plate (see cyan ellipses at $u = 1.80$ mm in Figure 3.16) such that the RS architecture started to slightly rotate counterclockwise in the experiments. It is likely that the rotation caused additional displacements and explains the presence of the first local maximum in the load and displacement graph. At this level of displacement, the interior structure of the RS specimens makes contact with the bottom loading plate. Nonetheless, at the first local minimum the RS design settles near 1.80 mm of displacement after which the curve starts ascending again. This increase in load continues until a displacement of about 2.25 mm, which approximately corresponds to the second local maximum in the force displacement curve. As shown in the photograph for $u = 2.25$ mm in Figure 3.16, several occasions happen in favor of a secondary or alternative 'validity limit'. To start with, the second and third exterior upper struts from the right that are directed towards each other start to make self-contact (upper right ellipse at $u = 2.25$ mm in Figure 3.16). Furthermore, the interior structure makes contact with the upper loading plate. Finally, contrary to the exterior struts, the joints between the diagonally opposing upper left and lower right inward-facing vertical struts begin to fail (circled in cyan for $u = 2.25$ mm in Figure 3.16). The latter explains the small descend in the load and displacement graph, while the deformed configuration of the RS specimen is provided for 3.00 mm of displacement in Figure 3.16 to illustrate that the aforementioned joints indeed fail (to such an extend that the adjacent horizontal exterior struts start to touch, see cyan circles). Hence, a displacement of $u = 2.25$ mm marks the 'validity limit' of the RS design. As explained for RE, frictional effects are less pronounced for the RS specimens because of their significantly smaller contact area with the loading plates.

Finally, two comments should be made before discussing the results. The first one is that although the 'validity limits' established here for the two planar auxetic designs

seem small compared to their corresponding force displacement curves, it is important to note that the present study is only concerned with their mechanical and failure behaviour under small deformations. Modelling large deformations, including self-contact or even compaction, is beyond the scope of the current work. Moreover, this is reflected by the chosen modelling technique, LBM, of which the previously described limitations are duly noted. Therefore, with the intention of modelling small deformations and failure of planar auxetic structures, LBM simulations are very well capable of capturing their characteristic traits within its valid range. Secondly, it should be noted that discrepancies in strut widths exist among the Computer Aided Design (CAD) models and actually printed specimens. The CAD models are in agreement with the configured printer settings provided in Table 3.1 (i.e., nozzle size = 0.6 mm), such that the strut widths are modelled to have two neighboring beads in each strut (i.e., $2L = 1.2$ mm). However, the strut widths measured from the actually printed specimens by means of a caliper show to be larger, having a value of 1.4 mm: a difference of nearly 17 %. The planar auxetic models used in the LBM simulations are therefore not directly obtained from the original CAD models, but are modified according to this 17 % increase in strut width to facilitate more realistic representations.

3.4. RESULTS

The results from the proposed two-scale modelling of 3D printed auxetics will be discussed here. Starting with the material scale through the idealized microstructural cubical RVE containing four stacked layers of FDM 3D printed polymer with the explicit incorporation of both porosity as well as inter-layer and intra-layer bond properties. The calibrated experimentally obtained input used for the LBM simulations of the RVE can be found in Table 3.5. From these microstructural simulations, constitutive relationships are determined to be used as input for the auxetic structure scale LBM analyses of the planar auxetic designs. Subsequently, printing path-dependent characteristics are allocated to the lattice beam elements of the FDM 3D printed auxetic structure models corresponding to all different printing path directions. Two different discretizations of directional element domains are considered in this study. The first one distinguishes mechanical properties for 7 RVE directions, while the other utilizes a coarser decomposition wherein only the three main directions are included. As discussed before, the considered auxetic designs are the Re-Entrant (RE) and Rotating Square (RS) architectures.

3.4.1. MICROSTRUCTURAL CONSTITUTIVE RELATIONSHIPS

After the calibration of the microstructural RVE of FDM 3D printed material in Figure 3.10, its constitutive relationships are determined to be used in the auxetic structure scale LBM analyses of the planar auxetic designs. To match their printing path-dependent properties for all directions, each direction requires a separate constitutive relationship. These are obtained from simulated uniaxial (**n**, **s** and **t**), biaxial (**ns**, **st** and **nt**) or triaxial (**nst**) tensile tests of the microstructural RVE. The multi-axial tensile tests require stress and strain transformations, as provided in Equations (3.6) and (3.7), respectively. The stress strain curves resulting from the numerical simulations of the 3D RVE are provided in Figures 3.17 and 3.18, together with their corresponding constitutive relationships that will serve

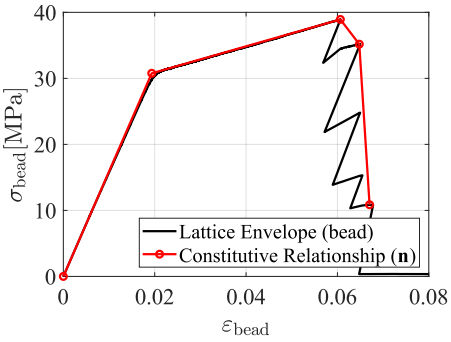

(a) Uniaxial bead or **n** direction

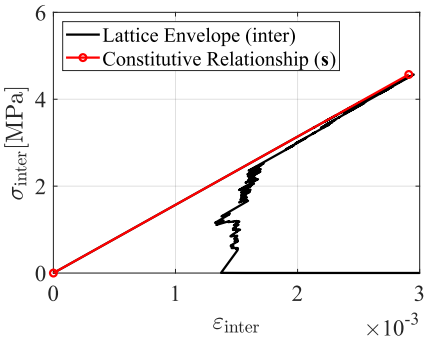

(b) Uniaxial inter-layer or **s** direction

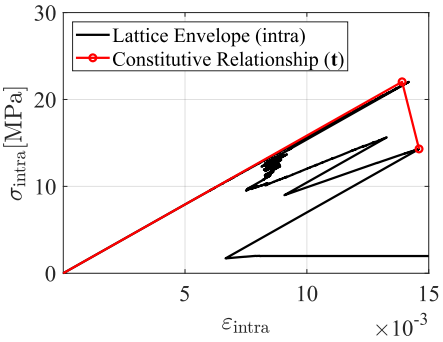

(c) Uniaxial intra-layer or **t** direction

Figure 3.17: Stress strain curves from 3D RVE and their corresponding constitutive relationships for 3 main directions

as input for the auxetic structure scale models. These segmented curves determined from the microstructural RVE responses are provided in Table 3.6 and will serve as input for the LBM simulations of the auxetic architectures. Recall that the local strength inputs in Table 3.6 may be somewhat different from the experimentally obtained strengths, because the calibrated radii of the beam elements affect their strength. Young's moduli and strength values are determined from the multi-linear constitutive relationships resulting from the RVE simulations in Figures 3.17 and 3.18. Furthermore, as described in Section 3.3.1, the shear moduli for all segments are computed through Equation 3.4. Note that all of the seven relations are implemented in the 7 RVE directions model, whilst only those in Figure 3.17 are used for the 3 main directions model. The given mesh size matching the microstructural cubical RVE dimensions (0.6 mm) required the radii of the circular beam elements of the lattice meshes to be 0.2636 mm to have a global Young's modulus of E = 1590 MPa as provided by the manufacturer.

3.4.2. TWO-SCALE MODELS FOR PLANAR AUXETIC DESIGNS

Printing path-dependent properties are assigned to the lattice beam elements corresponding to all different printing path directions as illustrated in Figure 3.10 for the RE design.

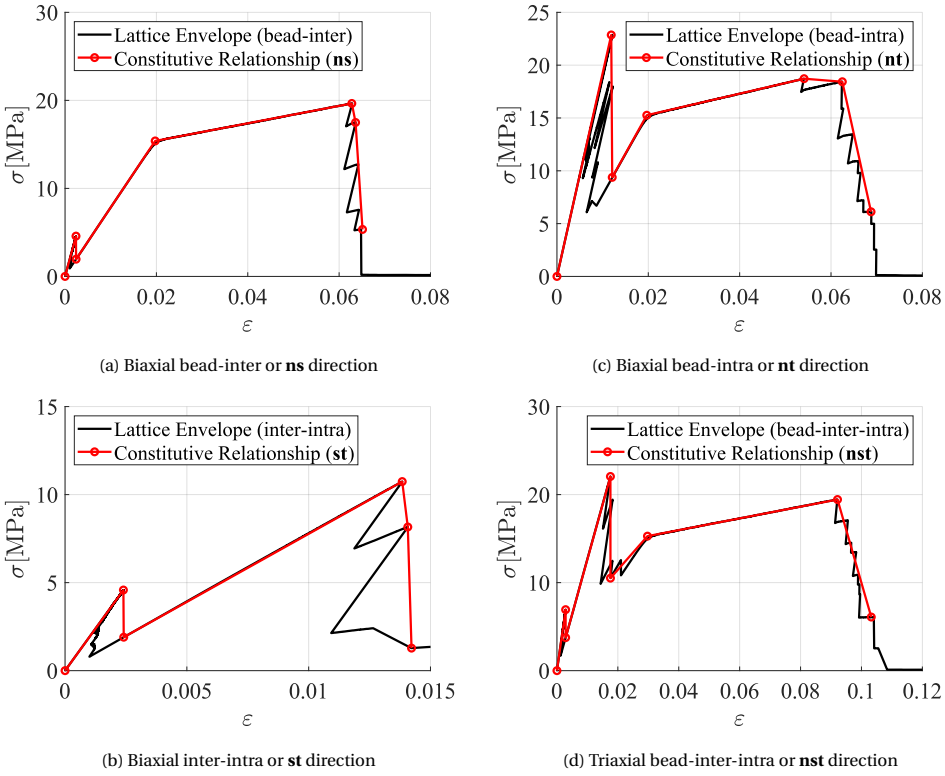

(a) Biaxial bead-inter or **ns** direction

(c) Biaxial bead-intra or **nt** direction

(b) Biaxial inter-intra or **st** direction

(d) Triaxial bead-inter-intra or **nst** direction

Figure 3.18: Stress strain curves from 3D RVE and their corresponding constitutive relationships for intermediate directions

Recall that two different directional discretizations are considered: 7 RVE directions and 3 main directions models. The former models use all of the seven constitutive relationships that are listed in Table 3.6, whilst the latter models merely incorporate the n_i, s_i and t_i directions.

First the deformations and failure mechanisms will be treated. The experimental load and displacement graphs (Figure 3.14) as well as their corresponding 'validity limit' with respect to the LBM simulations have already been discussed in Section 3.3.4. For the RE and RS architectures the validity limits are determined to be 3.00 mm and 2.25 mm, respectively. These particular deformations are depicted in Figure 3.19, including indications of their failure mechanisms. The RE design clearly exhibits diagonal shear failure prior to self-contact (see cyan dashed lines Figure 3.19(a)). In the RS design, however, first the two diagonally opposing lower and upper struts fail almost simultaneously before the interior structure makes contact with the bottom loading plate. Afterwards, as explained in Section 3.3.4, the second and third exterior upper struts from the right that are directed towards each other start to make self-contact and the interior structure makes contact with the upper loading plate. The final and actually considered failure mode comprises, contrary to the exterior struts, the onset of failure of the joints between the diagonally

Table 3.6: Printing path-dependent directional element properties

Properties (MPa)	**n**	**s**	**t**	**ns**	**st**	**nt**	**nst**
E_1	1590	1570	1584	1912	1912	1923	2430
G_1	530	523.33	528	637.33	637.33	641	81
$f_{t,1}$	30.77	4.57	22.03	4.58	4.58	22.86	6.93
$f_{c,1}$	-38.46	-5.71	-27.54	-5.73	-5.73	-28.58	-8.66
E_2	642		980	812	789	775	1313
G_2	214		326.67	270.67	263	258.33	437.67
$f_{t,2}$	38.93		14.31	1.96	1.90	9.38	3.75
$f_{c,2}$	-48.66		-17.89	-2.45	-2.38	-11.73	-4.69
E_3	543			780	776	776	1256
G_3	181			260	258.67	258.67	418.67
$f_{t,3}$	35.18			15.39	10.74	15.26	22.06
$f_{c,3}$	-43.98			-19.24	-13.43	-19.08	-27.58
E_4	162			313	580	346	598
G_4	54			104.33	193.33	115.33	199.33
$f_{t,4}$	10.86			19.65	8.16	18.72	10.51
$f_{c,4}$	-13.58			-24.56	-10.20	-23.40	-13.14
E_5				275	90	295	514
G_5				91.67	30	98.33	171.33
$f_{t,5}$				17.49	1.28	18.43	15.28
$f_{c,5}$				-21.86	-1.60	-23.04	-19.10
E_6				82		89	211
G_6				27.33		29.67	70.33
$f_{t,6}$				5.34		6.12	19.44
$f_{c,6}$				-6.68		-7.65	-24.30
E_7							59
G_7							19.67
$f_{t,7}$							6.09
$f_{c,7}$							-7.61

opposing upper left and lower right inward-facing vertical struts (see cyan dots in Figure 3.19(b)).

As explained in Section 3.2.2, disorder in the lattice mesh is introduced through population of a single lattice node inside each sub-cell based on random seeds obtained from a list of generated pseudo random numbers. To see if the occurring failure mechanisms happened consistently, three numerical simulations of uniaxial compression tests are performed using different seeds for both planar auxetic designs. To this end, each auxetic cellular architecture is modelled six times: three times using different seeds for both the 7 RVE directions and 3 main directions models. The numerically obtained deformations and failure mechanisms for the RE and RS designs near their corresponding validity limits are contained in Figures 3.20 and 3.21, respectively.

Figure 3.20 showing the numerically simulated deformations and failure mechanisms of the RE architecture correspond well with the experimentally obtained phenomena in

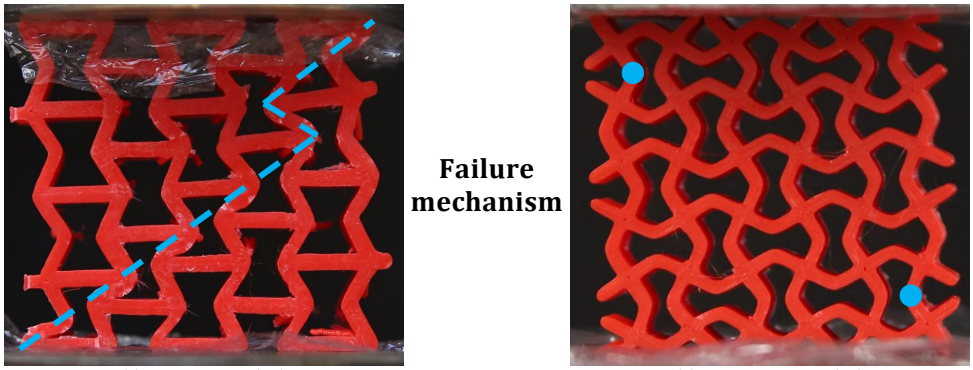

(a) Re − Entrant (RE)
$u = 3.00$ mm

(b) Rotating Square (RS)
$u = 2.25$ mm

Figure 3.19: Failure mechanisms for (a) Re-Entrant (RE) and (b) Rotating Square (RS) architectures

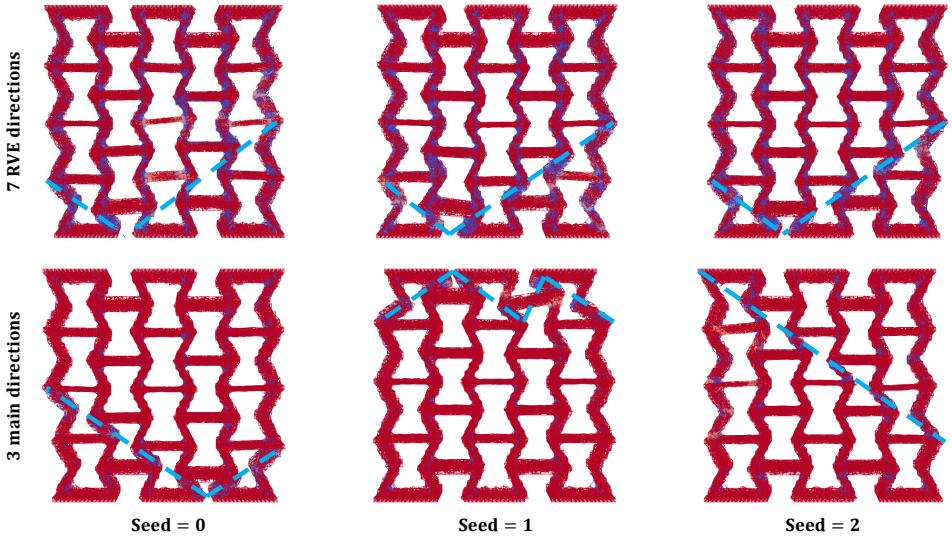

Figure 3.20: Deformations and failure mechanisms of Re-Entrant (RE) architecture

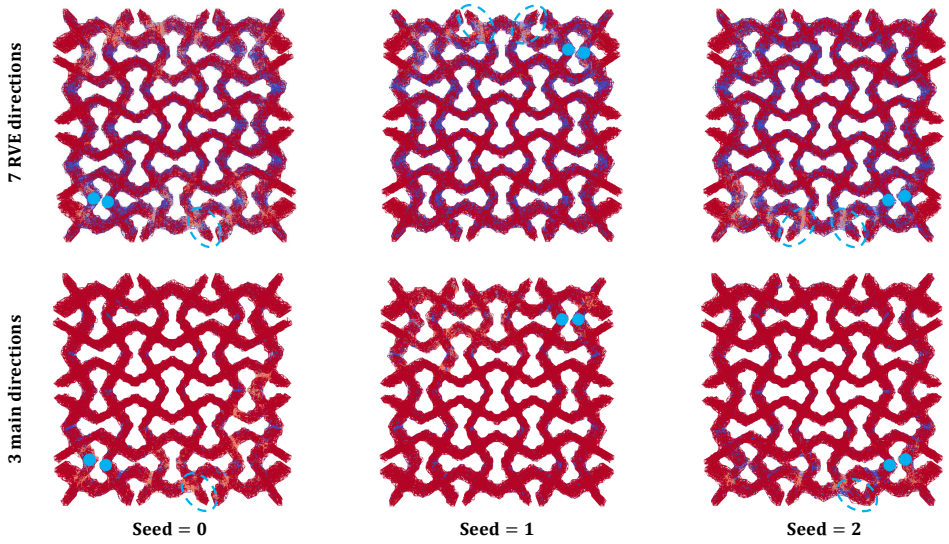

Figure 3.21: Deformations and failure mechanisms of Rotating Square (RS) architecture

Figure 3.19(a). Irrespective of the seed or discretization of directional element domains, all modelled structures show diagonal shear failure in which the inward-facing re-entrant ribs fold inwards prior to self-contact (see cyan dashed lines in Figure 3.20). Nonetheless, it can be noted that the failure modes can be different depending on the element domain discretization. The computationally obtained deformations and failure mechanisms of the RS design shown in Figure 3.21 are also in good agreement with the test results from Figure 3.19(b). For both 7 RVE directions and 3 main directions models and all seeds, the simulated RS designs start failing at the joints between one of the inward-facing vertical struts at the bottom left (Seed = 0), upper right (Seed = 1), and bottom right (Seed = 2) as indicated by the cyan dots in Figure 3.21. Directly after the failure initiation of the first joint, a second joint between the horizontally neighboring inward-facing vertical struts fails almost simultaneously in all of the simulations - hence the double joint indications in Figure 3.21. Conversely to the experimental observations, wherein first the exterior struts start to fail followed by the joints between the diagonally opposing inward-facing vertical struts, the simulated RS architectures primarily fail at the aforementioned joints after which (most of the time) at least one exterior strut fails. In Figure 3.21, these later failing exterior struts are indicated by means of cyan dashed ellipses. It can thus be concluded that both failure mechanisms are captured by the numerical models, only in a different sequence. Finally, it can also be seen here that regardless of the number of considered directions (i.e., 7 or 3), the specific joints failing for the same mesh seed are consistent.

The comparison between the first eight experimentally and numerically obtained force displacement curves in Figures 3.22 and 3.23 will be discussed next. The RS design was tested by a hydraulic press INSTRON 8872, which can directly record both the load and displacement, while the RE design was compressed by an electronic press UNITRONIC which requires LVDTs (as can be seen in Figure 3.13(a)). The experimental results of the RE design (RE1 and RE2 in Figure 3.22) are compared with their corresponding numerical

counterparts (7 RVE directions, 3 main directions, and homogeneous). The stiffness of both experimental and numerical responses are very similar, with the numerical curves being slightly steeper. Furthermore, the peak loads are reached at approximately the same value of about 1200 N with percentage differences of maximally only 6 % for both directional discretization models. Also, the influence of the mesh seed shows to be marginal. The post-peak response prior to self-contact, however, is more brittle and less ductile for the simulated curves than for the test data. This is most likely caused by the nature of LBM simulations in which a stepwise element removal procedure is used. Although multi-linear constitutive relationships are used here, such that elements are not immediately removed, their stiffness and strength change in a stepwise fashion throughout the analyses. These transitions from one point on the multi-linear curve to the next tend to happen more rapidly and may even be accelerated through adjacent element removals near stress concentrations. As a result, the inward-facing re-entrant ribs fold inwards sooner causing the diagonal shear failure to propagate faster through the RE architecture after the onset of failure. This may also explain why in the experiments self-contact occurred only after a displacement of 3.00 mm, whereas for the simulations this already happened near 1.50 mm. Besides, there are only minor differences between the 7 RVE and 3 main directions models. The only ones worth mentioning are the fact that the stiffness of the 7 RVE directions model is somewhat larger compared to the 3 main directions model, with the slope of the former curve degenerating faster than the latter, leading to a 5 % smaller strength.

The comparison of experimental (RS1 and RS2) and first six simulated (7 RVE directions and 3 main directions) force displacement curves for the RS design in Figure 3.23 will be elaborated here. In this case, the experimentally and numerically obtained stiffness are almost identical as the curves align perfectly in the initial linear-elastic stage. Only after approximately 1 mm of displacement or near 700 N do they start to deviate, that is, once both results start to behave non-linearly. It is at this very moment (1 mm displacement) that at least one exterior strut starts to fail in the experiments, such that the specimen becomes non-uniformly loaded. As a result, the RS architecture started to slightly rotate counterclockwise in the experiments. However, this may have been induced by the primary failure mode happening therein since the two diagonally opposing lower and upper struts failed almost simultaneously: the rotations may have enabled and caused additional displacements. As discussed before, this rotation is not captured in the deformations from the LBM simulations which is a possible explanation of their different non-linear trajectories. Because of these differences, the peak loads are reached at somewhat different displacement values: the experiments reach their maximum around 2.25 mm, while the simulations do so within 1.75 mm and 2.00 mm displacement. Nevertheless, their corresponding validity limits are reached at nearly the same deformations. Identical to the RE design simulations, the LBM simulations of the RS architecture yield approximately the same strengths compared to the experiments. Only here the difference in strength is a bit more protruding with values up to about 10 % and 12 % for the 7 RVE and 3 main directions models, respectively. Similar observations as already mentioned for the RE design can be made for the RS architecture when comparing the two different element differentiation strategy models.

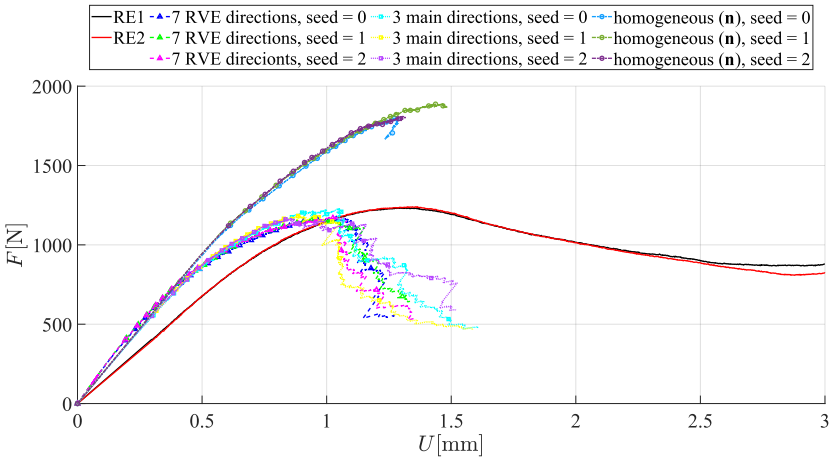

Figure 3.22: Comparison of experimental, numerical and homogeneous force displacement curves for RE architecture

Analogous to the microstructural analyses in the previous section, six additional homogeneous LBM simulations have been performed here: three different mesh seeds for each of the two planar auxetics. All elements were assigned homogeneous isotropic properties of the bead phase, in this case provided in Table 3.6 for the n_i direction as shown in Figure 3.17(a). Be aware that the directional domain discretization is irrelevant here, as all elements are the same. The corresponding force displacement curves are plotted in Figures 3.22 and 3.23. For the RE design the strength overestimation is more prominent when looking at the homogeneous Lattice Envelopes and the experimental curves (RE1 and RE2 in Figure 3.22) having a percentage difference of roughly 52 %. The RS architecture simulation results show a smaller discrepancy among the homogeneous and heterogeneous models (30 %), even though the homogeneous curves and testing data (RS1 and RS2 in Figure 3.23) deviate around 40 %. This shows once more that neglecting the anisotropic (bond) properties in numerical models for FDM 3D printed polymers results in an overestimation in strength.

Finally, using Figure 3.24 the LBM deformations and failure mechanisms for the homogeneous simulations can be compared to the corresponding heterogeneous simulations. Starting with the RE auxetic architecture, the homogeneous simulations (Figure 3.24) fail in a more or less similar manner as the heterogeneous ones (Figure 3.19(a)) having a diagonal shear band as indicated in both figures by the cyan dashed lines. Besides, the homogeneous RE structures fail in a much more brittle manner, which is also evident from the force displacement graph in Figure 3.22 where it can be seen that the validity limit for all homogeneous simulations is reached at the peak load without any descending branch. In the homogeneous representations of the RS design, the deformations and failure initiations are similar to their heterogeneous predecessors. Identical to the heterogeneous simulations, the indicated joints between one of the inward-facing vertical struts fail first for homogeneous properties too (see cyan dots in Figure 3.24). Similarly, a second neighboring joint between inward-facing vertical struts fails almost simultane-

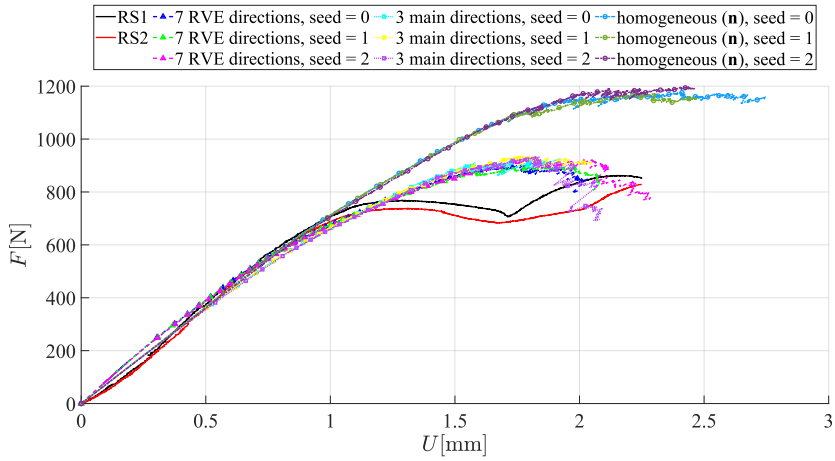

Figure 3.23: Comparison of experimental, numerical and homogeneous force displacement curves for RS architecture

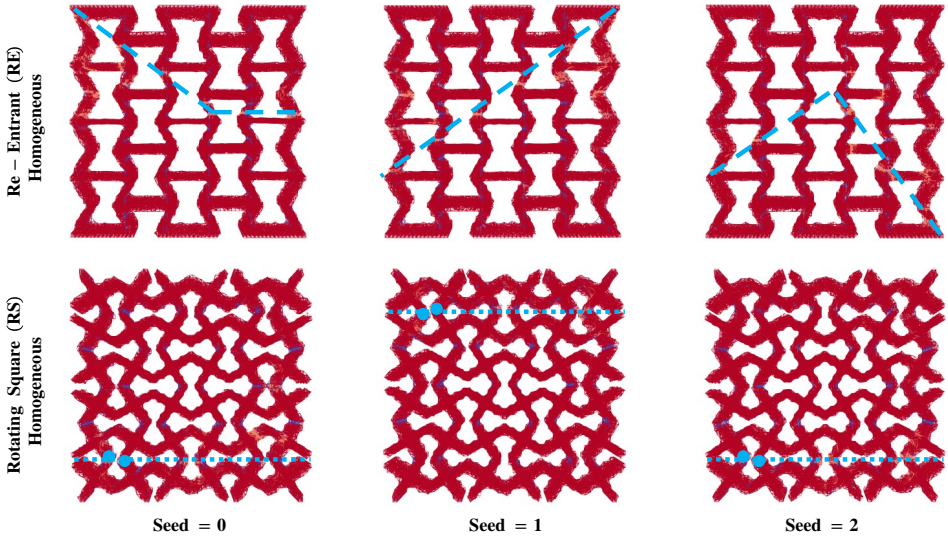

Figure 3.24: Deformations and failure mechanisms for homogeneous Re-Entrant (RE) and Rotating Square (RS) architectures

ously afterwards (again, hence the double indications in Figure 3.24). In contrast with the experimental observations and heterogeneous simulations, no external strut failure occurs for the homogeneous RS structures. Instead, all of the horizontally aligned joints between inward-facing vertical struts fail consecutively as indicated by the cyan dash-dotted line in Figure 3.24. The latter observations are inconsistent with the experiments and heterogeneous models.

3.4.3. OUTPUT ANALYSIS

To understand numerically what the sensitivity of the simulated results is with respect to the interface properties, the percentage of completely failed elements so far is plotted against the analysis progress. This is only done for one of the simulated meshing seeds here, i.e., Seed = 0, because the results are very similar for other meshes. Besides, the deformations and failure mechanisms for this seed show to be most consistent for the considered directional discretizations (i.e., 7 RVE directions, 3 main directions and homogeneous). To make a fair comparison between each of these three different element differentiation strategy models, all of their evolutions over the analysis progress are discretized using the three main directions (n_i, s_i and t_i) that correspond to the intra-layer bond, inter-layer bond and bead phases, respectively. It should be noted that this representation indeed only directly reflects the 3 main directions models, but it is used for the 7 RVE directions models and homogeneous models here too since it would be arbitrary to compare the fully discretized seven directions models with models that contain no discretization at all.

Figure 3.25 displays the percentage of failed elements versus the analysis progress of the RE design for the 7 RVE directions model (left column), 3 main directions model (middle column) and homogeneous model (right column). From the graphs contained therein it can be seen that both the 7 RVE directions and 3 main directions models primarily fail in tension, whereas the homogeneous model solely fails in compression. It is also clear that in the aforementioned heterogeneous models inter-layer failure is governing, while in the homogeneous model bead failure is dominant. In fact, the heterogeneous models mainly demonstrate interfacial failure with intra-layer failure being secondary. Figure 3.26 has the same format, but distinction is made between elements failing in tension (upper row) and compression (lower row). These graphs emphasize the primary failure mode for the 7 RVE directions and 3 main directions models, which is tension, with no tensile failure occurring in the homogeneous model at all (hence no graph). They further illustrate that tensile failure in the heterogeneous models (almost) only happens at the inter-layer interface. This may be an indication of the initiation of delamination, or at least a prerequisite of the auxetics' out-of-plane behaviour. Additionally, Figure 3.26 shows that the percentages of failure in tension among the 7 RVE directions and 3 main directions models are almost identical. The homogeneous model, however, only exhibits interfacial failure in a minor fraction of elements. In compression, the discretized percentages of failed elements for the 7 RVE directions model are rather close with intra-layer, inter-layer and bead failure being primary, secondary and tertiary, respectively. Nevertheless, please recall that the chosen domain discretization reflects the 3 main directions model and that in the 7 directions model there are four additional element directions having different properties (e.g., more strain capacity) that are now also partially contained in one of the three main directions, which may cause a somewhat distorted image. To conclude, no (significant) bead failure occurs in the heterogeneous models until near the end of the analysis progress whilst in the homogeneous model barely any interface failure takes place at all. This is a possible explanation of both the strength overestimation as well as the much more brittle failure happening in the homogeneous simulations. Contrary, given the absence of (significant) bead failure and the fact that a substantial fraction of interface elements initially fails in the heterogeneous simulations endorse their softening behaviour.

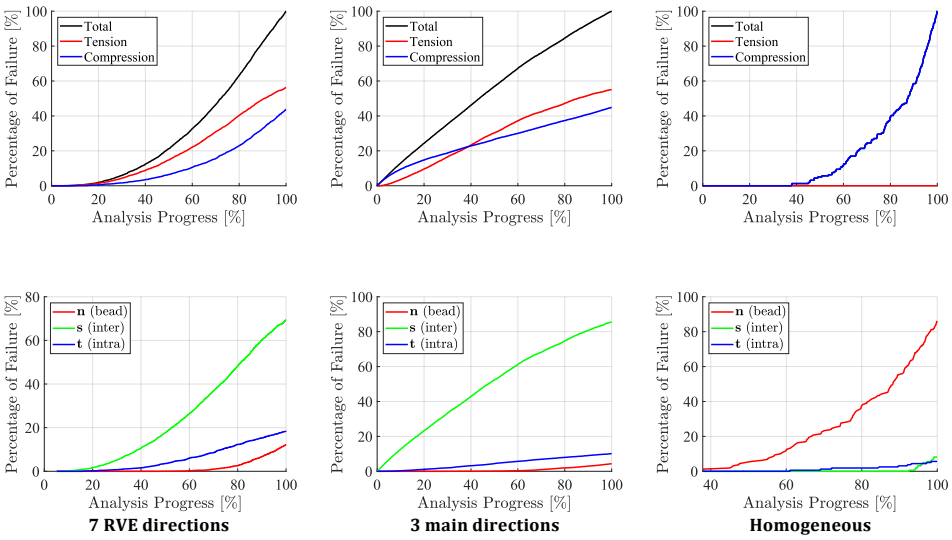

Figure 3.25: Percentage of locally failed elements versus analysis progress of RE architecture

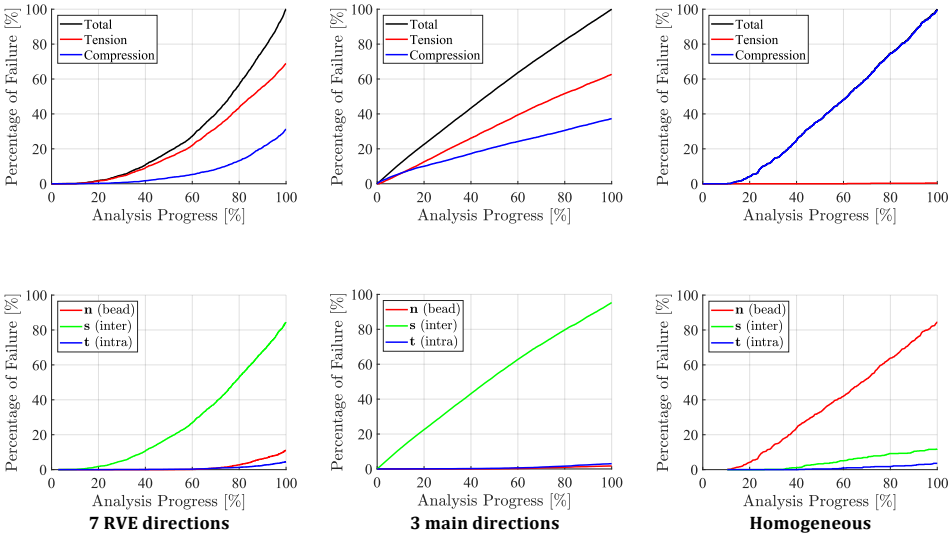

Figure 3.26: Percentage of locally failed elements in Tension (T) and Compression (C) versus analysis progress of RE architecture

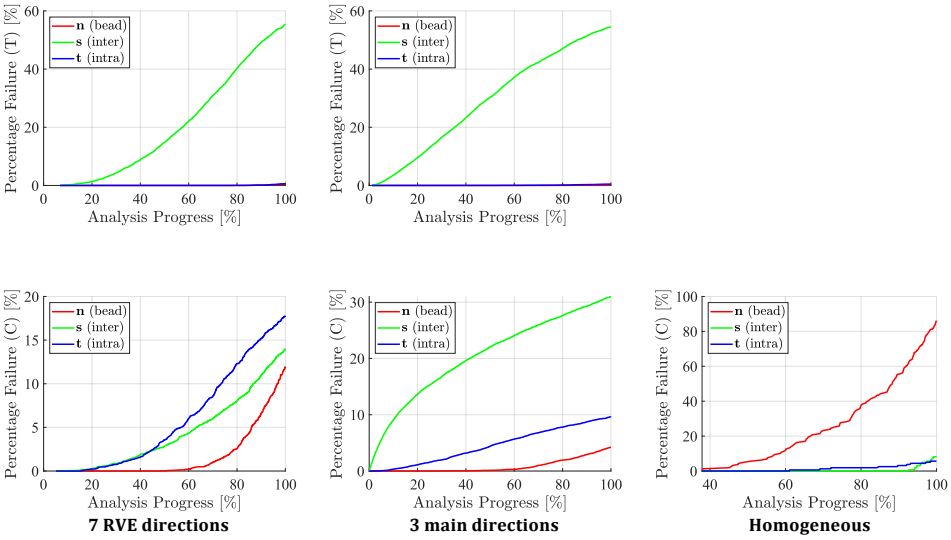

Figure 3.27: Percentage of locally failed elements versus analysis progress of RS architecture

In Figures 3.27 and 3.28, the percentages of failed elements against the analysis progress for the RS architecture are provided in a similar configuration. Nearly identical observations as for the RE design can be made for the RS simulations, starting with Figure 3.27, the major tensile failure in the 7 RVE directions and 3 main directions models and (almost) sole compressive failure in the homogeneous model. Only here the fraction of tensile failure sticks out more compared to the RE simulations. Furthermore, the heterogeneous models primarily fail at the inter-layer bond here too, as well as the homogeneous model's dominant bead failure. A major difference for the heterogeneous models with respect to their RE counterparts is that besides the inter-layer failure, the fraction of failed elements (in either tension or compression) is much more limited and starting to develop later for the RS structures. Similar things can be concluded from Figure 3.28, such as the 7 RVE directions and 3 main directions models primarily failing in tension, whilst the homogeneous simulation mainly fails in compression with only a marginal fraction of tensile failure. It is again noteworthy that the heterogeneous models in tension (almost) fail at the inter-layer bond alone. Once more, this observation is in favor of initiation of delamination of the planar auxetics. Analogous to the RE architecture, the homogeneous model of the RS design experiences limited failure in the intra-layer and inter-layer bonds. Finally, similar to the RE simulations, no (significant) bead failure occurs in the heterogeneous models until near the end of the analysis progress while in the homogeneous model barely any interface failure takes place at all. These observations, together with the evidence that in the heterogeneous models there is almost no bead failure when there is a lot of interfacial failure happening, could explain the overestimation in strength for the homogeneous models. Finally, to check the influence of the variability in the material scale dog bone specimens results as shown in Figure 3.7, additional auxetic structure scale simulations are carried out in Appendix A.1.

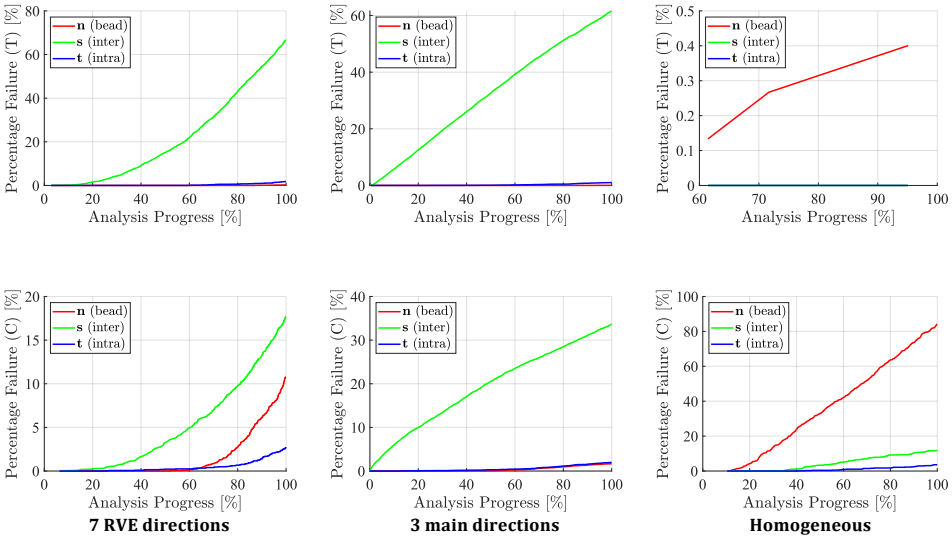

Figure 3.28: Percentage of locally failed elements in Tension (T) and Compression (C) versus analysis progress of RS architecture

3.5. SUMMARY & CONCLUSIONS

The deformation and fracture of FDM 3D printed planar auxetics have been modelled by means of the proposed two-scale modelling procedure presented in this study. First, models on the material scale from an idealized microstructural cubical RVE obtained from CT data are considered to explicitly incorporate the observed porosity and interface properties (i.e., inter-layer and intra-layer bonds). The output from this microstructural model was used as input for auxetic structure scale LBM simulations of planar auxetic designs having printing path-dependent properties. Two auxetic architectures are considered: Re-Entrant (RE) and Rotating Square (RS) designs.

Based on the results from the idealized microstructural RVE, it has been demonstrated that only including the porosity in numerical simulations of FDM printed parts is not sufficient. This argument is supported by numerical results of a homogeneous RVE (including porosity), yielding higher strengths and more ductile responses than the experimentally obtained constitutive relationships. Moreover, force displacement curves of the auxetic structure scale models of the RE and RS architectures show that neglecting the anisotropic (bond) properties in numerical models for FDM 3D printed polymers results in an overestimation in strength. The corresponding deformations and failure mechanisms (i.e., fracture) also correspond well with experimental test results. All modelled RE designs show diagonal shear failure in which the inward-facing re-entrant ribs fold inwards prior to self-contact, which is similar to experimental observations. In accordance with test recordings, the numerical RS structures all comprise failure of the joints between one of the inward-facing vertical struts and failure of one or more exterior struts touching the (virtual) loading plates. The aforementioned results hold independent of the meshing seed and directional element discretization with only minor differences between the 7 RVE directions and 3 main directions models. In terms of mechanical response, the

experimentally and numerically obtained force displacement curves agree reasonably well too: the stiffness of both planar auxetic designs fit well with the experimentally measured ones while the LBM simulations generally provide a good estimation in strength with maximal percentage differences of only 6 % and 10 % to 12 % for the RE and RS architectures, respectively.

Furthermore, it has been shown on both the material and auxetic structure scales that incorporation of the interfacial bond strengths in numerical models for FDM 3D printed polymers is important. On the material scale, neglecting the weaker inter-layer and intra-layer bond properties resulted in a significantly stronger RVE response having increased deformation capacity after yielding. In the auxetic structure scale models, the homogeneous isotropic material properties illustrated that neglecting the anisotropic (bond) properties provided large discrepancies between the LBM simulations and experimental measurements. Also, the obtained deformations and failure mechanisms changed when implementing homogeneous material characteristics, especially for the RS design, while the RE design exhibited a much more brittle response. The aforementioned arguments are supported by numerical investigations in which the percentage of failed elements are plotted against the analysis progress. These results clearly demonstrate that models considering interface properties primarily fail in tension, while models using homogeneous isotropic material properties mainly fail in compression. The heterogeneous models show governing failure of the inter-layer bond and that bead failure is limited until near the end of the analysis progress. In the homogeneous models, however, the majority of bead elements fail with barely any interfacial failure occurring prior to completion of the analysis.

Finally, it is important to note that the present study is only concerned with the mechanical and failure behaviour of planar auxetics under small deformations. Modelling large deformations, including self-contact or even compaction, is beyond the scope of the current study. Therefore, with the intention of modelling small deformations and failure in mind, it can be concluded that the printing path-dependent two-scale models for FDM 3D printed planar auxetics by means of LBM simulations prove to be very well capable of capturing their characteristic traits within its valid range.

4

UNDERSTANDING THE BOND BETWEEN 3D PRINTED REINFORCEMENT AND CEMENTITIOUS MATRIX

The use of 3D printed polymers in the form of lattice reinforcement can enhance the mechanical properties of cementitious composites. Methods like Fused Deposition Modelling (FDM) 3D printing enable their creation, but this process has a large (negative) effect on their mechanical properties, with a large dependency on the printing direction. Continuing on Chapter 3 concerned with modelling the anisotropic behaviour of 3D printed polymeric reinforcement, this work focuses on the reinforcement-matrix bond. Because of the layer-by-layer filament extrusion process of the 3D printing technique, the edges of FDM 3D printed polymers are typically composed of ellipses. Based on this, it is hypothesized that morphological effects as a result of the 3D printing technique enhance the bond between 3D printed reinforcement and cementitious matrix: The elliptic geometry potentially facilitates interlocking with the cementitious mortar, thereby possibly enhancing the bond behaviour in certain directions. To investigate the geometrical directional-dependent features at the edges of 3D printed polymers in more detail, micro-scale models are developed. Geometrical effects induced by different printing configurations are studied. The simulation results are verified through meso-scale pull-out experiments. The interlocking effects as a result of the 3D printing technique show to be significant seeing a bond strength increase of up to 56 % *in one of the print configurations compared to the direction without any geometrical effects.*

With the exception of minor textual adjustments, this chapter is reproduced from: R.J.M. Bol, Y. Xu, M. Luković, B. Šavija, *Does printing direction influence the bond between 3D printed polymeric reinforcement and cementitious matrix?*, Engineering Failure Analysis **174**, 109471 (2025).

4.1. INTRODUCTION

3D printed polymers in the form of lattice reinforcement can enhance the properties of cementitious composites [75, 108, 109]. One of the considered composite categories exhibits excellent compressive ductility, which is achieved by auxetic reinforcement architectures [110]. These auxetic architectures are mechanical metamaterials which have a negative Poisson's ratio [30–43]. Additive Manufacturing (AM) methods like 3D printing enable the creation of auxetic structures [32]. However, the production process of such reinforcements has a large effect on their mechanical properties, with a large dependency on the direction of printing and loading [111]. Some concerns for objects constructed through AM are, for instance, the containing of geometrical imperfections [39] and high level of anisotropy [34].

The literature review in Chapter 2 on micromechanical models for 3D printed polymers, focusing on Fused Deposition Modelling (FDM), covers numerous literature on the topic of so-called *printing process parameters*, elaborating their influences on mechanical properties and behavioral features. Among the investigated process parameters for FDM are surface roughness and quality (e.g., [50, 60, 62, 69–71]). Surface roughness, also described as surface quality, is related to the layer-by-layer filament extrusion process of the 3D printing technique. Therefore, the edges of FDM 3D printed polymers are typically composed of ellipses [72]. These can be regarded as superficial defects, because the intended shapes, usually modelled through 3D software, do not contain these edge effects [70]. As a result, the elliptic exterior surfaces of FDM 3D printed polymers include variations [72], which can be seen as 'porosity of the edges' (see Chapter 2).

Based on Chapter 2, it is hypothesized that morphological effects as a result of the 3D printing technique may enhance the bond behaviour between FDM 3D printed reinforcement and cementitious matrix: The elliptic geometry potentially facilitates interlocking with the cementitious mortar, thereby possibly enhancing the bond behaviour in certain directions. This, in combination with Chapter 3 on printing path-dependent two-scale models for 3D printed planar auxetics by material extrusion (i.e., FDM), is the next step in the development of a modelling framework for simulating deformation and fracture of Auxetic Cementitious Composites (ACCs). In the aforementioned chapter, the proposed experimentally validated two-scale model that was able to capture the *printing path-dependent anisotropy* of 3D printed polymers using the Lattice Beam Model (LBM). So far, the bond behaviour in LBM simulations for reinforced cementitious composites was considered either by parameter fitting [122, 146] or through analytical expressions [117, 147]. More recently, Mustafa et al. [130] determined the concrete-reinforcement interface element properties via inverse analysis to get the same crack widths as experimentally measured, and Gu et al. [129] proposed a generalized mathematical approach to model reinforcement-concrete bond.

The current chapter provides valuable insights regarding the effect of printing direction on the interface properties between 3D printed reinforcement and cementitious matrix. Using a novel approach to model pull-out experiments on two different length scales, this study offers a good understanding of bond properties between 3D printed reinforcement and cementitious matrix at the micro-scale. Microscopic investigations of failure mechanisms in additively manufactured reinforcement as well as amongst 3D printed reinforcement and cementitious matrix are considered. Failure analysis for

a 3D printed polymeric-cementitious composite system is performed with numerical simulations. To the best of the author's knowledge, this work is the first to quantitatively investigate the influence of printing direction on the bond between 3D printed polymeric reinforcement and cementitious matrix. A novel methodology for determining the bond between cementitious matrix and 3D printed polymers is explained, starting with pull-out experiments between FDM 3D printed Acrylonitrile Butadiene Styrene (ABS) bars and cementitious mortar (described in [148]), which are used to calibrate a meso-scale pull-out model. Morphological effects are studied by numerical simulations on two length scales, leading to a good understanding of the effects the geometrical directional-dependent edge features of 3D printed polymers have on the bond behaviour. Bond properties are first determined at the meso-scale using a pull-out model which resembles the pull-out experiments (as described in [148]). It should be noted, however, that these pull-out tests are performed on ABS bars in which the printing path is parallel to the direction of loading to avoid any influence from the intra-layer and inter-layer bonds caused by the printing process. Monaldo & Marfia [74] describe the inter-layer bond as cohesion among layers stacked vertically during the printing process, and the intra-layer bond as cohesion among filaments deposited next to each other horizontally within the same layer (see Figure 4.6). Secondly, to explicitly model the geometrical directional-dependent features at the edges of FDM 3D printed polymers, micro-scale models are developed using the meso-scale properties as a reference. The material properties of the ABS bars for both the meso-scale and micro-scale models are adopted from Chapter 3 and are calibrated based on experimental results.

4.2. LITERATURE

4.2.1. REINFORCEMENT-MATRIX BOND BEHAVIOUR

The bond between cementitious materials and reinforcement has been investigated for almost 150 years since Hyatt [149] performed tests on concrete and iron bars as early as 1876 [150]. This action of force transfer plays a crucial role in the performance of Reinforced Concrete (RC) elements [151–153]. Bond properties significantly affect the structural response of RC members, such as their load-carrying capacity (i.e., strength), crack propagation, crack widths, and deformation capacity and seismic resistance (i.e., energy absorption and dissipation capacity) [129, 152]. It is therefore essential to provide accurate constitutive relationships for interface elements in numerical simulations of RC structures [129, 154]. Although extensively researched by both experimental and analytical means [151], the bond between cementitious materials and reinforcement remains complex because of its dependency on numerous parameters (e.g., cover thickness, confinement conditions and concrete strength) [129].

Generally, bond behaviour can be defined as the force transfer or bond stress between concrete and reinforcement [155]. The term *bond stress* is often used to describe this shear stress or unit shear force that acts parallel to a reinforcement bar on its interface with surrounding concrete [156]. The bond transfers the reinforcement bar forces to the cementitious matrix, or vice versa, by which the bond stress alters the steel stress: '(...) there can be no bond stress unless the bar stress changes, and there can be no change in bar stress without bond stress.' [156]. As defined by the American Concrete

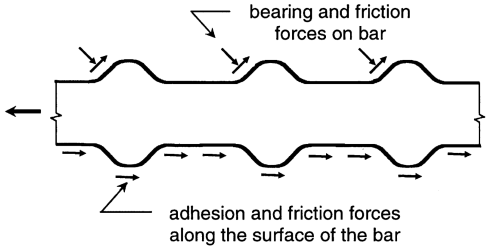

Figure 4.1: Bond force transfer mechanisms [157]

Institute (ACI), bond is composed of the following three constituents (Figure 4.1): (i) chemical adhesion between the concrete and the reinforcement bar; (ii) friction as a result of interfacial surface roughness, transverse forces exerted on the bar, and relative slip between the concrete and the reinforcement bar; and (iii) mechanical interaction between the cementitious matrix and steel by means of anchorage or interlocking of the surrounding concrete and ribs on deformed reinforcement bars [155, 157]. Moreover, it is asserted that the bond stress varies with respect to the *bond slip*, which represents the difference in displacements between the concrete and reinforcement [151]. It is this bond slip that causes local concrete failure, which in turn deteriorates the bond behaviour.

4.2.2. EXPERIMENTAL CONTRIBUTIONS

Various test setups can be utilized for investigating the bond between concrete and (deformed) reinforcement bars [157]. Due to its convenient manufacturing and straightforward testing procedure [151], the majority of experiments for obtaining bond are performed using a pull-out set-up [157]. In these tests, a reinforcement bar is embedded in a concrete cylinder or prism and directly pulled out from one end whilst the matrix is held in place from the same side [156]. However, it is argued in several studies (e.g., [151, 157]) that the pull-out configuration is not representative or even unrealistic because of its boundary conditions: the compressive reaction stresses in the concrete near the supports cause an induced confinement of the interface, which is not present in most RC members. American Concrete Institute (ACI) Committee 408 [157] therefore discourages the use of this testing configuration. This view is supported in [158] for deformed reinforcement bars, where it is remarked that pull-out tests typically overestimate the bond capacity. Nevertheless, the latter reference also reflects on the case for plain reinforcement bars for which it is concluded that pull-out tests capture the actual failure mode and enable for precise evaluation of their bond behaviour as these do not (primarily) rely on mechanical interlock.

After the occurrence of slip, the bond stress along the reinforcement bar is assumed to be uniform. In view of this, most (experimental) studies consider a bond unit stress (e.g., [122, 150, 156, 158, 159]):

$$\tau = \frac{P}{mh} = \frac{P}{\pi d L}, \tag{4.1}$$

where τ is the nominal (average) bond stress or interfacial shear stress, P is the applied pull-out load or reinforcement bar force, $m = \pi d$ the circumference of the reinforcement bar, d the reinforcement bar diameter, and h and L are the embedded length (sometimes

simply equal to the specimen length [150, 156], depending on the reference and test setup).

Recent developments have led researchers to study the mechanical bonding of the interface between cementitious matrix and 3D printed polymer material as reinforcement in composites, such as the work by Namakiaraghi et al. [160]. In particular, they investigate the influence of surface texture on the bond behaviour by means of performing pull-out experiments on rectangular 3D printed PLA specimens having smooth and textured exterior surfaces (see Figure 4.2). Their experimental campaign involves specimens having two dimensions (D) of 5×5 and 6.75×6.75 mm^2, as well as five different embedded lengths (L) equal to $2D$, $6D$, $10D$, $14D$, and $18D$. Results indicate that larger tensile stresses need larger embedded lengths to prevent bond failure and that if the PLA specimens broke before pull-out, bond stresses are proportional with the embedded length L. The exterior surface texture has a positive effect on the bond behaviour such that equal embedded lengths can sustain higher tensile stresses compared to the smooth specimens. This means that a rough surface results in a stronger bond than a smooth surface. Through extrapolating fitted linear regression curves critical bond lengths (l_c) are found, which are explained as a lower bound for when tensile stresses cause rupture of the 3D printed material instead of pull-out. Phrased differently, one should ensure that $l \geq l_c$ to exploit the reinforcement to its full potential. Using the experimental data and determined critical bond lengths, shear bond strengths are computed as:

$$\tau = \frac{P_{max}}{\pi d l_c}, \tag{4.2}$$

where P_{max} is the maximum force measured upon breaking of the bond at l_c, and d the size of the square cross-section. Bond strengths of 0.76, 0.67, and 1.35 MPa were found for specimens having 5 and 6.25 mm smooth, and 6.75 mm textured exterior surfaces, respectively. Similar to conventional reinforcement (i.e., ribbed steel reinforcement bars), this points out that the mechanical bonding of the interface between cementitious matrix and 3D printed polymer material is dependent on both the embedded length and the surface texture, where the latter facilitates a significant raise in bond strength of over 100 %. Finally, Namakiaraghi et al. [160] also consider, both experimentally and numerically, flexural beam specimens. Bond behaviour is related then to the fact whether the surface texture of the reinforced samples are smooth or having vertical anchorage of the PLA reinforcement. These are found to exhibit the same characteristics as plain mortar beams up to initial cracking, however, the anchored beams regain their strength by over 250 % and show ultimate mid-span deflections reaching more than ten times that of plain mortar before failure of the reinforcement. However, in their numerical models of the flexural beam specimens Namakiaraghi et al. [160] assume no bond failure will occur before the PLA reinforcement fails. They reason that the Young's moduli of the cementitious matrix and 3D printed material have the same order of magnitude, as opposed to conventional RC beams, and therefore argue that no slipping nor detachment of the reinforcement will occur. Instead, it is discussed that both materials are likely to mutually fail such that the bond behaviour can be modelled using the Embedded Region (ER) constraint available in commercially available FEM software (e.g., ABAQUS Explicit). Nevertheless, this constraint does not enable the implementation of a bond stress-slip relationship between cementitious matrix and 3D printed polymer material.

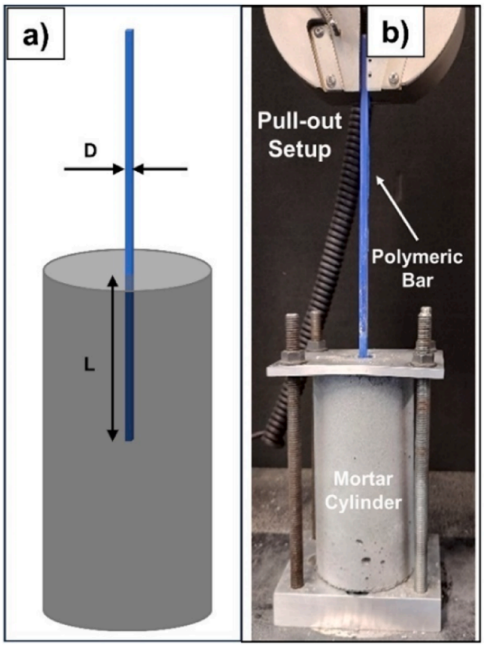

Figure 4.2: Pull-out experiments on rectangular 3D printed PLA specimens having varying cross-section sizes (D) and embedded lengths (L): a) Schematic, b) Setup [160]

4.2.3. ANALYTICAL MODELS

Experimental results are often generalized in terms of analytical models that represent the observed behaviour in a mathematical manner. This is mainly done to quantify these relationships under different boundary conditions [129]. A large number of analytical models has been developed that describe the bond behaviour between concrete and deformed reinforcement bars (e.g., [152, 154, 156, 159, 161, 162]). A recent study by Gu et al. [129] proposed a methodology for LBM simulations to determine the mechanical properties (strength and Young's modulus) of interface elements between concrete and deformed reinforcement bars. Therein, a particularly interesting analytical model by Harajli et al. [152, 159, 162] was used. The analytical model is graphically displayed in Figure 4.3. The analytical model shows similarities with one previously proposed by Eligehausen et al. [161]. It can be seen that the pull-out envelope consists of four phases, starting with an ascending branch that was derived using similar experiments as performed by Eligehausen et al. [161].

4.3. METHODOLOGY

Determining the bond behaviour between cementitious mortar (i.e., matrix) and 3D printed polymers (e.g., ABS) is relevant for all cases where 3D printed reinforcement is used in cementitious composites. In fact, it is a crucial intermediate step when moving from solely modelling 3D printed polymeric reinforcement architectures (see Chapter 3) towards modelling composites. Therefore, it is important that this behaviour is imple-

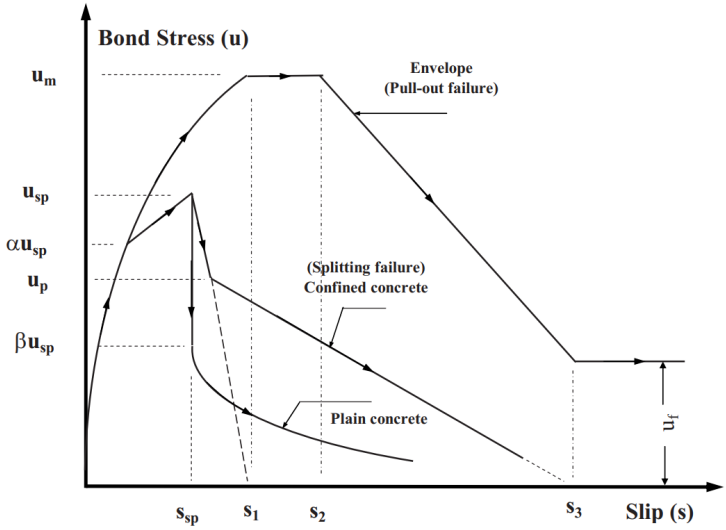

Figure 4.3: Monotonic envelope model [162]

mented into numerical simulations. The starting point for this are pull-out experiments between FDM 3D printed ABS bars and cementitious mortar (described in [148]), which are used to calibrate a meso-scale pull-out model. From this meso-scale bond model, the calibrated bond properties could be directly used in specimen-scale models for simulating the composite behaviour of cementitious mortar reinforced with auxetic architectures like the Re-Entrant (RE) and Rotating Square (RS) designs in Chapter 3. However, based on Chapter 2, as well as the Scanning Electron Microscope (SEM) pictures in Figure 4.4, it is hypothesized that morphological effects as a result of the 3D printing technique may have a beneficial effect on the bond behaviour between FDM 3D printed polymers and cementitious matrix.

To study the influence of these morphological effects on the bond behaviour, numerical simulations on two length scales using LBM simulations are proposed in this section. To begin with, bond properties shall be determined on the meso-scale using a pull-out model which resembles the pull-out experiments (as described in [148]). These pull-out tests are performed on ABS bars in which the printing path is parallel to the direction of loading to avoid any influence from the intra-layer and inter-layer bonds caused by the printing process, see Figure 4.6. In other words: the pull-out behaviour is experimentally measured in the bead or filament direction (i.e., the 'bulk material' without interfaces perpendicular to the loading direction, see Chapter 2).

4.3.1. EXPERIMENTAL ANALYSIS

The cementitious matrix is a high-volume fly ash mortar, for which the mix design was adopted from [139] and is given in Table 4.2. The binder consists of CEM I 42.5 N Portland cement (550 gL^{-1}) blended with siliceous fly ash (650 gL^{-1}). The aggregate is an ultra-fine silica sand with a narrow grading of 0.125-0.250 mm, dosed at 550 gL^{-1}, corresponding to a sand-to-binder ratio of 0.46 by mass. Workability at this low water content is achieved

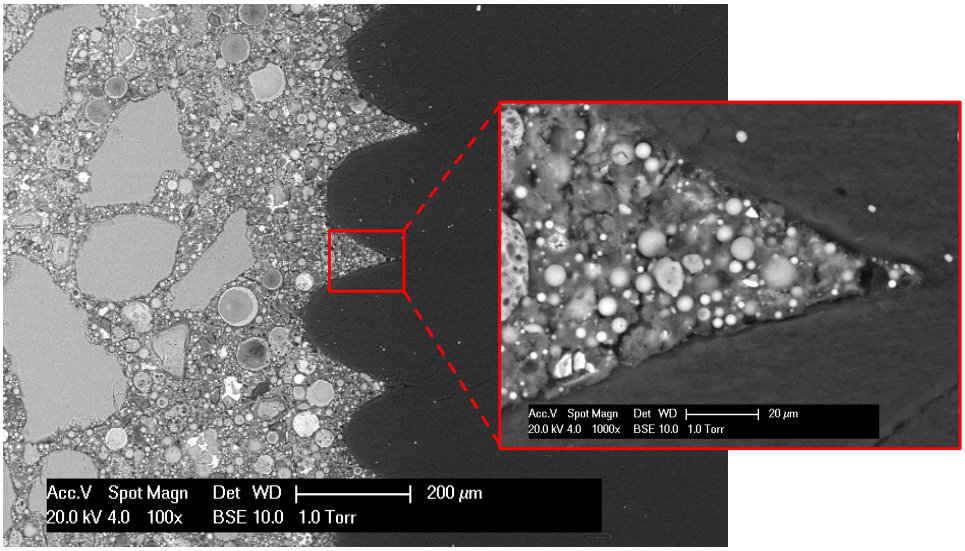

Figure 4.4: SEM picture of the interface between FDM 3D printed ABS and cementitious mortar before testing

with a superplasticizer (Glenium 51, 2 gL^{-1}). It should be emphasized that the water-to-binder ratio of 0.33 reported previously in [139] counts both the cement and the fly ash as binder. Expressed with respect to the Portland cement alone, the water-to-cement ratio of the mix is 0.72. The distinction matters here because of the unusually high fly ash replacement level: a substantial fraction of the fly ash does not react at 28 days and instead acts as a fine filler, improving particle packing and workability. These mix proportions were deliberately developed to achieve relatively high fluidity to facilitate the filling of the hollow cells of the printed reinforcement in this study. This combination of a high fly ash content, an ultra-fine sand and a low water-to-binder ratio further ensures a well-defined reinforcement–matrix interface as illustrated in Figure 4.4. Specimens were cured for 28 days prior to testing.

The experimental pull-out results are adopted from [148] in which four specimens were created by a commercially available FDM 3D printer (Ultimaker 2+) provided the printing parameters in Table 4.1. The resulting 2 × 3 mm ABS bars with a length of 50 mm were placed in plastic cylindrical moulds having a radius of 10 mm. To prevent any boundary effects near the bonded region, the first 5 mm of the cementitious cylinder was prevented to touch the ABS bar by means of a plastic tube with a radius of 5 mm, while the embedded length was 10 mm. When cured and demoulded, the specimens were cut into rectangular pull-out samples. The creation and dimensions of the pull-out specimens are depicted in Figure 4.5. All experiments were conducted at room temperature.

The pull-out tests were executed by a hydraulic press INSTRON 8872, in which the cementitious cylinders were installed upside down within the steel loading frame of the device (see Figure 4.6). The ABS bars were loaded by means of a clamp that was fixed to the hydraulic press and displaced at a rate of 5×10^{-3} mms^{-1}. The force and deformation recordings were performed through the INSTRON itself and Linear Variable Differential Transducers (LVDTs) at both sides of the clamp, respectively, as shown in Figure 4.6.

Table 4.1: Printing parameters from [148]

Parameters	Configuration
Nozzle diameter (mm)	0.8
Temperature (°C)	260
Layer height (mm)	0.2
Line width (mm)	0.7
Infill density (%)	100
Printing speed ($mm\,s^{-1}$)	40

Table 4.2: Mixture design of cementitious matrix from [148]

Mixture components	Quantities ($g\,L^{-1}$)
CEM I 42.5 N	550
Fly ash	650
Sand (0.125-0.250 mm)	550
Superplasticizer (Glenium 51)	2
Water	395

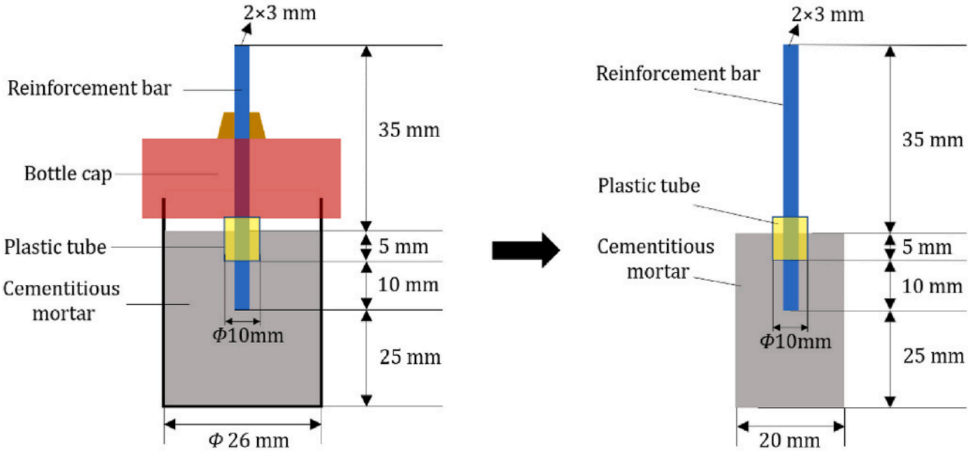

Figure 4.5: Bars fixed in cylindrical molds (left) and dimensions of the prismatic pull-out specimens after cutting (right) [148]

Experimental pull-out results [148] are presented as bond stress-slip curves in Figure 4.13. The bond stress in Figure 4.13 is calculated using the actual circumference obtained from the expanded geometrical model described in Chapter 3 as shown in Figure 3.8. This model describes the cross-sectional shape of 3D printed materials and requires the following input parameters: the layer thickness (t), vertical overlap interval (c), air gap (H), raster orientation (β), cross-sectional shape parameters (a, b) or the ratio between the bead's semi-major and semi-minor axes ($r = a/b$), the layer width (L), horizontal overlap interval (d), inter-layer bond width (w_{inter}), and intra-layer bond height (h_{intra}).

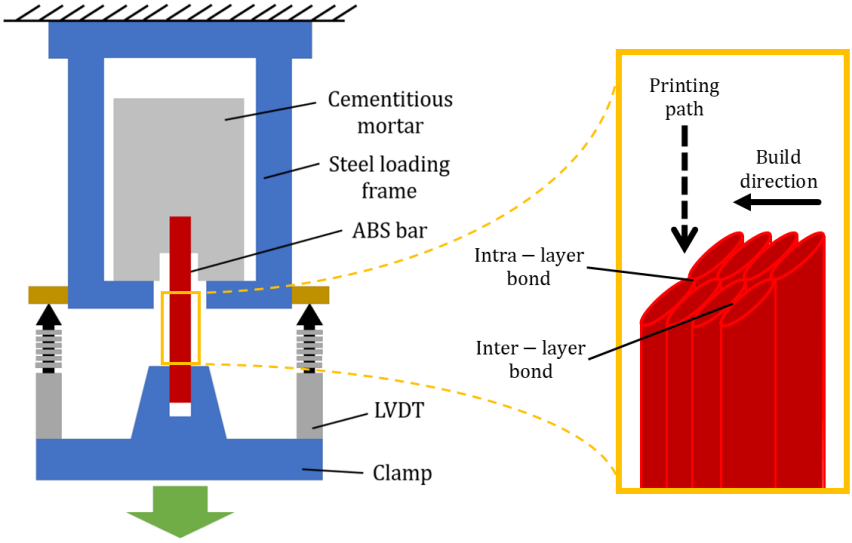

Figure 4.6: Schematics of the pull-out test set-up [148]

The average input parameters for the extended geometrical model shown in Figure 3.8 as obtained from the microstructural experimental analysis performed in Chapter 3 are listed in Table 3.2.

From the bond stress-slip results in Figure 4.13 it can be observed that the bond strength between FDM 3D printed ABS and cementitious matrix is very low, i.e., below 1 MPa. Because all experiments resulted in successful bar pull-out, the weak bonding can be attributed to the fact that, at the molecular scale, ABS consists of hydrophobic groups [148]. As a result, there is no chemical adhesion with the cementitious mortar. Because of the absence of chemical adhesion, the bond strength mainly reflects the contribution of friction.

To better understand the bond behaviour between the FDM 3D printed ABS and cementitious matrix, SEM pictures are taken to visualize the interface amongst the two materials. Figure 4.4 depicts two 20.0 kV images at different magnifications of 100 and 1000, clearly showing the elliptical morphology at the edges of the ABS 3D print. Furthermore, Figure 4.4 shows that the cementitious mortar has completely filled the sharp interior portions at the intersections between the stacked bead layers. This raised the hypothesis that interlocking effects as a result of the 3D printing technique could be facilitated, particularly in the inter-layer direction which has a strong resemblance with deformed reinforcement bars. Nevertheless, aside from potentially elevating the ABS-matrix bond, the interlocking matrix could also induce deterioration: If the elliptical edges of the ABS 3D print are pushed into the cementitious matrix (or vice versa), the matrix could act like a splitting wedge leading to separation of the 3D printed layers. This may cause out-of-plane failure of the weak inter-layer bond within ABS 3D printed reinforcement as observed in [110] (i.e., adhesion failure among different printed layers), see Figure 4.7.

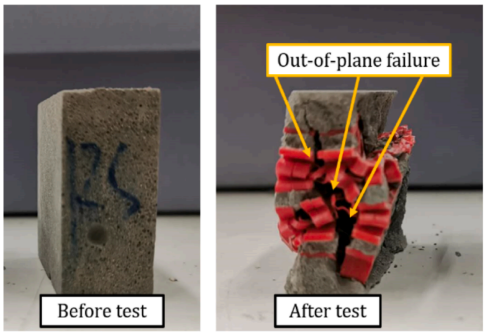

Figure 4.7: Auxetic cementitious composite specimens before and after uniaxial compression tests [110]

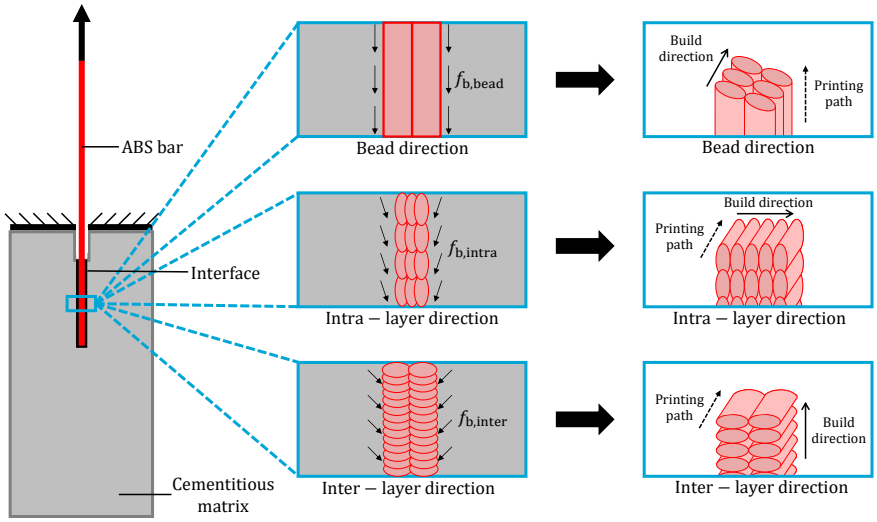

Figure 4.8: Bond behaviour of hypothesized mechanical interactions caused by different (local) shapes of reinforcements depending on printing path and build direction

Figure 4.8 illustrates the bond behaviour of the hypothesized mechanical interactions for the three different directions as a result of morphological effects. Please note that the intra-layer and inter-layer directions are only investigated numerically at the micro-scale. These two directions can be regarded as if the ABS bars in the experiment were printed in the two mutually orthogonal build directions with respect to the bead direction.

4.3.2. NUMERICAL SIMULATIONS ON TWO LENGTH SCALES

LATTICE BEAM MODEL

Realistic mechanical and fracture responses were obtained through LBM by Xu et al. [111] for FDM 3D printed specimens subjected to uniaxial tension. Therein, the anisotropy caused by the manufacturing technique was captured implicitly. Chapter 3 successfully improved upon this by explicitly modelling the anisotropy as a result of the intra-layer

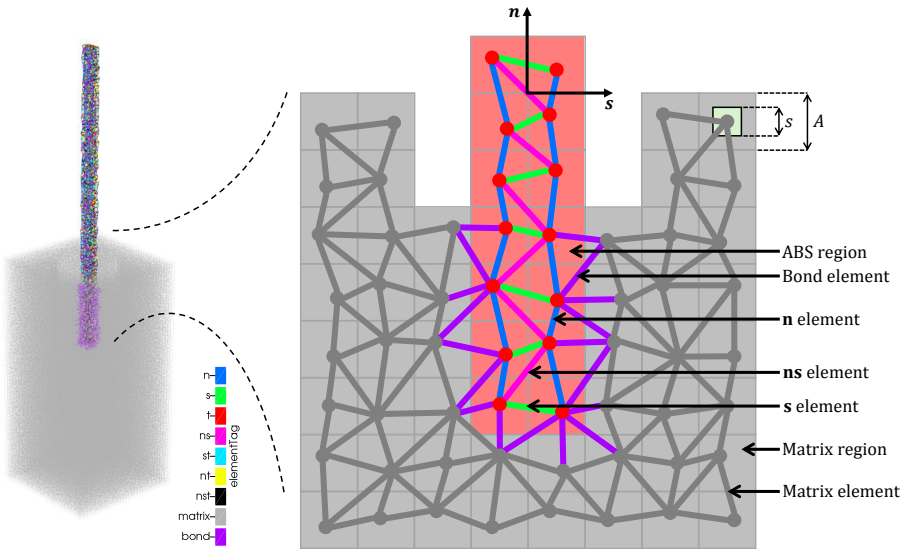

Figure 4.9: Generated lattice mesh for meso-scale pull-out model

and inter-layer bonds present in FDM 3D printed polymers. More recently, Xu et al. [148] implemented experimentally validated properties for the bond behaviour between FDM 3D printed ABS and cementitious matrix. However, their LBM simulations assumed the 3D printed bars, as well as the interface among the two materials, to be homogeneous and isotropic. Therefore, the LBM simulations presented herein can be regarded as an extension of the previous model in [148] through incorporation of the anisotropic response observed in FDM 3D printed polymers. In this study, the hypothesis that morphological effects as a result of the 3D printing technique may have an beneficial effect on the bond behaviour between FDM 3D printed (auxetic) reinforcement and cementitious matrix will be tested. The numerical procedure used is similar to that of Chapter 3, whereas the phase of each lattice beam element is determined using two strategies here, depending on the location of its two end nodes. The first strategy takes care that if both end nodes are located in the same region, the lattice beam element receives material properties belonging to that region (i.e., cementitious matrix in Figure 4.9). When the two end nodes are in different regions, such that the element crosses between them, it is considered an interfacial element having properties corresponding to that particular interface (i.e., ABS-matrix bond in Figure 4.9). The second strategy, proposed in Chapter 3, only concerns elements with both end nodes inside 3D printed material (i.e., ABS region in Figure 4.9). In that case, mechanical properties are assigned based on the element's orientation with respect to the printing path (n_i in Figure 4.9).

The same directional element domain discretization strategies as elaborated in Chapter 3 are used to capture the anisotropic behaviour of the ABS material as a result of the FDM 3D printing technique. Printing path-dependent lattice properties are assigned by introducing a local coordinate system consisting of unit vectors n_i, s_i and t_i. As shown in Figure 4.9, n_i corresponds to the ABS bar's longitudinal axis, which is parallel to the printing path, whilst s_i is perpendicular to n_i and lies in the same plane. t_i is the normal

vector of this plane and is therefore not depicted in the two-dimensional representation in Figure 4.9. Directional element categories are imposed in every local coordinate system by means of spherical angles, where θ_{nst} is the azimuth angle of the projection on the plane formed by unit vectors n_i and t_i, measured from vector n_i, and ϕ_{nst} is the polar angle measured from the unit vector s_i. Now, the directional element categories can be decomposed into directional element domains in the local coordinate system with respect to the spherical angles. The decomposed directional element domains are listed in Table 3.3. Each colour of the lattice beam elements in Figure 4.9 corresponds to a different constitutive relationship. The input properties for the lattice beam elements corresponding to matrix phase are calibrated according to the experimental data presented in [110].

MODELLING PROCEDURE

The generated lattice mesh for the meso-scale pull-out simulations is displayed in Figure 4.9, having a mesh size of 0.6 mm that is chosen to match the dimensions of a cubical Representative Volume Element (RVE) of FDM 3D printed ABS material from Chapter 3. This RVE is calibrated based on microstructural experimental analysis to explicitly include the anisotropy present in FDM 3D printed material caused by the layer-by-layer deposition process elaborated in Chapter 2. Hence, it provides the constitutive relationships based on the beam element's orientation with respect to the printing path (n_i in Figure 4.9). The input parameters for the ABS filament in the LBM simulations presented here can therefore be directly adopted from Chapter 3, which are provided in Table 3.6. The matrix phase input is calibrated according to the standard procedure for LBM simulations described in Chapter 3, which entails the beam element radii and their local strength: First the element radii are iteratively determined in order to have matching local and global Young's moduli, followed by setting the local strength input such that the material's global strength matches experimental observations in the same manner. As pointed out before, the input properties for the lattice beam elements corresponding to matrix phase are calibrated according to the experimental data presented in [110]. With the bond phase being the only unknown, the meso-scale model allows for calibration of the ABS-mortar bond properties through parameter fitting.

Once the ABS-mortar bond properties at the meso-scale are fitted with the experimental pull-out results, these are scaled down to the micro-scale. To enable explicit modelling of the microstructural morphology as a result of the FDM 3D printing technique (see Chapter 2), a very fine mesh is required that would yield too computationally expensive numerical simulations at the meso-scale [148]. Therefore, taking into account the geometrical analyses described in Chapter 2 and Figure 4.4, three different directions with respect to the printing path will be studied by means of micro-scale LBM simulations: i) the bead or filament direction (parallel to the printing path, n_i), ii) the intra-layer direction (t_i), and iii) the inter-layer direction (s_i). These are the three mutually orthogonal print configurations in extrusion-basd 3D printing, such as FDM, which is the method applied here. Particularly the inter-layer direction has a strong resemblance with deformed reinforcement bars, see Figure 4.4.

The bead direction is the only direction that was successfully tested by means of pull-out experiments. It is therefore assumed that the bond behaviour between ABS and cementitious matrix is the same in terms of chemical adhesion and friction. Accordingly,

morphological effects only contribute to the mechanical interaction through anchorage or interlocking of the mortar and elliptical edges.

MICRO-SCALE PULL-OUT MODELS

At the micro-scale, a mesh size of 25 µm is used throughout all models. Similar to Section 4.3.2, this matches with the discretization used for the ABS cubical RVE in Chapter 3. Therefore, the experimentally calibrated microstructural constitutive relationships used therein can be directly adopted too (see Table 3.5). The out-of-plane model thickness is set to 750 µm with a matrix width kept constant at 1000 µm. All other dimensions related to the ABS bar correspond to the microstructural experimental analysis performed in Chapter 3 and are modelled via Rhinoceros® using Grasshopper according to the geometrical models by Ahn et al. [72] and its extension in [70] (see Figure 3.8 and Table 3.2). The cementitious matrix is calibrated using the same iterative procedure as described in Section 4.3.2 for finding the element radii and local strength input at the micro-scale, according to the experimental data presented in [110]. The local strength input parameters for the ABS-mortar bond elements is scaled accordingly.

To reduce computational costs only a half of each cutout is modelled in view of symmetry. To approximate experimental conditions, the loading and constraints are directly applied to the cutout portions of the ABS and surrounding matrix. In total, four scenarios are modelled at the micro-scale: a reference for the intra-layer direction which mimics the bead direction (Figure 4.10(a)), the intra-layer direction containing two adjacent beads (Figure 4.10(b)), a reference for the inter-layer direction that reflects the bead direction (Figure 4.10(c)), and the inter-layer direction consisting of eight stacked layers (Figure 4.10(d)). Because the semi-minor axis of the elliptic cross-section in the intra-layer direction (i.e., b in Figure 3.8) is smaller compared to the semi-major axis in the inter-layer direction (i.e., a in Figure 3.8), there is less polymer phase (i.e., ABS) in the micro-scale pull-out models for the intra-layer compared to the inter-layer (see Figure 4.10). Due to this difference in dimensions, as well as the randomness of the lattice mesh, a reference simulation for each direction is required to make a fair comparison. Hence, the two references in Figures 4.10(a) and 4.10(c) reflecting the bead direction are there to prevent any mesh dependencies when comparing the reference and morphological featured cases for the intra-layer and inter-layer, respectively.

MICRO-SCALE PUSH-OUT MODELS

Another methodology to test micromechanical bond behaviour is the push-out test [163] (see Section 4.2.2). This procedure allows to see the isolated effect of morphological features without any influence of the intra-layer and inter-layer bonds within the 3D printed ABS material. By exposing the reinforcement to compression, tensile failure of the internal bonds will not be governing. Hence, given the same experimentally-fitted bond properties as before, the push-out tests can measure the contribution of mechanical interactions. Similar to the micro-scale pull-out simulations, LBM push-out simulations are performed on the same small virtual cutouts from the experimental setup as displayed in Figure 4.8. The only difference with the models in Figure 4.10 are the boundary conditions, which are modified to simulate push-out conditions. Four push-out scenarios are modelled in parallel at the micro-scale to prevent any interfacial failure modes: a reference for the intra-layer direction which mimics the bead direction

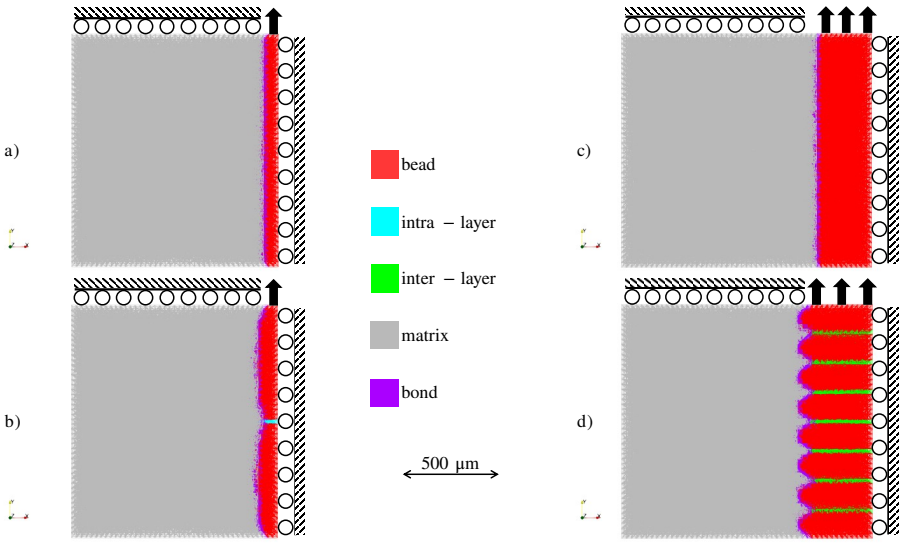

Figure 4.10: Generated lattice meshes for micro-scale pull-out models of a) intra-layer reference, b) intra-layer direction, c) inter-layer reference, and d) inter-layer direction

(Figure 4.11(a)), the intra-layer direction containing two adjacent beads (Figure 4.11(b)), a reference for the inter-layer direction that reflects the bead direction (Figure 4.11(c)), and the inter-layer direction consisting of eight stacked layers (Figure 4.11(d)). Similar to the micro-scale pull-out models, the two references in Figures 4.11(a) and 4.11(c) reflecting the bead direction are there to avoid mesh dependencies due to the randomness of the lattice mesh and the difference in dimensions amongst the intra-layer and inter-layer, respectively.

4.4. RESULTS

4.4.1. MESO-SCALE BOND STRESS-SLIP RELATIONSHIP

The meso-scale bond stress-slip relationship is fitted with experimental pull-out data, similar to [148]. The starting point is to model the ABS bar, which is done in accordance with the printing path-dependent two-scale modelling scheme data explained in Chapter 3. The local input for the matrix phase is calibrated with experimental data in [110] and lattice properties used in [148], corresponding globally to mortar with a Young's modulus of 11 417 MPa. The local input therefore yields $E = 11\,417$ MPa, $G = 3805.7$ MPa, $f_t = 4.07$ MPa, and $f_c = -32.59$ MPa. Please note that local input (i.e., element properties) are always calibrated in such a way so that the global specimen response is achieved. Hence, depending on the mesh parameters (e.g., size and randomness), slightly different local properties are needed to mimic the same global behaviour [164].

The constitutive relationship for the bond elements between FDM 3D printed ABS bars and cementitious matrix is defined as a multi-linear curve composed of five segments (see Figure 4.12), similar to the pull-out models developed in [148]. Hence, their stiffness and strength are modified accordingly throughout the analyses rather than being directly

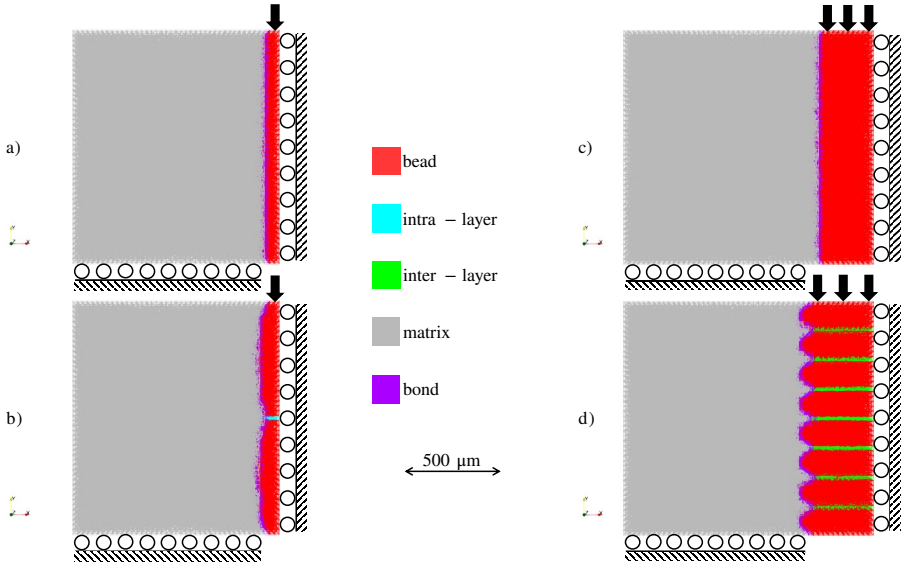

Figure 4.11: Generated lattice meshes for micro-scale push-out models of a) intra-layer reference, b) intra-layer direction, c) inter-layer reference, and d) inter-layer direction

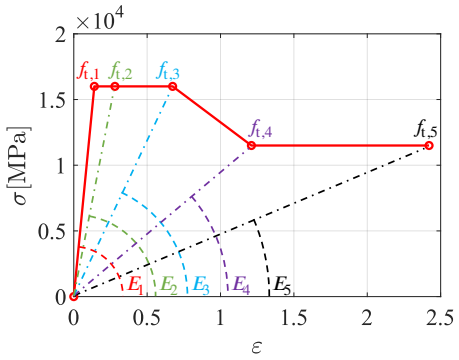

Figure 4.12: Multi-linear constitutive relationship for ABS-mortar bond

discarded. The input parameters for the bond phase regarding the meso-scale pull-out model in Figure 4.9 are contained in Table 4.3. The values for the ABS bars from Chapter 3, including the directional discretizations to capture their anisotropy, can be found in Table 3.6.

The shape of the multi-linear constitutive relationship for ABS-mortar bond in Figure 4.12 shows strong similarities with analytical models described in Section 4.2.3. It resembles the analytical model by Harajli et al. [152, 159, 162] displayed in Figure 4.3. Other analytical models discussed in Section 4.2.3 contain strikingly equivalent (portions of these) shapes [151, 161, 165]. As explained in Section 4.2.1, the analytical model by Harajli et al. [152, 159, 162] has been implemented successfully before in LBM simulations

Table 4.3: Input parameters for meso-scale ABS-mortar bond phase elements, following the curve shown in Figure 4.12

Properties	**Segment** 1	**Segment** 2	**Segment** 3	**Segment** 4	**Segment** 5
E_i (MPa)	114170	57085	23750	9500	4750
G_i (MPa)	38057	19028	7917	3167	1583
$f_{t,i}$ (MPa)	16000	16000	16000	11500	11500
$f_{c,i}$ (MPa)	−16000	−16000	−16000	−11500	−11500

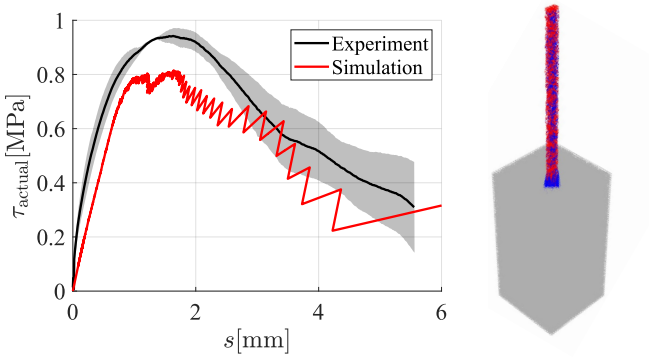

Figure 4.13: Comparison of meso-scale pull-out bond stress-slip curves and failure mode showing damage in blue

for obtaining input parameters of interface elements between concrete and deformed reinforcement bars by Gu et al. [129]. The implemented multi-linear constitutive relation approximates the experimental curves in a realistic manner as shown in Figure 4.13. The maximum bond stress that can be reached without breaking the ABS bar in the LBM simulations is 0.8 MPa, which is about 16 % lower compared to the experimental data.

4.4.2. MICRO-SCALE BOND STRESS-SLIP ANALYSIS

Small virtual cutouts from the meso-scale pull-out experiments as described in Section 4.3.2 are subjected to LBM simulations of micro-scale pull-out tests. The micro-scale bond stress-slip relationships resulting from the four scenarios described therein are displayed in Figure 4.14, maintaining the same format as Figure 4.10. However, the micro-scale slip values in Figure 4.14 cannot be compared to their meso-scale counterparts, because the latter include elastic deformation from the ABS bar whilst the former does not [128]. The micro-scale input for the bead, inter-layer and intra-layer phases is used from Chapter 3. These are provided in Table 3.5, where the subscripts correspond to the segment number of a (multi-)linear curve (see Figure 3.3). The local input for the matrix phase is recalibrated for the different mesh size at the micro-scale (E = 11417 MPa, G = 3805.7 MPa, f_t = 4.23 MPa, and f_c = −33.84 MPa). Compared to the meso-scale simulations, in the micro-scale simulations the local strength input parameters for the matrix (see Table 3.5) and ABS-mortar bond elements (see Table 4.4) are slightly reduced.

Table 4.4: Input parameters for micro-scale ABS-mortar bond phase elements

Properties	**Segment** 1	**Segment** 2	**Segment** 3	**Segment** 4	**Segment** 5
E_i (MPa)	114170	57085	23750	9500	4750
G_i (MPa)	38057	19028	7917	3167	1583
$f_{t,i}$ (MPa)	12075	12075	12075	8682	8682
$f_{c,i}$ (MPa)	−12075	−12075	−12075	−8682	−8682

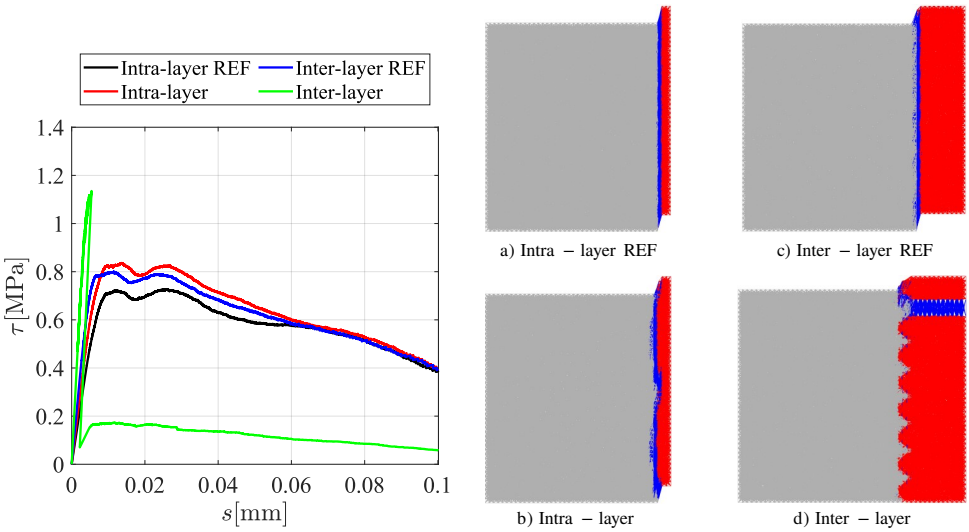

Figure 4.14: Micro-scale pull-out simulation bond stress-slip and fracture results. Deformed meshes showing cracks in blue at final stage of the analyses.

Figure 4.14(a) shows the reference pull-out behaviour for the intra-layer direction model which reflects the bead direction and therefore directly corresponds to the experimental pull-out observations. It can be seen that the obtained bond strength of about 0.73 MPa is almost identical to the meso-scale pull-out results in Figure 4.13 of about 0.8 MPa. This difference can be attributed to small differences in the lattice mesh because of its randomness. Moreover, the shape of the pull-out bond stress-slip curve and failure mode are similar to those obtained experimentally and numerically at the meso-scale (see Figure 4.13). Please recall that the micro-scale slip values in Figure 4.15 are not comparable to the meso-scale as the latter include elastic deformation from the ABS bar whilst the former does not [128]. Furthermore, Figure 4.14(a) also includes the deformed mesh showing cracks in blue at final stage of the analysis which clearly indicates a clean pull-out response as observed during the experiments. Figure 4.14(b) displays the intra-layer direction having a similar response with a slightly higher bond strength of nearly 0.84 MPa and also a clean pull-out. Figure 4.14(c) depicts the reference pull-out behaviour for the inter-layer direction model which also corresponds to the bead direction. In this case, the obtained bond strength of 0.80 MPa perfectly matches the meso-scale pull-out results in Figure 4.13 and the fracture of the model also clearly indicates a clean pull-out response

as found during testing. However, Figure 4.14(d) displays the inter-layer direction having a very sharp peak of nearly 1.14 MPa that can be attributed to the fact that the inter-layer bond inside the ABS bar fails. Hence, the matrix-reinforcement bond behaviour cannot be measured as there is no full pull-out in this case, i.e., the bond is too strong. The fact that the bar could not be pulled out validates the micro-scale model in a qualitative manner, as similar preliminary findings have been recorded. The directional-dependent bond behaviour of the intra-layer and inter-layer directions at the micro-scale can be related to that of the bead direction using a strength ratio:

$$r_{\mathrm{b},i} = \frac{f_{\mathrm{b},i}}{f_{\mathrm{b,bead}}}. \tag{4.3}$$

In Equation (4.3), $f_{\mathrm{b},i}$ can be regarded as $f_{\mathrm{b,intra}}$ and $f_{\mathrm{b,inter}}$ corresponding to the bond strengths in the intra-layer and inter-layer directions at the micro-scale, respectively, and $f_{\mathrm{b,bead}}$ is the bond strength in the bead direction at the micro-scale. Considering the directional-dependencies described by Equation (4.3), bond strength ratios of 1.15 and 1.56 are obtained for the intra-layer and inter-layer directions, respectively. Nevertheless, the inter-layer direction ratio does not constitute successful pull-out. Preliminary experimental results have also shown that the inter-layer bonds present in the FDM 3D printed ABS are too weak and result in breakage of the filament instead of the bar pull-out. To see the actual bond behaviour in the inter-layer direction, micro-scale push-out simulations are needed.

Given the same experimentally-fitted bond properties provided earlier, micro-scale push-out simulations are used to purely measure the contribution of mechanical interactions without any interfacial failure modes. The same small virtual cutouts from the meso-scale pull-out tests are simulated, with the only difference being the boundary conditions as illustrated in Figure 4.11. Again, resulting micro-scale bond stress-slip relationships are contained in Figure 4.14, having the same format as the aforementioned figure. The exact same constitutive relation as in the LBM micro-scale pull-out simulations is used for the bond behaviour here.

Figure 4.15(a) shows the push-out results for the intra-layer reference case. It is noteworthy that the bond strength perfectly matches the value of the micro-scale pull-out intra-layer reference (0.73 MPa). Additionally, the shape in Figure 4.15(a) is identical to that of Figure 4.14(a), which is in favor of the utilized numerical acquisition procedure of directional-dependent bond properties, irrespective of the boundary conditions (i.e., pull-out versus push-out). The fracture of the aforementioned case also constitutes a clean and successful push-out response. Similarly, Figure 4.15(b) displays the intra-layer direction, again comprising a clean push-out with softening behaviour after reaching an identically increased bond strength of 0.84 MPa compared to Figure 4.10(b). Figure 4.15(c) depicts the inter-layer reference case where it is notable that the bond strength of 0.80 MPa is maintained once more, thereby exactly matching the bond strength values of both the meso-scale and micro-scale pull-out LBM results. The model's fracture behaviour also indicates a clean push-out response. Where the inter-layer direction failed prematurely under pull-out conditions, Figure 4.15(d) displays a successful push-out in which the inter-layer bond within the ABS bar survives. Even though the peak is not as smooth as the others in Figure 4.15, a bond strength of about 1.24 MPa is reached. Therefore, this

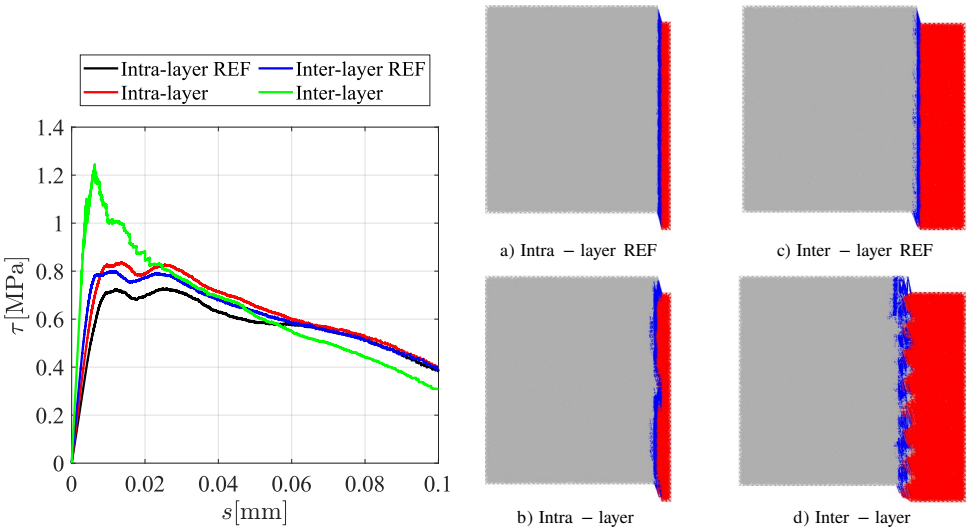

Figure 4.15: Micro-scale push-out simulation bond stress-slip and fracture results. Deformed meshes showing cracks in blue at final stage of the analyses.

result truly shows the isolated effect of morphological features without any influence of the intra-layer and inter-layer bonds within the 3D printed ABS material. It can also be observed in Figure 4.16(d) that due to the wedging of the morphological features, some splitting of the matrix occurs. As a result, the aforementioned bond stress-slip curve looks similar in shape as the monotonic envelope for splitting failure displayed in Figure 4.3. Finally, revisiting the bond strength ratios in Equation (4.3) that relate the directional-dependent bond behaviour of the intra-layer and inter-layer directions to that of the bead direction at the micro-scale, the intra-layer and inter-layer directions yield values of 1.15 and 1.56, respectively.

4.5. DISCUSSION

In this study, it is hypothesized that the elliptical geometry resulting from 3D printing may enhance the bond strength between the polymeric reinforcement and cementitious matrix. This is based on the following considerations:

1. From literature on reinforced concrete (i.e., with steel reinforcement, see Section 4.2.1) it is known that the bond comprises three components: Chemical (adhesive) bond, frictional bond and physical bond. The former two are geometry independent, whilst the latter is strongly dependent on the geometry. This is why ribbed reinforcement bars have stronger bond and, consequently, shorter transfer length than plain reinforcement bars.

2. In a previous work on ABS reinforcement [139], it was observed that intentionally adding ribs on 3D printed reinforcement meshes enhances the bonding by physical interlocking.

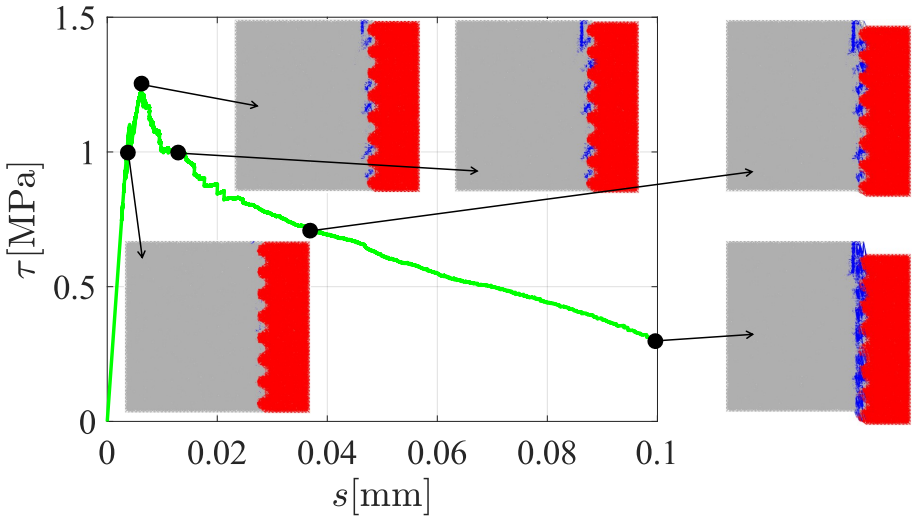

Figure 4.16: Inter-layer push-out simulation damage evolution. Deformed meshes showing cracks in blue at indicated stages of the analysis.

To conclusively support the hypothesis, additional experimental investigations are necessary for validation purposes. Specifically, the effect of the different geometrical configurations should be quantified (e.g., elliptic versus plain). Although it is acknowledged that specific experiments relating the polymer geometry with the bond strength are not present, the Luković et al. [166] have shown in the past that LBM simulations as used herein are able to replicate the experimentally observed geometrical surface configurations in concrete/concrete repair systems without any additional parameters. In that work, simulations of the direct tension, shear and three point bending test clearly showed that rough surface results in a higher strength compared to smooth surface, simply as a result of the geometry of the bond.

In the current work, a similar approach was taken with the first step being meso-scale pull-out simulations to determine the bond stress-slip curve between the 3D printed polymer bars and the cementitious matrix. This resulted in Figure 4.13, which holds for the "bead" printing direction (i.e., flat bond between the polymer and the matrix, see Figure 4.8). The bond was also tested for the inter-layer direction, but proved to be too strong: The reinforcement broke, and the pull-out curve could not be measured. Nevertheless, from the pull-out curves of the "bead direction" printed bars, micro-scale adhesive bond properties could be determined, which hold for any printing direction. Since the only difference between the printing directions is the geometry, these properties could be confidently used to simulate the bond behaviour for the other printing directions (i.e., with elliptical bond instead of "flat"), as shown in Luković et al. [166].

A comparison between experimental pull-out tests and numerical results is given in Figure 4.13. As explained above, for other printing directions (inter-layer and intra-layer), the bond was too strong (i.e., the reinforcement too weak) to perform a successful pull-out test due to rupture of the reinforcement. This clearly does not allow quantitative

comparison with the simulations: However, such behaviour is clearly expected based on the modelling work presented here. Based on the discussion above, the modelling framework entails a high level of confidence. Nonetheless, developing a dedicated small-scale setup for testing the bond strength between the polymeric reinforcement and cementitious matrix will be the focus of future research.

4.6. SUMMARY AND CONCLUSIONS

The bond behaviour between cementitious mortar (i.e., matrix) and 3D printed polymers (e.g., Acrylonitrile Butadiene Styrene (ABS)) has been studied using the Lattice Beam Model (LBM) on two length scales. To numerically investigate the hypothesis that morphological features as a result of the Fused Deposition Modelling (FDM) 3D printing technique may enhance the bond, the first step was to use pull-out experiments to calibrate a replica meso-scale model by means of parameter fitting. This model provided constitutive relationships at the meso-scale which served as a reference for micro-scale models that explicitly capture the directional-dependent mechanical interaction coming from geometrical features at the edges of FDM 3D printed parts. The anisotropy present in FDM 3D printed reinforcement (i.e., intra-layer and inter-layer bonds) was modelled according to Chapter 3, but the ABS-matrix bond was calibrated in the current chapter. By explicitly modelling the geometry, and without changing input parameters, the effect that printing direction has on the bond between 3D printed polymeric reinforcement and cementitious matrix was understood. Because of premature pull-out failure of the ABS bar in the inter-layer direction, push-out micro-scale models are considered in parallel to measure the contribution purely related to mechanical interactions. Their results will be used to inform specimen-scale models for simulating the composite behaviour of Auxetic Cementitious Composites (ACCs). The properties of the ABS material for both the meso-scale and micro-scale models discussed here are directly adopted from earlier developed printing path-dependent two-scale models.

From the presented work, it can be concluded that push-out models are needed to see the actual bond behaviour between cementitious matrix and FDM 3D printed ABS bars in the inter-layer printing direction. In this direction, pull-out models are found unable to reach full bond failure without breaking the inter-layer bond present within FDM 3D printed ABS. The interlocking effects as a result of the 3D printing technique in the inter-layer direction show to be significant, seeing a bond strength increase of 56 % with respect to the (reference) bead direction (i.e., the 'bulk material' without interfaces perpendicular to the loading direction). However, these mechanical interaction effects in the intra-layer direction are found to be much smaller with a bond strength increase of only 15 % compared to the reference direction. Finally, the hypothesized directional-dependent bond behaviour as a result of morphological features at the edges of FDM 3D printed ABS has been quantified and proven to exist.

5

MULTI-SCALE MODELLING OF AUXETIC CEMENTITIOUS COMPOSITES

This chapter presents a multi-scale modelling framework based on the Lattice Beam Model (LBM) to simulate deformation and fracture in Auxetic Cementitious Composites (ACCs). The experimentally-validated strategy combines two preceding modelling methodologies to explicitly incorporate (i) the anisotropy in 3D printed auxetic reinforcement, and (ii) 3D printing-induced geometrical effects on the bond stress-slip response between ABS and cementitious mortar. Applied to Re-Entrant and Rotating Square ACC designs under uniaxial compression, the models successfully capture the ductile post-peak softening behaviour observed experimentally, a response that prior 2D Finite Element Method (FEM) approaches failed to reproduce due to their inability to account for out-of-plane inter-layer failure. Compared to previous modelling attempts, the LBM simulations reduce the percentage difference in energy absorption capacity from over 40 % *to below* 12 %*, while maintaining comparable compressive strength predictions. The simulations further reveal that the auxetic reinforcement actively confines the cementitious matrix already at* 1 % *compressive axial strain, and that all failure initiates at the reinforcement–matrix interface before progressing into the matrix and reinforcement phases. Homogeneous material models consistently overestimate composite strength and underestimate toughness, underscoring the importance of incorporating printing path-dependent anisotropy. The proposed framework constitutes a versatile tool for simulating additively manufactured cementitious composites across an arbitrary range of geometries.*

With the exception of minor textual adjustments, this chapter is reproduced from: R.J.M. Bol, Y. Xu, Z. Meng, J. Xie, B. Šavija, *Multi-Scale Lattice Modelling of Deformation and Fracture in Auxetic Cementitious Composites Subjected to Uniaxial Compression*, Under Consideration.

5.1. INTRODUCTION

Using polymeric lattice reinforcement has been demonstrated to enhance the mechanical behaviour of cement-based composites [75, 108, 109], where reinforcement designs with a negative Poisson's ratio (i.e., auxetics) are proven to exhibit excellent compressive energy absorption capacity [111]. Auxetic materials often possess a relatively low overall stiffness which makes their applicability questionable when multiple of their favorable characteristics (e.g., high strength and energy absorption) are required at the same time [41]. However, it is believed that auxetic composite materials can overcome this limitation. The combination of auxetic and conventional (non-auxetic) materials could lead towards material characteristics that are unseen in both conventional as well as auxetic materials alone [37]. Li et al. [167] started focusing on compressive crushing characteristics of auxetic composite materials and reported increased mean crushing forces in comparison with non-auxetic reinforced composites, thereby indicating enhanced energy absorption capacities. The auxeticity of the reinforcement is utilized when compressed, where the matrix experiences a state of biaxial or triaxial compression as a result [41]. Later studies on Auxetic Cementitious Composites (ACCs) mostly direct their attention to these compressive applications, where this lateral confinement mechanism shows great potential [168].

It is common knowledge that cement-based material is weak in tension, resulting in low fracture toughness and energy absorption capacity. The literature reports numerous efforts to prevent these disadvantageous traits, seeking to increase the energy absorption capacity by means of ACCs [105, 168, 169]. The latter study applied cementitious matrix together with Acrylonitrile Butadiene Styrene (ABS) polymer in engineering their composites to replicate the microstructure of nacre. The resulting composites exhibited superior behaviour over reference samples. It was reported that mechanical interactions and frictional sliding between the two materials assisted in distributing deformations for allowing plasticity after the first cracks [107, 169]. Because of this, it is argued in [169] that their architected (auxetic) composites could pave the way towards solving the issue of brittle concrete failure. However, a lower stiffness has been reported for these composites as concrete possesses a higher stiffness than ABS. Their overall conclusion is that architected composites clearly illustrate a positive effect on the material characteristics.

Furthermore, the authors realized that investigations into the interface between ABS material and cement-based mortar were lacking, leading them to investigate the effects of imperfect contacts between ABS and cementitious material [169]. Results indicate that the bonding quality has a negative effect on both strength and stiffness of composites, where especially the ultimate strength is greatly deteriorated in the extreme case of no friction. Moreover, an extensive state-of-the-art review on ACCs by Momoh et al. [168] points out that the number of studies on such composites for structural purposes has risen by approximately 230 % over a 14-year period, indicating the demand for their (usually) enhanced properties. It also addresses the lack of knowledge about the bond between auxetic reinforcement and cementitious matrix. They advocate for more experimental investigations on this topic (e.g., pull-out behaviour) to support the development of accurate numerical simulation tools, particularly regarding the local stress values present at the reinforcement-matrix interface as a result of negative Poisson's ratios.

Xu & Šavija [110] modelled ACCs reinforced with FDM 3D printed ABS auxetic structures by means of 2D Finite Element Method (FEM) in the commercial software ABAQUS/Explicit. The ABS received a plastic material description, whilst the cementitious matrix was described by a Concrete Damaged Plasticity Model (CDPM) [110]. However, these 2D FEM, used to reduce computational demand, failed to capture the out-of-plane behaviour observed during experiments, wherein delamination of the extruded filaments occurred (see Figure 4.7). This caused discrepancies between experimental and numerical results: Whereas experiments saw out-of-plane failure of the 3D printed ABS leading to significant strain softening behaviour, simulations showed an almost ideal plastic response. The latter proves once again the importance of explicitly capturing the weaker inter-layer and intra-layer bond strengths into simulations of FDM 3D printed polymers as described in Chapter 2, which led to the development of the 3D printing path-dependent two-scale models elaborated in Chapter 3. Another aspect is the bond relationship among ABS and cementitious mortar, which previous FEM simulations of similar ACCs did not intend to model realistically [110], wherein an arbitrary friction coefficient equal to 1.0 was assumed. It is realized that the bond properties amongst constituents of composites can have a major influence on their behaviour [148] and that the chosen value in [110] is likely to be an overestimation in view of the weak bond strengths observed in [148]. Incorporating more detailed descriptions of constitutive relationships for bond behaviours in models is therefore crucial, like the multi-scale bond modelling scheme explained in Chapter 4.

To develop a modelling framework able to simulate deformation and fracture of ACCs, it is important to select a suitable modelling approach considering the materials involved and their respective characteristics. As for the current stage of ACCs, these materials concern cementitious matrix (i.e., concrete) and 3D printed polymers (i.e., plastic). Starting with the modelling of concrete, which is a heterogeneous, multi-scale [127], and quasi-brittle material [126], fracture has been extensively researched [119]. This material exhibits porosity and anisotropy, resulting in complex fracture mechanisms that are related to its microstructure [141]. In general, cracks propagate orthogonal to the maximum tensile stresses, thereby following the weakest material links [170]. After crack initiation, the stress distribution present in the material (induced by loads) in combination with the mechanical characteristics dictate the final crack pattern. To this end, using numerical multi-scale modelling of deformation and fracture behaviour of concrete can provide a more profound understanding.

Quasi brittle fracture is most widely studied by means of FEM [119]. Popular approaches described in the literature [119, 141] include eXtended-Finite Element Method (X-FEM), damage models, cohesive zone models, discrete element models, smeared crack models, and phase-field models. However, all of the aforementioned approaches are subject to drawbacks like mesh dependency, high computational costs, failing to include crack initiation and propagation, crack alignment with inter-element lines, and singularity-related issues, as addressed in [119, 138]. Therefore, another modelling approach is considered here for fracture analysis of cementitious materials.

In the light of previous FEM attempts to model ACCs, an approach based on the successful Lattice Beam Model (LBM) is proposed here. LBM, also referred to as the Delft lattice model [138], comprises advantages when it comes to concrete fracture analysis,

specifically for modelling crack propagation [113, 129]. According to Qian [113], these advantages are its ability to capture detailed crack information, high computational efficiency and stability. Because of its discontinuous formulation, singularity-related issues that commonly occur in continuum-based numerical (finite element) methods are avoided [133, 138]. Especially for fracture analysis of materials where disorder is considerable, the preferred modelling approach is lattice models [170]. It is therefore one of the most widely used approaches for fracture analysis of cement-based materials [171] because the model is able to predict realistic crack patterns using relatively simple constitutive relationships and failure modes, and simple implementation of material heterogeneity at various scales [121]. Furthermore, through the use of parallel computing, which means that LBM operates on a multi-core computer or clusters, computation efforts are significantly decreased such that applications for large-scale structures having a considerable amount of elements are still feasible [138]. As a result, LBM is considered to be a useful design tool for creating novel composite materials having improved mechanical characteristics, because of its ability to analyze their fracture behaviour for varying constituent properties [172].

The experimentally-validated multi-scale strategy proposed in this study combines the two preceding modelling methodologies for printing path-dependency in FDM 3D printed auxetic structures in Chapter 3 and bond behaviour between polymeric lattice reinforcement and cementitious matrix in Chapter 4. The multi-scale modelling framework starts at the micro-scale and gradually works its way up to simulate various ACC designs under uniaxial compression. The models developed here explicitly incorporate (i) the anisotropy observed in 3D printed auxetic reinforcement through FDM from Chapter 3, and (ii) 3D printing-induced geometrical effects on the bond stress-slip response between ABS and cementitious mortar from Chapter 4. In the end, the overarching composite model unravels the mechanical behaviour of ACCs. It should be noted that the proposed multi-scale strategy presents a versatile numerical tool for simulating an infinite amount of geometries, no matter how simple or complex. For any polymeric shape printed through material extrusion, the developed model can be utilized for automated identification and assignment of anisotropic material properties in correspondence to its printing path, provided the printer code (G-code) is available. Moreover, the modelling framework can be extended to 3D-printed materials incorporating other types of filling matrices, such as silicone rubber, foam, or epoxy, provided realistic bond stress-slip relationships are available in the literature or experimentally obtained.

The aim of this chapter is to develop a more profound understanding of ACCs using numerical models. To date, ACCs reinforced with 3D printed polymeric auxetic structures are typically modelled by means of (2D) FEM. Therein, polymers usually receive a plastic material description, whilst the cementitious matrix gets generally described by CDPM. However, these methods fail to capture the (large) anisotropy exhibited by the polymeric lattice reinforcements which is caused by popular 3D printing techniques like Fused Deposition Modelling (FDM) as described in Chapter 2. The importance of explicitly capturing this anisotropic response of 3D printed polymers by FDM led to the development of printing path-dependent two-scale models elaborated in Chapter 3. Another important aspect for ACCs is the bond between the 3D printed reinforcement and cementitious matrix. Improving the understanding of the bond behaviour in ACCs is a general concern,

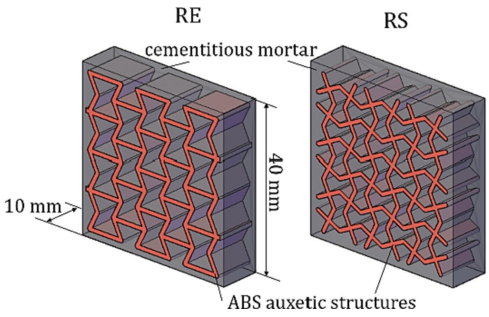

Figure 5.1: Schematics of the Auxetic Cementitious Composites (ACCs) [110]

because it is realized that the bond properties amongst constituents of composites can have a major influence on their behaviour [168]. Current bond modelling procedures are likely to overestimate the weak bond strengths observed in the literature. Incorporating more detailed descriptions of constitutive relationships for bond behaviours in models is therefore crucial as illustrated in Chapter 4.

5.2. EXPERIMENTAL

5.2.1. SPECIMEN DESIGN

To verify the multi-scale modelling strategy, the specimen-scale LBM analyses are checked against experiments on ACCs. Two auxetic reinforcement designs from a previous study [110] were selected: Re-Entrant (RE) and Rotating Square (RS) structures as shown in Figure 3.1, both having the same volume. The auxetic structures were printed from ABS in the out-of-plane direction by the Ultimaker 2+ commercial FDM 3D printer. The printing parameters are kept constant to avoid deviations in the 3D prints throughout the multi-scale modelling campaign, see Table 3.1. The RE and RS designs were embedded in cementitious matrix, see Figure 5.1. Both ACCs had similar dimensions of $40 \times 40 \times 10$ mm with the volumetric ratio of both ABS auxetic structures with respect to the entire ACC being equal to 28 %. Four samples were manufactured and tested for each case.

5.2.2. MIX DESIGN AND SPECIMEN PREPARATION

Starting with the mixture design containing binders CEM I 42.5 N and fly ash, wherein a high fluidity water-to-binder ratio (w/b) of 0.4 was used to simplify filling the voids within the rather complex auxetic designs. The mixture design is provided in Table 5.1.

Once printed, the FDM auxetic reinforcement architectures were glued by tape and positioned in Styrofoam molds before casting the cementitious matrix. Regarding mixing, casting and curing: First the dry materials were mixed for 4 minutes, after which the water and superplasticizer joined the mixture that was finally mixed for an additional 4 minutes. Afterwards, the obtained mix was poured over the ABS auxetic structures inside the Styrofoam molds. Both specimens were demolded after 24 hours and kept in a curing room with a temperature of 20 ± 2 °C and a relative humidity of 96 ± 2 % for 28 days. Prior to the experiments, the cast specimens were separated by cutting them in accordance with the dimensions provided in Figure 5.1.

Table 5.1: Mixture design of cementitious matrix [110]

Mixture components	Quantities
Water-to-binder ratio	0.4
CEM I 42.5 N (gL^{-1})	473
Fly ash (gL^{-1})	559
Sand (0.125 ~ 0.250 mm) (gL^{-1})	473
Water (gL^{-1})	413
Superplasticizer (Glenium 51) (gL^{-1})	2

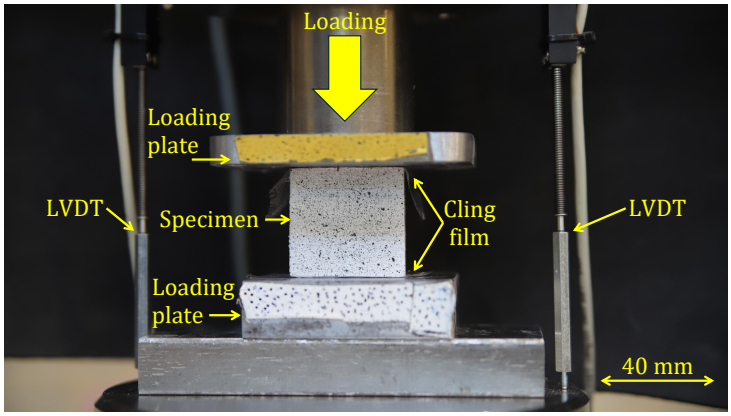

Figure 5.2: Experiment setup for uniaxial compression test

5.2.3. TEST SETUP

All samples were subjected to uniaxial compression tests using a UNITRONIC machine provided a displacement rate of 0.01 mm s^{-1}, including a plain mortar reference having the same dimensions as the ACCs but without any reinforcement. The FDM 3D printed auxetic structures were also tested without cementitious matrix, for which the experimental results and numerical comparisons can be found in Chapter 3. Figure 5.2 shows the test setup, where it can be seen that the surfaces of ACCs were spray painted with a black-and-white dotted pattern to perform Digital Image Correlation (DIC) during the experiments. Images were captured by a Canon EOS 6D Mark II digital camera using a 75 mm focal length lens at an aperture of $f/2.8$, resulting in a resolution of 6240×4160 to be analyzed in the commercial software ZEISS INSPECT Correlate. Linear Variable Displacement Transducers (LVDT) on both sides of the specimens were used to record deformations. Steel loading plates applied external loading to the specimens with a thin transparent cling film inserted in between to reduce friction. From previous modelling experience [138], which studied the influence of friction-restrained and frictionless boundary conditions on uniaxial compressive failure, it is known that the latter is closer to reality. Hence, the boundary conditions at the loading plates are assumed to be frictionless in the simulations of the ACCs.

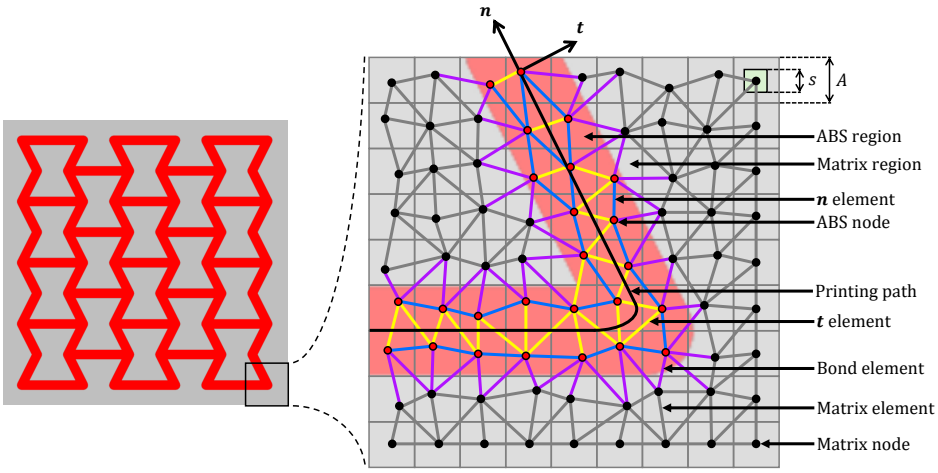

Figure 5.3: Schematics of domain discretization and element definition (shown in 2D for simplicity)

5.3. NUMERICAL

5.3.1. MULTI-SCALE MODELLING OF DEFORMATION AND FRACTURE

LATTICE GENERATION

The interconnection of lattice nodes is typically done through Delaunay triangulation, yielding irregular networks of beams in which each node has six degrees of freedom (i.e., x, y and z translations and rotations). The mechanical properties of all beams are distinguished by means of superimposing the mesh onto a virtual representation of the ACCs herein. First an identification based on the location of the two lattice nodes is made: If both end nodes belong to the same region, the beam element between these nodes corresponds to that region and obtains input properties measured for that particular region (i.e., matrix in Figure 5.3). In case the two nodes fall in different regions, e.g., the beam element intersects a boundary, interfacial properties are assigned (i.e., ABS-matrix bond in Figure 5.3). A second identification proposed in Chapters 3 and 4 only considers elements corresponding to 3D printed polymers (i.e., both end nodes inside the ABS region in Figure 5.3). Those elements receive material properties related to their orientation with respect to the printing path (n_i in Figure 5.3) and its aligned local coordinate system: n_i is in the same direction as the 3D printed filaments, which is the strongest print configuration, whilst t_i is perpendicular to n_i and represents the intra-layer bond among adjacent filaments, which is found to be weaker in Chapter 3. s_i points in the out-of-plane direction (therefore not shown in Figure 5.3) and resembles the inter-layer bond between stacked layers as a result of the layer-by-layer deposition procedure, which is the weakest link in FDM 3D printed parts as established in Chapters 2 and 3.

FROM MICRO-SCALE TO SPECIMEN-SCALE

To unravel the mechanical behaviour of ACCs, a series of models across different scales are combined into one overarching composite model. The multi-scale modelling strategy starts at the micro-scale and gradually works its way up to simulate various ACC designs at the specimen-scale by means of LBM. The individual models as well as their joint modelling schemes are provided in Figure 5.4, which shows all models over the scales including their interdependence. In what follows, a brief outline covering the proposed multi-scale modelling approach so far will be given, after which its extension to capture directional-dependent bond behaviour will be elaborated. Similar to the anisotropy found within FDM 3D printed polymers in Chapters 2 to 4, this directional dependency can be coupled to the printing path such that it can be regarded as printing path-dependent bond behaviour. For more detailed descriptions of the printing path-dependent two-scale models and multi-scale bond models, the reader is referred to the latter three chapters, respectively.

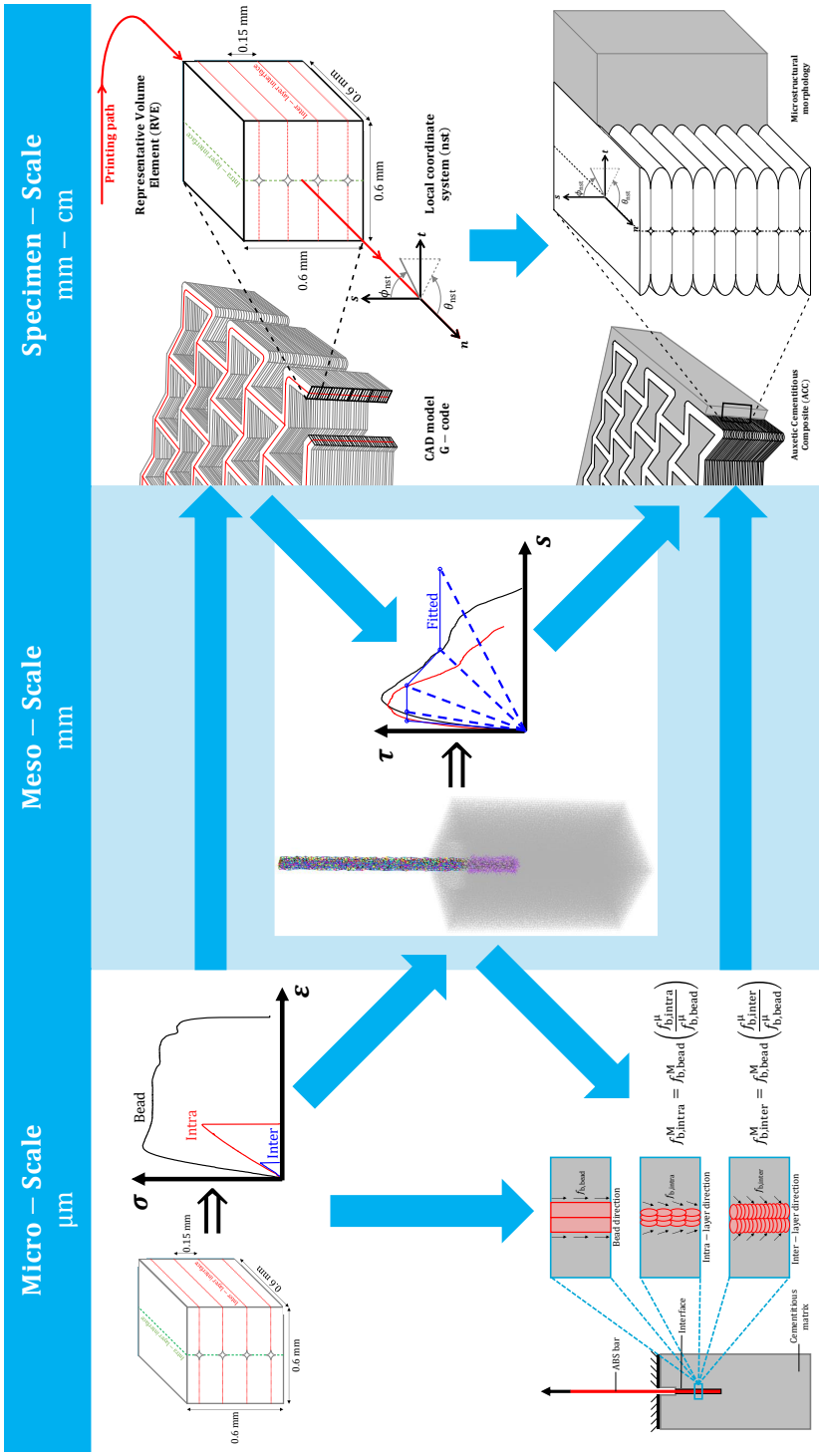

Figure 5.4: Multi-scale modelling of Auxetic Cementitious Composites (ACCs)

The model that was created first concerns the idealized microstructural Representative Volume Element (RVE) of FDM 3D printed polymers, comprising four stacked layers based on microstructural experimental analysis in Chapter 3. This model explicitly represents the characteristic cross-sectional shape including voids and pores at the micro-scale, as well as interfacial deficiencies like the intra-layer and inter-layer bonds resulting from the 3D printing technique. LBM simulations of the RVE provided constitutive relationships that can be used in models at larger scales, thereby accounting for the effects of both porosity and internal bonds found in 3D printed polymers through FDM. In Figure 5.4, the model can be found at the upper left corner under the micro-scale.

The stress strain relationships following from the microstructural RVE discussed above are assigned to lattice beam elements within specimen-scale FDM 3D printed reinforcement models of auxetic structures according to their orientation with respect to the printing path, as described in Chapter 3. To facilitate the assignment of these printing path-dependent properties, a local coordinate system is introduced which aligns with the printing path such that the n_i axis corresponds to the bead phase (parallel to the printing path), whilst the other axes s_i and t_i reflect the inter-layer and intra-layer bond phases, respectively. Directional element categories are imposed by means of the azimuth angle θ_{nst} and polar angle ϕ_{nst}, see the upper right model under specimen-scale in Figure 5.4.

Next is the intermediate step of finding the bond stress-slip relationship between cementitious mortar and FDM 3D printed polymers, and implementing this into LBM simulations explained in Chapter 4. Based on pull-out experiments of FDM 3D printed ABS bars, bond properties are fitted using a replica meso-scale pull-out model. The material properties and element assignment procedure of the ABS bars are directly adopted from the printing path-dependent two-scale models explained before, as shown by the dependency in Figure 5.4. To avoid any influence from the weak interfacial bonds, the ABS bars are tested and simulated with printing paths that are parallel to the pull-out direction (i.e., the bead direction). The model and fitted bond stress-slip envelope are shown under meso-scale at the center of Figure 5.4.

Because FDM 3D printed parts have edges that are typically composed of ellipses, which possibly facilitate mechanical interaction (i.e., interlocking) with the cementitious mortar, their bond behaviour can be elevated in certain directions according to Chapter 4. To enable explicit bond modelling amongst the microstructural morphology as a result of the printing technique and matrix, three mutually orthogonal printing directions are studied numerically by means of both micro-scale pull-out and push-out LBM simulations, some of which have a strong resemblance with ribbed reinforcement bars. The dependencies shown in Figure 5.4 are as follows: Input parameters for the ABS material (i.e., bead, intra-layer and inter-layer bonds) are directly taken from the microstructural RVE elaborated at the beginning, whilst bond properties are scaled down from the meso-scale pull-out model. LBM simulations of the small virtual cutouts provided strength ratios that can be used in the ACC specimen-scale model, thereby incorporating morphological edge effects of the bond between FDM 3D printed polymers and cementitious mortar. In Figure 5.4, the model can be found at the lower left corner under the micro-scale.

Finally, all information coming from the aforementioned models is combined into one overarching composite model, used to simulate deformation and fracture of ACCs at the specimen-scale as graphically presented in Figure 5.4: The printing path-dependent

two-scale models, used to simulate FDM 3D printed auxetic structures, are embedded in cementitious matrix to serve as reinforcement, whereas the bond behaviour between these two constituents is informed by the multi-scale bond modelling strategy. Hence, the methodology for multi-scale modelling of ACCs is completed. To explicitly incorporate the 3D printing-induced geometrical effects on the bond stress-slip response between ABS and cementitious mortar, its constitutive relationship is scaled by the strength ratios given in Equation (5.1) in accordance with its respective printing path orientation (i.e., the bead, intra-layer or inter-layer direction). The directional-dependent bond behaviour at the micro-scale can be related to that of the bead direction at the meso-scale using a strength ratio, which also holds for specimen-scale models:

$$f_{\mathrm{b},i}^{\mathrm{M}} = f_{\mathrm{b,bead}}^{\mathrm{M}} \left(\frac{f_{\mathrm{b},i}^{\mu}}{f_{\mathrm{b,bead}}^{\mu}} \right). \tag{5.1}$$

In Equation (5.1), $f_{\mathrm{b},i}^{\mathrm{M}}$ can be regarded as $f_{\mathrm{b,intra}}^{\mathrm{M}}$ and $f_{\mathrm{b,inter}}^{\mathrm{M}}$ corresponding to the bond strengths in the intra-layer and inter-layer directions at the meso-scale, respectively, and $f_{\mathrm{b,bead}}^{\mathrm{M}}$ is the bond strength in the bead direction at the meso-scale. Similarly, $f_{\mathrm{b},i}^{\mu}$ can be regarded as $f_{\mathrm{b,intra}}^{\mu}$ and $f_{\mathrm{b,inter}}^{\mu}$ corresponding to the bond strengths in the intra-layer and inter-layer directions at the micro-scale, respectively, and $f_{\mathrm{b,bead}}^{\mu}$ is the bond strength in the bead direction at the micro-scale. Considering the directional-dependencies described by Equation (5.1), bond strength ratios of 1.15 and 1.56 have been obtained in Chapter 4 for the intra-layer and inter-layer directions, respectively. In fact, this printing path-dependency can be implemented using identical definitions as the element property assignment of the FDM 3D printed reinforcement models in Chapter 3. To this end, the exact same local coordinate system composed of the three mutually orthogonal unit vectors, n_i, s_i and t_i, is used, with n_i in the direction of the printing path as described in Section 5.3.1. The only difference is that bond elements have one node inside the FDM 3D printed ABS reinforcement and one node inside the cementitious matrix, whereas in the auxetic structure models both element nodes are located within the ABS material (see Figure 5.3). Therefore, the one node of a bond element inside the FDM 3D printed reinforcement can be related to the printing path to facilitate the assignment of directional-dependent properties. In theory, the three studied bond behaviour directions at the micro-scale in Chapter 4 can be accommodated in the specimen-scale model, which can be directly coupled to the decomposition of directional element domains in Table 3.4. However, because the ACCs considered in this study contain no ABS-mortar interfaces in the intra-layer direction (i.e., there is no matrix at the intra-layer faces), it is found to be more realistic to only include the inter-layer bond direction besides the bead direction. To end up with a continuous bond description, the intra-layer bond direction angles (θ_{nst} and ϕ_{nst}) are therefore merged with the inter-layer bond domain, see Table 5.2.

Table 5.2: Directional bond element domain discretization for printing path-dependent property assignment

Directions	θ_{nst} **(rad)**	ϕ_{nst} **(rad)**
Bead	$[0, \frac{1}{4}\pi] \cup [\frac{3}{4}\pi, \frac{5}{4}\pi] \cup [\frac{7}{4}\pi, 2\pi)$	$[\frac{1}{4}\pi, \frac{3}{4}\pi]$
Inter-layer	$[0, 2\pi)$	$[0, \frac{1}{4}\pi] \cup [\frac{3}{4}\pi, \pi]$
Inter-layer	$[\frac{1}{4}\pi, \frac{3}{4}\pi] \cup [\frac{5}{4}\pi, \frac{7}{4}\pi]$	$[\frac{1}{4}\pi, \frac{3}{4}\pi]$

INPUT PARAMETERS

The input parameters used throughout the multi-scale LBM analyses for the ABS polymer material are adopted from Chapter 3. Therein, microstructural experimental analysis on FDM 3D printed dog bone shaped ABS specimens revealed the mechanical behaviour in the bead (n_i), inter-layer (s_i), and intra-layer (t_i) directions for the same printer settings as in Table 3.1, which was used to calibrate the multi-scale model input in Table 3.6. This material input is assigned to elements in the lattice mesh based on their spherical angles with respect to the local coordinate system **nst**, see Table 3.4. It was shown that for the polymeric auxetic reinforcement these 3 main directions were sufficient to capture the printing path-dependent anisotropy.

The input parameters for the cementitious mortar were fitted with the mechanical properties of the plain mortar reference samples without reinforcement recorded during the uniaxial compression tests. These corresponded to the following local input values: A Young's modulus of 3400 MPa, a shear modulus of 1417 MPa, a tensile strength of 6.27 MPa and a compressive strength of 62.7 MPa (constituting a compression-to-tension strength ratio of 10). Be aware that these are calibrated local element properties to fit the global experimental behaviour. This can cause discrepancies among local simulation inputs and global experimental observations caused by numerical parameters (e.g., mesh size and randomness) [164].

Even though the randomness of the mesh is non-zero ($R = 0.5$), the randomness at the boundaries is set to zero in order to evenly apply the loads and support conditions. Furthermore, to prevent element failure near the boundary conditions, the surface elements are usually set to be unbreakable [130] to maintain a continuous loading path for force transfer [111]. However, modelling the surface elements as such prevented tensile splitting cracks to fully propagate through the digital specimens, which made the simulated results unrealistically strong. On the other hand, if the surface elements were allowed to break, these failed prematurely causing discontinuities in the load application. Therefore, to circumvent this issue, an intermediate solution was chosen by modeling the surface elements with a higher tension-to-compression ratio (15 instead of 10) to allow them to fail realistically, but not prematurely to ensure a continuous loading path.

Finally, the bond stress-slip relationship was calibrated in tension with experimental pull-out data in Chapter 4 by means of a multi-linear curve having five segments. However, compressive properties were lacking, such that the constitutive relationship was modified according to the normal stress strain curve of the joint element model described in Kurihara et al. [173]. In tension the bond behaviour dominated by adhesion and friction from Chapter 4 is preserved, whilst in compression a closed joint behaviour as in [173] is implemented. This involved adding an initial segment with a greater stiffness in compression

Table 5.3: Properties for ABS-mortar bond phase elements

Properties	**Segment** 1	**Segment** 2	**Segment** 3	**Segment** 4	**Segment** 5	**Segment** 6
E_i (MPa)	159	114.17	57.085	23.75	9.5	4.75
G_i (MPa)	53	38.057	19.028	7.917	3.2	1.58
$f_{t,i}$ (MPa)	0.01	16	16	16	11.5	11.5

to incorporate the normal contact between the ABS and mortar, which was fitted from experimental data. Moreover, the joint element model maintains this initial stiffness value throughout compressive strains, meaning that bond elements under compression do not transition from the first segment to the next despite exceeding their strength value. In tension, the bond elements can transition between segments and ultimately fail according to the five remaining tensile segments in the constitutive relationship provided in Table 5.3. In the LBM simulations this is realized by allowing the bond elements to only fail in tension, thereby disregarding their compressive strength value in the analyses to prevent stiffness reduction (hence, $f_{c,i}$ is not provided in Table 5.3). It should be noted that shear is typically not included in the failure criterion of LBM simulations (see Equation (3.3)), where the primary focus is on normal actions and bending mechanisms. However, since the models have finite-thickness interface elements, shearing will cause tensile stresses which eventually lead to tensile failure. Models considering directional-dependent bond behaviour receive input properties in accordance with Equation (5.1) and Table 5.2.

5.4. RESULTS

5.4.1. PLAIN REFERENCE MORTAR

First, the numerical and experimental responses of the plain reference mortar samples are discussed. Starting with the mechanical behaviour, Figure 5.5 shows that the obtained stress strain curves correspond well for uniaxial compression. As argued by Yip et al. [118] and Chang et al. [138], lattice models are known for their relatively brittle post-peak behaviour, which makes simulating compressive failure more challenging [174]. This is partly caused by the lack of incorporating frictional effects after cracking, but also by the linear-elastic constitutive relationship provided for the cementitious matrix as described before. Implementing more sophisticated material relations for the mortar (like multi-linear curves, e.g., from meso-scale simulations [113]) can partly alleviate this brittleness at the cost of significantly increasing computational demand. Hence, the presented results are considered reasonably acceptable.

Figure 5.6 illustrates the ability of the LBM to capture the cracking pattern of the cementitious matrix. Both the experiment and simulation ultimately show a major continuous horizontal crack that is staggering, combined with minor vertical dispersed crack branches diverting outwards to the top and bottom of the specimen.

5.4.2. AUXETIC CEMENTITIOUS COMPOSITES (ACCS)

This subsection compares the experimental tests with the developed LBM simulations of the considered ACCs. To illustrate the effects of printing path-dependent anisotropy in FDM 3D printed auxetic structures from Chapter 3 and bond behaviour between ABS and

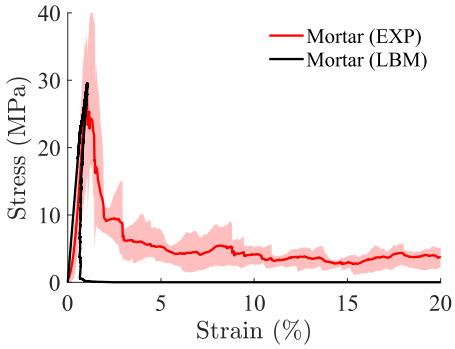

Figure 5.5: Comparison of experimental (EXP) and numerical (LBM) stress strain curves for uniaxial compression of plain reference mortar. For experimental data, the shaded bands reflect the spread observed among four parallel measurements, and the solid lines denote the mean outcomes.

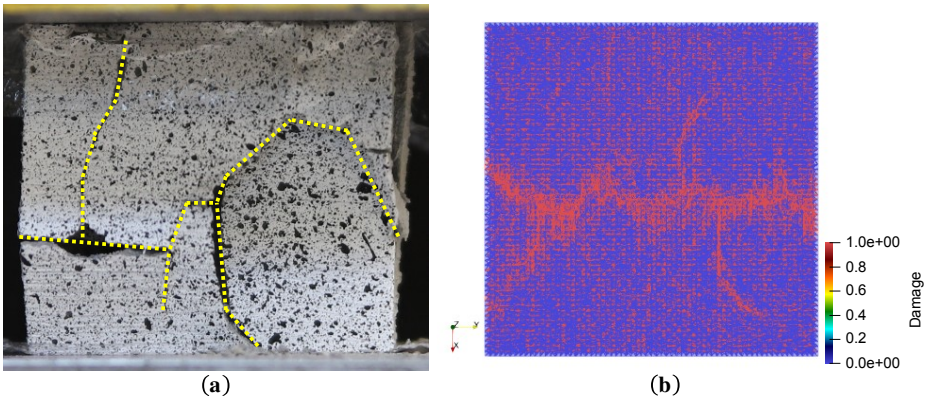

Figure 5.6: Comparison of (a) experimental and (b) numerical fracture for uniaxial compression of plain reference mortar. Experimental fracture is traced in yellow, numerical cracks correspond to Damage = 1.

cementitious matrix from Chapter 4, each ACC is modelled three times with a different set of input properties. As a result, one has the following four datasets:

- (EXP): Experimental data recorded during testing. Shaded areas represent the variations across parallel testing, and the solid lines represent the average results.
- (3 main): Simulation results where printing path-dependent anisotropy in FDM 3D printed auxetic structures is considered in the 3 main directions (i.e., the three mutually orthogonal unit vectors, n_i, s_i and t_i, with n_i in the direction of the printing path as described in Section 5.3.1). In these models, no directional-dependent bond behaviour is implemented, such that the bond stress-slip relationship is isotropic according to Table 5.3.
- (3 main bond): Simulation results where printing path-dependent anisotropy in FDM 3D printed auxetic structures is considered in the 3 main directions, whereas

now directional-dependent bond behaviour is implemented according to Equation 5.1 for inter-layer bond elements.

- (homogeneous): Simulation results where printing path-dependent anisotropy is neglected such that FDM 3D printed auxetic structures are modelled as homogeneous isotropic where all reinforcement elements receive mechanical properties corresponding to the direction of the printing path n_i. Analogously, these models contain no directional-dependent bond behaviour.

ACC RE

Unlike plain reference mortar showing brittle behaviour in Figure 5.5, the inclusion of polymeric auxetic reinforcement drastically improved the post-peak performance of the ACCs. A considerably ductile response is found as shown in Figure 5.7(a) for both the experiments and simulations of ACC RE. Similar results are reported in [110], but the updated printing parameters established in Chapter 3 improved the ACC's compressive strength values, as well as the consistency in mechanical behaviour (i.e., less deviations, see Appendix A.2) in this current study. Remarkably, all LBM simulations show that, although the mortar is modelled as linear-elastic brittle, the composite models display ductile softening behaviour a result of the ABS auxetic reinforcement. An extraordinary post-peak softening trend can be observed, which is an indication of a slow and gradual failure mechanism as opposed to the plain mortar reference. The compressive strengths in Figure 5.7(b) and Table 5.4(a) show good agreement, with little differences between the experiments, 3 main and 3 main bond LBM simulations. Only the homogeneous model exhibits higher strength, which can be attributed to the overestimation in strength of the polymer phase as found in Chapter 3. However, the effect of homogeneous ABS properties on the composite strength is less pronounced compared to the isolated 3D printed structures considered in Chapter 3. This does not detract from the model's general improvement of incorporating the experimentally-validated bond stress-slip relation from Chapter 4 as opposed to the arbitrary friction coefficients in FEM [110]. To quantify the energy absorption capacity of the ACCs, the toughness is evaluated as the area underneath the stress strain curve until 20 % strain as in Chapter 6. As contained in Figure 5.7(c) and Table 5.4(b), the 3 main directions model just falls within the standard deviation of the test results, whilst the 3 main bond and homogeneous models yield slightly lower values. Previous modelling attempts of similar specimens using 2D FEM [110] found a notable overestimation in energy absorption due to the simulation's lack of capturing the post-peak softening response by maintaining a plateau, see Appendix A.2 (Figures A.2 and A.3). The model presented here manages to simulate the long softening tail with improved accuracy, thereby improving the model's predictive capabilities.

As discussed in [110], the enhancement in mechanical behaviour comes from the auxetic structure's deformation mechanism, which contracts laterally under axial compression, causing confinement of the cementitious matrix and thereby actively restrain crack localization. In Figure 5.8 this is illustrated as multiple smaller cracks following a more or less diagonal pattern as opposed to forming a straight cracking plane in both the tests and simulations. This effectively improves the energy absorption capacity of the developed composites, which explains the significant gradual damage and softening behaviour observed.

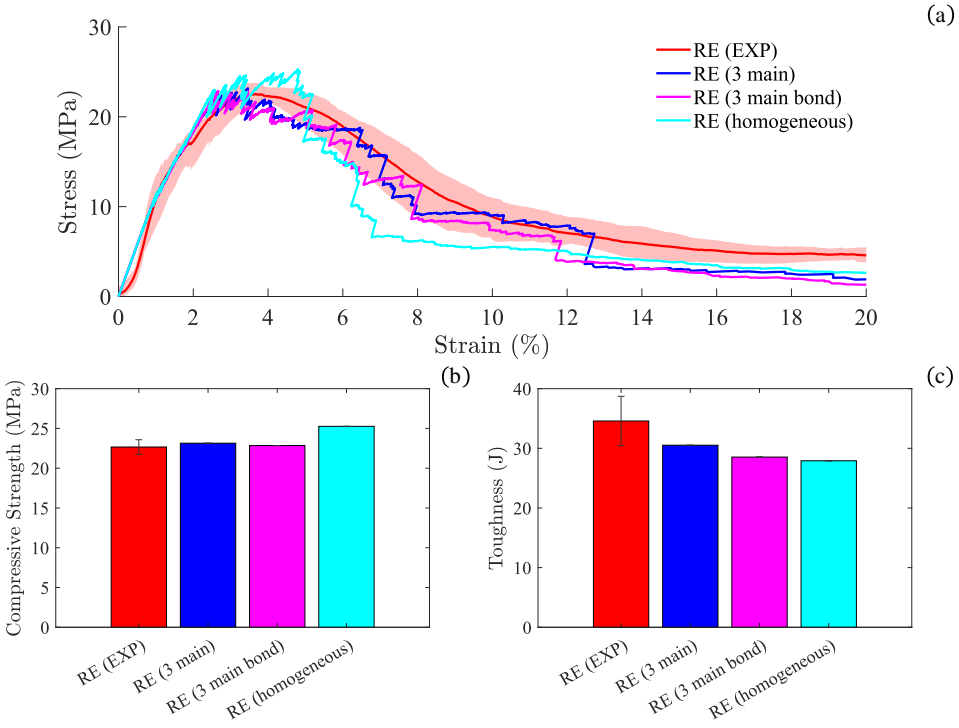

Figure 5.7: Comparison of experimental and numerical mechanical properties for uniaxial compression of ACC RE: (a) Stress strain curves, (b) compressive strengths, and (c) toughness values. For experimental data, the shaded bands reflect the spread observed among four parallel measurements, and the solid lines denote the mean outcomes.

Table 5.4: Mechanical properties of ACC RE

ACC	**Load Capacity** (kN)	**Toughness** (J)
RE (EXP)	22.7 ± 0.9	34.6 ± 4.1
RE (3 main)	23.1	30.5
RE (3 main bond)	22.8	28.5
RE (homogeneous)	25.3	27.9

The RE architecture's confining ability can be seen in Figure 5.9. Already before reaching the maximum load, at 1 % compressive axial strain, the 3D printed reinforcement is actively confining the surrounded cementitious mortar. This is indicated by the negative lateral stress concentrations within the reinforcement's unit cells found in the simulations, causing a diagonal grid of confined cementitious material.

To better comprehend the differences between the simulations, the percentage of failed elements is plotted against the compressive axial strain. For comparative purposes, the reinforcement and bond elements are discretized the same. This means that the reinforcement elements in the homogeneous model are categorized according to their

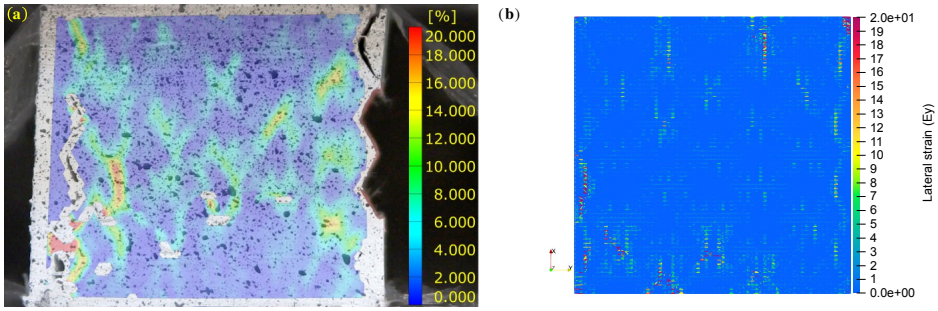

Figure 5.8: Comparison of (a) DIC and (b) LBM lateral strain for 5 % compressive axial strain of ACC RE. Only the 3 main directions model is shown in view of similarities among the models.

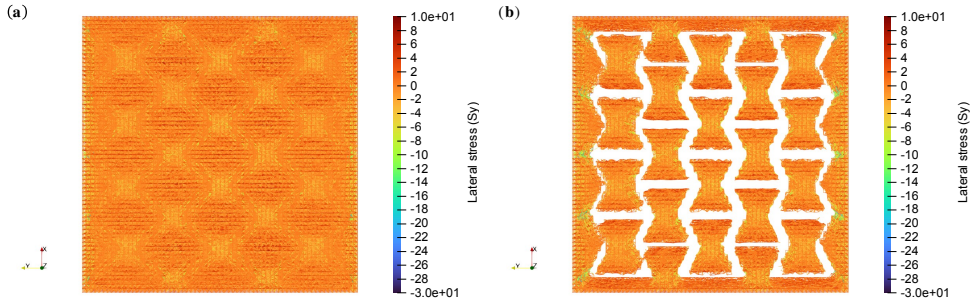

Figure 5.9: LBM lateral stress for 1 % compressive axial strain of ACC RE in all phases (a), and only in the matrix phase (b). Only the 3 main directions model is shown in view of similarities among the models.

directions with respect to the printing path (through the local coordinate system **nst**) even though these are assigned the same properties, and that all bond elements fall within one category irrespective of the incorporation of directional dependencies. Figure 5.10 depicts the percentage of failed elements versus the compressive axial strain for the 3 main and 3 main bond (left), and homogeneous (right) models. Only the 3 main directions model is shown in view of its almost identical failure evolution compared to the 3 main bond model. These graphs, representing the models' evolutions of failure, all initiate with interfacial bond failure (IF), caused by the low tensile strength of the first segment in the ABS-mortar bond phase constitutive relationship (see Table 5.3). This essentially allows the bond elements under tensile loading to transition into the five remaining segments reflecting the calibrated bond stress slip curve from Chapter 4.

However, it also indicates that minor debonding is occurring after loading has started, mainly at the less deforming upper and lower edges of the auxetic unit cells as evidenced in Figure 5.11. These are the regions that are not confined by the auxetic reinforcement, as shown in Figure 5.9. It is notable that although the 3 main bond model incorporates directional dependent bond behaviour, its failure evolution (Figure 5.10) and stress strain curve (Figure 5.7) are not very different from the other models without this additional dependency. When the interfacial failure rate is decreased, cementitious mortar (CM) failure is triggered and prevails until the peak load is reached (see Figure 5.7(a)), after which its failure rate also decreases. The 3 main and 3 main bond models perform nearly

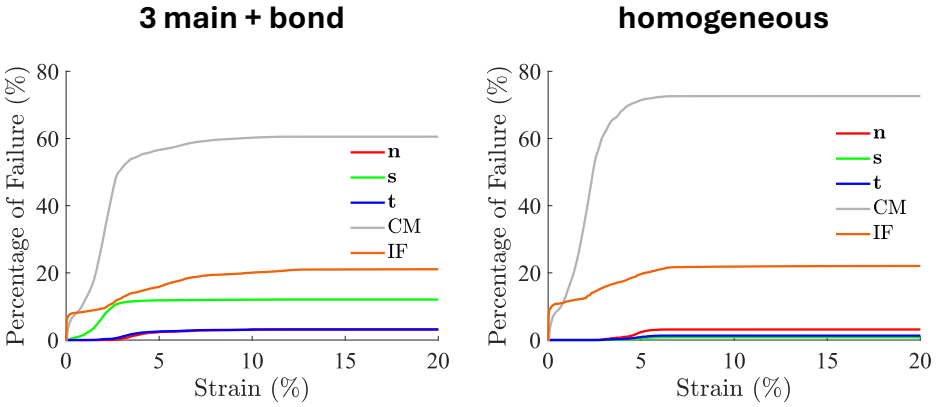

Figure 5.10: Percentage of locally failed elements versus compressive axial strain of ACC RE. Note: n_i refers to the bead direction, s_i to the inter-layer direction, t_i to the intra-layer direction, CM to the cementitious mortar and IF to interfacial bond elements.

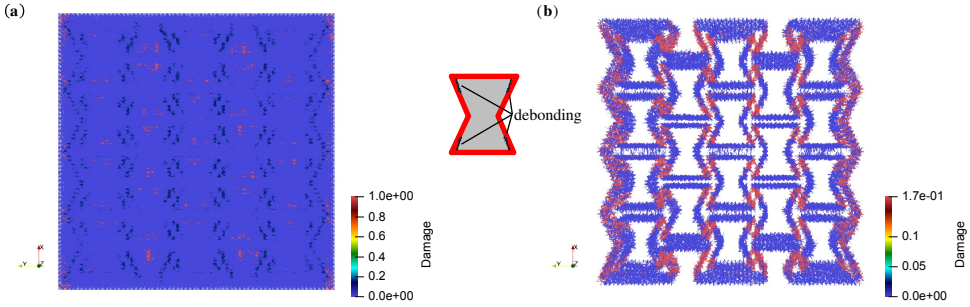

Figure 5.11: LBM fracture at 1 % compressive axial strain of ACC RE in all phases (a), and only in the bond phase (b). The middle schematically represents the debonding regions. Only the 3 main directions model is shown in view of similarities among the models. Numerical cracks correspond to Damage = 1.

identically with both having inter-layer failure (s_i) contributing to approximately 10 % of the percentage of failure. As discussed in Chapter 3, this is a strong indication of the FDM 3D printed auxetics' out-of-plane failure where the inter-layer bond breaks. The remaining two ABS directions, n_i and t_i, only start to fail after the inter-layer failure is stabilized. The most important difference with the homogeneous simulation is the absence of inter-layer failure in the out-of-plane direction, which suggests the mismatch in energy absorption capacity for 2D FEM models [110] can be attributed to the lack of considering out-of-plane behaviour. However, it is also notable that in the 3 main and 3 main bond models the interface failure continues to increase until the end of the analysis, whereas in the homogeneous model this is suddenly put to a hold near the initiation of bead failure (n_i). Finally, the homogeneous model undergoes enhanced mortar failure (about 70 %) with respect to the other two models (near 60 %).

Figures 5.12(a) and (b) show side views of the LBM fracture near peak load of the ABS reinforcement inside ACC RE for the 3 main directions and homogeneous models, respectively. When comparing the cracking behaviour (Damage = 1), it can be seen that

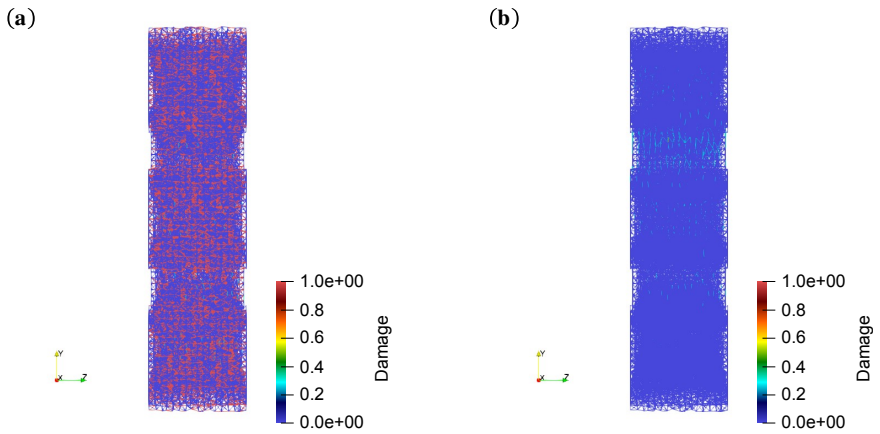

Figure 5.12: Side views of LBM fracture near peak load of ABS reinforcement inside ACC RE: (a) 3 main directions and (b) homogeneous. Numerical cracks correspond to Damage = 1.

the 3 main directions model is already severely damaged in the inter-layer bond phase throughout the reinforcement, whereas the homogeneous model has little to no damage at all and will only fail near the peak load (as indicated by Figure 5.10). In some places the out-of-plane fractures in the 3 main directions reinforcement coalesce, but delamination followed by buckling as observed in [110] (Figure 4.7) is not incorporated in the current version of LBM. Even though no explicit out-of-plane buckling is captured, the significant damage illustrates realistic weakening of the ABS. Moreover, inter-layer damage shows to be spread across the specimen and not to initiate at the ABS-mortar interface, suggesting that no interlocking or wedging action of the mortar is causing delamination of the reinforcement as hypothesized in Chapter 4.

Ending with the global fracture response in Figure 5.13, Figure 5.13(b) displays that the 3 main simulation's fracture response aligns well with the experiment in Figure 5.13(a). Similar to Chapter 3, ACC RE exhibits diagonal shear failure as opposed to the straight fracture plane observed for the plain reference mortar in Figure 5.6. The fracture in Figure 5.13(b) roughly follows the high localized lateral strain regions in Figure 5.8. Careful inspection of Figure 5.13(b) reveals multiple occasions of strut failure in the outermost horizontal legs of the 3D printed reinforcement (i.e., those closest to the top and bottom boundaries of the specimen). However, the damage in these struts is spread out over multiple elements, including intra-layer failure besides the orthogonal bead direction. On the other hand, Figure 5.13(c) depicts the damage in the homogeneous simulation, which follows a more horizontal failure pattern with significantly more localized failure in the exterior horizontal struts of the RE reinforcement (i.e., bead failure), and hardly any intra-layer failure. The localized damage in the homogeneous simulation, together with its lack of out-of-plane (inter-layer) failure in the ABS reinforcement, clarify the more brittle post-peak response in Figure 5.7(a). This explicit fracture behaviour could not be captured by previous 2D FEM simulations in [110].

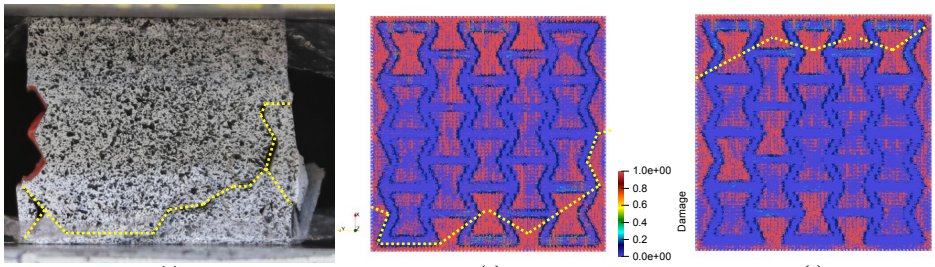

(a) (b) (c)

Figure 5.13: Comparison of (a) experimental, (b) 3 main, and (c) homogeneous fracture for uniaxial compression of ACC RE. Global failure mechanisms are traced in yellow, numerical cracks correspond to Damage = 1.

Table 5.5: Mechanical properties of ACC RS

ACC	**Load Capacity** (kN)	**Toughness** (J)
RS (EXP)	22.3 ± 0.4	44.5 ± 1.4
RS (3 main)	25.8	42.0
RS (3 main bond)	25.7	45.4
RS (homogeneous)	27.7	30.6

5

ACC RS

ACC RS also shows a global ductile response in the experiments and simulations, see Figure 5.14(a). In this case, the mortar's linear-elastic brittle constitutive relationship becomes more evident in the post-peak behaviour. However, most simulations recover afterwards and continue following the experimental curve. This is likely caused by the alternating unit cell orientations of the RS structure as addressed by Xu et al. [175], which will be discussed later. The LBM compressive strengths in Figure 5.14(b) and Table 5.5(a) are somewhat higher than the experimental average. Again, the homogeneous model clearly exhibits higher strength related to the strength overestimation of the polymer phase observed in Chapter 3. The toughness values in Figure 5.14(c) and Table 5.5(b) illustrate that the simulations are equal or less than the experiments. The homogeneous simulation is the only one that does not recover after the load drop, which implies that reaching the higher compressive strength comes at the cost of more localized failure causing a weaker post-peak response. This is also visible for ACC RE in Figure 5.7(a), albeit less evident therein. As a result, the toughness for the homogeneous model is lower than in the other simulations.

Figure 5.15 illustrates the substantial multiple cracking behaviour recorded in the experimental and numerical results of ACC RS. At 5 % vertical axial strain, which is beyond the peak load of the experiments and most models (see Figure 5.14(a)), minor lateral cracks are observed throughout the specimen which explains the ductile softening response.

The FDM 3D printed RS reinforcement structure also actively confines the surrounded cementitious mortar, even at 1 % compressive strain as shown in Figure 5.16. Similar to

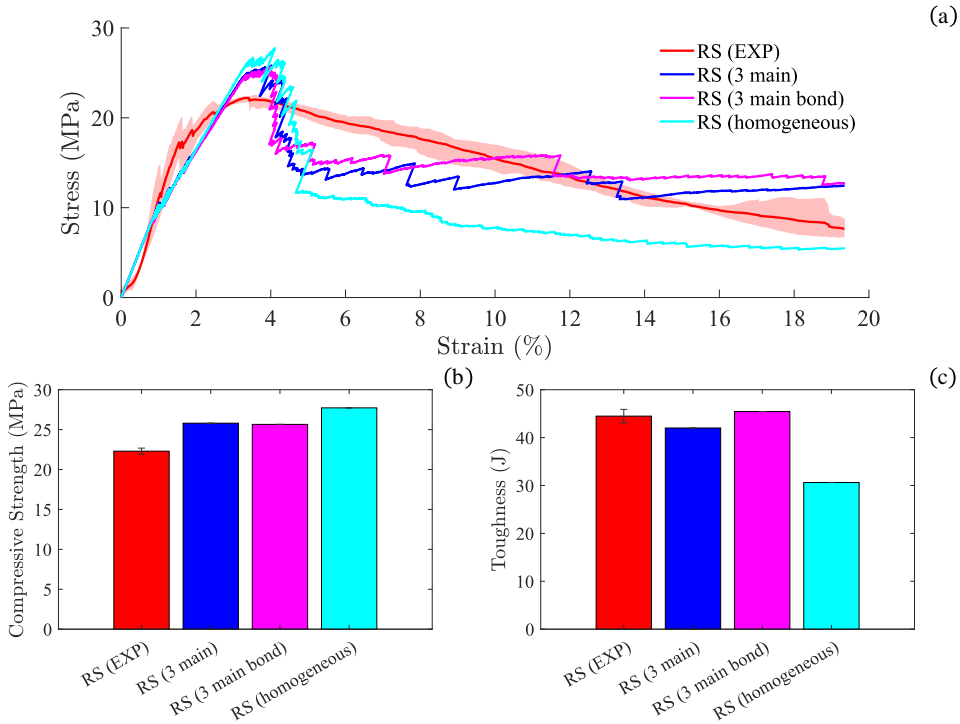

Figure 5.14: Comparison of experimental and numerical mechanical properties for uniaxial compression of ACC RS: (a) Stress strain curves, (b) compressive strengths, and (c) toughness values. For experimental data, the shaded bands reflect the spread observed among four parallel measurements, and the solid lines denote the mean outcomes.

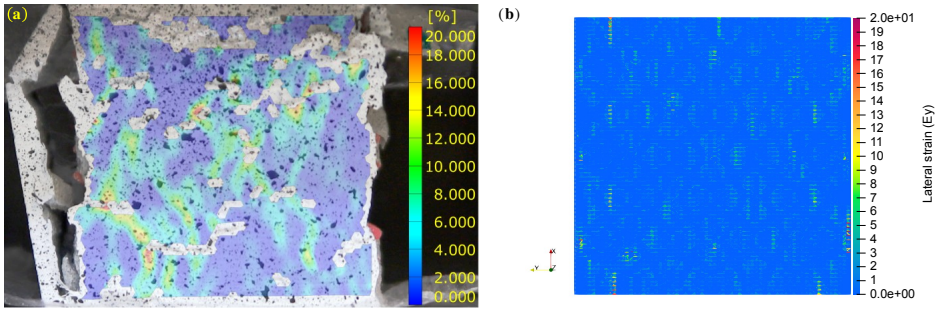

Figure 5.15: Comparison of (a) DIC and (b) LBM lateral strain for 5 % compressive axial strain of ACC RS. Only the 3 main directions model is shown in view of similarities among the models.

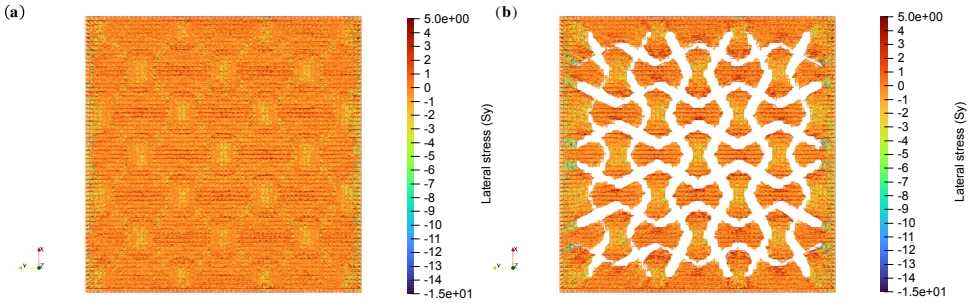

Figure 5.16: LBM lateral stress for 1 % compressive axial strain of ACC RS in all phases (a), and only in the matrix phase (b). Only the 3 main directions model is shown in view of similarities among the models.

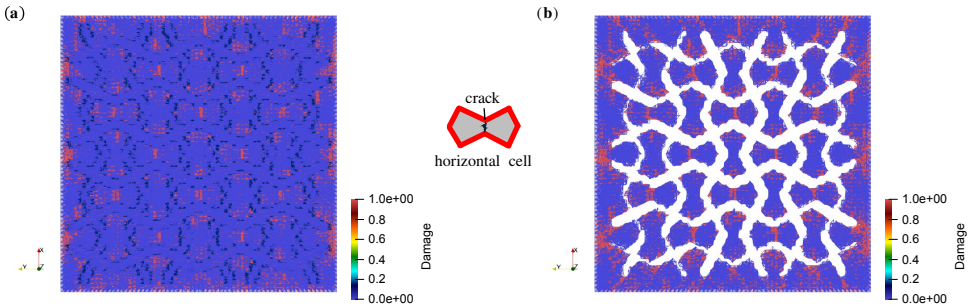

Figure 5.17: LBM fracture near peak load of ACC RS in all phases (a), and only in the matrix phase (b). The middle schematically represents the cracked horizontal cells. Only the 3 main directions model is shown in view of similarities among the models. Numerical cracks correspond to Damage = 1.

ACC RE, the simulations of ACC RS display negative lateral stress concentrations inside the unit cells forming a diagonal grid. However, the simulated mortar in Figure 5.16(b) uncovers the differentiated orientation of unit cells within ACC RS. As explained in [175], the RS architecture contains horizontal cells having a bowtie shape, and vertical cells with an hourglass shape. The intended confinement mechanism only occurs in the vertical cells, which display a negative lateral stress concentration at their centers in Figure 5.16(b). On the other hand, the horizontal cells exhibit small positive lateral stresses in the middle, indicating vertical cracks.

These vertical cracks in the horizontal unit cells are captured by the LBM simulations near the peak load in Figure 5.17. Given the brittle material behaviour of the cementitious mortar (see Figure 5.5) and the alternating unit cell orientations of ACC RS, the occurrence of these vertical cracks most likely caused the more sudden load drop in the LBM simulations.

Figure 5.18 depicts the percentage of failed elements versus the compressive axial strain. ACC RS also initiates with interfacial bond failure (IF). Again, the 3 main and 3 main bond behaved identically. The same minor debonding is occurring immediately after loading at the upper and lower edges of the vertical unit cells as evidenced in Figure 5.19, mainly in the regions that are not confined by the auxetic reinforcement (see Figure 5.16). After the rate of interfacial failure decreases, cementitious mortar (CM) failure continues

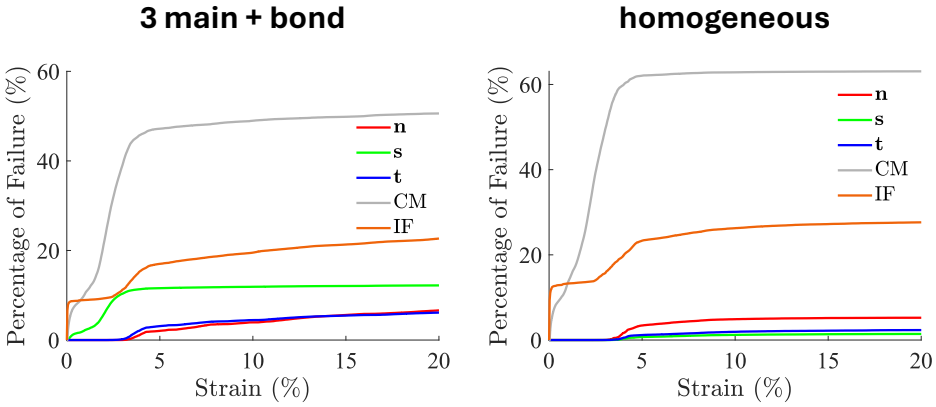

Figure 5.18: Percentage of locally failed elements versus compressive axial strain of ACC RS. Note: n_i refers to the bead direction, s_i to the inter-layer direction, t_i to the intra-layer direction, CM to the cementitious mortar and IF to interfacial bond elements.

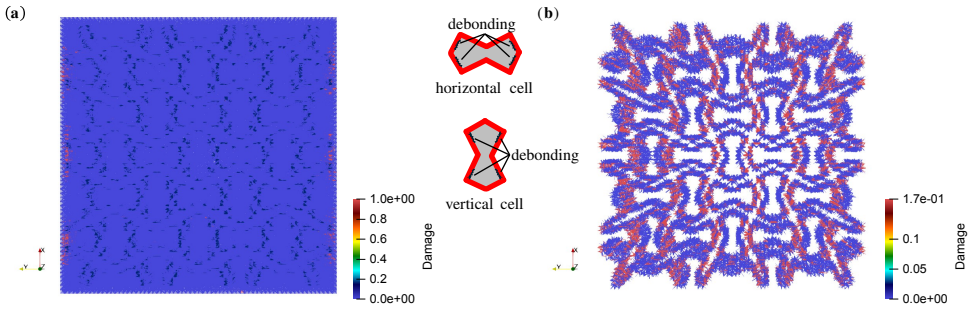

Figure 5.19: LBM fracture at 1 % compressive axial strain of ACC RS in all phases (a), and only in the bond phase (b). The middle schematically represents the debonding regions. Only the 3 main directions model is shown in view of similarities among the models. Numerical cracks correspond to Damage = 1.

to increase, followed by inter-layer failure (s_i) plateauing close to 10 % failure like in ACC RE. Similarly, this reflects the 3D printed reinforcement's out-of-plane delamination behaviour [110]. The other two ABS directions, n_i and t_i, start to fail after the inter-layer failure rate stabilizes. The homogeneous model exhibits no failure in the polymer phase until the peak load (see Figure 5.14(a)), exhibits more bead failure (n_i) compared to the other models, and is lacking the increase of inter-layer failure at the beginning analysis. Similar to ACC RE, the homogeneous model of ACC RS undergoes more matrix failure (about 60 %) compared to the other two models (near 50 %).

Side views of the LBM fracture near peak load of the ABS reinforcement in ACC RS are compared for the 3 main directions and homogeneous models in Figures 5.20(a) and (b), respectively. Once more, inter-layer cracking (Damage = 1) can be observed spread across the RS reinforcement for the 3 main directions model, whilst the homogeneous model is still fully intact near the peak load. Only at the end of the analysis does the ABS in the latter model fail locally.

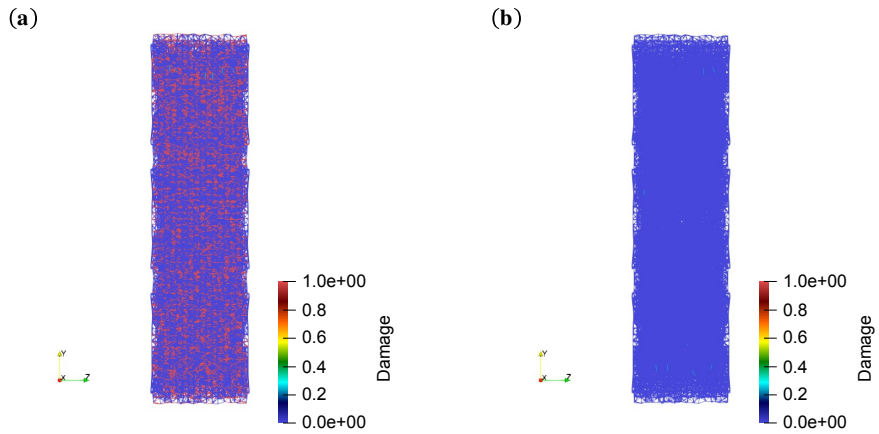

Figure 5.20: Side views of LBM fracture near peak load of ABS reinforcement inside ACC RS: (a) 3 main directions and (b) homogeneous. Numerical cracks correspond to Damage = 1.

The global fracture response in Figure 5.21 illustrates the experimental and numerical failure mechanisms. In both tests and simulations, ACC RS fails through diagonal shear failure. The 3 main model in Figure 5.21(b) shows a broad diagonal damage zone which explains the ductility of ACC RS. It is notable that the polymer phase in this region exhibits substantial damage, particularly in the intra-layer bond phase. As a result, the ABS material failed closer to or at the joints where the RS struts meet. On the contrary, the homogeneous model in Figure 5.21(c) displays complete fracture of the 3D printed reinforcement due to strut failure, all located in the narrow damage band following the matrix damage. The more localized damage in both the matrix and ABS reinforcement, combined with the lack of out-of-plane damage (i.e., inter-layer failure), further explain the brittle post-peak response of the homogeneous LBM simulation of ACC RS in Figure 5.14(a). Similar to ACC RE, the ABS material mainly fails in the printing direction (i.e., bead failure) with hardly any breakage in the other two directions (i.e., intra-layer and inter-layer). This explicit fracture behaviour could not be captured by previous 2D FEM simulations in [110], and indicates that the reinforcement exhibits different failure mechanisms for printing path-dependent material properties and homogeneous input. Similar findings were obtained for the isolated 3D printed reinforcement architectures in Chapter 3.

Ultimately, the experimental and numerical results of the presented research using the updated printing process parameters and proposed multi-scale model based on LBM can be compared with the printer settings and 2D FEM models presented in [110], see Appendix A.2. Starting with compressive strength, the previous methods by Xu & Šavija [110] (see Table A.6) resulted in average experimental values of 19.9 MPa and 20.7 MPa for ACC RE and ACC RS with standard deviations of 2.4 MPa and 1.3 MPa, respectively. Their numerical compressive strengths (Table A.6) comprised 19.4 MPa and 18.3 MPa, yielding percentage differences of 2.5 % and 11.6 % for ACC RE and ACC RS, respectively. The uniaxial compressive strengths for the improved printer settings (see Tables 5.4 and 5.5) resulted in average experimental compressive strength values of 22.7 MPa and 22.3 MPa

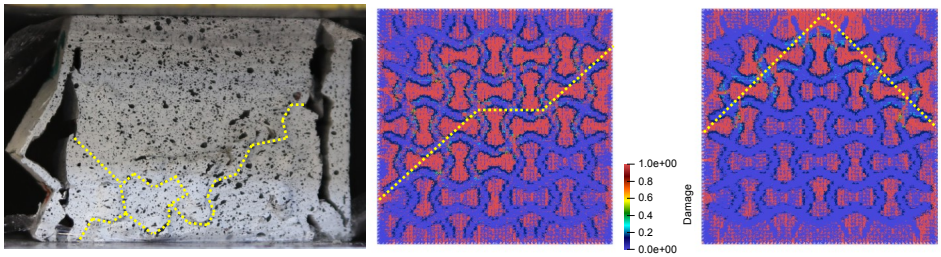

Figure 5.21: Comparison of (a) experimental, (b) 3 main, and (c) homogeneous fracture for uniaxial compression of ACC RS. Global failure mechanisms are traced in yellow, numerical cracks correspond to Damage = 1.

for ACC RE and ACC RS with standard deviations of only 0.9 MPa and 0.4 MPa, respectively. These numbers already show the increased compressive strength and consistency among the parallel tested specimens. The numerical compressive strengths (Tables 5.4 and 5.5) found using the 3 main models developed in this work yield 23.1 MPa and 25.8 MPa for ACC RE and ACC RS, respectively, providing percentage differences of 1.8 % and 15.7 % with the experiments.

However, when looking at the energy absorption capacity (i.e., toughness) the experimental results in [110] (see Table A.6) display 31.6 J and 29.8 J with significantly larger standard deviations of 7.0 MPa and 4.2 MPa for the tests of ACC RE and ACC RS, respectively. The 2D FEM results in [110] (Table A.6) comprised 45.1 J and 42.8 J, having percentage differences of 42.7 % and 43.6 % with the experiments of ACC RE and ACC RS, respectively. The ACCs with updated printer settings (Tables 5.4 and 5.5) exhibit considerably greater toughness values of 34.6 J and 44.5 MPa, again with drastically smaller standard deviations of 4.1 J and 1.4 J compared to [110] for ACC RE and ACC RS, respectively. The toughness values from the LBM simulations (3 main models in Tables 5.4 and 5.5) are 30.5 J and 42.0 J for ACC RE and ACC RS, respectively, giving significantly smaller percentage differences of 11.8 % and 5.6 % with the test data compared to [110]. Overall, the LBM simulations accounting for the anisotropy present within the FDM 3D printed auxetic reinforcements through the proposed multi-scale modelling approach were able to improve the predictive capabilities for energy absorption capacity.

5.5. CONCLUSIONS

In this chapter, a multi-scale model for simulating deformation and fracture of Auxetic Cementitious Composites (ACCs) has been developed. A numerical approach based on the Lattice Beam Model (LBM) is proposed, wherein an experimentally-validated multi-scale strategy combines two preceding modelling methodologies to explicitly incorporate (i) the anisotropy present within FDM 3D printed auxetic reinforcement made of ABS, and (ii) 3D printing-induced geometrical effects on the bond stress-slip response between ABS and cementitious mortar. The main conclusions are as follows:

- The proposed multi-scale LBM framework successfully captures the ductile post-peak softening behaviour of ACCs, which prior 2D FEM simulations failed to repro-

duce. Incorporating printing path-dependent anisotropy, particularly the out-of-plane inter-layer failure mechanism, reduces the percentage difference in energy absorption capacity from over 40 % to below 12 % compared to experiments, while maintaining comparable compressive strength predictions.

- The simulations reveal that the auxetic reinforcement actively confines the surrounding cementitious matrix already at 1 % compressive axial strain, well before peak load, and that failure universally initiates at the reinforcement–matrix interface before progressing into the mortar and reinforcement phases.
- Neglecting printing path-dependent anisotropy by modelling the reinforcement as homogeneous consistently overestimates composite strength and underestimates toughness, confirming that out-of-plane inter-layer failure is a governing mechanism in FDM 3D printed auxetic reinforcement that cannot be captured by 2D models.
- Incorporating the experimentally-validated bond stress-slip relationship yields a more physically representative composite response compared to the arbitrary friction coefficients assumed in prior FEM work, although the directional dependency of bond behaviour has limited influence under the uniaxial compression loading configuration studied here.

6

TAILORING THE POISSON'S RATIO OF 3D PRINTED REINFORCEMENT FOR FLEXURAL APPLICATIONS

In this chapter, Tailored Poisson's Ratio-reinforcements (TPR) are proposed, characterized by a linear gradient of Poisson's ratios along the height of the reinforcement to accommodate varying stress profiles within beams. Specifically, the top chords of TPR exhibit negative Poisson's ratios (auxetic), undergoing lateral contraction under compression and providing confinement to the surrounded matrix. Conversely, the bottom chords possess positive Poisson's ratios, contributing to lateral contraction under tension. These lateral deformations cause a shift in the principal stress state of the confined matrix, extending the loading path in stress space and actively delaying failure. Three novel Tailored Poisson's Ratio-reinforced Cementitious Composite (TPRCC) designs are developed and tested under four-point bending in this study. Experimental recordings indicate increases in load capacity and toughness of up to 191 % *and* 6900 % *with respect to plain mortar, respectively.*

With the exception of minor textual adjustments, this chapter is reproduced from: R.J.M. Bol, W. Zhou, Z. Meng, E. Schlangen, B. Šavija, *Tailored Poisson's Ratio-reinforced Cementitious Composites for flexural applications*, Cement and Concrete Composites **168**, 106485 (2026).

6.1. INTRODUCTION

The use of Additive Manufacturing (AM) to create reinforcements for cementitious composites has become a popular research topic in recent years [109, 168, 176]. Various AM techniques enable the construction of polymeric and metallic reinforcements, such as Fused Filament Fabrication (FFF) or Fused Deposition Modelling (FDM) [106, 139, 175, 177], StereoLithograPhy (SLA) [178–180], and Powder Bed Fusion (PBF) or Selective Laser Sintering (SLS) [181–183]. These processes can build structural designs having complicated geometries with virtually any shape, thereby potentially facilitating improved mechanical behaviour inconceivable in the past [184]. AM is thus a powerful tool which allows for tailored reinforcements providing optimal properties for cementitious composites. For instance, Dong et al. [185] describe various functionally graded lattice structures as reinforcement for cementitious composites which reached about 40 % to 50 % improvements in specific stiffness compared to uniform meshes. Clausen et al. [186] produced a novel class of architected materials having programmable Poisson's ratios between −0.8 and 0.8 which sustain under large deformations (i.e., up to 20 % strain). Stepinac & Galić [187] investigated optimized (functionally) graded auxetic cores for sandwich structures, only feasible through AM (i.e., FDM). Panesar et al. [188] derived functionally graded lattice structures for AM applications through topology optimization, whilst Xu & Šavija [75] created functionally graded lattice reinforcement for cementitious composites by means of 3D printing.

The symbiosis of 3D-printed polymeric architectures embedded in cementitious matrix has led to numerous favourable mechanical properties like enhanced strength, toughness, and energy absorption capacity [109, 189]. One illustrative example of such composites are Auxetic Cementitious Composites (ACCs) [110]. ACCs use auxetic structures having a negative Poisson's ratio [30–43, 167] as reinforcement in cementitious matrices. However, the development of ACCs mainly focuses on compressive applications [168, 190]. Xu & Šavija [110] proposed novel ACCs that benefit from the outstanding compressive strength of cementitious materials while exploiting the large deformation capacity of polymeric Acrylonitrile Butadiene Styrene (ABS) auxetic architectures. Their findings show that all of the designed ACCs have excellent compressive ductility. Particularly the re-entrant and rotating-square structures exhibit lower Poisson's ratios compared to the others, such that these two ACC designs display better crack-arresting effect under compressive loads. As a result of these traits, the auxeticity of the re-entrant and rotating-square architectures provide more confinement to the cementitious matrix, such that similar compressive strength values as obtained for plain mortar are achieved by the ACCs. A very similar experimental and numerical study by Choudhry et al. [191], also using ABS auxetic designs in their Lattice-Reinforced Cementitious Composites (LRCCs), explored fracture patterns, compressive ductility and energy absorption capacity. Additionally, they investigate the effect of reinforcement ratio on the mechanical behaviour in compression in the range of 25 % to 40 %. Identical to Xu & Šavija [110], Choudhry et al. [191] conclude that the use of auxetic reinforcement in cementitious mortar changes the fracture behaviour from brittle to ductile. Again, the re-entrant design (LRCC 4 in [191]) showed the highest increase in ductility (i.e., over 200 %), which is attributed to the auxetic reinforcement's ability to hinder the matrix to shear, thereby actively restraining (micro-)crack propagation by means of bi-axial compression. The aforementioned

publications both report small reductions in strength as a result of adding polymeric reinforcement, thereby illustrating a trade-off among strength and ductility. Although other studies have found ductility to increase together with strength [176, 192, 193], it remains unknown how to balance these mechanical properties.

Most studies on ACCs have only limited attention for tension and bending [49, 169, 194, 195], albeit promising. Cementitious materials are known to have a low tensile strength, fracture toughness and ductility [169]. Hence, the latter reference lists some of the efforts to overcome these issues, such as fiber-reinforcement that can improve structural ductility. In their work, architected composites have been developed by combining cement mortar with an ABS polymer phase, thereby imitating the microstructure of nacre. They found that these composites outperformed control specimens. If flexural auxetic reinforcement is implemented, it is mostly oriented in-plane (i.e., the auxetic deformation mechanisms occur in the same plane as the loading) [168, 169, 196]. Particularly, cementitious composites with re-entrant auxetic reinforcements accomplish promising strength and ductility values when subjected to compression and bending [49].

Few publications tested ACCs where the auxetic response of the reinforcement takes place out-of-plane (e.g., [194]). Current flexural studies on cementitious composites consider planar [6, 109, 139, 169, 194, 195, 197] as well as three-dimensional [185, 198, 199] reinforcement designs. Planar reinforcement is often implemented in thin beams resulting in high reinforcement ratios [139, 194]. Other configurations, including three-dimensional reinforcements, seek to achieve a flexural hardening response with volume fractions ranging from 20 % up to 50 % [108, 109, 185, 200]. Nevertheless, examples with lower reinforcement ratios exist that exhibit flexural softening [195]. More recently, Zhou et al. [201] investigated the flexural behaviour of LRCCs with considerably small volume fractions (2.5 % to 3.8 %). Therein, all LRCCs reached flexural strengths that were roughly the same as the reference mortar, even though significant increases in energy absorption capacities were reported (500 % to 2300 %). On the other hand, flexural applications of Architected Polymer-Concrete Composites (APCCs) containing significantly higher reinforcement ratios (~80.7 %) have also been reported that exhibit strain hardening behaviour [6]. The latter reference argues in favour of polymeric reinforcements in view of their low mass and high corrosion resistance, as well as the APCCs' potential for upscaling to practical applications. It was observed that the mechanical behaviour of the APCCs is dependent on the reinforcement's geometry and dimensions, which were optimized to maximize specific flexural strength and toughness. The optimization process involved sequential surrogate modelling using Finite Element Analysis (FEA) in which the constitutive relationships for the cementitious matrix and ABS reinforcement were implemented through a Concrete Damaged Plasticity Model (CDPM) and multi-linear ductile material model. The bond amongst the two materials was modelled via 'embedded region', assuming a fully perfect bond. However, experimentally observed damage mechanisms revealed that debonding, shown by horizontal cracking, assisted in diminishing strain levels through (re)distribution over increased lengths. As a result, stress concentrations were reduced, thereby restraining crack propagation and increasing the energy dissipation capacity.

In ordinary Reinforced Concrete (RC) beams subjected to downward bending, the bottom reinforcement adopts the stresses in the tensile region whilst the reinforcement at

the top mitigates cracking and enhances stiffness in the compression zone [184]. However, it is questionable whether lateral expansion of auxetic bending reinforcement deteriorates the load-bearing capacity, particularly in the lower region subjected to tension. On the other hand, the reinforcement's deformation mechanism will bring the mortar in a state of biaxial compression in the upper zone, which is beneficial in terms of both strength and ductility [41, 184]. More recent works concerning ACCs focus on the latter application, in which lateral confinement is an important factor [168].

This contradiction raised the idea to tailor the Poisson's ratio of the reinforcement according to the bending stress-strain distribution, meaning that the reinforcements in this study have a through-thickness gradient of Poisson's ratio that is aligned with the elastic bending stress distribution, distinguishing it from previous architected reinforcements with uniform Poisson's ratio. It is thereby the aim to laterally confine the cementitious matrix throughout its maximally stressed locations. The hypothesis is that Tailored Poisson's Ratio-reinforcement (TPR) will cause a shift in the principal stress state, leading to an extended loading path in stress space, actively postponing failure of the surrounded matrix. The top chord of the reinforcement will be auxetic, resulting in lateral confinement under compressive strain. In contrast, the bottom chord receives a positive Poisson's ratio, providing lateral compressive stress when loaded in tension. The neutral axis has a Poisson's ratio that is virtually zero, such that it varies linearly over the height. A similar conceptualization is envisioned by Vitalis et al. [184] for Interpenetrating Phase Composite (IPC) beams in a RC frame. However, their conceptualized (auxetic) lattice bending reinforcement is yet again oriented in-plane, such that it cannot accommodate continuous confinement pressure over the height of the beams. In contrast, the proposed out-of-plane TPR is continuous, allowing for lateral confinement throughout the height of the beam.

The literature shows that prior work has mainly focused on compression or in-plane applications of auxetic reinforcement, often at high reinforcement ratios. Moreover, experimental explorations of reinforcement with a tailored Poisson's ratio to align with local stress distributions in flexure are currently lacking, especially out-of-plane lattices at low reinforcement ratios. The main objectives of this work are therefore as follows:

1. To design 3D-printed reinforcements with a prescribed gradient in Poisson's ratio suitable for flexural applications.

2. To experimentally assess the flexural behaviour of these reinforcements and corresponding reinforced cementitious composites.

3. To evaluate the hypothesized lateral confinement mechanism and its impact on load capacity and toughness.

To this end, three Tailored Poisson's Ratio-reinforced Cementitious Composite (TPRCC) designs having a relatively low reinforcement ratio (14.6 % to 14.7 %) are developed and tested. Experimental recordings indicate increases in load capacity and toughness of up to 191 % and 6900 % with respect to plain mortar, respectively. CT scans after testing reveal the fracture behaviour and key interfacial phenomena (e.g., debonding and load transfer) of the considered TPRCCs.

6.2. EXPERIMENTAL DETAILS

6.2.1. TAILORED POISSON'S RATIO-REINFORCEMENT (TPR)

The Tailored Poisson's Ratio-reinforcement (TPR) designs developed in this work are based on common auxetic and non-auxetic unit cell geometries from literature having varying deformation mechanisms. The novelties of the proposed TPR designs are: (i) orienting the flexural auxetic reinforcement out-of-plane (i.e., the auxetic deformation mechanisms occur in the plane perpendicular to the loading) instead of in-plane, and (ii) rather than having planar reinforcement geometries and constant Poisson's ratios along the height, here the geometries gradually change to have a linear gradient of Poisson's ratios for accommodating varying stress profiles within beams. Therefore, each unit cell geometry is selected from literature based on the following requirements:

1. Unit cell geometries should exhibit a comparable Poisson's ratio under deformation, regardless of the direction of the load (tension versus compression).

2. The geometry of the unit cell should be highly porous so that cementitious matrix can easily fill the gaps.

3. A pair of corresponding auxetic and non-auxetic unit cell geometries should share the same deformation mechanism.

4. Similar unit cell geometries should be available in a wide range of Poisson's ratios or adjustable to possess a prescribed Poisson's ratio.

The first geometry meeting all of the aforementioned criteria is based on Gibson's model [41, 103, 104] and named after honeycomb arrangements of Re-Entrant (RE) models, see Figure 6.1. In this study, square unit cells are considered having dimensions of $h = l = 18\,\text{mm}$, providing enough space for cementitious mortar to flow in. Similarly to Li et al. [41], the RE unit cell geometries can be adjusted to possess an assumed and prescribed theoretical Poisson's ratio, ν, by computing $\theta = \arctan \nu l/h$, $H = (h - l\tan\theta)/2$ and $L = l/2\cos\theta$. In Figure 6.1, the top RE figure illustrates a traditional honeycomb with a positive Poisson's ratio and the bottom RE figure displays a re-entrant shape that is auxetic. The second geometry concerns a combination of two rotational designs discussed in [167, 202], referred to as star structure (positive Poisson's ratio) and 3D cross-chiral structure (auxetic), also referred to as Rotating Square (RS) [110, 189, 201] in Figure 6.1. In this case, the unit cell geometry varies similar to RE (i.e., by altering the internal strut angles), provided that two of the four internal strut angles that are opposite must remain re-entrant. The final geometry in Figure 6.1 considers nine Topology Optimized (TO) architectures with programmable Poisson's ratios that are strain-independent (i.e., nearly constant over large deformations) in the range of $-0.8 \leq \nu \leq 0.8$ by Clausen et al. [186]. This was achieved through the application of a geometrically non-linear model, elaborated by Sigmund and co-workers [203], in an optimization framework aiming to minimize the discrepancy among real and prescribed Poisson's ratios for nominal strains at intervals until 20 %.

The selected unit cell geometries in Figure 6.1 formed the basis for the three TPR designs shown in Figure 6.2. The TPR unit cell geometry based on RE varies linearly over the height in agreement with the theoretical Poisson's ratio $-0.5 \leq \nu(Z) \leq 0.5$, such that the

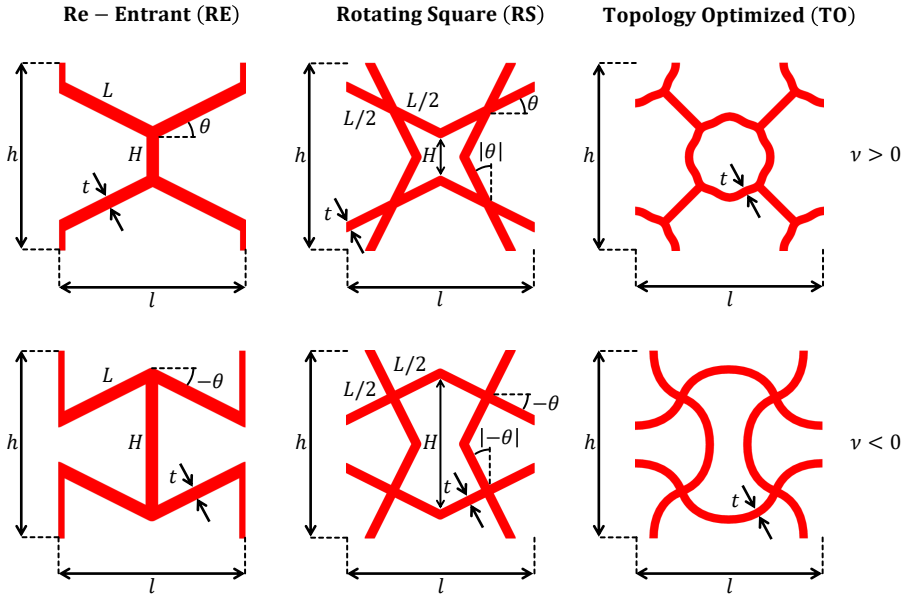

Figure 6.1: Unit cell geometries. Parameters h and l are the unit cell dimensions; H is the length of vertical cell walls or vertical distance between inclined cell walls and L the length of the inclined cell walls; t the thickness of the cell walls; θ the inclination angle, which is negative for $\nu < 0$.

top is auxetic ($\nu(36) = -0.5$) and the bottom has a positive Poisson's ratio ($\nu(0) = 0.5$). The neutral axis has a Poisson's ratio that is virtually zero (i.e., $\nu(18) = 0$). Similarly, the TPR RS unit cell design is constructed by linearly interpolating its horizontal cross-sections over the height in accordance with $-0.5 \leq \nu(Z) \leq 0.5$. To end up with a continuous reinforcement layout, the nine unit cell curves corresponding to TO were vertically distributed over the height of 36 mm through which a lofted surface was created by means of Rhinoceros® using Grasshopper. The strut widths are different to ensure comparable volumes among the designs. Please note that the Poisson's ratio distributions in Figure 6.2 are theoretical, based on analytical and topology optimized unit cell models, and not measured in this work. The TPR designs were manufactured by an Ultimaker S5 commercial FDM 3D printer using Ultimaker ABS material (ø2.85 mm, 750 g) as polymer filament. The printing process parameters are provided in Table 6.1 and the build orientation was along the height (Z in Figure 6.2). Due to the maximum strut width of 1.2 mm for RE, the nozzle size being 0.4 mm and a wall line count (number of perimeters) of 2 did not require infill patterns during FDM printing.

6.2.2. FOUR-POINT BENDING TESTS OF TPR

To have more insight into the TPR's flexural behaviour, the ABS 3D prints were first subjected to four-point bending tests without cementitious matrix. All designs are composed of 8 × 2 unit cells and each TPR was tested in two configurations: UpRight (UR) and

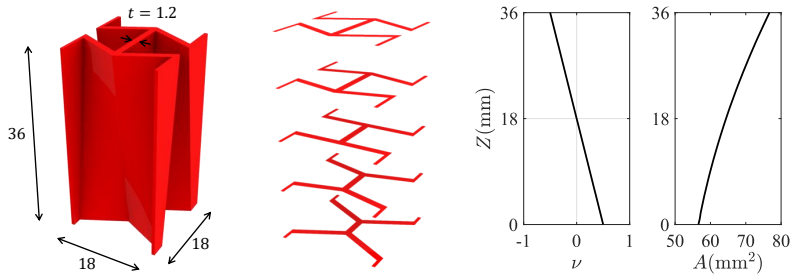

Re − Entrant (RE)

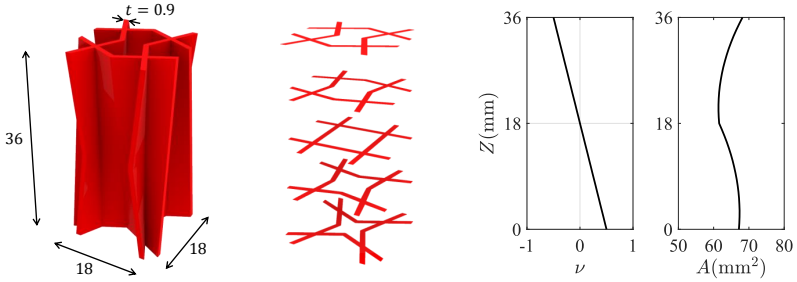

Rotating Square (RS)

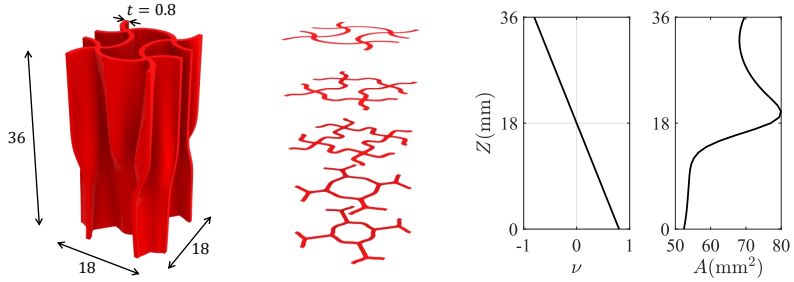

Topology Optimized (TO)

Figure 6.2: Tailored Poisson's Ratio-reinforcement (TPR) designs. From left to right: Unit cell dimensions (mm), horizontal cross-sections, theoretical Poisson's ratio (ν) over height (Z), and horizontal cross-sectional area (A) over height (Z). Strut widths are constant over the height.

Table 6.1: Printing process parameters for Tailored Poisson's Ratio-reinforcement (TPR)

Printing parameters	**Configurations**
Layer height (mm)	0.2
Nozzle size (mm)	0.4
Wall thickness (mm)	0.4
Wall line count	2
Horizontal expansion (mm)	0.01
Infill density (%)	100
Printing temperature (°C)	245
Build plate temperature (°C)	85
Flow (%)	120
Print speed ($mm\,s^{-1}$)	60

Upside Down (UD), see Figure 6.3. The six resulting TPR layouts allow for comparison in mechanical properties considering the variation in both the theoretical Poisson's ratio and horizontal cross-sectional area over the height (see Figure 6.2) for the 3D prints and eventually for the composites. UR samples are auxetic at the top and have a positive Poisson's ratio at the bottom, whilst UD samples have a positive Poisson's ratio at the top and are auxetic at the bottom. Each TPR design was tested twice in the UR and UD configurations, which adds up to a total of 12 samples. Figure 6.3 further shows that small legs were added to correctly position the TPR ABS 3D prints in the mould to later casting the composites.

Figure 6.4 shows the experimental setup. The TPR ABS samples were loaded to bend at a constant displacement rate of $0.02\,mm\,s^{-1}$ by a hydraulic press INSTRON 8872. The loading pins have a diameter of 10 mm and were not lubricated. During the test, the load was recorded directly by the device itself whilst a Linear Variable Displacement Transducer (LVDT) was used to measure the cross-head displacement which did not observe machine compliance, see Figure 6.4.

6.2.3. FOUR-POINT BENDING TESTS OF TPRCC

Similar to the four-point bending tests of the TPR ABS 3D prints, the experiments regarding the Tailored Poisson's Ratio-reinforced Cementitious Composite (TPRCC) designs comprise six layouts denoted by UR and UD as shown in Figure 6.5. Each TPRCC design was tested three times in both the UR and UD configuration, resulting in a total of 18 samples. Prior to casting the cementitious matrix, the small additional legs of the TPR ABS 3D prints were glued to the bottom of styrofoam moulds to prevent floating. Given the location of these legs, all TPR prints were cast in their upside-down configuration (see Figure 6.6). Nonetheless, each TPRCC design was tested in UR and UD configuration, see Figure 6.5. No surface preparation nor post-treatment of the ABS was used before casting. Similar to the TPR, the six resulting TPRCC layouts allow for comparison in mechanical properties considering the variation in both the theoretical Poisson's ratio and horizontal cross-sectional area over the height (see Figure 6.2). The final TPRCC samples have dimensions of $160 \times 40 \times 40$ mm such that the TPR has a cover of at least 2 mm, see Figure 6.7. This resulted in reinforcement ratios of 14.6 % to 14.7 %.

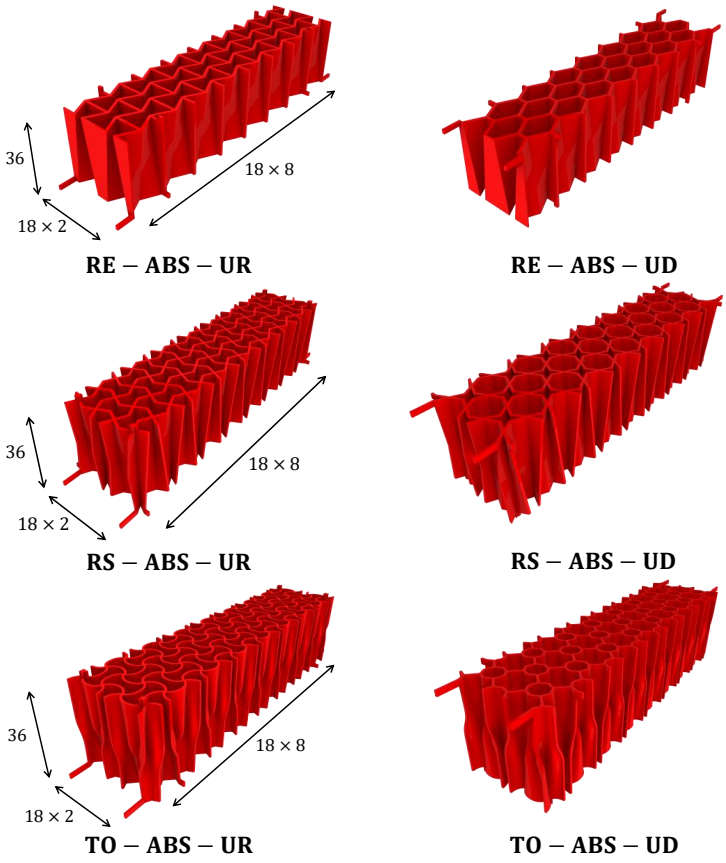

Figure 6.3: Tailored Poisson's Ratio-reinforcement (TPR) ABS 3D prints (unit: mm). Each design has two configurations: UpRight (UR) and Upside Down (UD).

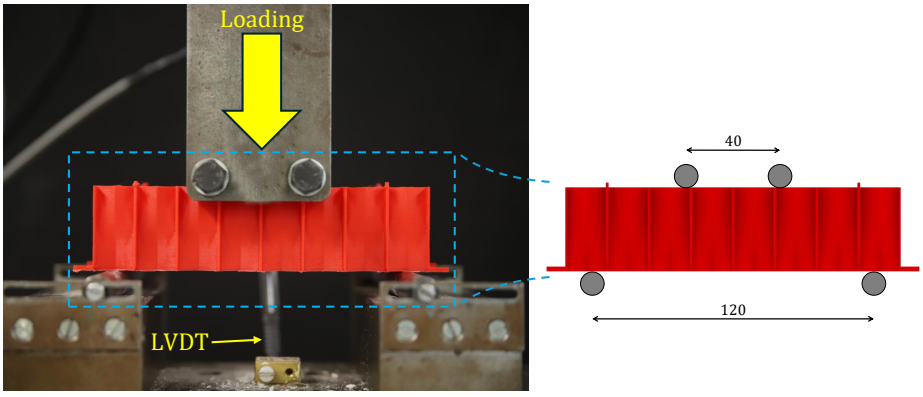

Figure 6.4: Experimental setup for TPR ABS specimens (unit: mm).

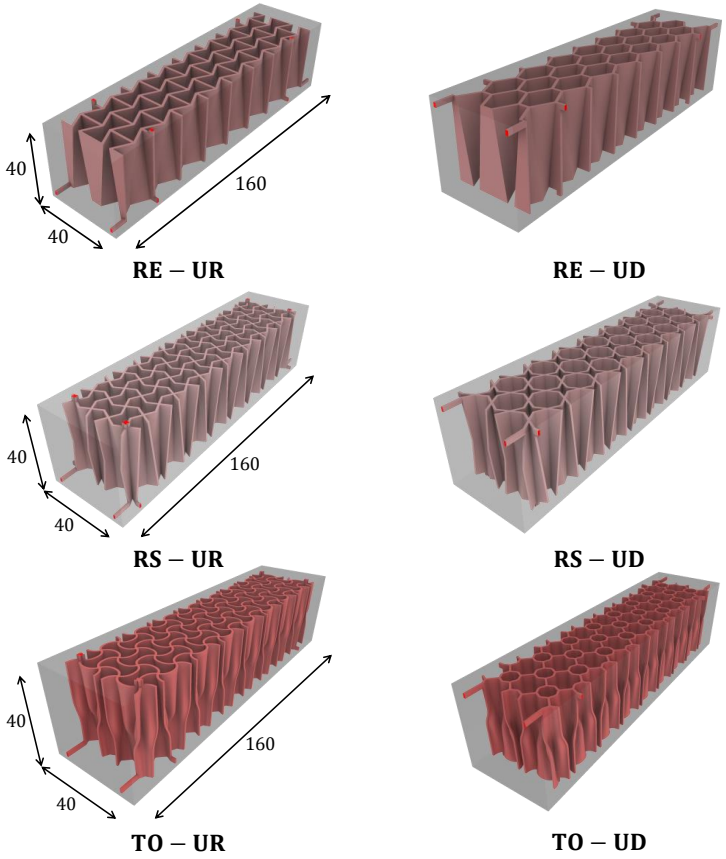

Figure 6.5: Tailored Poisson's Ratio-reinforcemed Cementitious Composite (TPRCC) specimens (unit: mm). Each design has two configurations: UpRight (UR) and Upside Down (UD).

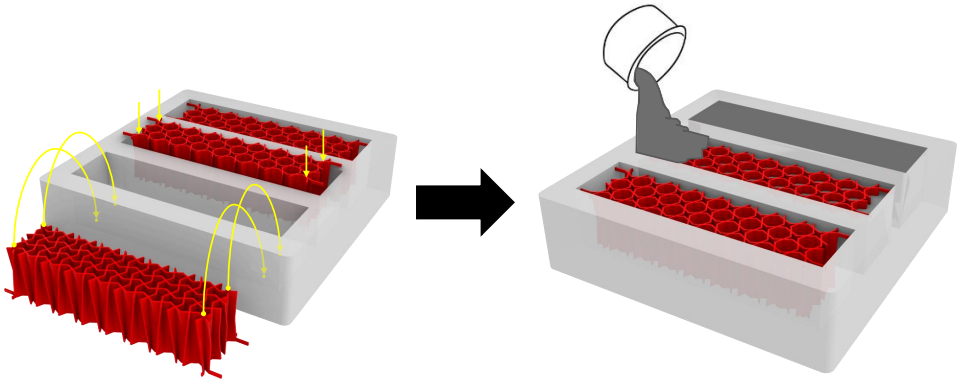

Figure 6.6: Specimen preparation and casting procedure.

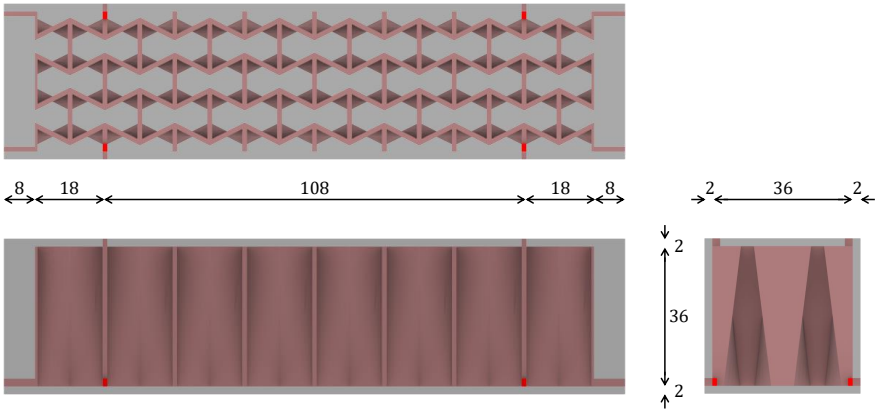

Figure 6.7: TPRCC specimen dimensions (unit: mm).

Table 6.2: Mixture design

Mixture components	**Quantities** (gL^{-1})
CEM I 42.5N	473
Fly ash	559
Sand (0.125-0.250 mm)	473
Water	413
Superplasticizer (Glenium 51)	2.0

The cementitious matrix consists of ordinary Portland cement (CEM I 42.5N) and fly ash as binders, silica sand (0.125-0.250 mm) as fine aggregate, and superplasticizer (Glenium 51) to tailor its rheology. The mix design, having water-to-binder and sand-to-binder ratios of 0.40 and 0.46, respectively, is provided in Table 6.2. The mixing process initiated by pre-mixing the dry ingredients for 2 min, followed by adding and mixing the water and superplasticizer for an additional 4 min. Once the cementitious matrix was cast into the moulds, these were put on a vibration table for 30 s. Demoulding of the TPRCC specimens took place after 48 h and these were moved to a curing room for 26 d (temperature 20 ± 2 °C, humidity 96 ± 2 %) to be tested after 28 d in total. The same matrix has been experimentally characterized at similar age in previous works [110, 201] and corresponds to a compressive strength of 24 MPa, flexural strength of 3.5 MPa and modulus of 10 105 MPa.

Analogous to the TPR ABS 3D prints, four-point bending tests of the six TPRCC layouts are used to compare the flexural behaviour and test the TPR's hypothesized lateral confinement mechanism given their varying Poisson's ratio and cross-section over the height (Figure 6.2). The UR configurations will show the effects of reinforcements having strain-tailored Poisson's ratios according to the bending stresses. UD configurations are

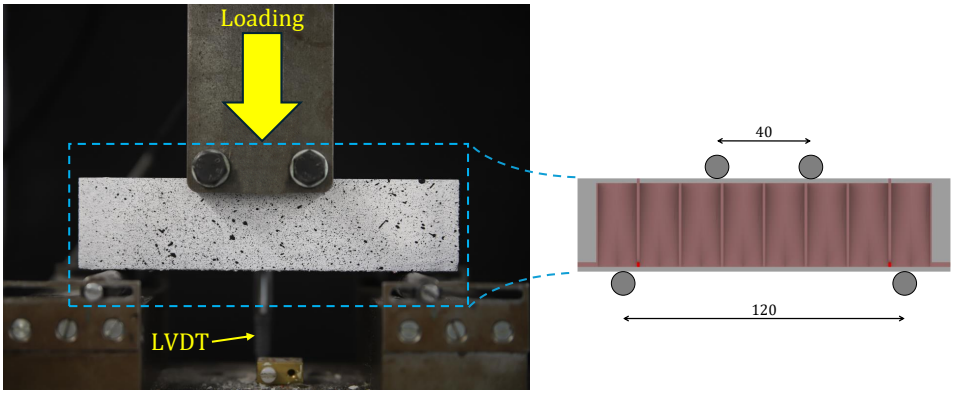

Figure 6.8: Experimental setup for TPRCC specimens (unit: mm).

expected to perform worse since these would cause lateral expansion, thereby deteriorating the composite's mechanical properties. Figure 6.8 depicts the same experimental setup, now loading a TPRCC specimen in bending at 0.02 mm s^{-1} using a LVDT to record the machine displacement.

Before testing, a side surface for each of the TPRCC specimens was covered with white paint and sprinkled with black dots for 2D Digital Image Correlation (DIC) analysis to study their exterior cracking patterns. A Canon EOS 6D Mark II digital camera was positioned 600 mm away from the specimen surface to acquire high-resolution images throughout the tests. The camera was equipped with a 75 mm focal length lens and operated at an aperture of $f/2.8$. Images were captured at a resolution of 6240 × 4160 pixels and analysed in the software ZEISS INSPECT Correlate. Moreover, since the hypothesized lateral contraction mechanism occurs inside the unit cells of the TPR, X-ray micro Computed Tomography (XCT) scans were made to visualize the internal state of damage in the TPRCC samples. During testing, all specimens were loaded until ultimate failure. One of each UR and UD configurations of the TPRCC designs were selected to be scanned by a TESCAN CoreTOM μ-CT scanner, operated at a tube voltage of 120 kV and a current of 125 mA. In view of the specimen's dimensions, a Region Of Interest (ROI) was considered at mid-span where the bending moment is maximum and constant (i.e., in between the two point loads). The sequentially acquired 4283 projections (number of slices) of the damaged samples were reconstructed using StudioMax software and visualized in Dragonfly software at a resolution of 15 μm.

6.3. RESULTS AND DISCUSSION

6.3.1. FLEXURAL BEHAVIOUR OF TPR

The load-displacement curves, deformation and fracture patterns of the six TPR layouts are displayed in Figure 6.9. All experiments show a high level of consistency among the tested samples, particularly in the linear-elastic regime. Only at larger displacements, more deviations in mechanical response occur.

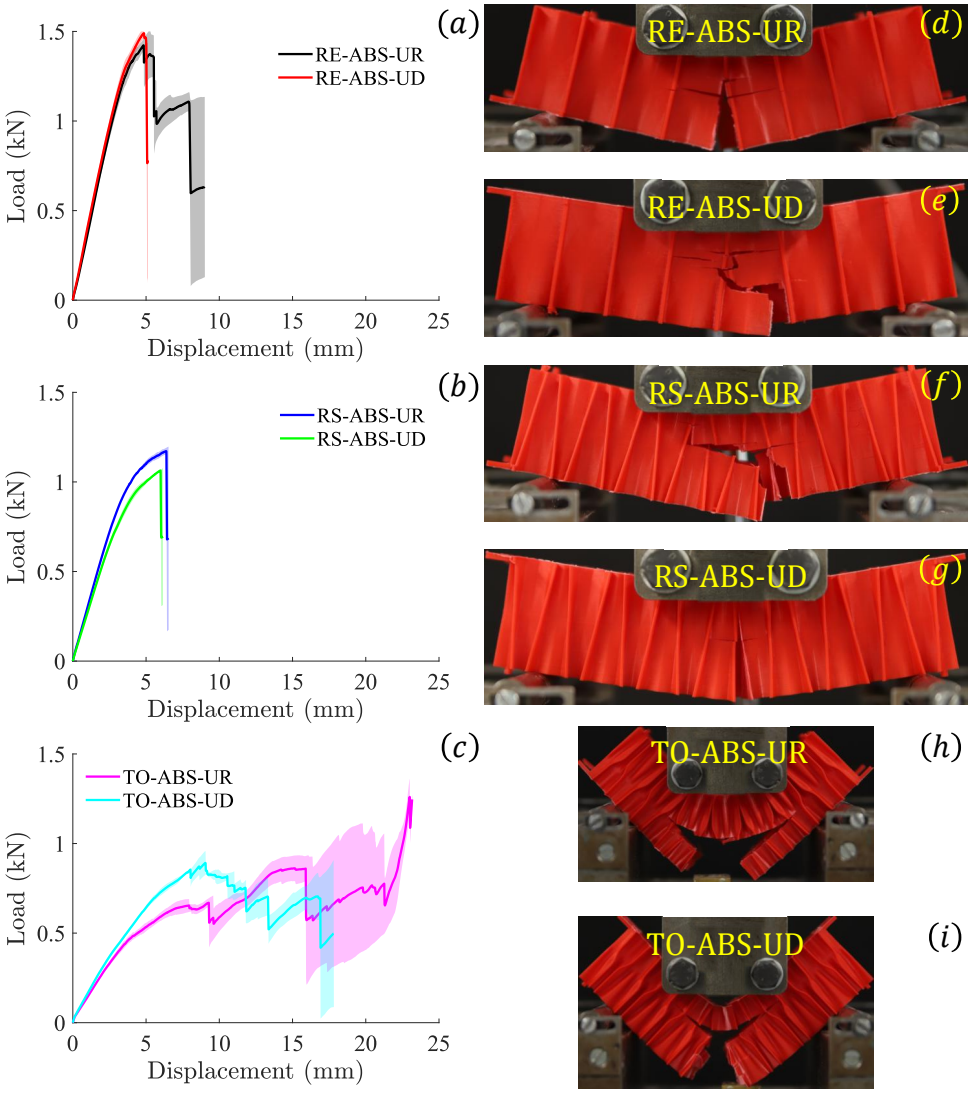

Figure 6.9: Flexural behaviour of TPR ABS 3D prints: (a-c) Load-displacement curves, (d-i) deformation and fracture patterns. Note: (d,f,h) UR, (e,g,i) UD. The shaded areas represent the variations across three parallel tested specimens, and the solid lines represent the average results.

Figures 6.9(a-c) show that the TPR ABS 3D prints exhibit comparable load capacities among UR and UD configurations, despite their differences in horizontal cross-sectional area over the height (see Figure 6.2). RE-ABS designs (Figure 6.9(a)) display the greatest peak load and stiffness, followed by RS-ABS (Figure 6.9(b)) and TO-ABS (Figure 6.9(c)) in decreasing order, see Figure 6.10(a). Error bars represent the standard deviation. Note that for TO-ABS-UR the first local maximum is considered as load capacity. When looking at Figure 6.2, it can be observed that the TPR load capacity and stiffness are

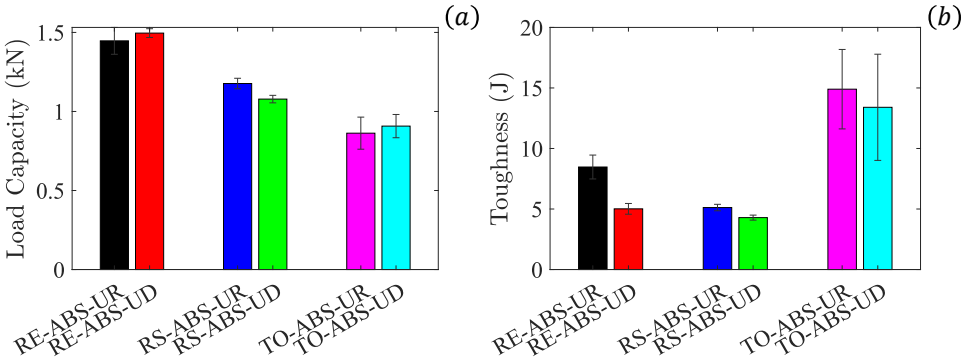

Figure 6.10: Flexural properties of TPR ABS 3D prints: (a) Load capacity, (b) toughness.

Table 6.3: Flexural properties of TPR ABS 3D prints

TPR ABS 3D print	**Load Capacity** (kN)	**Toughness** (J)
RE-ABS-UR	1.45 ± 0.09	8.47 ± 0.99
RE-ABS-UD	1.50 ± 0.03	5.01 ± 0.44
RS-ABS-UR	1.18 ± 0.03	5.12 ± 0.27
RS-ABS-UD	1.08 ± 0.02	4.29 ± 0.21
TO-ABS-UR	0.86 ± 0.10	14.9 ± 3.28
TO-ABS-UD	0.91 ± 0.07	13.4 ± 4.39

positively associated with their strut thickness. In terms of toughness, measured as the area underneath the load-displacement curve [6] until ultimate failure of the samples, TO-ABS significantly outperforms the others, with RS-ABS performing the worst (Figure 6.10(b)). A summary of flexural properties of TPR ABS 3D prints, including standard deviations, is provided in Table 6.3. Both Figure 6.10(a) and Table 6.3 exemplify a small variability in the observed load capacities of each TPR design with differences between the UR and UD configurations below the experimental scatter.

Remarkably, the TPR ABS 3D prints seem to only possess post-peak load-bearing capacity if the horizontal cross-sectional area increases with respect to its value at the bottom. Figure 6.11 plots the horizontal cross-sectional area over the height for all TPR design configurations, wherein it can be seen that only for RE-ABS-UR, TO-ABS-UR and TO-ABS-UD this is the case. This is evidenced by Figures 6.9(a) and 6.9(c).

Furthermore, Figures 6.9(d-i) display typical fracture patterns for all TPR ABS 3D prints: Cracking initiates vertically, up to the position where the unit cell geometry becomes rectangular, followed by horizontal delamination, caused by inter-layer failure as a result of the printing path-dependent anisotropy present in FDM 3D printed polymers as seen in Chapter 3. For RE-ABS and RS-ABS, the rectangular cross-section is located at the neutral axis (i.e., halfway up the beam where $\nu = 0$, see Figure 6.2). However, in TO-ABS this transition takes place at $\nu = 0.2$ as defined for the nine reference architectures by Clausen et al. [186]. This difference originates from the geometrically non-linear model by Sigmund and co-workers [203] used to derive the strain-independent architectures,

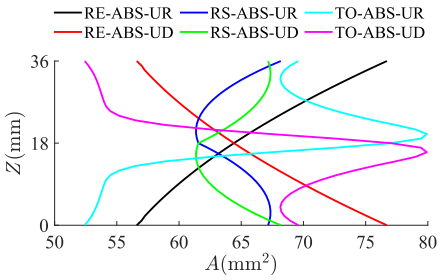

Figure 6.11: All TPR unit cell horizontal cross-sectional areas (A) over height (Z).

whereas RE and RS are based on linear designs. Hence, the horizontal crack is slightly shifted downwards for TO-ABS-UR (Figure 6.9(h)) whilst it occurs somewhat higher in TO-ABS-UD (Figure 6.9(i)).

The TPR load capacities can be related to the printing path-dependent anisotropy inherent to FDM 3D printed polymers in Chapter 3. Figure 6.12 shows bottom views of the tested TPR specimens. RE-ABS exhibited the highest load capacity (Figures 6.9(a) and 6.10(a)) and suffered from pure strut failure due to stress concentrations at its sharp corners (see Figures 6.12(a) and (d)). Therefore, failure occurred in the direction of the filament (i.e., the bead direction) which was the strongest in Chapter 3. RS-ABS yielded a lower load capacity (Figures 6.9(b) and 6.10(a)) and displayed a mixed failure mode. Similar to RE-ABS, RS-ABS mostly failed at its struts (again near the joints), but also showed some vertical delamination among neighbouring filaments (i.e., intra-layer failure), see Figures 6.12(b) and (e). Chapter 3 found that the latter is weaker compared to the bead direction, which explains the lower load capacity of RS-ABS. TO-ABS reached the lowest peak load (Figures 6.9(c) and 6.10(a)) and illustrated the same failure behaviour as RS-ABS. However, TO-ABS samples contained significantly more intra-layer delamination and less strut failure, probably because of their lack of sharp angles (see Figures 6.12(c) and (f)). This explains TO-ABS' lowest load capacity.

Finally, Figure 6.13 illustrates how the auxetic top chords of the RE-ABS-UR and TO-ABS-UR specimens undergo lateral contraction during loading. Through comparison of Figures 6.13(a) and (c) as well as Figures 6.13(b) and (d) for RE-ABS-UR and TO-ABS-UR, respectively, it can be clearly observed that the TPR designs exhibit more lateral contraction as a result of increasing compressive bending strains for larger vertical displacements.

Based on the four-point bending tests of the TPR layouts, the following flexural characteristics could be observed:

1. *Reinforcement load capacities are comparable among UR and UD configurations.* Despite their differences in horizontal cross-sectional area over the height, see Figure 6.2.

2. *Reinforcement load capacity and stiffness are positively associated with strut thickness.* RE has the largest strut thickness ($t = 1.2$ mm), load capacity and stiffness. RS ($t = 0.9$ mm) shows intermediate values for all of these properties. TO, having the smallest strut thickness ($t = 0.8$ mm), scores lowest when it comes to peak load and

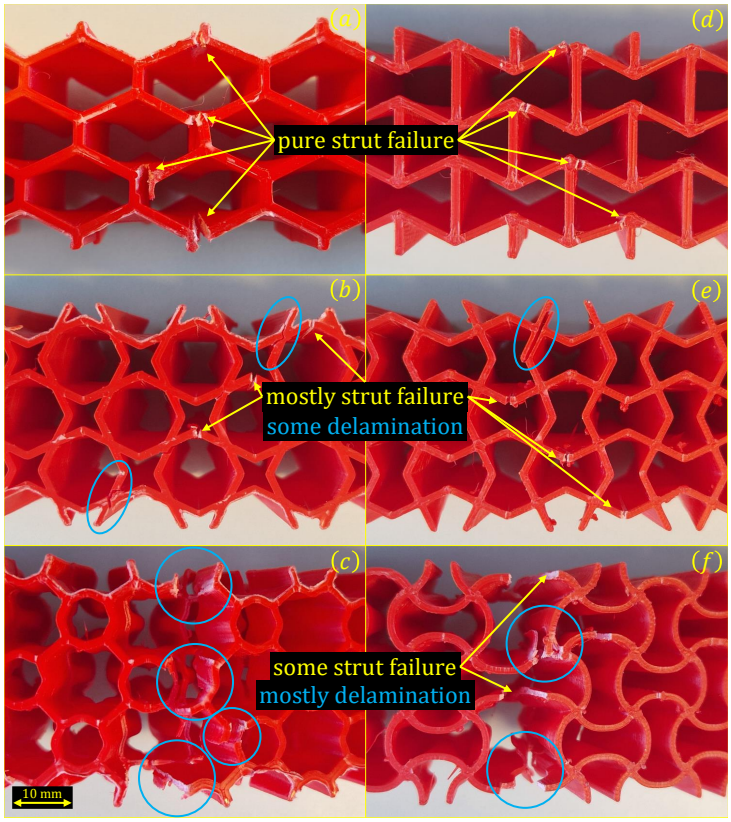

Figure 6.12: Failure modes of TPR ABS 3D prints: (a) RE-ABS-UR, (b) RS-ABS-UR, (c) TO-ABS-UR, (d) RE-ABS-UD, (e) RS-ABS-UD, (f) TO-ABS-UD. Note: (a-c) bottom views of UR configurations, (d-f) bottom views of UD configurations.

stiffness. From all the measured flexural properties, only toughness does not follow the aforementioned trend. This mechanical performance is mainly affected by the failure mode of the TPR designs.

3. *Reinforcement only has post-peak load-bearing capacity if the horizontal cross-sectional area increases with respect to its value at the bottom.* This is only the case for RE-ABS-UR, TO-ABS-UR and TO-ABS-UD as shown in Figures 6.9(a-c) and 6.11.

4. *Reinforcement load capacity can be related to failure mode.* RE-ABS specimens suffered from pure strut failure in the direction of the filament (i.e., the bead direction) which is the strongest print configuration, resulting in the highest load capacity. RS-ABS displayed a mixed failure mode of strut failure near joints and vertical delamination among neighbouring filaments (i.e., intra-layer failure). This yielded intermediate load capacity, because the intra-layer print configuration is weaker. TO-ABS mainly contained intra-layer delamination with minor strut failure, explaining its lowest load capacity.

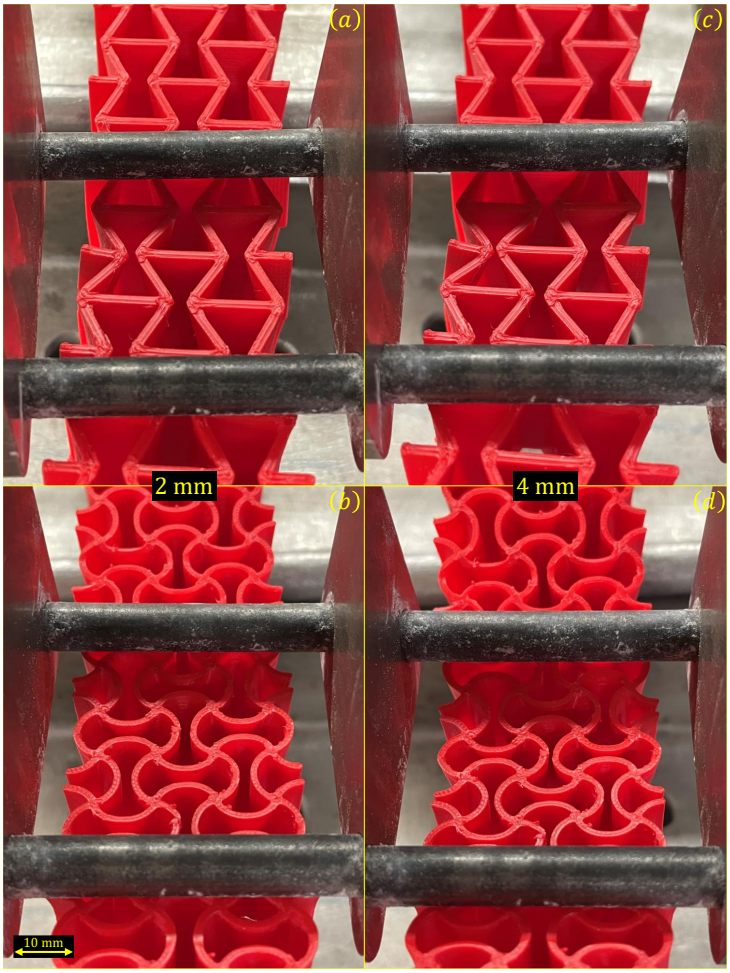

Figure 6.13: Lateral contraction of TPR ABS 3D prints: (a,c) top views of RE-ABS-UR, (b,d) top views of TO-ABS-UR. Note: (a,b) 2 mm vertical displacement, (c,d) 4 mm vertical displacement.

5. *3D printed reinforcements show printing path-enabled horizontal crack deflection.* The typical fracture pattern initiates vertically, up to the position where the unit cell geometry becomes rectangular, followed by horizontal delamination, caused by inter-layer failure as a result of the printing path-dependent anisotropy present in 3D printed polymers.

6.3.2. FLEXURAL BEHAVIOUR OF TPRCC

MECHANICAL PERFORMANCE

The load-displacement curves, deformation and fracture patterns of the six TPRCC layouts are shown in Figure 6.14. Similar to the flexural TPR tests, all TPRCC specimens behave strikingly consistent, also at substantially larger displacements.

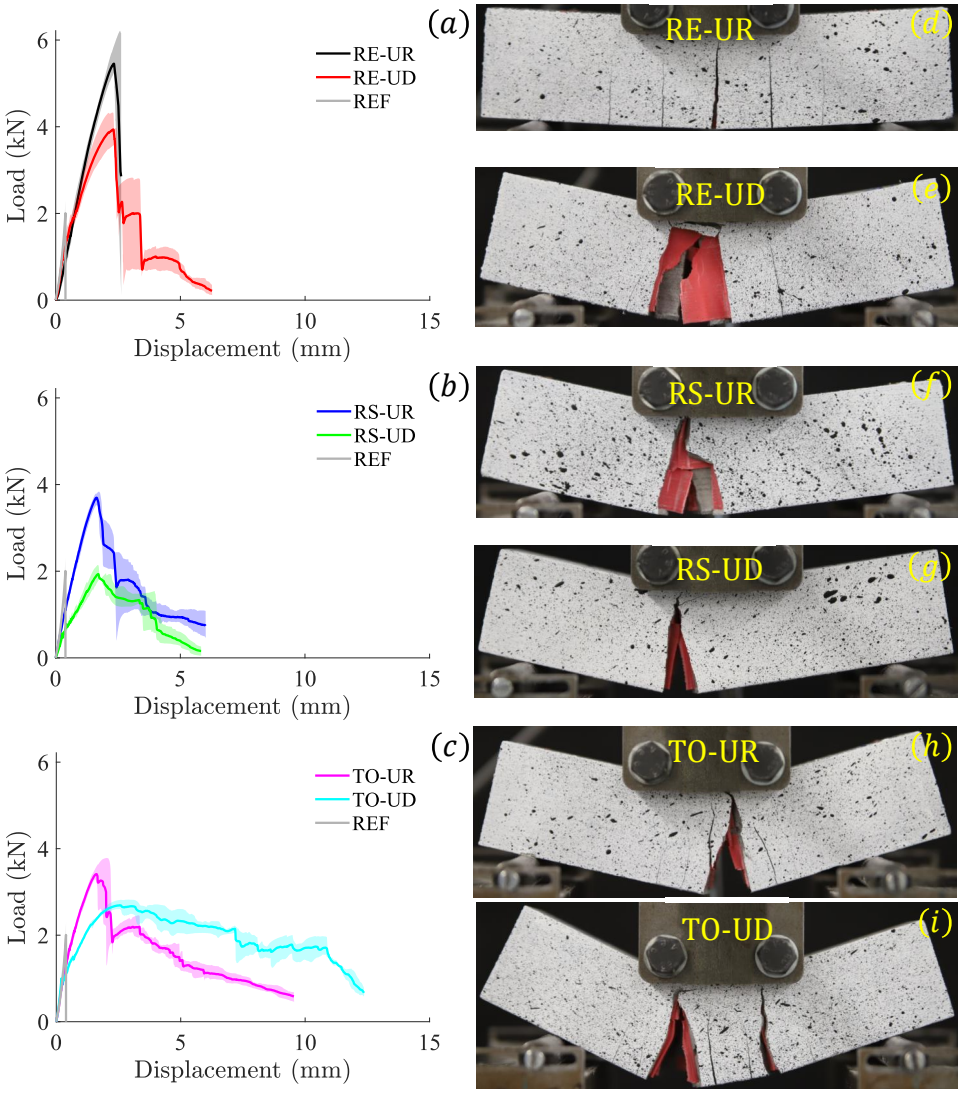

Figure 6.14: Flexural behaviour of TPRCC specimens: (a-c) Load-displacement curves, (d-i) deformation and fracture patterns. Note: (d,f,h) UR, (e,g,i) UD. The shaded areas represent the variations across three parallel tested specimens, and the solid lines represent the average results.

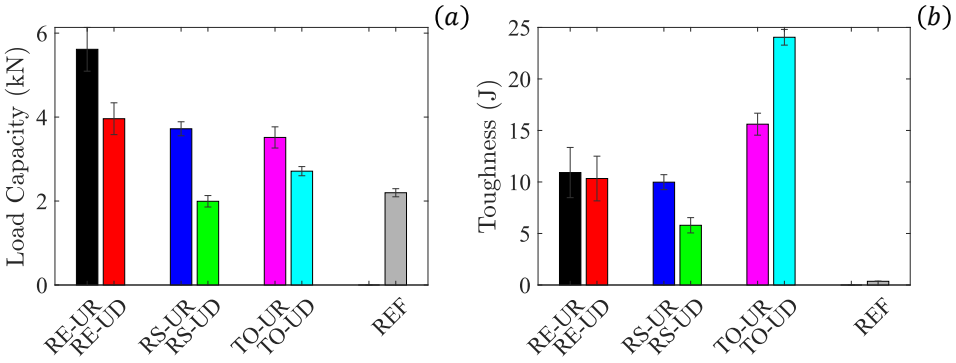

Figure 6.15: Flexural properties of TPRCC specimens: (a) Load capacity, (b) toughness.

Table 6.4: Flexural properties of TPRCC specimens

TPRCC specimens	**Load Capacity** (kN)	**Toughness** (J)
RE-UR	5.61 ± 0.52	10.91 ± 2.44
RE-UD	3.96 ± 0.38	10.33 ± 2.17
RS-UR	3.72 ± 0.17	9.98 ± 0.73
RS-UD	1.99 ± 0.14	5.80 ± 0.74
TO-UR	3.52 ± 0.25	15.61 ± 1.07
TO-UD	2.71 ± 0.11	24.05 ± 0.76
REF	2.20 ± 0.10	0.36 ± 0.01

Figures 6.14(a-c) illustrate that the TPRCC-UR specimens have significantly higher load capacities with respect to their UD counterparts. RE-UR (Figure 6.14(a)) exhibits load capacities of more than 6 kN, which is an improvement of 191 % with respect to the plain reference mortar (REF, see Figure 6.15(a)). RE-UD has a significantly lower load capacity, reaching only about 4 kN (Figures 6.14(a) and 6.15(a)), although their toughness values are very close (Figure 6.15(b)). RS-UR (Figure 6.14(b)) performs slightly less than RE-UD in both load capacity and toughness, as shown in Figures 6.15(a) and 6.15(b). Similarly, RS-UD (Figure 6.14(b)) yields a lower load capacity compared to RS-UR (see Figure 6.15(a)). TO-UR (Figure 6.14(c)) has a somewhat lower load capacity with respect to RS-UR (see Figure 6.15(a)), but gained more than 1.6 times the toughness (see Figure 6.15(b)). This is an increase of more than 4700 % with respect to the plain reference mortar (see Figure 6.15(b)). Following the same trend, Figures 6.14(c) and 6.15(a) show that the load capacity of TO-UD is lower than TO-UR. However, TO-UD displays toughness values of nearly 25 J, thereby drastically increasing the energy absorption capacity by 6900 % compared to the plain reference mortar (see Figure 6.15(b)). A summary of flexural properties of TPRCC specimens, including standard deviations, is provided in Table 6.4. Both Figure 6.15(a) and Table 6.4 exemplify a small variability in the observed load capacities of each TPRCC design with differences between the UR and UD configurations significantly above the experimental scatter.

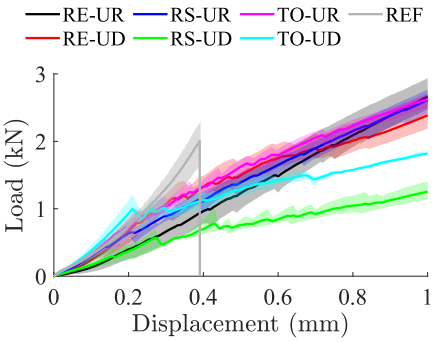

Figure 6.16: First mm of TPRCC load-displacement curves indicating multiple cracking. The shaded areas represent the variations across three parallel tested specimens, and the solid lines represent the average results.

Figures 6.14(d-i) also illustrate the TPRCC fracture patterns. Most specimens show a single major crack somewhere in the constant bending moment region, except for the TO-UD layout having consistently two main cracks below the points of load application (see Figure 6.14(i)). Nonetheless, all tested samples exhibit multiple cracking behaviour, indicating their ability to redistribute bending stresses. This can be seen by looking at the small load drops in the first mm of displacement plotted in Figure 6.16. RS has limited multiple cracking, followed by RE and TO in increasing order, directly correlated to their toughness values in Figure 6.15(b).

Analogous to TPR, the TPRCC load capacities can be related to the printing path-dependent anisotropy of the 3D printed reinforcement in a similar manner. Figure 6.17 shows bottom views of the tested TPRCC specimens, wherein RE (Figures 6.17(a) and 6.17(d)) again suffered from pure strut failure in the strongest printing direction measured in Chapter 3 reflecting the highest load capacity in Figure 6.14(a). However, RS and TO (Figures 6.17(b-c) and 6.17(e-f)) only showed vertical delamination between adjacent filaments (i.e., intra-layer failure), which is weaker according to Chapter 3 and thus produces relatively close load capacities (see Figure 6.15(a)). However, especially TO-UD (Figure 6.17(f)) displayed significantly more intra-layer delamination, relating to the astonishing high toughness in Figure 6.15(b). Hence, the printing path-dependent anisotropy of TPR seems to be the limiting factor in the developed TPRCC specimens.

Since the TPR ABS 3D prints exhibit comparable load capacities among UR and UD configurations (Figures 6.9(a-c) and 6.10(a)), the difference in TPRCC-UR and TPRCC-UD load capacities are consistent with the hypothesized lateral confinement mechanism present in UR, which is absent in UD. Figure 6.18(a) displays the principal stress state for plain reference mortar, without lateral confinement. In this scenario, the top chord would fail in uniaxial compression, see the left side of Figure 6.18(a), whilst the bottom chord would fail in uniaxial tension as plotted on the right side of Figure 6.18(a). However, as shown in Figure 6.18(b) for RE-UR, the auxetic re-entrant reinforcement in the top chord provides lateral confinement under compressive strain. Therefore, the failure state in the upper region of the cementitious matrix gets shifted from a more or less uniaxial compression towards a minor biaxial compression stress state, see the left side of Figure 6.18(b). As a result, the stress state is changed, leading to an extended loading path which

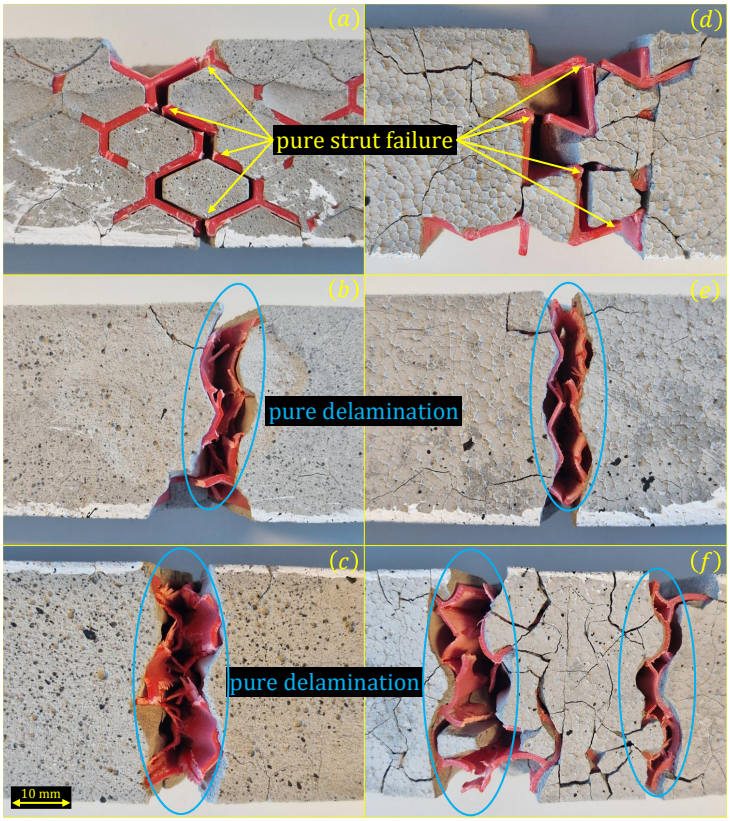

Figure 6.17: Tensile surface images of TPRCC specimens after failure: (a) RE-UR, (b) RS-UR, (c) TO-UR, (d) RE-UD, (e) RS-UD, (f) TO-UD. Note: (a-c) bottom views of UR configurations, (d-f) bottom views of UD configurations.

actively postpones failure of the surrounded cementitious matrix. On the other hand, the positive Poisson's ratio honeycomb arrangement at the bottom exerts lateral compressive stress when loaded in tension. Hence, the failure state in the lower part of the composite is transferred from a kind of uniaxial tensile stress state to a mixed mode in the direction of uniaxial compression as depicted on the right side of Figure 6.18(b). Again, changing the direction of loading yields a longer loading path that suspends failure. The driving factor behind the mechanism can be attributed to a mismatch in transverse strain between the cementitious matrix and the reinforcement that already occurs in the elastic regime (i.e., small strain) [184]. Similar to hoops in ordinary RC members, this causes arching confinement stresses as explained by Mander et al. [204]. In UD configurations, the exact opposite happens. The top chord of the reinforcement has a positive Poisson's ratio, resulting in lateral expansion under compressive strain, thereby pushing the failure state from uniaxial compression to a mixed mode in the direction of uniaxial tension. This shortens the loading path which increases the chance of matrix failure. In contrast, the bottom chord will be auxetic, providing lateral tensile stress when loaded in tension. As a consequence, the failure state is changed from uniaxial tensile towards a small

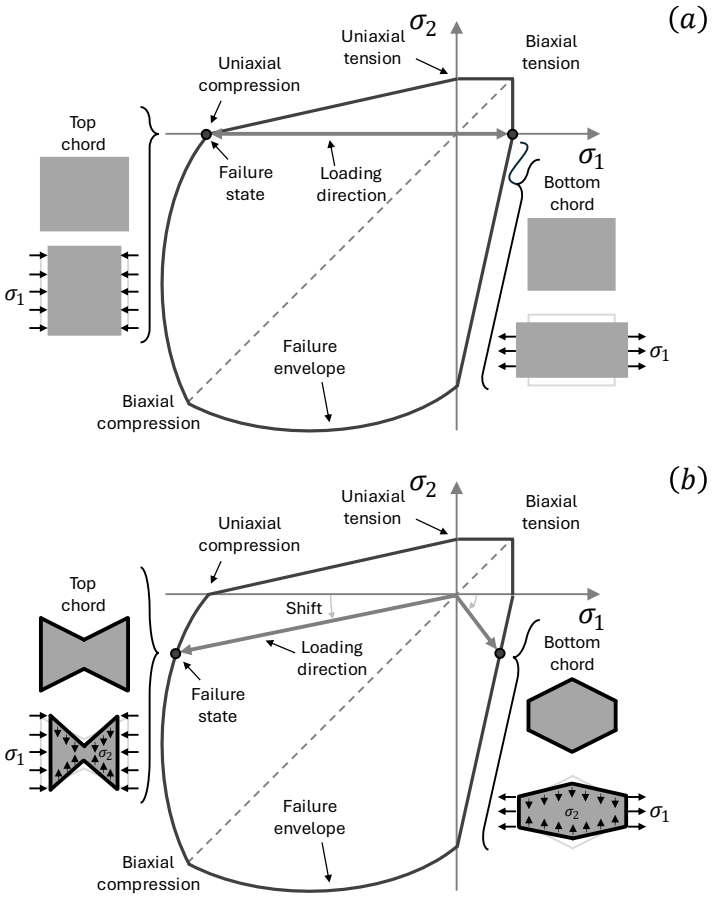

Figure 6.18: Schematic representation of failure envelope for (a) plain reference mortar, and (b) RE-UR layout illustrating a conceptual, hypothesized shift in the principal stress state, leading to an extended loading path in stress space, actively postponing failure of the surrounded matrix.

biaxial tensile stress state, thus decreasing the strength and accelerating failure of the cementitious matrix. Simulations in Chapter 7 will provide additional evidence of this hypothesized lateral confinement mechanism.

Figure 6.19(a) shows that RE-UR significantly outperforms its constituents (i.e., REF+TPR) in terms of load capacity. For most of the other TPRCC specimens the overachievement is less pronounced, but approximately the same. Only RS-UD and TO-UD fail to overcome the combined load capacity from the individual constituent materials. Nevertheless, all UR configurations exhibit load capacity improvements compared to the summation of plain reference mortar and TPR load capacities. Figure 6.19(b) illustrates that TO-UD yields toughness values that are unavailable from its separate components. Moreover, all TPRCC specimens exceed their contributor's joint toughness values.

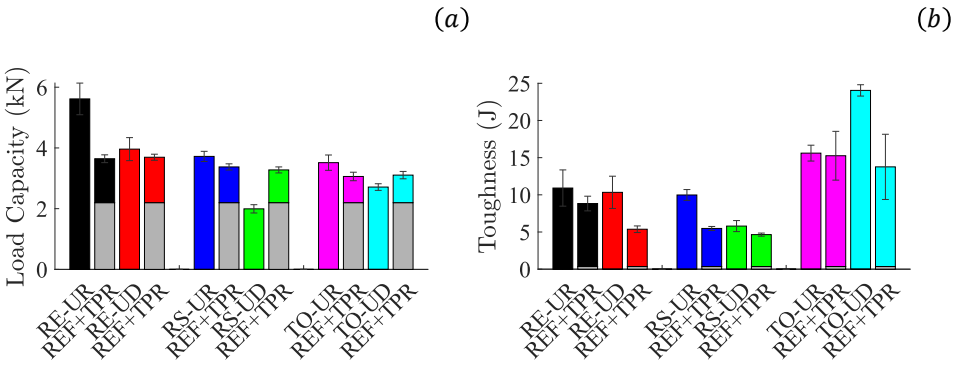

Figure 6.19: Stacked flexural properties of TPRCC specimens: (a) Load capacity, (b) toughness. Note: Bars represented by REF+TPR comprise the joint response of plain reference mortar (REF) and TPR without cementitious matrix. Flexural properties of TPR and TPRCC are taken from Figures 6.10 and 6.15.

Two properties used to compare the mechanical performance of the developed TPRCC specimens with literature are specific load capacity (δ in kN$\cdot$mm^3/kg) and specific toughness (β in kN$\cdot$mm^4/kg) as described by Barhemat et al. [6]. However, this is a comparison based on mass such that having a high volume of polymeric reinforcement inside cementitious composites will automatically yield higher specific properties. To illustrate the efficiency of the reinforcement methodologies, these values are normalized with respect to their volume fractions here:

$$\frac{\delta}{\rho} = \frac{S}{D}\frac{V}{V_\mathrm{r}}, \tag{6.1}$$

$$\frac{\beta}{\rho} = \frac{T}{D}\frac{V}{V_\mathrm{r}}, \tag{6.2}$$

where ρ is the reinforcement ratio, S the load capacity in kN, D the density of the composite in kgmm^{-3}, V the volume of the composite in mm^3, V_r the volume of the reinforcement in mm^3, and T the toughness in J. Table 6.5 contains flexural data from various researchers as provided by Barhemat et al. [6], thereby only focusing on cementitious composites reinforced with polymeric reinforcement (i.e., APCC). All respective reinforcement ratios are provided accordingly. Nonetheless, different matrices, geometries and test setups may be used in the literature, such that the comparison presented here is indicative rather than definitive. The CES plot in Figure 6.20(a) shows the specific load capacity versus specific toughness for comparison, whilst Figure 6.20(b) displays the same graph with all values normalized with respect to their volume fractions.

As depicted in Figure 6.20(a), the APCC by Barhemat et al. [6] reaches a substantially high combination of specific load capacity and toughness, leaving all others far behind. Nonetheless, their design has a reinforcement ratio of about 80.7 %. When looking at the efficiency of the reinforcement strategy by normalizing these values with respect to the volume fraction (Figure6.20(b)), one can see that APCC [6] still showed a higher specific load capacity, but delivered a similar specific toughness compared to APCC [198] (ρ = 33.7 %) and RS-UD in this research (ρ = 14.6 %), despite a significantly higher reinforcement fraction.

Table 6.5: Comparison between developed TPRCC specimens and literature (adopted from [6]).

Reference	δ (10^6 kN·mm^3/kg)	β (10^6 kN·mm^4/kg)	ρ	δ/ρ	β/ρ
RE-UR	3.80	7.76	0.147	25.9	52.8
RE-UD	2.70	7.72	0.147	18.4	52.5
RS-UR	2.37	6.48	0.146	16.2	44.4
RS-UD	1.32	4.10	0.146	9.04	28.1
TO-UR	2.25	9.99	0.146	15.4	68.4
TO-UD	1.74	15.1	0.146	11.9	103.4
APCC [139]	0.03	6.08	0.092	0.33	66.1
APCC [6]	9.04	22.0	0.807	11.2	27.3
APCC [198]	8.38	7.93	0.337	24.9	23.5
APCC [205]	6.87	5.15	0.305	22.5	16.9
APCC [206]	0.36	1.62	0.069	5.22	23.5

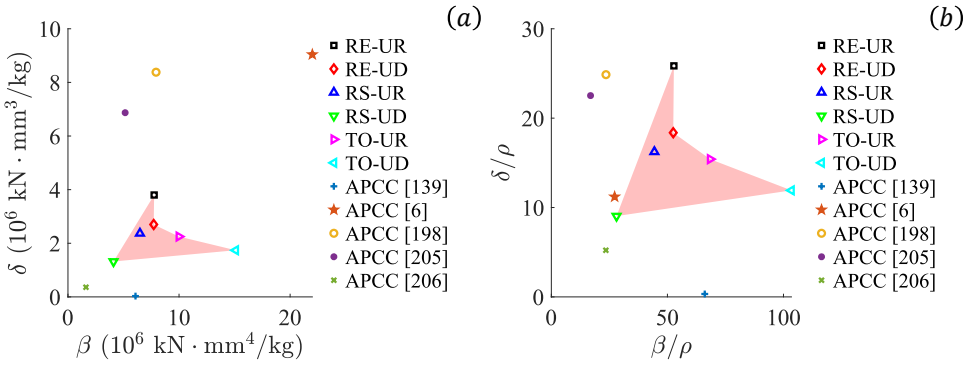

Figure 6.20: Comparison of (a) specific load capacity (δ) and specific toughness (β), and (b) normalized with respect to reinforcement ratios (ρ) between developed TPRCC specimens and literature (adopted from [6]). The shaded area highlights the TPRCC specimens developed in this work.

Figure 6.20(b) clearly shows that the developed TPRCC specimens are more efficient in terms of both load capacity and toughness. The TPR used in RE-UR turns out to be the most effective for load capacity, outperforming all other APCCs including those having significantly higher reinforcement ratios (i.e., 0.807, 0.337 and 0.305 versus 0.147 in [6], [198] and [205] versus RE-UR, respectively, see Table 6.5). The TPR in TO layouts illustrate to be significantly more profitable for toughness, particularly TO-UD. Furthermore, Figure 6.20(b) visualizes the trade-off between load capacity (e.g., RE-UR) and toughness (e.g., TO-UD), almost representing a Pareto front.

DIC analysis results for all TPRCC specimens are presented in Figure 6.21. The images illustrate the cracking patterns prior to reaching peak load, with the coloured regions indicating localized horizontal strain. All layouts exhibited multiple cracking behaviour, although the specific crack patterns vary slightly. The RE-UR layout showed distinct, parallel cracks with uniform spacing (see Figure 6.21(a)) which are likely reflections of the straight, vertical unit cell endings located right behind the longitudinal side surface as shown in Figure 6.5. All other specimens displayed a denser arrangement of unevenly

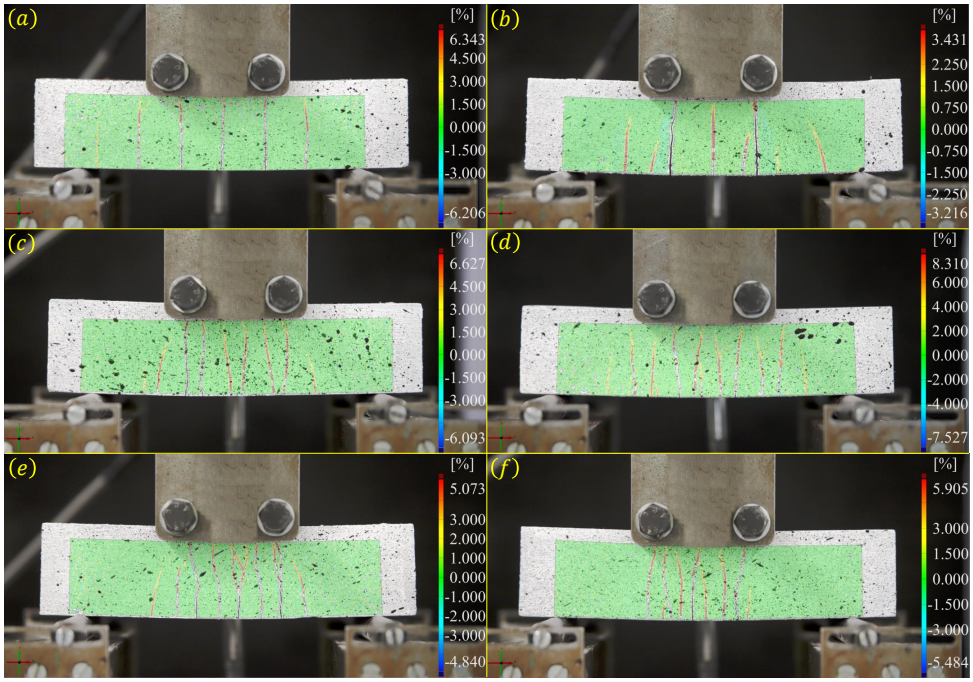

Figure 6.21: DIC analysis images of TPRCC specimens before reaching peak load: (a) RE-UR, (b) RE-UD, (c) RS-UR, (d) RS-UD, (e) TO-UR, (f) TO-UD. coloured regions indicate fine cracks or areas with concentrated horizontal strain.

spaced cracks in the bent region. Among them, TO-UR (Figure 6.21(e)) exhibited pronounced crack branching and deflection, primarily occurring near the height of the neutral axis. Although the cracking pattern of different layouts exhibit certain variations, the observed surface cracks are largely governed by the cracking and spalling behaviour of the outer mortar protective layer, which is approximately 2 mm thick. As a result, these surface features may not accurately represent the progression of internal damage within the composite. Therefore, the following section presents CT scanning results to identify key internal damage mechanisms and provide further insights into the behaviour of TPRCC.

Based on the four-point bending tests of the TPRCC specimens, the following flexural characteristics could be observed:

1. *Composite stiffness is barely impaired.* Compared to the plain reference mortar, the initial stiffness of most TPRCC configurations is not much affected by the significantly softer polymeric reinforcement phase. Moreover, the gradual increase in stiffness (and load capacity) occurs along the same trend as shown in Figure 6.16.

2. *Multiple cracking achieved.* All tested samples exhibit multiple cracking behaviour, indicating their ability to redistribute bending stresses. This is evidenced by the small load drops in Figure 6.16. RS has the least multiple cracking, which is directly related to toughness. RE shows increased multiple cracking and toughness. TO

displays the most considerable amount of multiple cracks whilst maintaining a significantly higher toughness.

3. *The majority of composites outperform reference mortar.* All TPRCC specimens outperform the reference mortar in terms of load capacity, except for RS-UD reaching about the same value of 2 kN. Furthermore, all TPRCC layouts reach substantially larger toughness values than plain mortar.

4. *TPRCC-UR outperforms TPRCC-UD in load capacity for all reinforcement specimens.* The TPRCC-UR layouts have significantly higher load capacities with respect to their UD counterparts. Since the TPR ABS 3D prints exhibit comparable load capacities among UR and UD configurations, the difference in TPRCC-UR and TPRCC-UD load capacities are consistent with the hypothesized lateral confinement mechanism present in UR, which is absent in UD. TPRCC-UR specimens reach 73.8 %, 104.1 % and 45.2 % greater load capacities compared to UD configurations for RE, RS and TO, respectively.

5. *TO design shows exceptional toughness.* Especially TO-UD, which exhibits an increase in toughness of 6900 % with respect to the plain reference mortar. This relates to its consistent fracture pattern having two major cracks and the significant amount of intra-layer delamination observed in the 3D printed reinforcement.

6. *TPRCC yields significant improvements with respect to plain reference mortar.* Load capacity ratios yield improvements of 2.91, 1.80, 1.77 and 1.32 compared to the reference mortar for RE-UR, RS-UR, TO-UR and TO-UD, respectively. Similarly, toughness ratios display 35.41, 29.94, 48.07 and 70.00, respectively.

7. *TPRCC shows exceptional specific performance compared to literature.* The efficiency of the reinforcement methodologies is measured with respect to their volume factions. Based on reinforcement ratio, the TPRCC specimens developed in this work are more efficient in terms of both load capacity and toughness as shown in Figure 6.20(b).

8. *Synergy between reinforcement and mortar.* Seeing that most flexural (auxetic) reinforcement applications in literature are compromising load capacity for considerable ductility at large deformations (i.e., in the Ultimate Limit State (ULS)), the focus was on achieving synergistic composite action without clearly visible constituent separation at the Serviceability Limit State (SLS) for practical applications. This is evidenced by the continuous ascending curves before reaching the maximum load for all TPRCC specimens in Figure 6.14.

CT SCANNING

The internal damage mechanisms of the composites were investigated via μ-CT scanning, as shown in the reconstructed images of the ROIs in Figure 6.22 and Figure 6.23. Top-view slices were extracted from heights corresponding to one-quarter (purple), one-half (green), and three-quarters (blue) of the specimen, while front-view slices (yellow) were taken along the central symmetry axis of the unit cell.

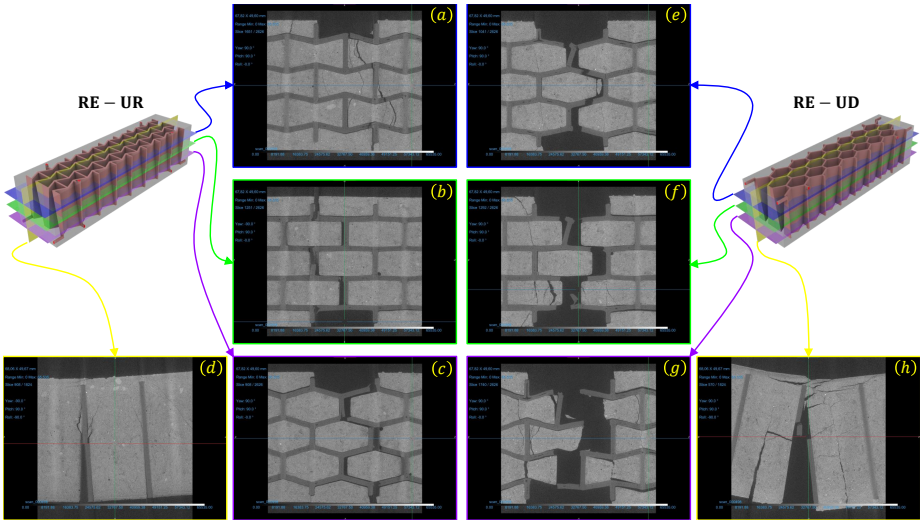

Figure 6.22: Reconstructed μ-CT images of TPRCC: (a-d) RE-UR, and (e-h) RE-UD.

A comparison of the damage patterns in RE-UR and RE-UD at one-quarter height (Figures 6.22(c) and 6.22(g)) reveals that in both cases, the TPR struts fractured. However, RE-UD exhibits more severe internal damage in the mortar matrix, with crack concentration observed particularly at the TPR corners. This phenomenon is attributed to the lateral expansion induced by the negative Poisson's ratio behaviour of the RE unit under tension. Such expansion intensifies at the corners, leading to stress concentration and consequent matrix cracking. In contrast, the mortar within the RE-UR cell remains largely intact, with no apparent macro-cracks. Debonding is limited to some TPR–mortar interfaces, likely caused by the minor contraction of the positive Poisson's ratio part under tension and the low bond strength between FDM 3D printed ABS and cementitious matrix as found in Chapter 4. Nevertheless, this lateral contraction introduces confining effects on the mortar, keeping it within the elastic range and subjecting it to a multi-axial tensile-compressive state (as shown in Figure 6.18), which enhances the load-bearing capacity without inducing substantial plastic damage. At mid-height (Figures 6.22(b) and 6.22(f)), RE-UD again demonstrates more pronounced mortar deterioration than RE-UR. This can be caused by the upward propagation of tensile cracks originating from the bottom, lacking constraint from the surrounding lattices.

Near the top of the specimen, mortar failure in RE-UD (Figure 6.22(e)) diminishes, whereas RE-UR (Figure 6.22(a)) begins to exhibit damage within the mortar. This trend can be understood in light of the evolving stress distribution during four-point bending. As the main crack propagates upward, the effective height of the beam decreases, causing the neutral axis to shift upward. Consequently, the auxetic region in RE-UR transitions from a purely compressive zone to a mixed-mode region with tension at the bottom and compression at the top. This induces lateral expansion in the lower tensile region, resulting in a damage morphology comparable to that observed in the lower part of RE-UD in Figure 6.22(g). The failure patterns in both cases reflect the influence of the auxetic deformation mechanism.

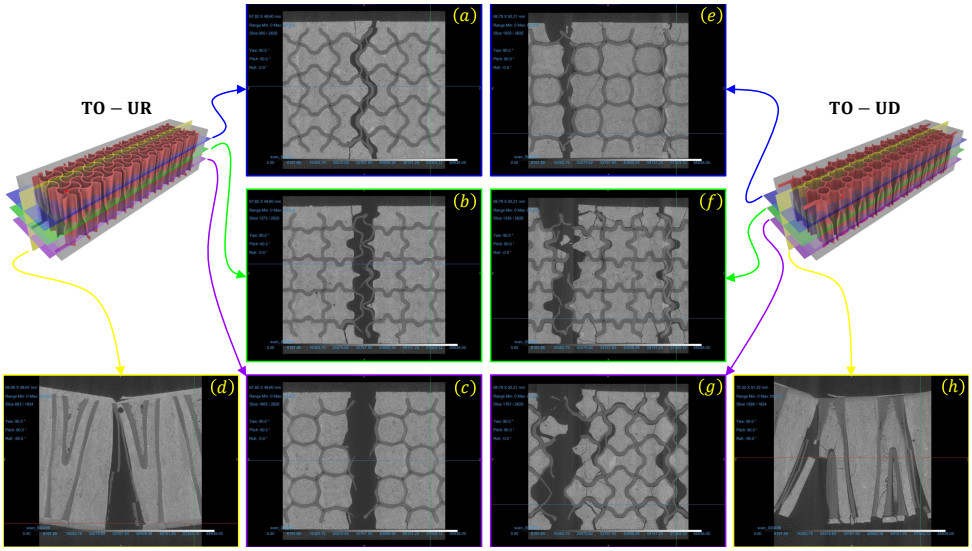

Figure 6.23: Reconstructed μ-CT images of TPRCC: (a-d) TO-UR, and (e-h) TO-UD.

The front-view slices further elucidate the contrasting damage evolution between RE-UR and RE-UD. In RE-UR (Figure 6.22(d)), the TPR element undergoes noticeable fracture and lateral displacement near the neutral axis, with mortar cracking primarily initiating above the axis and propagating upward. Below the axis, the mortar remains virtually undamaged. This localization of failure in the negative Poisson's ratio zone aligns with earlier observations. Conversely, RE-UD (Figure 6.22(h)) shows widespread cracking throughout the cementitious matrix along the specimen height. These μ-CT scanning analyses confirm that RE-UR more effectively confines internal damage compared to RE-UD, significantly mitigating matrix cracking and enhancing composite performance.

A similar failure mechanism is also observed in the TO group, as depicted in Figure 6.23. While the dominant failure modes of TPRs differ, i.e., strut fracture in RE versus delamination in TO, the underlying TPR deformation behaviour and its role in mitigating matrix damage are consistent. Notably, the matrix in Figure 6.23(a) shows less severe damage, potentially due to the fact that delamination of the ABS 3D printed reinforcement takes less force than the strut failure observed in Figure 6.22(a).

6.4. CONCLUSIONS

In this study, the hypothesis is tested that Tailored Poisson's Ratio-reinforcement (TPR) causes a shift in the principal stress state of the cementitious matrix, leading to an extended loading path in stress space, thereby actively postponing failure. Three Tailored Poisson's Ratio-reinforced Cementitious Composite (TPRCC) designs are developed and tested, leading to the following conclusions:

1. *Reinforcement*: 3D-printed reinforcements with a prescribed gradient in Poisson's ratio suitable for flexural applications have been successfully designed and tested in bending. The resulting TPR 3D prints exhibit similar load capacities among

UpRight (UR) and Upside Down (UD) configurations, despite their differences in horizontal cross-sectional area over the height. TPR load capacity and stiffness are positively associated with their strut thickness. In terms of toughness, TO significantly outperforms the others. The TPR load capacities can be related to the printing path-dependent anisotropy inherent to 3D printed polymers: Pure strut failure near stress concentrations exhibited the highest load capacity, whilst intra-layer delamination provided the lowest load-bearing capacity. Mixed failure modes provided intermediate values.

2. *Composite*: The hypothesized lateral confinement mechanism and its impact on load capacity and toughness have been evaluated in UR and UD configurations. TPRCC-UR layouts have significantly higher load capacities compared to their UD counterparts, yielding improvements of up to 191 % with respect to plain reference mortar. Since the TPR 3D prints exhibit comparable load capacities among UR and UD configurations, the difference in TPRCC-UR and TPRCC-UD load capacities are consistent with the hypothesized lateral confinement mechanism present in UR, which is absent in UD. This strongly supports the hypothesis that TPR causes a shift in the principal stress state, leading to an extended loading path in stress space, actively postponing failure of the surrounded matrix. The TPRCC-UR bottom chords contain reinforcement with a positive Poisson's ratio which contracts laterally when loaded in tension, thereby providing lateral confinement to the surrounded mortar. However, lateral confinement remains a hypothesized mechanism because it is not directly quantified in this study. Confirmation requires simulations enabling full 3D stress analyses. Moreover, increases in energy absorption capacity of 6900 % compared to plain reference mortar are recorded. All tested samples exhibited multiple cracking behaviour, indicating their ability to redistribute bending stresses. Similarly, the TPRCC load capacities can be related to the printing path-dependent anisotropy of the 3D printed reinforcement: Pure strut failure reflected the highest load capacity and is related to bead failure (the strongest anisotropic direction in the 3D-printed material), whilst vertical delamination related to intra-layer failure (caused by the printing path-dependent anisotropy of the reinforcement) is weaker. Nonetheless, the latter failure mode can be related to the astonishing gain in toughness for some of the TPRCC designs, albeit that the 3D printed reinforcement seems to be the limiting factor.

3. *Efficiency*: All TPRCC-UR configurations exhibit load capacity improvements compared to the summation of plain reference mortar and TPR load capacities. Moreover, all TPRCC specimens exceed their contributor's joint toughness values. Based on reinforcement ratio, the TPRCC designs developed in this work are more efficient in terms of both load capacity and toughness compared to other cementitious composites reinforced with polymeric reinforcement (i.e., APCC) in the literature. The TPR used in RE-UR turns out to be the most effective for load capacity, whilst the TPR in TO layouts illustrate to be significantly more profitable for toughness, particularly TO-UD. However, there remains a trade-off between load capacity and toughness.

4. *Fracture*: μ-CT scanning confirms that TPRCC-UR more effectively mitigates internal damage compared to TPRCC-UD. In TPRCC-UD, mortar cracking is distributed throughout the specimen height, with the most severe damage occurring in the lower tensile zone due to lack of lateral confinement. In contrast, the lattices with a positive Poisson's ratio in the tensile zone of TPRCC-UR induce lateral contraction, effectively confining the mortar below the neutral axis and preventing significant damage. Minor matrix cracking is observed only in the upper region of the specimen, which can be attributed to the progressive upward shift of the neutral axis during loading. As a result, the auxetic lattices in TPRCC-UR begin to carry redistributed tensile stress, leading to lateral expansion and localized matrix damage in this region.

5. *Synergy*: All TPRCC designs developed in this work achieve synergistic composite action without clearly visible constituent separation at small deformations (i.e., Serviceability Limit State (SLS)). Further, the composite action already comes into play before significant matrix damage has occurred: All load displacement curves exhibit a continuous ascend until one distinct peak is reached, and only after that fracture progresses.

6. *Potential*: TPRCC designs provide great potential for upscaling to practical applications. Based on the literature, polymeric reinforcements are favourable because of their low mass and high corrosion resistance, as well as the ability to apply 3D printing at larger scales. The latter is also true for metallic reinforcements. Further, the TPR 3D prints developed here are tailored according to the bending stress-strain distribution in beams, which is a common scenario in real-world load cases, making them financially viable. Finally, the synergistic composite action already present at small deformations enables its usability in cases where excessive deformations and crack widths need to be limited to prevent loss of the structure's durability (i.e., SLS).

7. *Limitations*: Given the exploratory nature of this chapter, several limitations must be acknowledged. For instance, the sample size per configuration is relatively small: Two for each TPR and three for each TPRCC. Larger number of specimens will allow for formal statistical analyses to substantiate and enhance the robustness of conclusions. Moreover, the focus was on a single matrix type and a single filament material (Acrylonitrile Butadiene Styrene ((ABS)), which may limit generalization. It should also be noted that the Poisson's ratio distributions in the TPR 3D prints rely on analytical and topology optimized unit cell models, without direct experimental measurements. Further, lateral confinement remains a hypothesized mechanism because it is not directly quantified in this study. Simulations in Chapter 7 will provide full 3D stress analyses. Finally, scale effects, structural boundary conditions (e.g., in real beams or slabs) and durability assessments are not covered and require future studies.

7

REVEALING FLEXURAL LATERAL CONFINEMENT MECHANISMS

The developed printing path-dependent Lattice Beam Model (LBM) is applied to numerically examine particularly intricate forms of Fused Deposition Modelling (FDM) 3D-printed reinforcement for cementitious composites under bending conditions. These reinforcements feature a Poisson's ratio engineered to align with the stress-strain distribution, resulting in cross-sections that vary along the height of the beams. The Tailored Poisson's Ratio-reinforcement (TPR) designs are simulated with consideration of printing path-dependent anisotropy arising from the FDM 3D printing process. Building on this, simulations of these reinforcements embedded in mortar to create Tailored Poisson's Ratio-reinforced Cementitious Composite (TPRCC) configurations are presented and discussed. Internal stress analysis of the TPRCC simulations reveal the hypothesized internal lateral confinement mechanisms induced by the TPR, and internal fracture analysis shows improved internal matrix damage mitigation if the Poisson's ratio distribution corresponds to the bending stresses. The significance of considering anisotropy induced by 3D printing is illustrated through additional simulations provided isotropic TPR properties corresponding to the bulk material, which indicate overestimation in strength, as well as entirely different cracking patterns, larger lateral stress concentrations near the peak loads, and significantly more dispersed matrix cracking.

With the exception of minor textual adjustments, this chapter is reproduced from: R.J.M. Bol, W. Zhou, Z. Meng, E. Schlangen, B. Šavija, *Revealing lateral confinements mechanisms in tailored Poisson's ratio-reinforced cementitious composites using lattice models*, Under Consideration.

7.1. INTRODUCTION

In Chapter 6, Tailored Poisson's Ratio-reinforcements (TPR) were proposed, characterised by a linear gradient of Poisson's ratios along the height of the reinforcement to accommodate varying stress profiles within beams subjected to bending (see Figure 7.1). Specifically, the top chords of the TPR designs exhibit negative Poisson's ratios (auxetic behaviour), undergoing lateral contraction under compression and providing confinement to the surrounded matrix. Conversely, the bottom chords possess positive Poisson's ratios, contributing to lateral contraction under tension. These lateral deformations cause a shift in the principal stress state of the confined matrix, extending the loading path in stress space and actively delaying failure in the 'Strong + confined' case in Figure 7.1, which ultimately fails due to rupture of the 3D-printed reinforcement. In the 'Ductile' case in Figure 7.1, however, the key failure mechanisms are related to the printing path-dependent anisotropy of the 3D-printed reinforcement: The TPR typically exhibits a combination of pure strut failure and delamination of the extruded filaments, governed by different directional-dependent strengths as established in Chapter 3. The 'Brittle' case in Figure 7.1 reflects plain mortar, which fails by one tension-induced crack propagating from the bottom to the top of the beam.

Three novel Tailored Poisson's Ratio-reinforced Cementitious Composite (TPRCC) designs were developed and tested under four-point bending in Chapter 6. Experimental results demonstrated remarkable improvements over unreinforced mortar, increases in load capacity and toughness of up to 191 % and 6900 %, respectively. The experimental programme in Chapter 6 included XCT imaging to characterize fracture patterns and damage evolution within the composites, revealing the reinforcement-matrix interaction mechanisms at different loading stages and confirming that the gradient Poisson's ratio concept effectively redirects and distributes cracking throughout the composite volume, in contrast to the localised failure typically observed in plain mortar or composites with uniform-property reinforcements. These results establish a compelling experimental basis but leave open the question of how accurately numerical models can reproduce the observed behaviour, particularly given the anisotropic nature of the FDM-manufactured reinforcements.

The present chapter extends and substantially elaborates lattice modelling of TPRCCs to support the lateral confinement hypothesis posted in Chapter 6. Therefore, LBM simulations are used to perform internal stress and fracture analysis. The stress states in the cementitious matrix phase at the bottom chords of the TPRCC specimens are visualized to prove the presence of lateral contraction before reinforcement failure, and experimental XCT images are compared to numerical crack widths for validation. Specifically, the printing path-dependent LBM methodology developed in Chapter 3 is now applied comprehensively to model the two best performing TPR designs characterised experimentally in Chapter 6, with intra-layer and inter-layer interface properties assigned on the basis of experimentally obtained interface data. Subsequently, full lattice simulations of the two best performing TPRCC configurations, comprising the TPR reinforcements embedded within the cementitious matrix, are presented and discussed, enabling a direct comparison with the experimental load-displacement responses, crack patterns, and XCT observations reported in Chapter 6. A central finding is that explicitly incorporating the 3D printing-induced anisotropy of the polymeric reinforcement is critical: simulations

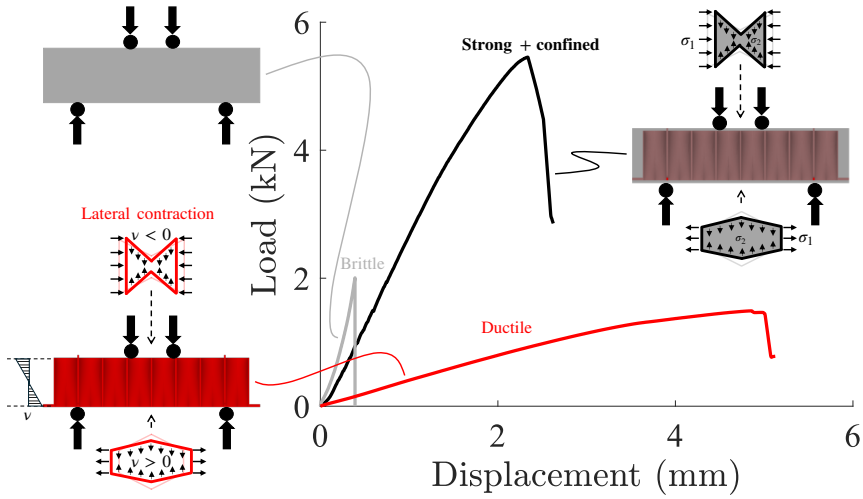

Figure 7.1: Conceptual schematic illustrating Tailored Poisson's Ratio-reinforcement (TPR) characterized by a linear gradient of Poison's ratio along the height of the reinforcement, aligned with the bending stress-strain distribution. The top chords are auxetic ($\nu < 0$), and the bottom chords possess positive Poisson's ratios ($\nu > 0$), both providing lateral confinement to the surrounded cementitious matrix under flexure.

that assume isotropic material behaviour lead to significant overestimation of structural strength and produce qualitatively different fracture patterns, underscoring the necessity of anisotropy-aware modelling for this class of additively manufactured composites in bending.

7.2. NUMERICAL

Complementary to the experimental analyses, LBM simulations were performed to gain more insight into the hypothesized lateral confinement mechanism of the TPR in relation to the composite behaviour of the TPRCC designs. Chapters 2 to 4 have focused on explicitly modelling the printing path-dependent anisotropy in FDM 3D-printed reinforcement (e.g., inter-layer and intra-layer bonds) and their bond stress-slip response against cementitious matrices. The numerical procedures therein are adopted here with a slightly different mesh connectivity. Adjacent nodes are joined by lattice beam elements in the three directions of the grid, resulting in a quadrangular mesh as illustrated in Figure 7.2. Unlike the typically implemented triangular mesh (see Chapters 3 and 4), a quadrangular mesh will cause the cementitious matrix to have a Poisson's ratio close to zero. This will result in lower lateral deformations, somewhat masking the interaction with the reinforcement. However, this effect is assumed to be limited. A quadrangular mesh is used in view of reducing the model's computational efforts regarding mesh generation, mechanical property assignment (see next step), and runtime. In view of the quadrangular mesh, only the three main directions as proposed in Chapter 3 (see Table 3.4) need to be considered: n_i in the same direction as the printing path, referred to as the bead direction; s_i corresponding to the inter-layer bond direction, among stacked layers; and t_i constituting the intra-layer bond direction, among neighboring beads.

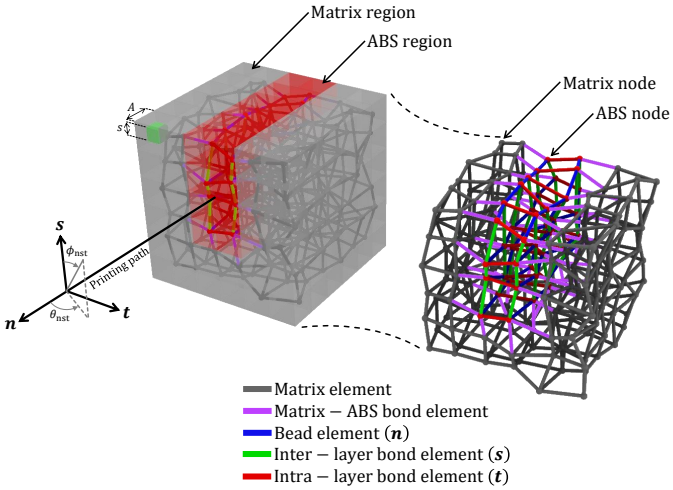

Figure 7.2: Schematic representation of lattice mesh.

To temper the computational demand of the simulations, symmetrical boundary conditions are used as shown in Figure 7.3. Therefore, the virtual samples are cut halfway their dimensions in the y-direction along the xz-plane. The displacements in y-direction, as well as the rotations along the x and z axes are restrained for lattice elements having nodes on the symmetry plane (maximum y values on the xz-plane). The vertical degrees of freedom of the two top rollers received negative displacement values (pushing downward on the halved specimens) and the bottom rollers were fixed.

7.2.1. MODEL CALIBRATION

The stress-strain input for the 3D-printed material is adopted from Chapter 3, as shown in Figure 3.3. The corresponding input parameters for the bead (n_i), inter-layer (s_i) and intra-layer (t_i) printing directions are given in Table 3.6. However, it should be noted that the actual values may be somewhat different due to the new printer settings used in this work displayed in Table 6.1. The properties of the cementitious matrix were calibrated in accordance with four-point bending tests on plain mortar reference samples having no reinforcement. This led to mechanical properties comprising a Young's modulus of 10 105 MPa, a shear modulus of 4210 MPa, and local tensile and compressive strengths of 26.1 MPa and 208.8 MPa (constituting a compression-to-tension strength ratio of 8), respectively. Note that these are local element properties that were fit to match the global experimental behaviour. Due to numerical parameters, such as the mesh size, randomness, and beam radii, local element inputs and global responses can be different as discussed in [164].

Although matrix-ABS bond properties were calibrated for a tensile pull-out response in Chapter 4, compressive behaviour has not been investigated previously. The complex geometries of the reinforcements cause complex and variational stress states in the bond elements during the analysis progress, such that their constitutive relationships remain a

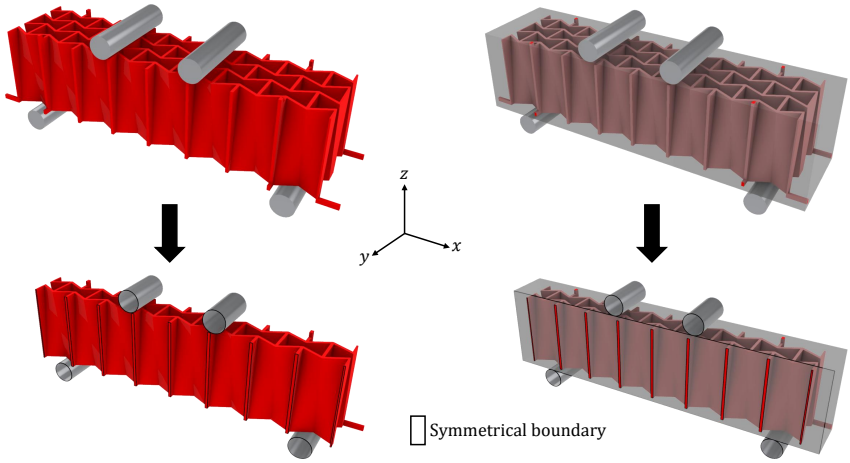

Figure 7.3: Schematic representation of halved specimens with symmetrical boundary.

disputable concern for the LBM simulations in this work. Due to strain incompatibilities between the TPR polymeric reinforcements and the surrounded cementitious mortar in the TPRCC simulations, many bond elements were initially loaded in tension (i.e., debonding) and changed to compression once the reinforcement started to deform and undergo lateral contraction in order to activate the lateral confinement mechanism discussed in Chapter 6. Therefore, bond elements were not allowed to fail, since their compressive behaviour is not known.

7.2.2. TPR SIMULATION RESULTS

Similar to the experimental campaign, the TPR's flexural behaviour was first simulated without cementitious matrix through LBM. Experimental and numerical comparisons of the mechanical response and cracking behaviour of the TPR designs are depicted in Figures 7.4 and 7.5 for UR and UD configurations, respectively. The initial ascending region of the LBM results align well with the flexural test results. Seeing the substantial deflections in Figures 7.4 and 7.5, large deformations are becoming important in realistically describing the post-peak behaviour. However, geometric nonlinearities are not included in the present LBM, such that second order effects are not considered. This explains the larger discrepancies in the softening portion of the post-peak branch. It should also be noted that the experimental curves display several load drops. This is an indication of snap-back behaviour, which the load controlled tests cannot capture. Nonetheless, the simulations are actually able to capture these snap-backs, which makes their curves arguably more realistic.

Figures 7.4(a,b) and 7.5(a,b) clearly show a similar shape in the simulation's load-displacement response as obtained experimentally. All simulated TPR have comparable strengths and stiffness among UR and UD configurations with RE-ABS designs (Figures 7.4(a) and 7.5(a)) being consistently the strongest and stiffest, and TO-ABS (Figures 7.4(b)

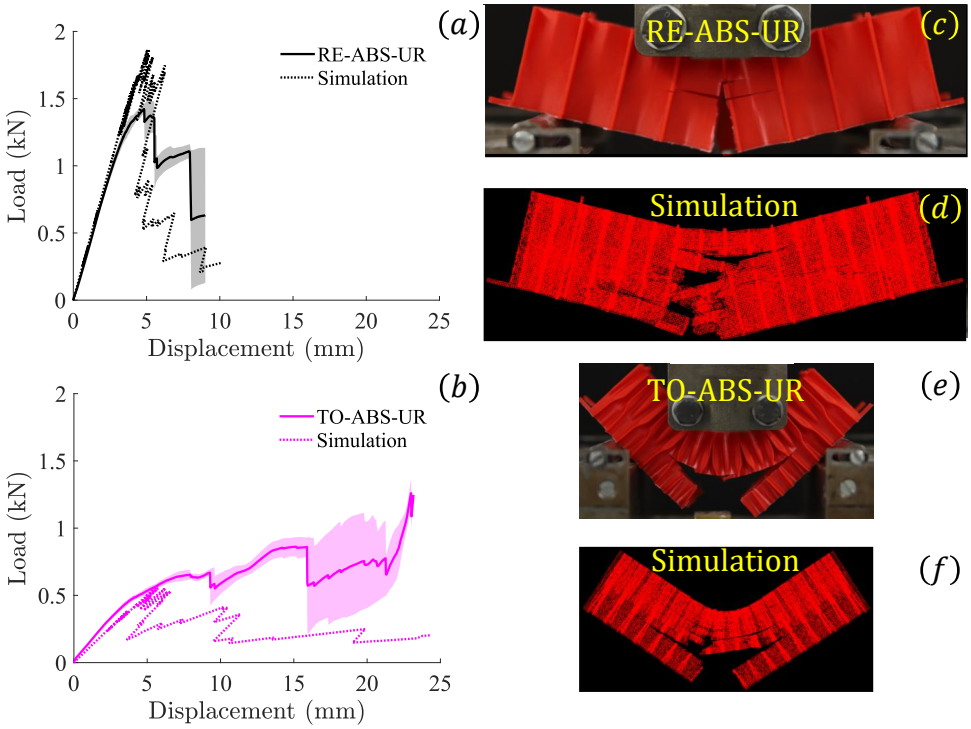

Figure 7.4: Comparisons of the numerical and experimental flexural behaviour of TPR-UR: (a,b) Load-displacement curves, (c-f) deformation and fracture patterns. Note: (c,e) experimental, (d,f) numerical.

and 7.5(b)) yielding lower strength and stiffness. The experimental and simulation's comparison in load capacity is displayed in Figure 7.6 and quantified in Table 7.1.

Likewise, Figures 7.4(c-f) and 7.5(c-f) demonstrate incredibly equable cracking behaviour among experiments (c,e) and simulations (d,f) for all TPR, except for the simulation of RE-ABS-UR (Figure 7.4(d)) displaying a more dispersed fracture pattern, which may explain its slightly higher strength. The 3D printing-induced anisotropy described in Chapter 2 is properly captured as illustrated by the combination of vertical cracks and inter-layer horizontal delamination. To showcase the importance of this behaviour, simulations with isotropic material properties are run as well (see Figures A.5 and A.6, as well as Table A.7 in Appendix A.3). Their mechanical response reveals drastic strength overestimation, combined with completely different cracking behaviour as established in Chapter 3 on ABS auxetic reinforcement structures.

7.2.3. TPRCC SIMULATION RESULTS

Experimental and numerical comparisons of the mechanical and cracking responses of the TPRCC designs are shown in Figures 7.7 and 7.8 for UR and UD configurations, respectively. The simulations match well with the experimental curves and clearly show the onset of cementitious matrix damage near 2 kN, marked by the end of the initial elastic region. At this onset of stiffness degradation, the TPR takes over the tensile loading.

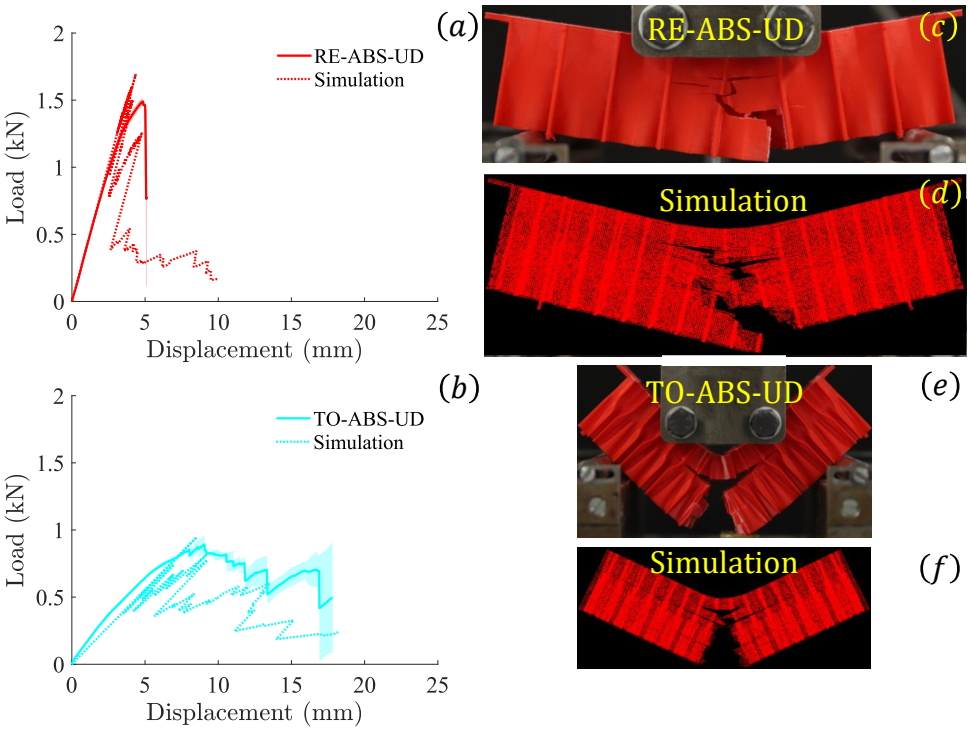

Figure 7.5: Comparisons of the numerical and experimental flexural behaviour of TPR-UD: (a,b) Load-displacement curves, (c-f) deformation and fracture patterns. Note: (c,e) experimental, (d,f) numerical.

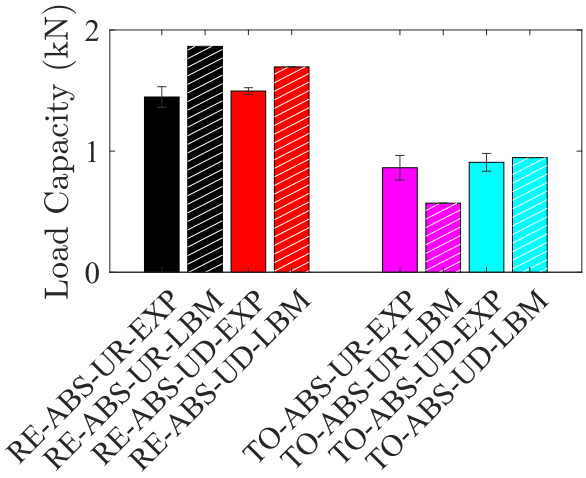

Figure 7.6: Comparison of experimental (EXP) and numerical (LBM) load capacities of TPR ABS 3D prints.

Table 7.1: Load capacities of TPR ABS 3D prints

TPR	**Load Capacity** (kN)
RE-ABS-UR-EXP	1.45 ± 0.08
RE-ABS-UR-LBM	1.86
RE-ABS-UD-EXP	1.50 ± 0.03
RE-ABS-UD-LBM	1.70
TO-ABS-UR-EXP	0.86 ± 0.10
TO-ABS-UR-LBM	0.57
TO-ABS-UD-EXP	0.91 ± 0.07
TO-ABS-UD-LBM	0.95

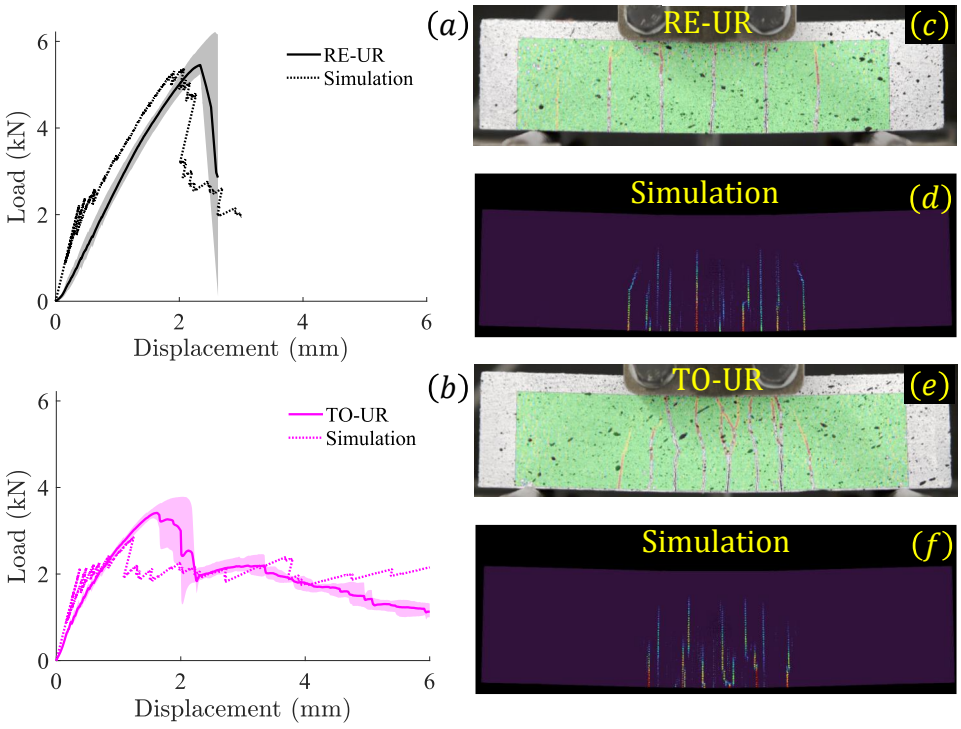

Figure 7.7: Qualitative comparisons of the experimental and numerical flexural behaviour of TPRCC-UR: (a,b) Load-displacement curves, (c-f) fracture patterns prior to reaching peak load. Note: (c,e) experimental cracks recorded by DIC, (d,f) numerical cracks recorded by LBM.

As elaborated for the experimental observations in Chapter 6 (see Figure 6.17), the 3D-printed reinforcement seems to be the limiting factor, which fails at the peak load.

Figures 7.7(a,b) and 7.8(a,b) display similarities in the experimental and numerical load-displacement behaviour. RE-UR (Figure 7.7(a)) reaches almost identical load values in the test and simulation, and has a significantly higher load capacity compared to RE-UD (Figure 7.8(a)). Both TPRCC-RE configurations exhibit sudden load drops after

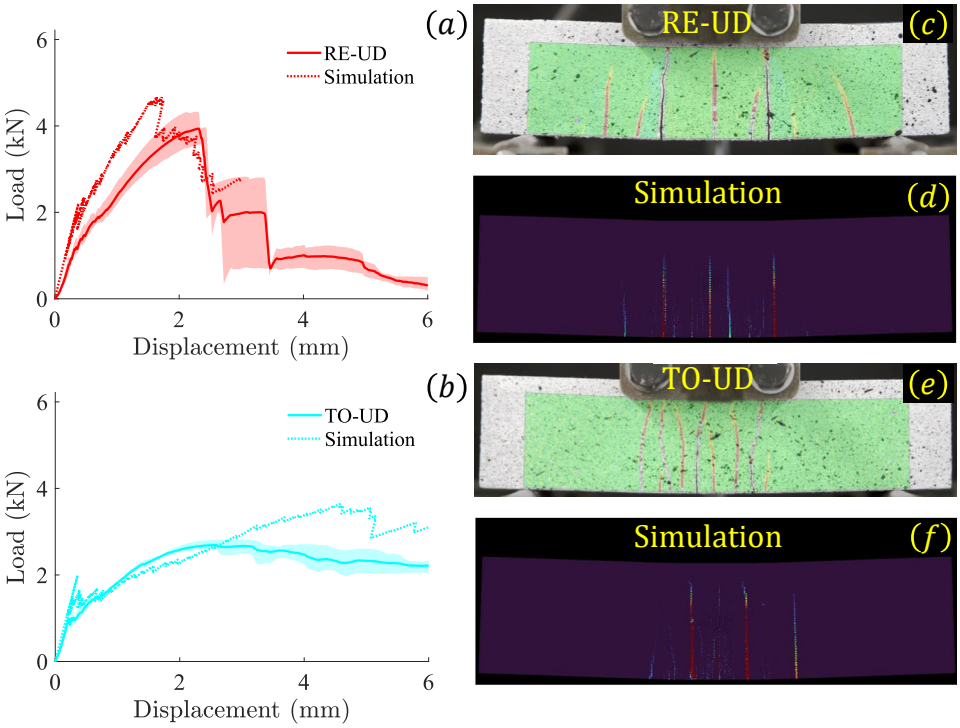

Figure 7.8: Qualitative comparisons of the experimental and numerical flexural behaviour of TPRCC-UD: (a,b) Load-displacement curves, (c-f) fracture patterns prior to reaching peak load. Note: (c,e) experimental cracks recorded by DIC, (d,f) numerical cracks recorded by LBM.

reaching their maximum loads in the experiments and numerical representations. The secondary stiffness of the RE-UR simulation, after the initiation of mortar damage near 2 kN, closely follows the experimental curve in Figure 7.7(a). However, this secondary stiffness is somewhat higher for RE-UD, causing the maximum loads to reach slightly different displacements (see Figure 7.8(a)). The TO-UR simulation (Figure 7.7(b)) underestimates the load capacity, whilst the TO-UD simulation (Figure 7.8(b)) overestimates this mechanical property. Both TO-UR and TO-UD show significantly more ductile responses with respect to RE-UR and RE-UD, matching the experimental observations. Experimental and numerical load capacities are compared in Figure 7.9 and Table 7.2.

Figures 7.7(c-f) and 7.8(c-f) show qualitative comparisons of the experimental (c,e) and numerical (d,f) fracture patterns prior to reaching peak load. All designs display multiple cracks, despite specific fracture patterns that have slight variations. RE-UR shows evenly spaced vertical cracks (see Figure 7.7(c)) which are primarily caused by the unit cell ends (Figure 6.2), hidden directly behind the matrix cover. The LBM simulation in Figure 7.7(d) captures most of the cracks described before, whilst several additional smaller cracks can be observed. Further, even though the numerical cracks start out vertical, those not located in between the two point loads have a tendency to become inclined at mid-height. The other samples display more densely spaced cracks in the central region

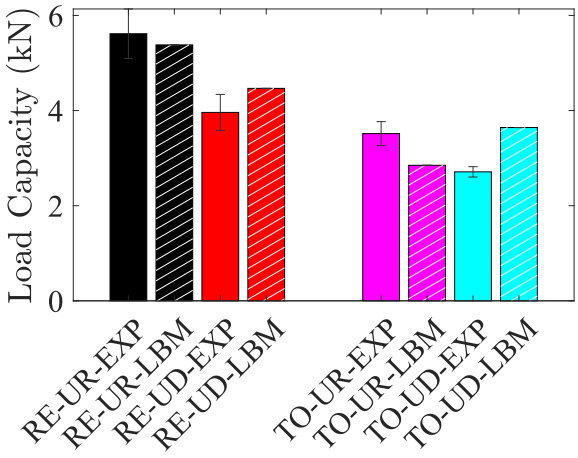

Figure 7.9: Comparison of experimental (EXP) and numerical (LBM) load capacities of TPRCC specimens.

of the beams. TO-UR (Figure 7.7(e)) illustrates a completely different fracture pattern by having notable branching and crack deflection, mainly appearing at mid-height, and more condensed in a narrower area below the loading. These inclined cracks may also be the result of surface cracks following the curved vertical edges of the TPR-TO designs (see Figure 6.2), due to the shallow cover thickness of 2 mm at these locations. Nonetheless, the numerical fracture pattern in Figure 7.7(f) contains the same decrease in crack spacing within a smaller area. RE-UD exhibits a similar fracture pattern as RE-UR, including two more developed vertical cracks right below the loading pins, but there are more smaller and inclined intermediate cracks as shown in Figure 7.8(c). These two distinct parallel cracks are also present in the LBM result in Figure 7.8(d), including some initial cracks in between at the bottom of the beam. TO-UD (Figure 7.8(e)) shows the most dense crack spacing, limited to the constant bending moment region in the center of the beam. Like TO-UR, the cracks observed in TO-UD start vertically and become somewhat more inclined near the neutral axis. However, the simulation of TO-UD in Figure 7.8(f) only resembles the two mostly developed cracks located between the point loads, together with some other minor crack initiations.

Analogous to the TPR analysis, the importance of the printing path-dependent anisotropic characteristics of the 3D-printed reinforcement is illustrated by means of additional TPRCC simulations provided with isotropic material input for the reinforcement, see Figures A.7 and A.8, as well as Table A.8 in Appendix A.3. Similarly, the mechanical responses obtained highlight drastic overestimation in load capacity as observed in Chapter 3.

7.2.4. INTERNAL STRESS ANALYSIS

To support the lateral confinement hypothesis posted in Chapter 6, the LBM simulations presented here are used to perform internal stress analysis. Therefore, stress values within the cementitious mortar phase in the bottom chords of the TPRCC specimens are

Table 7.2: Load capacities of TPRCC specimens

TPRCC	**Load Capacity** (kN)
RE-UR-EXP	5.61 ± 0.52
RE-UR-LBM	5.38
RE-UD-EXP	3.96 ± 0.38
RE-UD-LBM	4.47
TO-UR-EXP	3.52 ± 0.25
TO-UR-LBM	2.85
TO-UD-EXP	2.71 ± 0.11
TO-UD-LBM	3.64

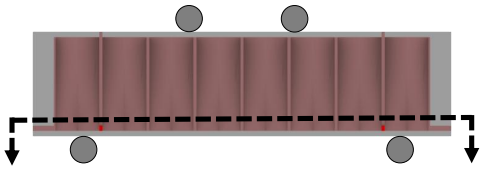

Figure 7.10: Schematic representation of section for internal stress analysis.

visualized to demonstrate the presence of the lateral confinement mechanism before the reinforcement breaks. Figure 7.10 shows a schematic representation of the location at which a section is made, and its direction to observe the internal stress states.

Figure 7.11 illustrates the internal lateral stress (S_y) in the cementitious matrix phase at 1 mm displacement of (a) RE-UR and (b) RE-UD bottom chords. At this displacement value, matrix cracking in the bottom chord has already begun (see Figures 7.7(a,b) and 7.8(a,b)), so that longitudinal tensile loads (along the x-axis in Figure 7.11) are taken by the reinforcement. The hypothesized lateral confinement mechanism in the mortar as a result of the reinforcement's deformation mechanism occurs in the y direction in Figure 7.11, which displays the lateral stress in this direction. In RE-UR (Figure 7.11(a)), the bottom part of the reinforcement has a positive Poisson's ratio, which means that it contracts laterally under positive longitudinal bending strain (top of Figure 7.12). The resulting internal lateral stress state in the cementitious matrix phase shows negative stress concentrations in the centers of the TPR unit cells that experience the highest bending moment. However, the outer regions of the mortar in the unit cells are under positive lateral stress due to their deformation mechanism (see Figure 7.12). It is likely that during the experiments debonding occurred at these locations, due to the low ABS-mortar bond strength obtained in Chapter 4, which could not be captured by the current model as explained in Section 7.2.1.

On the other hand, RE-UD (Figure 7.11(b)) depicts positive lateral stress concentrations in the middle of the central unit cells caused by the reinforcement's lateral expansion related to its positive Poisson's ratio (bottom of Figure 7.12). Therefore, significant debonding must have occurred while loading the specimens. In this case, the outer regions of the matrix are in compression, which is the exact opposite of the lateral stress state observed in RE-UR (Figure 7.12). Analogous to the hypothesis in Chapter 7, the lateral confinement

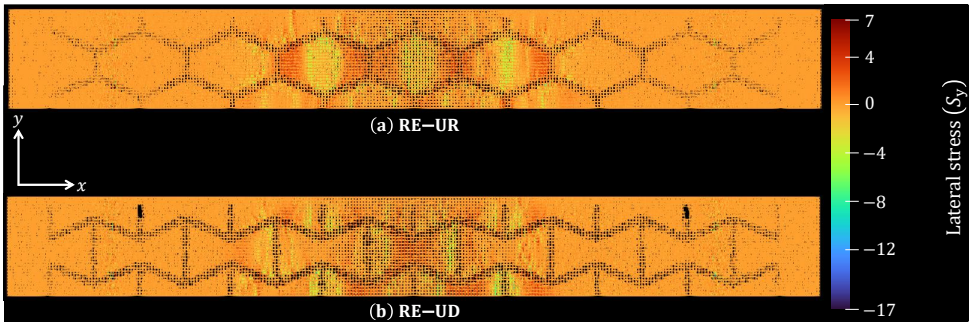

Figure 7.11: Internal lateral stress (S_y) in cementitious matrix phase at 1 mm displacement of (a) RE-UR and (b) RE-UD bottom chords (unit: MPa).

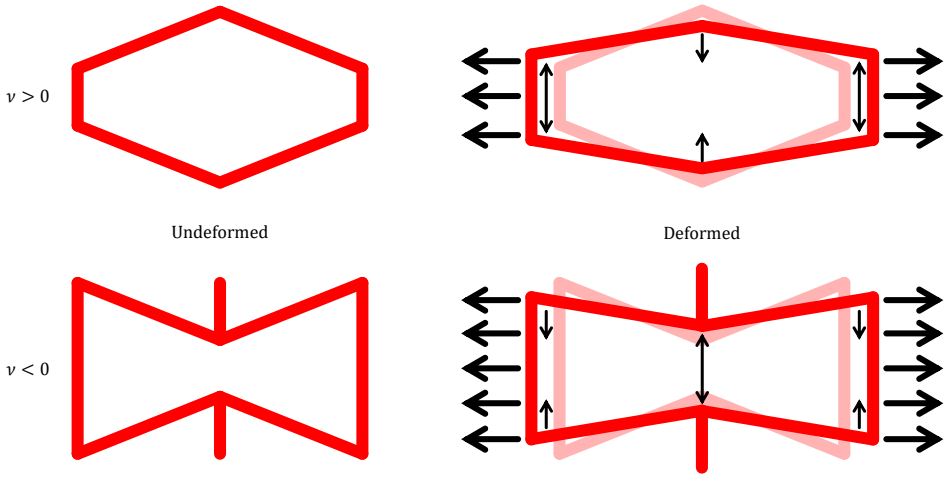

Figure 7.12: Deformation mechanisms of RE unit cells.

mechanism is present in RE-UR and absent in RE-UD. This explains why the load capacity of RE-UR is significantly larger than that of RE-UD, whilst RE-ABS-UR and RE-ABS-UD exhibit comparable load capacities.

Figure 7.13 shows the internal lateral stress (S_y) in the cementitious matrix phase at 1 mm displacement of (a) TO-UR and (b) TO-UD bottom chords. Since the initial cracking strength (approximately 2 kN) is also exceeded at this stage, the tensile forces at the bottom of the specimens are transferred through the reinforcement. The bottom reinforcement in TO-UR (Figure 7.13(a)) has a positive Poisson's ratio, causing lateral confinement when stretched longitudinally (top of Figure 7.14). As a result, the mortar displays negative lateral stress concentrations inside the TPR unit cells around the center of the beam. It is noteworthy that the TO architecture envelops two alternating shapes of matrix regions, whereas RE only encapsulates a single repetitive form. Due to its complex geometry, the bottom chord of TO-UR encloses larger unit cells (four-leaf clover shape)

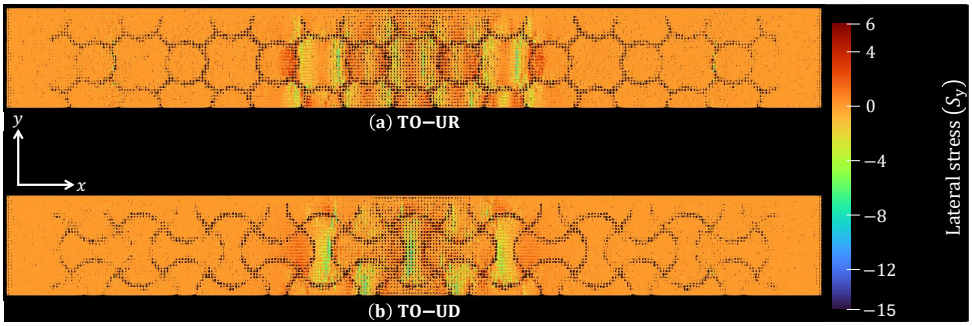

Figure 7.13: Internal lateral stress (S_y) in cementitious matrix phase at 1 mm displacement of (a) TO-UR and (b) TO-UD bottom chords (unit: MPa).

and smaller unit cells (nearly circular). Both are laterally confining the cementitious matrix, but to a different extend. The large clover cells develop the largest negative stress concentrations, particularly in between its greatest mortar dimensions. The small circular cells cause smaller stress concentrations at their centers. However, the struts that are closely aligned with the y direction in Figure 7.13(a) are slightly stretched, which results in positive lateral stress in the outer regions (see also Figure 7.14).

Contrary to RE-UD, TO-UD (Figure 7.13(b)) also exhibits negative lateral stress concentrations, despite the lateral expansion (bottom of Figure 7.14). The design of the bottom chord of TO-UD having alternating laterally (i.e., aligned with the y axis in Figure 7.13(b)) and longitudinally (i.e., aligned with the y axis in Figure 7.13(b)) hourglass-shaped unit cells. The mortar within the lateral hourglass cells experiences the largest stress concentrations, whilst the longitudinal hourglass cells show near zero or minor tensile stress (see Figure 7.13(b)). The presence of mortar confinement in the lateral cells is related to the deformation mechanism of the TO units with a negative Poisson's ratio, see the bottom right of Figure 7.14. The curved struts aligned with the loading in the bottom right of Figure 7.14 want to become straight, such that these exert an inward facing lateral force on the surrounded cementitious matrix.

Although the global theoretical Poisson's ratio of the TO-UD bottom chord is programmed as 0.8, locally the deformation of the inward moving struts is larger than that of the perpendicular ones. This is evidenced by Figure 7.15(a), showing the longitudinal stress (S_x) at the same displacement. The same mechanism occurs longitudinally (along the x axis in Figure 7.15(a)) as previously observed laterally. In this case, the longitudinally hourglass-shaped unit cells display minor compressive stress concentrations at their centers, whilst the lateral cells have near zero or minor tensile stress values. The comparative global stress state within the central unit cells of TO-UD (see Figure 7.15(b)) is therefore predominantly compressive in both of the alternating unit cell orientations, with the highest negative stress concentrations occurring in the lateral unit cells. This is a possible explanation for the larger load capacity observed in the TO-UD-LBM simulation compared to TO-UR-LBM, even though the experiments advocate the opposite. That discrepancy may be caused by the unrealistic bond behaviour used in the simulations, which prevent debonding at larger deformations. Another reason could be the near zero Poisson's ratio of the matrix, caused by the quadrangular mesh. However, it should be

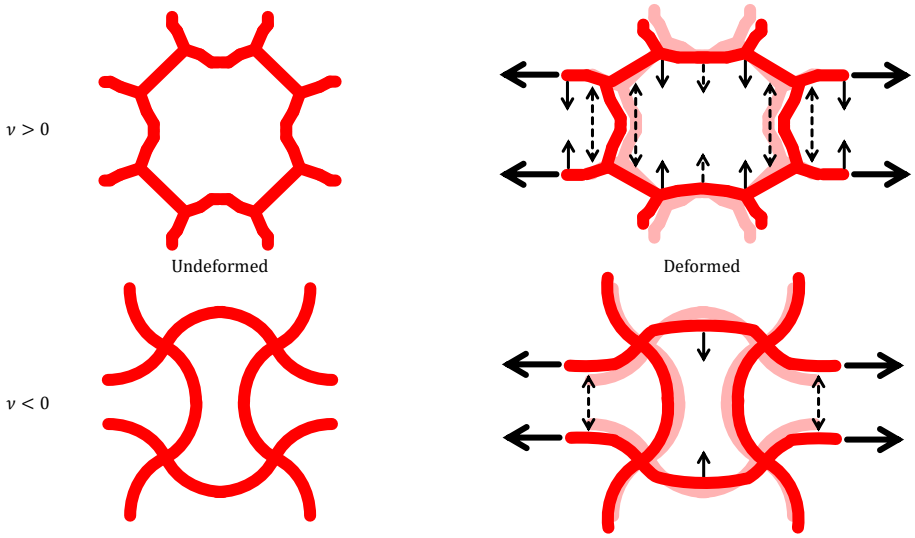

Figure 7.14: Deformation mechanisms of TO unit cells. Solid arrows indicate major deformations, dashed arrows indicate minor deformations.

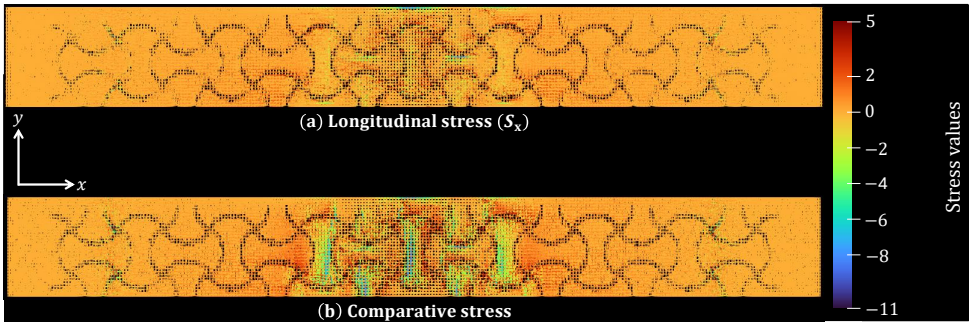

Figure 7.15: Internal stress values in cementitious matrix phase of TU-UD at 1 mm displacement: (a) longitudinal stress (S_X) and (b) comparative stress (unit: MPa).

noted that the organic TO geometries could be less accurately represented by the cubic cell discretization of the LBM simulations than the more straightforward RE designs. The strain-independent design of the TO architecture, which was programmed to have a nearly constant Poisson's ratio up to 20 % strain as elaborated by Sigmund and co-workers in [203], could also explain the more stable post-peak behaviour observed for TO compared to RE, both in experiments and simulations. The lateral confinement mechanism hypothesized in Chapter 6 is thus present in TO-UR as well as TO-UD, given its highly curved organic design.

The effects on internal stress states when having isotropic material properties assigned to the TPR are studied in Appendix A.3 too, see Figures A.9 and A.10. Larger negative stress concentrations are found, caused by the increased lateral confinement mechanism due to enhanced longitudinal strains.

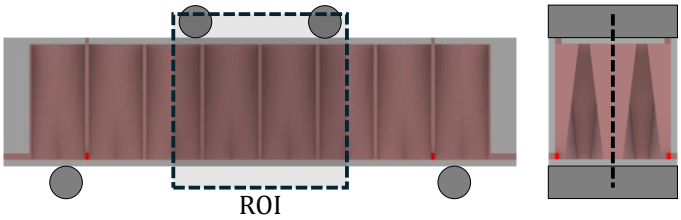

Figure 7.16: Schematic representation of Region Of Interest (ROI).

7.2.5. INTERNAL FRACTURE ANALYSIS

LBM also presents the opportunity to visualize the internal cracking patterns, which can be compared with XCT scans to validate the proposed modelling strategy. To this end, the four TPRCC designs considered were placed inside a TESCAN CoreTOM μ-CT scanner (120 kV, 125 mA). A Region Of Interest (ROI) was chosen between the two point loads, comprising a slice at half the depth as shown in Figure 7.16.

Figures 7.17(a) and (b) show the reconstructed μ-CT images of RE-UR and RE-UD, respectively, from Chapter 6. Figures 7.17(c) and (d) display the numerical crack widths of RE-UR and RE-UD, respectively, obtained by LBM simulations in this work. In RE-UR (Figure 7.17(a)), it is evident that cracking is initiated through debonding between the mortar and the reinforcement until mid-height, where the TPR fractured and matrix cracking propagates upward. An important observation is that most of the cementitious matrix remains intact, except for the straight vertical crack in the middle. Although bond elements are modelled as non-failing in the simulations, thereby preventing natural debonding, the adjacent mortar can still fail in tension near the reinforcement. This is exactly what happened in the LBM result for RE-UR in Figure 7.17(c): a single vertical crack running along the TPR, whilst other regions stay virtually undamaged. When looking at RE-UD (Figure 7.17(b), significantly more damage throughout the cementitious mortar can be observed, including (minor) horizontal crack deflections near the neutral axis. This is also captured by the LBM simulation of RE-UD as illustrated in Figure 7.17(d): alongside the large vertical crack, multiple smaller horizontal and additional vertical cracks developed in the matrix phase. In line with the experimental findings in Chapter 6, the proposed simulations support that RE-UR is capable of more effectively confining internal fracture compared to RE-UD, suggesting improved composite behaviour.

Similarly, Figures 7.18(a) and (b) depict the XCT images of TO-UR and TO-UD, respectively, from Chapter 6. Figures 7.18(c) and (d) showcase the numerical crack widths of TO-UR and TO-UD, respectively, observed from the simulation results presented here. The same behaviour is found for TPRCC-TO. For TO-UR, the experimental (Figure 7.18(a)) and numerical (Figure 7.18(c)) internal fracture analyses show in both cases only one localized crack following the organic reinforcement shape with no severe damage in the surrounding mortar. On the other hand, Figures 7.18(b) and (d) for TO-UD display substantially more internal fracture, with multiple internal cracks initiated at different locations. The simulation results even captured the smaller diagonal cracks in the bottom half and (minor) horizontal fractures occurring somewhat above the neutral axis of the beams. Although the global failure modes are different, TO-UR reinforcement's improved

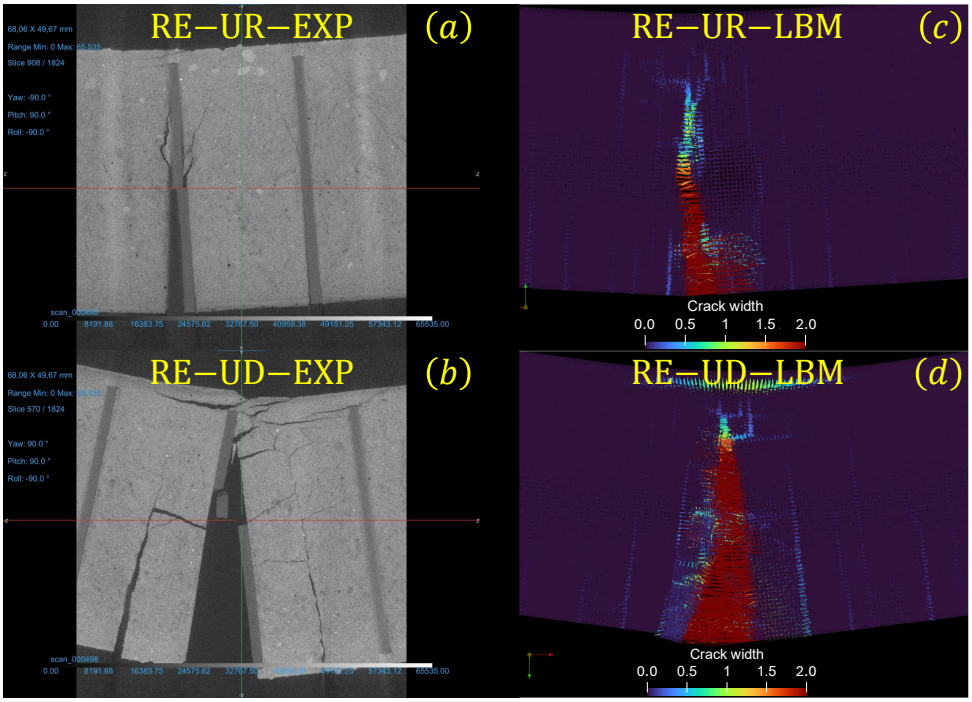

Figure 7.17: Comparisons of internal fracture at ROI: (a) Reconstructed μ-CT image of RE-UR, (b) reconstructed μ-CT image of RE-UD, (c) numerical crack width of RE-UR, and (d) numerical crack width of RE-UD (unit: mm).

ability to alleviate internal matrix damage compared to TO-UD is consistent with RE-UR and RE-UD, respectively.

Finally, additional internal fracture analyses are performed when considering isotropic TPR input for the TPRCC simulations (see Figure A.11 in Appendix A.3). Albeit that these results align well with the experimental findings in Chapter 6 and the printing path-dependent analyses performed here, significantly more dispersed cracking is observed for the isotropic cases.

7.3. CONCLUSIONS

The present chapter extends and substantially elaborates lattice modelling of Tailored Poisson's Ratio-reinforcement (TPR) to support the previously hypothesized lateral confinement mechanism exerted on the surrounded cementitious matrix. The two best performing TPR designs are embedded in mortar, enabling full lattice simulations of the resulting Tailored Poisson's Ratio-reinforced Cementitious Composite (TPRCC) designs. The Lattice Beam Model (LBM) simulations in this work are used to perform internal stress and fracture analysis, revealing the following conclusions:

- *Reinforcement*: Additively manufactured TPR has been successfully tested and simulated in bending. Both experimentally and numerically, the reinforcements display reasonably comparable load capacities in the UpRight (UR) and Upside

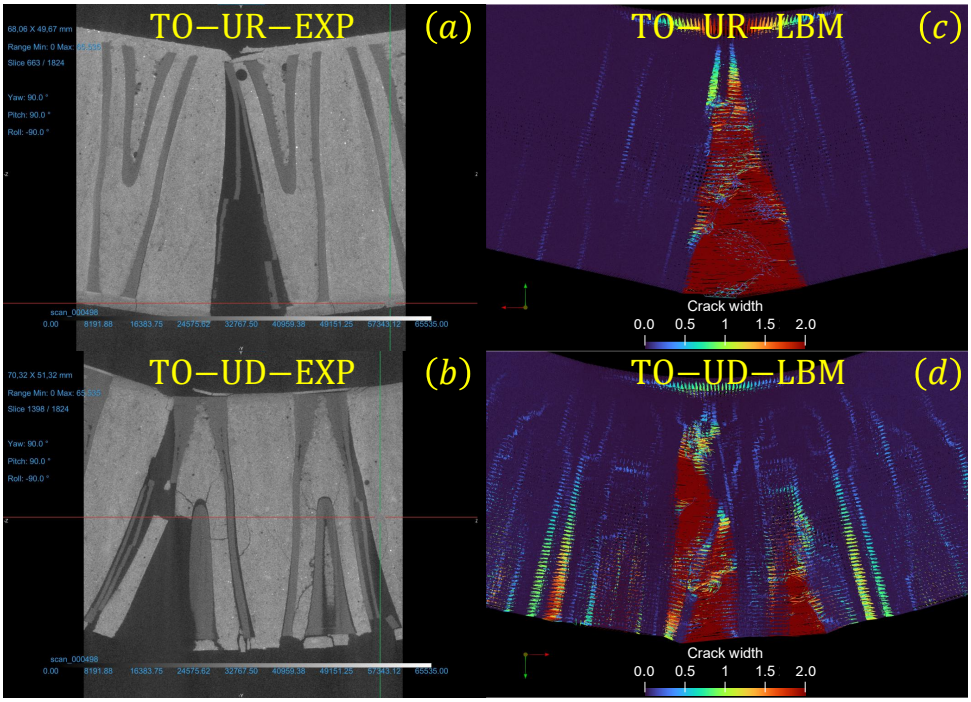

Figure 7.18: Comparisons of internal fracture at ROI: (a) Reconstructed μ-CT image of TO-UR, (b) reconstructed μ-CT image of TO-UD, (c) numerical crack width of TO-UR, and (d) numerical crack width of TO-UD (unit: mm).

Down (UD) directions. Strikingly similar fracture patterns among experiments and simulations are obtained too. The 3D printing-induced mechanical anisotropy present in the TPR is described accurately by the developed models, as shown by the combination of vertical cracking and inter-layer horizontal delamination. In contrast, complementary simulations with isotropic TPR input lead to pronounced overestimation in load capacity and completely different cracking patterns.

- *Composite*: Effects of the previously hypothesized TPR-induced lateral confinement mechanism in the TPRCC layouts were evaluated in the UR and UD directions. Experimentally, all TPRCC-UR designs showed substantially larger load capacities compared to their UD counterparts. Numerically, both directions of TPRCC-RE reached almost identical load values with the tests, where RE-UR exhibited significantly higher load capacity compared to RE-UD. However, the TO-UR simulation provided strength underestimation, whilst TO-UD yielded strength overestimation. This could be related to the cubic discretization of the LBM simulations and the highly non-linear geometry of TO causing a less accurate representation compared to the more straightforward RE design. Nonetheless, TPRCC-TO showed drastically more deformation capacity with respect to TPRCC-RE, matching experimental observations. All designs illustrated dispersed cracking, albeit that specific cracking patterns varied slightly. TPRCC-RE showed evenly spaced vertical cracks, most of

which were captured by the simulations. On the other hand, TPRCC-TO displayed notable branching and crack deflection, mainly appearing at mid-height, and more condensed in a narrower area below the loading. The importance of considering 3D printing-induced anisotropy of the TPR inside TPRCC designs is also elaborated by means of complementary simulations assuming isotropic TPR properties.

- *Stress*: Internal stress states in the cementitious matrix phase at the bottom chords of the TPRCC specimens are visualized to suggest the hypothesized presence of lateral confinement in UR configurations and the absence in UD configurations prior to reinforcement failure. RE-UR showed negative lateral stress concentrations in the centers of the TPR unit cells that experienced the highest bending moment. However, RE-UD depicted positive stress concentrations in the middle of the central unit cells caused by the lateral expansion of the reinforcement. TO-UR also displayed negative lateral stress concentrations in the surrounded cementitious matrix, albeit that its highly non-linear geometry results in an alternating pattern with different magnitudes. In contrast, TO-UD also exhibited negative lateral stress concentrations, despite the positive Poisson's ratio of the TPR at the bottom chord. The highly curved organic geometry contains curved struts aligned with the longitudinal direction of the beam wanting to become straight, such that these exert an inward facing lateral force on the surrounded cementitious matrix. The hypothesized lateral confinement mechanism is thus present in RE-UR, TO-UR and TO-UD, whilst it is absent in RE-UD. Internal stress states obtained for isotropic material properties found larger stress concentrations near the peak loads, caused by the increased lateral confinement mechanism due to enhanced longitudinal strains.

- *Fracture*: Internal cracking patterns are compared with XCT scans to validate the proposed modelling stragety. μ-CT scanning already confirmed the improved ability of TPRCC-UR to alleviate internal matrix damage compared to TPRCC-UD, leading to improved composite behaviour. In the tests and simulations of TPRCC-UR, most of the cementitious matrix remained intact, except for the final crack. However, in TPRCC-UD significantly more damage is observed throughout the cementitious mortar, including (minor) horizontal crack deflections near the neutral axis. TPRCC simulations considering isotropic TPR input were performed in parallel, showing significantly more dispersed matrix cracking.

8

CONCLUSIONS, RECOMMENDATIONS, AND LIMITATIONS

This chapter presents conclusions, recommendations, and limitations.

8.1. RESEARCH ACHIEVEMENTS

THE main objective, as well as its corresponding activities and related research questions, has been formulated in the Introduction of this work (Chapter 1). In what follows, this section aims to provide concise answers to these research questions that have led towards achieving the main objective of understanding the interaction mechanisms between deformable auxetic reinforcement and the stiff cementitious matrix through modelling the material at multiple length scales.

WHAT IMPACT HAVE 3D PRINTING TECHNIQUES AND THEIR RESULTING IMPERFECTIONS ON THE MECHANICAL RESPONSE OF (AUXETIC) REINFORCEMENT?

The 3D printing technique considered in this study is Fused Deposition Modelling (FDM), which is based on material extrusion. This Additive Manufacturing (AM) technique creates parts with heterogeneities at the micro (usually up to 1 mm) and meso (mm to cm) length scales, such as voids and pores, that are mainly influenced by so-called *printing process parameters*. A thorough literature review performed in this work concludes that these parameters affect the microstructural composition of FDM 3D printed polymers that in turn have a negative influence on characteristic mechanical properties. Two particular mechanical properties are highlighted therein, which are the intra-layer and inter-layer bond strengths. Together with porosity, these were found to be the most influential. To this end, experimentally validated printing path-dependent two-scale models that take microstructural information (i.e., porosity and interfacial bond strengths) into consideration are developed in the presented research. The impact on the mechanical response of the (auxetic) reinforcement architectures considered in this study will be elaborated next. First of all, it has been illustrated that only including the porosity in numerical simulations of FDM printed parts is not sufficient as these yield higher strengths and more ductile responses compared to experimental findings. Hence, it has been shown on both the material and auxetic structure scales that incorporation of the interfacial bond strengths in numerical models for FDM 3D printed polymers is important. Furthermore, preliminary tests and simulations showed that printing accuracy (i.e., part dimensions and porosity) had a particularly large influence on the stiffness of the reinforcement. It has also been identified that the obtained deformations and failure mechanisms changed when implementing interfacial bond properties or not. Numerical investigations clearly demonstrate that models considering interface properties fail in tension, while models using homogeneous isotropic material properties mainly fail in compression. The heterogeneous models show governing failure of the inter-layer bond, while the homogeneous models barely have any interfacial failure.

WHAT IS THE RELATIONSHIP BETWEEN CEMENTITIOUS MATRIX AND INTERFACE MICROSTRUCTURE OF 3D PRINTED REINFORCEMENT?

The 3D printed reinforcement used in this study is created through FDM causing parts to have edges that are typically composed of an array of elliptical shapes. Experimental analysis shows that the cementitious matrix completely fills the sharp interior portions of the elliptic geometry, which facilitates interlocking, thereby enhancing the bond behaviour in certain directions. The literature review performed in this work established that the bond transfer mechanism of plain re-bars is primarily dependent on chemical adhesion (about 11 %) and friction (roughly 89 %), whilst for deformed re-bars this mainly depends on mechanical interaction (nearly 81.7 %) with chemical adhesion (about 2 – 5

%) and friction (approximately 13.3 – 16.3 %) having a minor influence. Hence, plain re-bars usually fail in pull-out mode and deformed re-bars mostly fail by concrete splitting. To numerically investigate morphological effects on the bond behaviour between cementitious matrix and FDM 3D printed reinforcement, multi-scale bond models that consider different interface orientations with respect to the printing path are developed herein. The relationship between cementitious matrix and interface microstructure will be elaborated next. First, it has been illustrated that the inter-layer bond inside FDM 3D printed parts fails prematurely under pull-out conditions. Thus, the bond behaviour in this direction cannot be measured by means of pull-out experiments. Push-out conditions are therefore used to purely measure the contribution of mechanical interactions without any interfacial failure modes. It has been illustrated that interlocking effects as a result of the 3D printing technique can significantly increase the bond strength. The intra-layer direction only increased by 15 %, whilst the inter-layer direction, which has a strong resemblance with deformed re-bars, showed a major increase of 56 %. As a result, all cases displayed clean pull-out or push-out responses, similar to plain re-bars, except for the inter-layer direction under push-out conditions, which yielded some matrix splitting due to the wedging of its morphological features, similar to deformed re-bars.

WHAT IS THE INTERFACIAL STRENGTH BETWEEN CEMENTITIOUS MATRIX AND 3D PRINTED REINFORCEMENT?

The 3D printed reinforcement used in this study is made of Acrylonitrile Butadiene Styrene (ABS) filament, which consists of hydrophobic groups. As a result, there is limited chemical adhesion with the cementitious matrix, such that obtained bond strengths mainly reflect frictional contributions, leading to very low values, i.e., below 1 MPa. Based on the literature, the ABS-matrix bond is therefore comparable with that of fiber pull-out for concrete. Bond stress values are typically calculated through dividing the pull-out load by the circumference based on the contact area between the 3D printed part and cementitious matrix. However, it has been illustrated that large discrepancies exist amongst the nominal circumference, based on the CAD model, and actual circumference, measured from geometrical models developed in this work. The former assumes a rectangular perimeter, whilst the latter considers more realistic elliptical exterior shapes leading to a significantly larger perimeter of nearly 38 %. Hence, it has been shown that the choice of circumference size has a major influence on the determined bond strength. Furthermore, it is assumed that the bond behaviour between ABS and cementitious matrix is constant in terms of chemical adhesion and friction as a result of surface roughness, such that morphological effects only contribute to the mechanical interaction through anchorage or interlocking of the matrix and elliptical edges. It has also been identified that the maximum bond stress that can be reached in simulations without breaking the ABS material is 0.8 MPa, which is about 16 % lower compared to the experimental data. However, this difference lies within the 38 % deviation observed amongst circumferences, let alone geometrical inaccuracies induced by the FDM 3D printer. Therefore, the discrepancy is thought to be minor. Numerical investigations report bond strengths of 0.73 – 0.80 MPa in the direction parallel to the printing path, whilst those obtained in the intra-layer and inter-layer directions yield 0.84 MPa and 1.24 MPa, respectively. This clearly demonstrates the existence of printing path-dependency in the bond behaviour between cementitious matrix and 3D printed reinforcement.

WHAT ARE THE UNDERLYING MECHANISMS OF INTERACTION BETWEEN AUXETIC REINFORCEMENT AND CEMENTITIOUS MATRIX THAT RESULT IN COMPOSITE ACTION?

The underlying mechanisms of interaction between auxetic reinforcement and cementitious matrix are strongly dependent on the loading conditions. If auxetic reinforcement is under tension, it will expand laterally, thereby increasing the frictional bond with the cementitious matrix, leading to greater pull-out resistance as described in the literature for fiber-reinforced composites. However, if this lateral expansion becomes too large it may deteriorate the load-bearing capacity of the matrix due to cracking. Therefore, literature on load-bearing applications mainly focus on auxetics subjected to compression: The reinforcement contracts laterally and brings the surrounded mortar in a state of biaxial or triaxial compression, which is shown to be beneficial in terms of both strength and ductility. This lateral confinement mechanism is the most important factor in achieving synergistic composite action. The inclusion of auxetic reinforcement drastically improves the post-peak performance of the cementitious composites by displaying a long softening tail in their mechanical response. A slow and gradual failure mechanism is observed as opposed to plain mortar: The auxetic structure's deformation mechanism, which contracts laterally under axial compression, causes confinement of the matrix and thereby actively restrains crack localization. This effectively improves the energy absorption capacity by having multiple smaller cracks forming, instead of the straight cracking planes observed in samples without reinforcement. On the other hand, auxetic bending applications are far more limited: If flexural auxetic reinforcement is implemented in the literature, it is mostly oriented in-plane (i.e., the auxetic deformation mechanisms occur in the same plane as the loading). Only a few publications tested composites where the auxetic response of the reinforcement takes place out-of-plane. Whilst lateral expansion of auxetic bending reinforcement in the lower region subjected to tension may deteriorate the load-bearing capacity of the matrix, the reinforcement's deformation mechanism will bring the mortar in a state of biaxial compression in the upper zone. This contradiction raised the idea to tailor the Poisson's ratio of the reinforcement according to the bending stress-strain distribution, thereby taking advantage of the same lateral confinement mechanism in flexure as exploited under compression. The reinforcements developed in this study have a through-thickness gradient of Poisson's ratio that is aligned with the elastic bending stress distribution. The resulting composites experience lateral confinement of the cementitious matrix throughout their maximally stressed locations, causing a shift in the principal stress state, leading to an extended loading path in stress space, actively postponing failure of the surrounded matrix.

8.2. RECOMMENDATIONS

This work covers the development of multi-scale models for simulating deformation and fracture of cementitious composites with auxetic reinforcement subjected to uniaxial compression. The mechanisms observed in these Auxetic Cementitious Composites (ACCs) have been further explored for flexural applications, thereby extending their range of application. During the process of creating this thesis, based on the findings herein, ideas for future research emerged. These will be discussed in the following subsections.

8.2.1. 3D CONCRETE PRINTING

The multi-scale model developed in the presented study has illustrated its ability to simulate deformation and fracture of ACCs. The numerical approach explicitly incorporates two major implications caused in additively manufactured cement-based composites, particularly by means of FDM 3D printing. First, the model considers a novel element identification procedure for 3D printed polymeric materials by assigning material properties related to their orientation with respect to the printing path (i.e., printing path-dependent input). This method is not limited to polymeric 3D printing alone, but can also be applied to other 3D printing techniques based on material extrusion, like 3D Concrete Printing (3DCP), which faces similar challenges, particularly with the weak inter-layer bond [207, 208]. Especially for modelling more complex 3DCP configurations, such as the works by Zhou et al. [209, 210] on bio-inspired knitting/tilting and stitching of filaments wherein the printing paths are three-dimensionally intertwined, the developed methodology in this work has great potential. Secondly, the simulations account for elevated bond behaviour in certain directions as a result of FDM 3D printed parts having edges that are typically composed of ellipses, which potentially facilitate mechanical interaction (i.e., interlocking) with the cementitious mortar. This is comparable to the interfaces in reinforced concrete beams with self-healing cover zone as lost formwork [211], especially those being profiled with protruding shear keys, for which a similar modelling strategy as used in the current research can be applied.

Because the local coordinate system used to assign anisotropic material properties aligns with the printing path, it makes the proposed multi-scale strategy a versatile numerical tool for simulating an infinite amount of geometries, no matter how simple or complex. For any polymeric shape printed through material extrusion, the developed model can be utilized for automated identification and assignment of anisotropic material properties in correspondence to its printing path, provided the printer code (G-code) is available. Moreover, the presented modelling framework can be extended to 3D-printed materials incorporating other types of filling matrices, such as silicone rubber, foam, or epoxy, provided realistic bond stress-slip relationships are available in the literature or experimentally obtained. Future research could take advantage of the automated printing path-dependent property assignment via the established multi-scale modelling procedure. Finally, although the implementation of the directional-dependent bond behavior in this work is less pronounced due to the current loading configuration (i.e., uniaxial compression), it is certainly worth exploring its effects in the future for different setups like tensile tests in which these effects prevail.

8.2.2. MICROMECHANICAL CHARACTERIZATION OF ABS-MORTAR BOND

Chapter 4 focuses on the bond between 3D printed reinforcement and cementitious matrix. Because of the layer-by-layer filament extrusion process of the 3D printing technique, the edges of FDM 3D printed polymers are typically composed of ellipses. Based on this, it was hypothesized that morphological effects as a result of the 3D printing technique enhance the reinforcement-matrix bond: The elliptic geometry potentially facilitates interlocking with the cementitious mortar, thereby possibly enhancing the bond behaviour in certain directions. To investigate the geometrical directional-dependent features at the edges of 3D printed polymers in more detail, micro-scale models were developed.

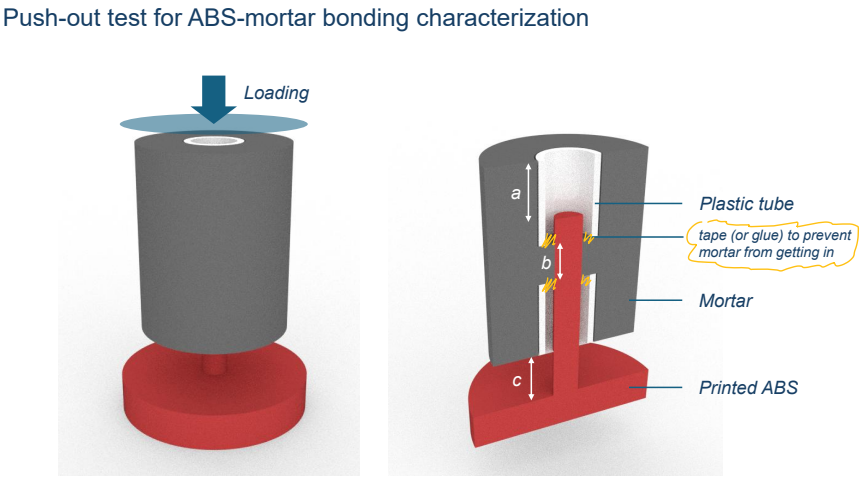

Figure 8.1: Push-out test for ABS-mortar bonding characterization

To conclusively support the hypothesis, additional experimental investigations are necessary for validation purposes. Specifically, the effect of the different geometrical configurations should be quantified (e.g., elliptic versus plain). The bond was successfully tested for the plain bead direction, but for the other printing directions with elliptical bond (inter-layer and intra-layer) the bond was too strong (i.e., the reinforcement too weak) to perform a successful pull-out test due to rupture of the reinforcement. To this end, the micro-scale models resorted to push-out tests. This procedure allowed to see the isolated effect of morphological features without any influence of the intra-layer and inter-layer bonds within the 3D printed ABS material. By exposing the reinforcement to compression, tensile failure of the internal bonds was not governing. Therefore, future research should focus on developing a dedicated small-scale setup for testing the bond strength between the polymeric reinforcement and cementitious matrix.

To prevent premature tensile failure of the interfacial bonds within the 3D printed ABS, it is recommended to use push-out tests for characterization of the bond stress-slip behaviour between ABS and cementitious matrix. An example of such a setup is given in Figure 8.1. Therein, a circular 3D printed ABS bar attached to a larger circular base is fixed at its bottom, whilst a partially hollow circular piece of mortar is pushed downward. A certain section of the mortar is in contact with the printed ABS, which can be used to measure the bond stress-slip response. A plastic tube should ensure that parts of the mortar remain hollow during casting. Tape (or glue) would prevent mortar from getting into these hollow portions. Important remaining questions are what the size of the sample should be, how large the load will be, and where and how to install a Linear Variable Displacement Transducer (LVDT). However, the author realizes that there is still a (minor) difference between tension (pull-out) and compression (push-out) due to Poisson's ratio effects. Since the 3D-printed ABS has a positive Poisson's ratio it expands in compression, thereby improving the bond under push-out conditions. In tension, the bond will be weaker due to lateral contraction of the ABS, causing more tensile stresses and strains in the bonded region during pull-out.

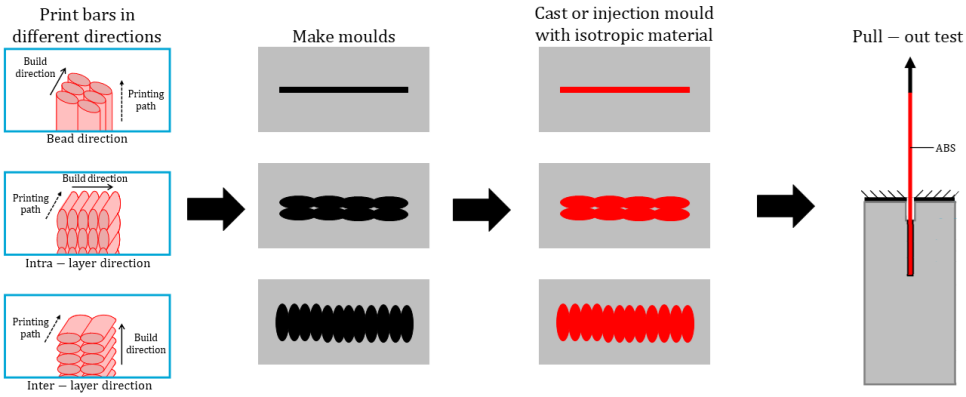

Figure 8.2: Pull-out test method for testing bond behaviour in mutually orthogonal printing configurations

Another method would be to first print ABS bars in the three different mutually orthogonal printing configurations and creating molds for each direction, see Figure 8.2. These could be used for casting or injection molding an isotropic material (e.g., ABS) without intra-layer and inter-layer bond weaknesses. Afterwards, the isotropic specimens containing effects of the different geometrical configurations could be casted into a cementitious matrix and subjected to pull-out tests for obtaining the directional-dependent bond behaviour.

8.2.3. TAILORED POISSON'S RATIO-REINFORCEMENT

Chapter 6 explored the opportunity to tailor the Poisson's ratio of 3D printed reinforcements to align with local stress distributions in bending. Tailored Poisson's Ratio-reinforcements (TPR) were proposed, characterized by a linear gradient of Poisson's ratio along the height of the reinforcement to accommodate varying stress profiles within beams. Specifically, the top chords of TPR exhibit negative Poisson's ratios (auxetic), undergoing lateral contraction under compression, and providing confinement to the surrounded matrix. Conversely, the bottom chords possess positive Poisson's ratios, contributing to lateral contraction under tension.

Even though the current work presented a novel reinforcement mechanism that shows a high degree of efficiency, synergy and potential practicality, it is important to identify remaining hurdles. To gain more insight in the composite interplay between TPR and cementitious matrix, some prospects for future research are listed below.

DECREASING REINFORCEMENT RATIO

Although Chapter 6 considered relatively low reinforcement ratios (14.6 % to 14.7 %), it is believed that this amount can be (significantly) decreased to get closer to traditional reinforcement values. Optimization methods, such as topology optimization, present opportunities to further reduce volume fractions in TPR designs provided the increases in load capacity and toughness are maintained. For instance, material could be removed from low stress regions by following examples from construction practice, like perforated beams where material is removed around the neutral axis.

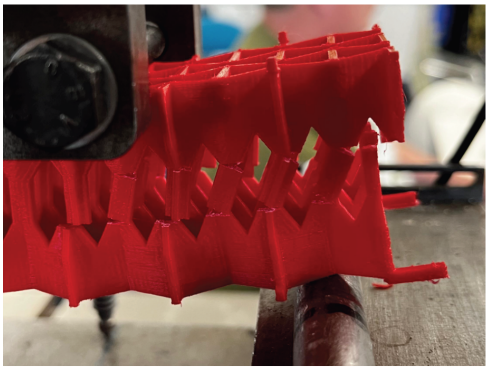

Figure 8.3: Designs with perforations failed due to shear fracture in the thin sections at the center of the reinforcement

Several BSc students (Quinten & Sybren) under supervision of the author investigated possibilities to decrease the reinforcement ratio of the developed TPR designs discussed in Chapter 6 by means of FDM 3D printing. However, their experimental results showed that reducing the amount of ABS significantly deteriorated the mechanical performance of both the standalone reinforcement and reinforced cementitious composites due to the material properties of the 3D printed material (i.e., mechanical anisotropy and limited strength). For instance, all the designs with perforations by Quinten failed due to shear fracture in the thin sections at the center of the reinforcement, caused by horizontal delamination as a result of the weak inter-layer bond. This is clearly visible in Figure 8.3. Sybren attempted to design the reinforcement perforations according to the principal stress directions in a concrete beam. Nonetheless, these designs suffered the same problems related to the FDM 3D printed material as pointed out before. Therefore, it is recommended to explore other reinforcing materials and printing techniques.

8

EXPLORING OTHER REINFORCING MATERIALS AND PRINTING TECHNIQUES

Building on the foregoing, ABS is a relatively strong and stiff polymer filament that is compatible with FDM 3D printing. However, there are many more filaments to choose from that have better inter-layer adhesion than ABS, such as Thermoplastic PolyUrethane (TPU). Additionally, various AM techniques besides FDM enable the construction of polymeric and metallic reinforcements, such as StereoLithograPhy (SLA), Powder Bed Fusion (PBF) or Selective Laser Sintering (SLS). These processes could mitigate the printing path-dependent anisotropy present in FDM 3D printed polymers. Another approach might be the Lost Mould Technique (LMT), which makes use of FDM to create a model of the reinforcement. Metallic reinforcements would also be stronger and stiffer compared to their polymeric counterparts.

COMPARISON WITH TRADITIONAL REINFORCEMENT

To truly evaluate the efficiency and potential of TPR with respect to construction practice, comparisons with traditionally reinforced cementitious composites on the same scale are needed. Only then will the real potential be uncovered before proceeding towards upscaling.

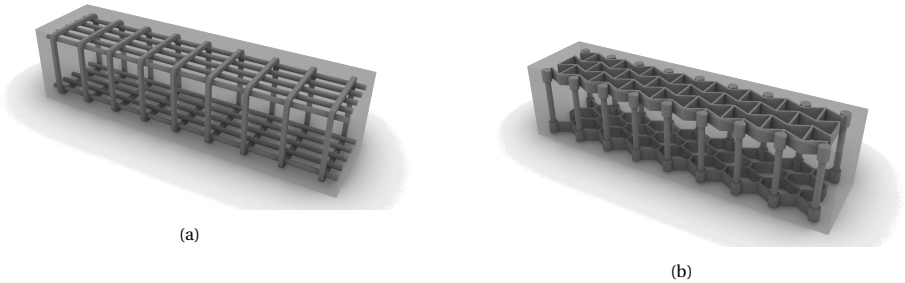

(a) (b)

Figure 8.4: Comparison between (a) traditional reinforcement and (b) TPR

As commented in Chapter 6, the printing path-dependent anisotropy of TPR seems to be the limiting factor in the developed cementitious composites. Considering the exploration of other reinforcement materials, it is therefore recommended to use steel TPR. To this end, a fair comparison with small-scale traditional reinforcement is proposed made of threaded rods (M3) having the same amount of top and bottom (i.e., compression and tension) reinforcement as planar versions of the auxetic top chords and positive Poisson's ratio bottom chords found in TPR, see Figure 8.4. Instead of having varying cross-sections along the height of the reinforcements, planar patterns are envisioned that can be cut from steel sheets and connected by bolted joints through threaded rods (M3) functioning as stirrups. It is particularly important to have the same effective longitudinal cross-sectional areas and longitudinal volumes in all reinforcement designs. As a reference, it was found that having five threaded rods of size M3 as traditional compression and tension reinforcement matches with planar TPR designs with a strut width of 1 mm cut from a steel plate of 6 mm in thickness.

UPSCALING

Chapter 6 only considers small-scale specimens (i.e., $160 \times 40 \times 40$ mm), such that size effects and structural boundary conditions (e.g., in real beams or slabs) are not covered and require future studies. Regarding upscaling, practical considerations in terms of materials, manufacturing techniques, and transportation need to be taken into account.

As a starting point for upscaling, one possibility would be to use "braided" traditional reinforcement as exemplified in Figure 8.5. Rather than needing novel materials, manufacturing techniques, and means of transportation, the idea is to braid traditional reinforcement bars into shapes representing the auxetic and non-auxetic geometries defined for the TPR designs. The steel bars representing longitudinal reinforcement could be continuous but bent in angles corresponding to the TPR geometries. The transverse struts connecting these longitudinal bars could be made of small hoops, enabling the combination of longitudinal and transverse reinforcement to exhibit deformation mechanisms in accordance to their designed Poisson's ratio. To keep a low reinforcement ratio (e.g., $\rho < 5\%$) small bar diameters should be applied, and increasing the laterally confined areas in the concrete could be achieved by using multiple layers of braided bars (see Figure 8.5).

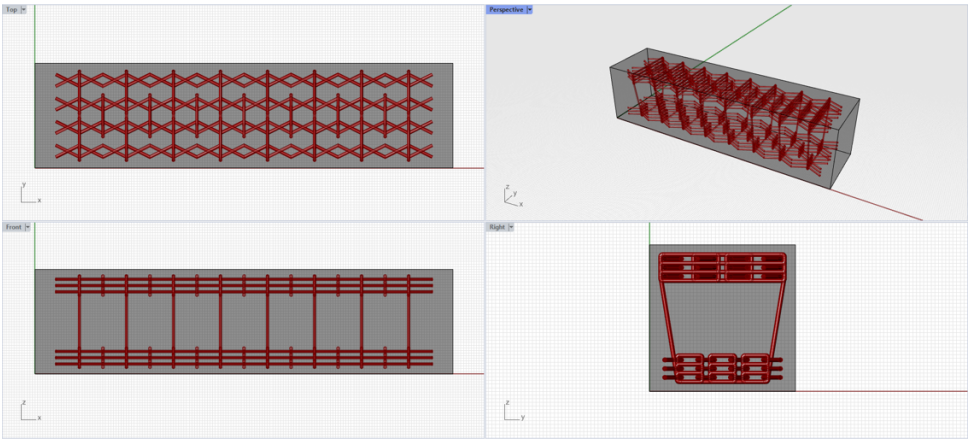

Figure 8.5: "Braided" traditional reinforcement bars into shapes representing auxetic and non-auxetic geometries

Moreover, the practical implementation of TPRCC requires consideration of manufacturing scalability, structural applicability, cost, durability, and material sustainability. The manufacturing cost of FDM-produced components depends not only on polymer feedstock but also on printing parameters, machine characteristics, production volume, and energy consumption [212]. For TPR, this suggests that economic feasibility should ultimately be assessed in terms of the cost per unit of structural performance rather than polymer mass alone. In particular, the material efficiency inherent to lattice reinforcement could be advantageous if polymer is concentrated only where required mechanically, which is currently not the case. Scaling conventional filament-based FDM to structural dimensions is nevertheless constrained by deposition rate, thermal management, and the trade-off between printing speed and geometric resolution [213]. Large-Format Additive Manufacturing (LFAM) based on pellet extrusion therefore provides a potentially more suitable route towards industrial-scale TPR production, as it enables substantially higher material throughput and avoids the additional processing required to manufacture filament [214]. However, larger deposition rates and nozzle dimensions introduce challenges associated with dimensional accuracy, thermal gradients, warpage, residual stresses, and inter-layer bonding [214]. These effects may be particularly important for TPR because deviations from the designed lattice geometry can directly affect its mechanical response. Future work should therefore investigate manufacturing-aware lattice optimization, in which minimum feature size, nozzle diameter, deposition rate, and process-induced geometric variability are incorporated alongside mechanical performance. Automated process monitoring could further improve reproducibility during large-scale production.

8.2.4. PRESTRESSING LATTICE METAMATERIALS

Prestressing in lattice metamaterials with the aim of improving load-bearing capacity remains largely unexplored. However, Li et al. [183] recently provided some useful insight into this niche subject, although their research was entirely based on computer simulations without physical testing. This led a BSc student, Jonathan, under supervision

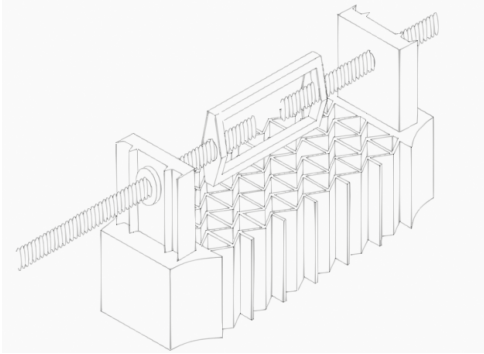

Figure 8.6: Schematic of the turnbuckle-based prestressing mechanism

of the author to design and manufacture a preliminary small-scale prestressing device (see Figure 8.6). Most auxetic designs consist of a periodic pattern, such that any practical pulling mechanism needs some standardized external grip points. These external grip points are the interface between the auxetic architecture and the mechanical parts of the prestressing mechanism. There are various ways to separate the two ends of a lattice under loading. One example is a reversed clamp, but the problem with such spreader is that they are often quite bulky, with a lot of appended parts. A more elegant option was found in the turnbuckle, a device/mechanical part which is most commonly used to adjust the tension of ropes and cables. It consists of two threaded eye bolts, and a small brass brace with two threaded openings. The trick is that these openings have threads going in opposite directions; one is a conventional right-handed thread, the other a left-handed thread. The same goes for the eye bolts. As such, one can attach their rope ends to the eye bolts and turning the turnbuckle will cause the bolts to thread towards each other, causing a tension increase. Naturally, this mechanism can also be used in the opposite way. This forms the basis for the design of the prestressing mechanism.

Figure 8.6 presents a lattice with two solid extensions. Each extension contains an identical slot, which goes all the way down. These slots facilitate pins which directly fit into the slots. Their cross-section is only slightly under dimensioned compared to the slot size so that it fits tightly. The pins stick out above the face of the lattice. In this external part there is a circular protrusion. These are guide holes for the eye bolts which will pass through. Two eye bolts can therefore meet inside the turnbuckle that hangs over the lattice. It is realized that this mechanism mechanism will not yet reach the desired result and that additional optimization is still needed. However, it is believed that there is great potential in future research on prestressing lattice metamaterials to further leverage the applications of lateral confinement mechanisms in cementitious materials.

8.3. LIMITATIONS

The developed methods and results contained in this thesis have provided valuable research insights. Nevertheless, the author acknowledges several limitations specifically related to the TPRCC designs and their corresponding simulations. The lattice modelling framework described in Chapter 7 is capable of successfully simulating the mechanical

and physical phenomena in TPRCC designs with reasonable accuracy, including the unveiling of internal lateral confinement mechanisms. However, it must be emphasized that the numerical descriptions have limitations for the following reasons:

- The constitutive relationships for the TPR in the current lattice models are calibrated for another 3D printer (Ultimaker S2+) and different printer settings than the experimental campaign in Chapter 6 (Ultimaker S5). For the results in this study it was assumed that the properties of the 3D-printed material will not be significantly different as a result of the other 3D printer and updated printer settings, although it is realized that changes in the printer settings can result in deviating mechanical response as pointed out in Chapter 2. Obtaining concluding results will therefore require new microstructural experimental analysis and recalibration of the lattice model using newly recorded material scale constitutive relationships for the different printer and printer settings.

- The complex geometries of the reinforcements cause complex and variational stress states in the bond elements with cementitious matrix during the analysis progress, such that their constitutive relationships remain a disputable concern for the lattice simulations in this work. Due to strain incompatibilities between the TPR polymeric reinforcements and the surrounded cementitious mortar in the TPRCC simulations, many bond elements were initially loaded in tension (i.e., debonding) and changed to compression once the reinforcement started to deform and undergo lateral contraction in order to activate the lateral confinement mechanism. When using the calibrated bond stress-slip behaviour described in Chapter 4, this meant that bond elements in the first phase of the analysis already transitioned into further segments of their multi-linear curve causing impaired stiffness (and strength) when moving from tension to compression later on. As a result of this, the model could not capture the lateral confinement mechanism because the TPR-mortar interface had become too soft. To mitigate this issue, the results presented here were obtained by having non-failing bond elements, meaning that these always keep their initial stiffness and are never removed from the lattice mesh. To ensure sufficient stiffness of the bond for active confinement of the mortar, the elements received the same stiffness as the cementitious matrix. However, finding a more accurate description of the constitutive relationship for the TPR-mortar interface is needed for concluding results, especially for the TPRCC simulations, where it seems that significant debonding and crack closure are necessary to accommodate the lateral confinement mechanism.

- The lack of realistic bond behaviour used in the simulations here is related to the general limitations of the current lattice model on which the proposed models are based. For instance, geometric non-linearities are not included, such that second order effects are neglected. Further, self-contact of initially unconnected elements is not implemented, which would have been particularly useful for a more realistically simulation of the initial debonding followed by the lateral confinement effects associated with compressive lateral loading of the surrounded cementitious matrix.

Besides the limitations of the lattice modelling framework, the author also recognizes that the continuously hollow TPRCC unit cells cause the developed composites to be composed of disconnected cementitious bodies. In other words, the TPR slices the mortar in several separate sections, which is different from conventional reinforcement methods. Analogous to the recommendation of decreasing the reinforcement ratio in the experimental work on TPRCC in Section 8.2.3, using perforated TPR would create a continuous matrix. The overall performance of the composites would most likely be similar, but also different in the sense that the bond between the reinforcement and cementitious material becomes less relevant. The deformations and internal stresses due to the Poisson's ratio effects would then be better transferred to the surrounded mortar.

BIBLIOGRAPHY

[1] C. Buchanan and L. Gardner, "Metal 3d printing in construction: A review of methods, research, applications, opportunities and challenges," *Engineering Structures*, vol. 180, pp. 332–348, 2 2019. [Online]. Available: https://doi.org/10.1016/j.engstruct.2018.11.045

[2] F. Bos, R. Wolfs, Z. Ahmed, and T. Salet, "Additive manufacturing of concrete in construction: potentials and challenges of 3d concrete printing," *Virtual and Physical Prototyping*, vol. 11, pp. 209–225, 7 2016. [Online]. Available: https://doi.org/10.1080/17452759.2016.1209867

[3] H. K. Kim, C. G. Cho, S. J. Lee, Y. H. Lee, and T. Kim, "Structural performance and reinforcement improvement of structural walls using strain-hardening cementitious composites," *Sustainability (Switzerland)*, vol. 13, 4 2021. [Online]. Available: https://doi.org/10.3390/su13073607

[4] R. Yu, L. V. Beers, P. Spiesz, and H. J. Brouwers, "Impact resistance of a sustainable ultra-high performance fibre reinforced concrete (uhpfrc) under pendulum impact loadings," *Construction and Building Materials*, vol. 107, pp. 203–215, 3 2016. [Online]. Available: https://doi.org/10.1016/j.conbuildmat.2015.12.157

[5] S. L. Billington and J. K. Yoon, "Cyclic response of unbonded posttensioned precast columns with ductile fiber-reinforced concrete," *Journal of Bridge Engineering*, vol. 9, pp. 353–363, 2004. [Online]. Available: https://doi.org/10.1061/ASCE1084-070220049:4353

[6] R. Barhemat, S. Mahjoubi, W. Meng, and Y. Bao, "Automated design of architectured polymer-concrete composites with high specific flexural strength and toughness using sequential learning," *Construction and Building Materials*, vol. 449, 10 2024. [Online]. Available: https://doi.org/10.1016/j.conbuildmat.2024.138311

[7] H. Tanaka, "Effect of lateral confining reinforcement on the ductile behaviour of reinforced concrete columns," Ph.D. dissertation, University of Canterbury, 1990. [Online]. Available: https://ir.canterbury.ac.nz/items/d1da440c-30bb-4786-bc88-036352475315

[8] H. Sezen, A. S. Whittaker, K. J. Elwood, and K. M. Mosalam, "Performance of reinforced concrete buildings during the kocaeli, turkey earthquake, and seismic design and construction practise in turkey," *Engineering Structures*, vol. 25, pp. 103–114, 2003. [Online]. Available: www.elsevier.com/locate/engstruct

[9] J. Du, W. Meng, K. H. Khayat, Y. Bao, P. Guo, Z. Lyu, A. Abu-obeidah, H. Nassif, and H. Wang, "New development of ultra-high-performance concrete (uhpc)," 11 2021. [Online]. Available: https://doi.org/10.1016/j.compositesb.2021.109220

[10] P. Guo, W. Meng, and Y. Bao, "Automatic identification and quantification of dense microcracks in high-performance fiber-reinforced cementitious composites through deep learning-based computer vision," *Cement and Concrete Research*, vol. 148, 10 2021. [Online]. Available: https://doi.org/10.1016/j.cemconres.2021.106532

[11] M. Xu, Y. Bao, K. Wu, T. Xia, H. L. Clack, H. Shi, and V. C. Li, "Influence of tio2 incorporation methods on nox abatement in engineered cementitious composites," *Construction and Building Materials*, vol. 221, pp. 375–383, 10 2019. [Online]. Available: https://doi.org/10.1016/j.conbuildmat.2019.06.053

[12] H. H. Nguyn, P. H. Nguyn, Q. H. Lng, W. Meng, and B. Y. Lee, "Mechanical and autogenous healing properties of high-strength and ultra-ductility engineered geopolymer composites reinforced by pe-pva hybrid fibers," *Cement and Concrete Composites*, vol. 142, 9 2023. [Online]. Available: https://doi.org/10.1016/j.cemconcomp.2023.105155

[13] L. Fan, Y. Bao, W. Meng, and G. Chen, "In-situ monitoring of corrosion-induced expansion and mass loss of steel bar in steel fiber reinforced concrete using a distributed fiber optic sensor," *Composites Part B: Engineering*, vol. 165, pp. 679–689, 5 2019. [Online]. Available: https://doi.org/10.1016/j.compositesb.2019.02.051

[14] L. Fan, W. Meng, L. Teng, and K. H. Khayat, "Effect of steel fibers with galvanized coatings on corrosion of steel bars embedded in uhpc," *Composites Part B: Engineering*, vol. 177, 11 2019. [Online]. Available: https://doi.org/10.1016/j.compositesb.2019.107445

[15] Y. Zeng, X. Zhou, A. Tang, and P. Sun, "Mechanical properties of chopped basalt fiber-reinforced lightweight aggregate concrete and chopped polyacrylonitrile fiber reinforced lightweight aggregate concrete," *Materials*, vol. 13, 4 2020. [Online]. Available: https://doi.org/10.3390/ma13071715

[16] W. Meng and K. H. Khayat, "Mechanical properties of ultra-high-performance concrete enhanced with graphite nanoplatelets and carbon nanofibers," *Composites Part B: Engineering*, vol. 107, pp. 113–122, 12 2016. [Online]. Available: https://doi.org/10.1016/j.compositesb.2016.09.069

[17] W. Meng, M. Valipour, and K. H. Khayat, "Optimization and performance of cost-effective ultra-high performance concrete," *Materials and Structures/Materiaux et Constructions*, vol. 50, 2 2017. [Online]. Available: https://doi.org/10.1617/s11527-016-0896-3

[18] W. Meng and K. H. Khayat, "Improving flexural performance of ultra-high-performance concrete by rheology control of suspending mortar," *Composites Part B: Engineering*, vol. 117, pp. 26–34, 5 2017. [Online]. Available: https://doi.org/10.1016/j.compositesb.2017.02.019

[19] L. Teng, W. Meng, and K. H. Khayat, "Rheology control of ultra-high-performance concrete made with different fiber contents," *Cement and Concrete Research*, vol. 138, 12 2020. [Online]. Available: https://doi.org/10.1016/j.cemconres.2020.106222

[20] S. Iqbal, A. Ali, K. Holschemacher, and T. A. Bier, "Mechanical properties of steel fiber reinforced high strength lightweight self-compacting concrete (shlscc)," *Construction and Building Materials*, vol. 98, pp. 325–333, 11 2015. [Online]. Available: https://doi.org/10.1016/j.conbuildmat.2015.08.112

[21] Y. Liu, Z. Zhang, C. Shi, D. Zhu, N. Li, and Y. Deng, "Development of ultra-high performance geopolymer concrete (uhpgc): Influence of steel fiber on mechanical properties," *Cement and Concrete Composites*, vol. 112, 9 2020. [Online]. Available: https://doi.org/10.1016/j.cemconcomp.2020.103670

[22] S. J. Barnett, J.-F. Lataste, and S. Millard, "Assessment of fibre orientation

in ultra high performance fibre reinforced concrete and its effect on flexural strength responsible sourcing in construction view project sus-con view project," *Materials and Structures*, vol. 43, pp. 1009–1023, 2009. [Online]. Available: https://www.researchgate.net/publication/312917132

[23] P. Stähli and J. G. van Mier, "Manufacturing, fibre anisotropy and fracture of hybrid fibre concrete," *Engineering Fracture Mechanics*, vol. 74, pp. 223–242, 1 2007. [Online]. Available: https://doi.org/10.1016/j.engfracmech.2006.01.028

[24] A. Mudadu, G. Tiberti, F. Germano, G. A. Plizzari, and A. Morbi, "The effect of fiber orientation on the post-cracking behavior of steel fiber reinforced concrete under bending and uniaxial tensile tests," *Cement and Concrete Composites*, vol. 93, pp. 274–288, 10 2018. [Online]. Available: https://doi.org/10.1016/j.cemconcomp.2018.07.012

[25] G. D. Schutter, K. Lesage, V. Mechtcherine, V. N. Nerella, G. Habert, and I. Agusti-Juan, "Vision of 3d printing with concrete — technical, economic and environmental potentials," *Cement and Concrete Research*, vol. 112, pp. 25–36, 10 2018. [Online]. Available: https://doi.org/10.1016/j.cemconres.2018.06.001

[26] C. Gosselin, R. Duballet, P. Roux, N. Gaudillière, J. Dirrenberger, and P. Morel, "Large-scale 3d printing of ultra-high performance concrete - a new processing route for architects and builders," *Materials and Design*, vol. 100, pp. 102–109, 6 2016. [Online]. Available: https://doi.org/10.1016/j.matdes.2016.03.097

[27] A. A. Zadpoor, "Mechanical meta-materials," *Materials Horizons*, vol. 3, pp. 371–381, 9 2016. [Online]. Available: https://doi.org/10.1039/c6mh00065g

[28] M. Kadic, G. W. Milton, M. V. Hecke, and M. Wegener, "3d metamaterials," *Nature Reviews Physics*, vol. 1, 2019. [Online]. Available: https://doi.org/10.1038/s42254-018-0018-y

[29] Y. Xu, "Architected cementitious cellular materials towards auxetic behavior," Ph.D. dissertation, Delft University of Technology, 2021. [Online]. Available: https://doi.org/10.4233/uuid:1a9e29a6-4868-4096-bc88-a1095cf568d3

[30] T. C. Lim, "Analogies across auxetic models based on deformation mechanism," *Physica Status Solidi - Rapid Research Letters*, vol. 11, 6 2017. [Online]. Available: https://doi.org/10.1002/pssr.201600440

[31] J. J. Warner, A. R. Gillies, H. H. Hwang, H. Zhang, R. L. Lieber, and S. Chen, "3d-printed biomaterials with regional auxetic properties," *Journal of the Mechanical Behavior of Biomedical Materials*, vol. 76, pp. 145–152, 12 2017. [Online]. Available: https://doi.org/10.1016/j.jmbbm.2017.05.016

[32] S. Maran, I. G. Masters, and G. J. Gibbons, "Additive manufacture of 3d auxetic structures by laser powder bed fusion—design influence on manufacturing accuracy and mechanical properties," *Applied Sciences (Switzerland)*, vol. 10, pp. 1–19, 11 2020. [Online]. Available: https://doi.org/10.3390/app10217738

[33] M. S. Rad, Y. Prawoto, and Z. Ahmad, "Analytical solution and finite element approach to the 3d re-entrant structures of auxetic materials," *Mechanics of Materials*, vol. 74, pp. 76–87, 2014. [Online]. Available: https://doi.org/10.1016/j.mechmat.2014.03.012

[34] A. Joseph, V. Mahesh, and D. Harursampath, "On the application of additive manufacturing methods for auxetic structures: a review," *Advances in*

Manufacturing, vol. 9, pp. 342–368, 9 2021. [Online]. Available: https://doi.org/10.1007/s40436-021-00357-y

[35] K. E. Evans and A. Alderson, "Auxetic materials: Functional materials and structures from lateral thinking!" *Advanced Materials*, vol. 12, pp. 617–628, 2000. [Online]. Available: https://doi.org/10.1002/(SICI)1521-4095(200005)12:9<617::AID-ADMA617>3.0.CO;2-3

[36] V. A. Lvov, F. S. Senatov, A. A. Stepashkin, A. A. Veveris, M. D. Pavlov, and A. A. Komissarov, "Low-cycle fatigue behavior of 3d-printed metallic auxetic structure," *Materials Today: Proceedings*, vol. 33, pp. 1979–1983, 2020. [Online]. Available: https://doi.org/10.1016/j.matpr.2020.06.130

[37] C.-H. Hsueh, S. Schmauder, C.-S. Chen, K. K. Chawla, N. Chawla, W. Chen, and Y. Kagawa, *Handbook of Mechanics of Materials*. Springer Nature Singapore Pte Ltd., 2019. [Online]. Available: https://doi.org/10.1007/978-981-10-6884-3

[38] J. Carlos, A. Elipe, and A. D. Lantada, "Comparative study of auxetic geometries by means of computer-aided design and engineering," *Smart Materials and Structures*, vol. 21, 2012. [Online]. Available: https://doi.org/10.1088/0964-1726/21/10/105004

[39] H. M. Kolken, K. Lietaert, T. van der Sloten, B. Pouran, A. Meynen, G. V. Loock, H. Weinans, L. Scheys, and A. A. Zadpoor, "Mechanical performance of auxetic meta-biomaterials," *Journal of the Mechanical Behavior of Biomedical Materials*, vol. 104, 4 2020. [Online]. Available: https://doi.org/10.1016/j.jmbbm.2020.103658

[40] X. T. Wang, B. Wang, X. W. Li, and L. Ma, "Mechanical properties of 3d re-entrant auxetic cellular structures," *International Journal of Mechanical Sciences*, vol. 131-132, pp. 396–407, 10 2017. [Online]. Available: https://doi.org/10.1016/j.ijmecsci.2017.05.048

[41] T. Li, Y. Chen, X. Hu, Y. Li, and L. Wang, "Exploiting negative poisson's ratio to design 3d-printed composites with enhanced mechanical properties," *Materials and Design*, vol. 142, pp. 247–258, 3 2018. [Online]. Available: https://doi.org/10.1016/j.matdes.2018.01.034

[42] Y. Xu, H. Zhang, E. Schlangen, M. Luković, and B. Šavija, "Cementitious cellular composites with auxetic behavior," *Cement and Concrete Composites*, vol. 111, 8 2020. [Online]. Available: https://doi.org/10.1016/j.cemconcomp.2020.103624

[43] Y. Xu, E. Schlangen, M. Luković, and B. Šavija, "Tunable mechanical behavior of auxetic cementitious cellular composites (cccs): Experiments and simulations," *Construction and Building Materials*, vol. 266, 1 2021. [Online]. Available: https://doi.org/10.1016/j.conbuildmat.2020.121388

[44] G. A. Lyngdoh, N. K. Kelter, S. Doner, N. M. Krishnan, and S. Das, "Elucidating the auxetic behavior of cementitious cellular composites using finite element analysis and interpretable machine learning," *Materials and Design*, vol. 213, 1 2022. [Online]. Available: https://doi.org/10.1016/j.matdes.2021.110341

[45] X. Ren, J. Shen, P. Tran, T. D. Ngo, and Y. M. Xie, "Auxetic nail: Design and experimental study," *Composite Structures*, vol. 184, pp. 288–298, 1 2018. [Online]. Available: https://doi.org/10.1016/j.compstruct.2017.10.013

[46] K. E. Evans, "Auxetic polymers: a new range of materials," *Endeavour*, vol. 15, pp. 170–174, 1991. [Online]. Available: https://doi.org/10.1016/0160-9327(91)90123-S

[47] R. Lakes, "Foam structures with a negative poisson's ratio," *Science*, vol. 235, pp.

1038–40, 2 1987. [Online]. Available: www.sciencemag.org

[48] Y. Yao, L. Wang, J. Li, S. Tian, M. Zhang, and Y. Fan, "A novel auxetic structure based bone screw design: Tensile mechanical characterization and pullout fixation strength evaluation," *Materials and Design*, vol. 188, 3 2020. [Online]. Available: https://doi.org/10.1016/j.matdes.2019.108424

[49] D. Edmund, T. Zahra, M. Asad, and J. Thamboo, "Experimental investigation on tensile characteristics of 3d printed auxetic embedded cementitious composites and shear bonding behaviour to masonry," *Journal of Building Engineering*, vol. 97, 11 2024. [Online]. Available: https://doi.org/10.1016/j.jobe.2024.110749

[50] S. Paul, "Finite element analysis in fused deposition modeling research: A literature review," *Measurement: Journal of the International Measurement Confederation*, vol. 178, 6 2021. [Online]. Available: https://doi.org/10.1016/j.measurement.2021.109320

[51] G. Alaimo, S. Marconi, L. Costato, and F. Auricchio, "Influence of meso-structure and chemical composition on fdm 3d-printed parts," *Composites Part B: Engineering*, vol. 113, pp. 371–380, 3 2017. [Online]. Available: https://doi.org/10.1016/j.compositesb.2017.01.019

[52] M. Domingo-Espin, J. M. Puigoriol-Forcada, A. A. Garcia-Granada, J. Llumà, S. Borros, and G. Reyes, "Mechanical property characterization and simulation of fused deposition modeling polycarbonate parts," *Materials and Design*, vol. 83, pp. 670–677, 10 2015. [Online]. Available: https://doi.org/10.1016/j.matdes.2015.06.074

[53] Y. Song, Y. Li, W. Song, K. Yee, K. Y. Lee, and V. L. Tagarielli, "Measurements of the mechanical response of unidirectional 3d-printed pla," *Materials and Design*, vol. 123, pp. 154–164, 6 2017. [Online]. Available: https://doi.org/10.1016/j.matdes.2017.03.051

[54] T. W. Kerekes, H. Lim, W. Y. Joe, and G. J. Yun, "Characterization of process–deformation/damage property relationship of fused deposition modeling (fdm) 3d-printed specimens," *Additive Manufacturing*, vol. 25, pp. 532–544, 1 2019. [Online]. Available: https://doi.org/10.1016/j.addma.2018.11.008

[55] A. Garg and A. Bhattacharya, "An insight to the failure of fdm parts under tensile loading: finite element analysis and experimental study," *International Journal of Mechanical Sciences*, vol. 120, pp. 225–236, 1 2017. [Online]. Available: https://doi.org/10.1016/j.ijmecsci.2016.11.032

[56] X. Wang, L. Zhao, J. Y. H. Fuh, and H. P. Lee, "Effect of porosity on mechanical properties of 3d printed polymers: Experiments and micromechanical modeling based on x-ray computed tomography analysis," *Polymers*, vol. 11, 2019. [Online]. Available: https://doi.org/10.3390/polym11071154

[57] D. Croccolo, M. D. Agostinis, and G. Olmi, "Experimental characterization and analytical modelling of the mechanical behaviour of fused deposition processed parts made of abs-m30," *Computational Materials Science*, vol. 79, pp. 506–518, 2013. [Online]. Available: https://doi.org/10.1016/j.commatsci.2013.06.041

[58] M. S. Anoop and P. Senthil, "Microscale representative volume element based numerical analysis on mechanical properties of fused deposition modelling components," *Materials Today: Proceedings*, vol. 39, pp. 563–571, 2020. [Online]. Available: https://doi.org/10.1016/j.matpr.2020.08.469

[59] S. Guessasma, H. Nouri, and F. Roger, "Microstructural and mechanical implications of microscaled assembly in droplet-based multi-material additive manufacturing," *Polymers*, vol. 9, 8 2017. [Online]. Available: https://doi.org/10.3390/polym9080372

[60] H. R. Dana, F. Barbe, L. Delbreilh, M. B. Azzouna, A. Guillet, and T. Breteau, "Polymer additive manufacturing of abs structure: Influence of printing direction on mechanical properties," *Journal of Manufacturing Processes*, vol. 44, pp. 288–298, 8 2019. [Online]. Available: https://doi.org/10.1016/j.jmapro.2019.06.015

[61] Q. Sun, G. M. Rizvi, C. T. Bellehumeur, and P. Gu, "Effect of processing conditions on the bonding quality of fdm polymer filaments," *Rapid Prototyping Journal*, vol. 14, pp. 72–80, 3 2008. [Online]. Available: https://doi.org/10.1108/13552540810862028

[62] J. C. Riddick, M. A. Haile, R. V. Wahlde, D. P. Cole, O. Bamiduro, and T. E. Johnson, "Fractographic analysis of tensile failure of acrylonitrile-butadiene-styrene fabricated by fused deposition modeling," *Additive Manufacturing*, vol. 11, pp. 49–59, 7 2016. [Online]. Available: https://doi.org/10.1016/j.addma.2016.03.007

[63] A. Nasirov and I. Fidan, "Prediction of mechanical properties of fused filament fabricated structures via asymptotic homogenization," *Mechanics of Materials*, vol. 145, 6 2020. [Online]. Available: https://doi.org/10.1016/j.mechmat.2020.103372

[64] T. Yao, K. Zhang, Z. Deng, and J. Ye, "A novel generalized stress invariant-based strength model for inter-layer failure of fff 3d printing pla material," *Materials and Design*, vol. 193, 8 2020. [Online]. Available: https://doi.org/10.1016/j.matdes.2020.108799

[65] D. Qiao, B. Wang, and H. Gu, "Additive manufacturing: Challenges and solutions for marine and offshore applications," in *Volume 3: Materials Technology*. American Society of Mechanical Engineers, 8 2020. [Online]. Available: https://doi.org/10.1115/OMAE2020-18922

[66] A. Bacciaglia, A. Ceruti, and A. Liverani, "A design of experiment approach to 3d-printed mouthpieces sound analysis," *Progress in Additive Manufacturing*, vol. 6, pp. 571–587, 8 2021. [Online]. Available: https://doi.org/10.1007/s40964-021-00183-5

[67] S. H. Ahn, M. Montero, D. Odell, S. Roundy, and P. K. Wright, "Anisotropic material properties of fused deposition modeling abs," *Rapid Prototyping Journal*, vol. 8, pp. 248–257, 2002. [Online]. Available: https://doi.org/10.1108/13552540210441166

[68] C. Koch, L. V. Hulle, and N. Rudolph, "Investigation of mechanical anisotropy of the fused filament fabrication process via customized tool path generation," *Additive Manufacturing*, vol. 16, pp. 138–145, 8 2017. [Online]. Available: https://doi.org/10.1016/j.addma.2017.06.003

[69] A. Armillotta, "Simulation of edge quality in fused deposition modeling," *Rapid Prototyping Journal*, vol. 25, pp. 541–554, 4 2019. [Online]. Available: https://doi.org/10.1108/RPJ-06-2018-0151

[70] L. D. Angelo, P. D. Stefano, and A. Marzola, "Surface quality prediction in fdm additive manufacturing," *International Journal of Advanced Manufacturing Technology*, vol. 93, pp. 3655–3662, 12 2017. [Online]. Available: https://doi.org/10.1007/s00170-017-0763-6

[71] M. E. Haque, D. Banerjee, S. B. Mishra, and B. K. Nanda, "A numerical approach to measure the surface roughness of fdm build part," *Materials Today: Proceedings*, vol. 18, pp. 5523–5529, 2019. [Online]. Available: www.sciencedirect.comwww.

materialstoday.com/proceedings2214-7853

[72] D. Ahn, J. H. Kweon, S. Kwon, J. Song, and S. Lee, "Representation of surface roughness in fused deposition modeling," *Journal of Materials Processing Technology*, vol. 209, pp. 5593–5600, 8 2009. [Online]. Available: https://doi.org/10.1016/j.jmatprotec.2009.05.016

[73] E. Monaldo and S. Marfia, "Multiscale technique for the analysis of 3d-printed materials," *International Journal of Solids and Structures*, vol. 232, 12 2021. [Online]. Available: https://doi.org/10.1016/j.ijsolstr.2021.111173

[74] ——, "Modelling of damage and plasticity phenomena in 3d printed materials via a multiscale approach," *European Journal of Mechanics - A/Solids*, p. 105140, 1 2023. [Online]. Available: https://doi.org/10.1016/j.euromechsol.2023.105140

[75] Y. Xu, H. Zhang, Y. Gan, and B. Šavija, "Cementitious composites reinforced with 3d printed functionally graded polymeric lattice structures: Experiments and modelling," *Additive Manufacturing*, vol. 39, 3 2021. [Online]. Available: https://doi.org/10.1016/j.addma.2021.101887

[76] E. Monaldo, M. Ricci, and S. Marfia, "Mechanical properties of 3d printed polylactic acid elements: Experimental and numerical insights," *Mechanics of Materials*, vol. 177, 2 2023. [Online]. Available: https://doi.org/10.1016/j.mechmat.2022.104551

[77] S. Sharafi, M. H. Santare, J. Gerdes, and S. G. Advani, "A multiscale modeling approach of the fused filament fabrication process to predict the mechanical response of 3d printed parts," *Additive Manufacturing*, vol. 51, 3 2022. [Online]. Available: https://doi.org/10.1016/j.addma.2022.102597

[78] T. D. McLouth, J. V. Severino, P. M. Adams, D. N. Patel, and R. J. Zaldivar, "The impact of print orientation and raster pattern on fracture toughness in additively manufactured abs," *Additive Manufacturing*, vol. 18, pp. 103–109, 12 2017. [Online]. Available: https://doi.org/10.1016/j.addma.2017.09.003

[79] P. K. Gurrala and S. P. Regalla, "Part strength evolution with bonding between filaments in fused deposition modelling: This paper studies how coalescence of filaments contributes to the strength of final fdm part," *Virtual and Physical Prototyping*, vol. 9, pp. 141–149, 2014. [Online]. Available: https://doi.org/10.1080/17452759.2014.913400

[80] C. S. Davis, K. E. Hillgartner, S. H. Han, and J. E. Seppala, "Mechanical strength of welding zones produced by polymer extrusion additive manufacturing," *Additive Manufacturing*, vol. 16, pp. 162–166, 8 2017. [Online]. Available: https://doi.org/10.1016/j.addma.2017.06.006

[81] N. Aliheidari, R. Tripuraneni, A. Ameli, and S. Nadimpalli, "Fracture resistance measurement of fused deposition modeling 3d printed polymers," *Polymer Testing*, vol. 60, pp. 94–101, 7 2017. [Online]. Available: https://doi.org/10.1016/j.polymertesting.2017.03.016

[82] N. Aliheidari, J. Christ, R. Tripuraneni, S. Nadimpalli, and A. Ameli, "Interlayer adhesion and fracture resistance of polymers printed through melt extrusion additive manufacturing process," *Materials and Design*, vol. 156, pp. 351–361, 10 2018. [Online]. Available: https://doi.org/10.1016/j.matdes.2018.07.001

[83] M. Dawoud, I. Taha, and S. J. Ebeid, "Mechanical behaviour of abs: An experimental study using fdm and injection moulding techniques," *Journal*

of Manufacturing Processes, vol. 21, pp. 39–45, 2016. [Online]. Available: https://doi.org/10.1016/j.jmapro.2015.11.002

[84] M. Faes, E. Ferraris, and D. Moens, "Influence of inter-layer cooling time on the quasi-static properties of abs components produced via fused deposition modelling," *Procedia CIRP*, vol. 42, pp. 748–753, 2016. [Online]. Available: https://doi.org/10.1016/j.procir.2016.02.313

[85] I. Khan and N. Kumar, "Fused deposition modelling process parameters influence on the mechanical properties of abs: A review," *Materials Today: Proceedings*, vol. 44, pp. 4004–4008, 2020. [Online]. Available: https://doi.org/10.1016/j.matpr.2020.10.202

[86] Y. Xu, H. Zhang, B. Šavija, S. C. Figueiredo, and E. Schlangen, "Deformation and fracture of 3d printed disordered lattice materials: Experiments and modeling," *Materials and Design*, vol. 162, pp. 143–153, 1 2019. [Online]. Available: https://doi.org/10.1016/j.matdes.2018.11.047

[87] N. Naveed, "Investigating the material properties and microstructural changes of fused filament fabricated pla and tough-pla parts," *Polymers*, vol. 13, 5 2021. [Online]. Available: https://doi.org/10.3390/polym13091487

[88] C. C. Shih, M. Burnette, D. Staack, J. Wang, and B. L. Tai, "Effects of cold plasma treatment on interlayer bonding strength in fff process," *Additive Manufacturing*, vol. 25, pp. 104–111, 1 2019. [Online]. Available: https://doi.org/10.1016/j.addma.2018.11.005

[89] A. Khudiakova, F. Arbeiter, M. Spoerk, M. Wolfahrt, D. Godec, and G. Pinter, "Interlayer bonding characterisation between materials with different degrees of stiffness processed by fused filament fabrication," *Additive Manufacturing*, vol. 28, pp. 184–193, 8 2019. [Online]. Available: https://doi.org/10.1016/j.addma.2019.05.006

[90] N. P. Levenhagen and M. D. Dadmun, "Interlayer diffusion of surface segregating additives to improve the isotropy of fused deposition modeling products," *Polymer*, vol. 152, pp. 35–41, 9 2018. [Online]. Available: https://doi.org/10.1016/j.polymer.2018.01.031

[91] N. Zohdi and R. C. Yang, "Material anisotropy in additively manufactured polymers and polymer composites: A review," *Polymers*, vol. 13, 10 2021. [Online]. Available: https://doi.org/10.3390/polym13193368

[92] H. Prajapati, S. S. Salvi, D. Ravoori, M. Qasaimeh, A. Adnan, and A. Jain, "Improved print quality in fused filament fabrication through localized dispensing of hot air around the deposited filament," *Additive Manufacturing*, vol. 40, 4 2021. [Online]. Available: https://doi.org/10.1016/j.addma.2021.101917

[93] D. Ravoori, H. Prajapati, V. Talluru, A. Adnan, and A. Jain, "Nozzle-integrated pre-deposition and post-deposition heating of previously deposited layers in polymer extrusion based additive manufacturing," *Additive Manufacturing*, vol. 28, pp. 719–726, 8 2019. [Online]. Available: https://doi.org/10.1016/j.addma.2019.06.006

[94] A. K. Ravi, A. Deshpande, and K. H. Hsu, "An in-process laser localized pre-deposition heating approach to inter-layer bond strengthening in extrusion based polymer additive manufacturing," *Journal of Manufacturing Processes*, vol. 24, pp. 179–185, 10 2016. [Online]. Available: https://doi.org/10.1016/j.jmapro.2016.08.007

[95] D. Ege, S. Serttürk, B. Acarkan, and A. Ademoğlu, "Machine learning

models to predict the relationship between printing parameters and tensile strength of 3d poly (lactic acid) scaffolds for tissue engineering applications," *Biomedical Physics & Engineering Express*, 8 2023. [Online]. Available: https://iopscience.iop.org/article/10.1088/2057-1976/acf581

[96] A. International, "Standard test method for tensile properties of plastics," 2014. [Online]. Available: http://www.ansi.org.

[97] ——, "Standard test methods for plane-strain fracture toughness and strain energy release rate of plastic materials," 2014. [Online]. Available: www.astm.org,

[98] ——, "Standard test method for tear-propagation resistance (trouser tear) of plastic film and thin sheeting by a single-tear method," 2014.

[99] O. Lampron, D. Therriault, and M. Lévesque, "Phase-field modeling of fracture in fused filament fabricated thermoplastic parts and experimental validation," *Engineering Fracture Mechanics*, p. 109667, 10 2023. [Online]. Available: https://linkinghub.elsevier.com/retrieve/pii/S0013794423006252

[100] P. Li, J. Yvonnet, C. Combescure, H. Makich, and M. Nouari, "Anisotropic elastoplastic phase field fracture modeling of 3d printed materials," *Computer Methods in Applied Mechanics and Engineering*, vol. 386, 12 2021. [Online]. Available: https://doi.org/10.1016/j.cma.2021.114086

[101] M. R. Khosravani, S. Rezaei, S. Faroughi, and T. Reinicke, "Experimental and numerical investigations of the fracture in 3d-printed open-hole plates," *Theoretical and Applied Fracture Mechanics*, vol. 121, 10 2022. [Online]. Available: https://doi.org/10.1016/j.tafmec.2022.103543

[102] M. R. Khosravani, S. Rezaei, H. Ruan, and T. Reinicke, "Fracture behavior of anisotropic 3d-printed parts: experiments and numerical simulations," *Journal of Materials Research and Technology*, vol. 19, pp. 1260–1270, 7 2022. [Online]. Available: https://doi.org/10.1016/j.jmrt.2022.05.068

[103] I. G. Masters and K. E. Evans, "Models for the elastic deformation of honeycombs," *Composirr Structures*, vol. 35, pp. 403–422, 1996. [Online]. Available: https://doi.org/10.1016/S0263-8223(96)00054-2

[104] L. J. Gibson, "Cellular solids," *MRS Bulletin*, vol. 28, pp. 270–274, 2003. [Online]. Available: https://doi.org/10.1557/mrs2003.79

[105] C. Zmuda, "Design of structural composite with auxetic behavior," Ph.D. dissertation, Worcester Polytechnic Institute, 4 2017. [Online]. Available: http://www.wpi.edu/Academics/Projects.

[106] E. Etemadi, M. Hosseinabadi, F. Scarpa, and H. Hu, "Design, fdm printing, fe and theoretical analysis of auxetic structures consisting of arc-shaped and dumbell-shaped struts under quasi-static loading," *Composite Structures*, vol. 326, 12 2023. [Online]. Available: https://doi.org/10.1016/j.compstruct.2023.117602

[107] S. Askarinejad, H. A. Choshali, C. Flavin, and N. Rahbar, "Effects of tablet waviness on the mechanical response of architected multilayered materials: Modeling and experiment," *Composite Structures*, vol. 195, pp. 118–125, 7 2018. [Online]. Available: https://doi.org/10.1016/j.compstruct.2018.04.047

[108] S. Qin, S. Cao, E. Yilmaz, and J. Li, "Influence of types and shapes of 3d printed polymeric lattice on ductility performance of cementitious backfill composites," *Construction and Building Materials*, vol. 307, 11 2021. [Online]. Available:

https://doi.org/10.1016/j.conbuildmat.2021.124973

[109] C. Tang, J. Liu, W. Hao, and Y. Wei, "Flexural properties of 3d printed graded lattice reinforced cementitious composites using digital image correlation," *Materials and Design*, vol. 227, 3 2023. [Online]. Available: https://doi.org/10.1016/j.matdes.2023.111734

[110] Y. Xu and B. Šavija, "Auxetic cementitious composites (accs) with excellent compressive ductility: Experiments and modeling," *Materials & Design*, vol. 237, p. 112572, 1 2024. [Online]. Available: https://linkinghub.elsevier.com/retrieve/pii/S0264127523009887

[111] Y. Xu, H. Zhang, B. Šavija, S. C. Figueiredo, and E. Schlangen, "Deformation and fracture of 3d printed disordered lattice materials: Experiments and modeling," *Materials and Design*, vol. 162, pp. 143–153, 1 2019. [Online]. Available: https://doi.org/10.1016/j.matdes.2018.11.047

[112] Z. Qian, "3d lattice analysis of cement paste," 4 2008. [Online]. Available: https://doi.org/10.4233/uuid:4137dbe5-fa40-482c-abed-aacae04ddc81

[113] ——, "Multiscale modeling of fracture processes in cementitious materials," Ph.D. dissertation, Delft University of Technology, 9 2012. [Online]. Available: http://resolver.tudelft.nl/uuid:734b276c-283a-4f7a-8db2-a184453e8dac

[114] E. Schlangen, "Experimental and numerical analysis of fracture processes in concrete," Ph.D. dissertation, Delft University of Technology, 1993. [Online]. Available: http://resolver.tudelft.nl/uuid:086bbfba-699b-43fd-a9c6-b0f2bed3e5af

[115] A. Hrennikoff, "Solution of problems of elasticity by the framework method," *Applied Mechanics*, vol. 12, pp. 169–175, 1941. [Online]. Available: http://asmedigitalcollection.asme.org/appliedmechanics/article-pdf/8/4/A169/6744200/a169_1.pdf

[116] B. Šavija, G. E. Smith, D. Liu, E. Schlangen, and P. E. Flewitt, "Modelling of deformation and fracture for a model quasi-brittle material with controlled porosity: Synthetic versus real microstructure," *Engineering Fracture Mechanics*, vol. 205, pp. 399–417, 1 2019. [Online]. Available: https://doi.org/10.1016/j.engfracmech.2018.11.008

[117] J. E. Bolander and S. Saito, "Fracture analyses using spring networks with random geometry," *Engineering Fracture Mechanics*, vol. 61, pp. 569–591, 1998. [Online]. Available: https://doi.org/10.1016/S0013-7944(98)00069-1

[118] M. Yip, Z. Li, B. S. Liao, and J. E. Bolander, "Irregular lattice models of fracture of multiphase particulate materials," *International Journal of Fracture*, vol. 140, pp. 113–124, 7 2006. [Online]. Available: https://doi.org/10.1007/s10704-006-7636-6

[119] M. Sage, J. Girardot, J. B. Kopp, and S. Morel, "A damaging beam-lattice model for quasi-brittle fracture," *International Journal of Solids and Structures*, vol. 239-240, 3 2022. [Online]. Available: https://doi.org/10.1016/j.ijsolstr.2021.111404

[120] J. Tejchman and J. Kozicki, *Experimental and Theoretical Investigations of Steel-Fibrous Concrete*, 2010th ed. Springer-Verlag, 9 2010. [Online]. Available: https://doi.org/10.1007/978-3-642-14603-9

[121] H. Zhang, Y. Xu, Y. Gan, Z. Chang, E. Schlangen, and B. Šavija, "Combined experimental and numerical study of uniaxial compression failure of hardened cement paste at micrometre length scale," *Cement and Concrete Research*, vol. 126,

12 2019. [Online]. Available: https://doi.org/10.1016/j.cemconres.2019.105925

[122] M. Luković, H. Dong, B. Šavija, E. Schlangen, G. Ye, and K. V. Breugel, "Tailoring strain-hardening cementitious composite repair systems through numerical experimentation," *Cement and Concrete Composites*, vol. 53, pp. 200–213, 2014. [Online]. Available: https://doi.org/10.1016/j.cemconcomp.2014.06.017

[123] N. Jiang, Z. Ge, Y. Guan, Z. Zuo, H. Zhang, Y. Ling, and B. Šavija, "Experimentally validated meso-scale fracture modelling of foamed concrete," *Theoretical and Applied Fracture Mechanics*, vol. 122, 12 2022. [Online]. Available: https://doi.org/10.1016/j.tafmec.2022.103631

[124] H. Zhang, Y. Xu, Y. Gan, Z. Chang, E. Schlangen, and B. Šavija, "Microstructure informed micromechanical modelling of hydrated cement paste: Techniques and challenges," *Construction and Building Materials*, vol. 251, 8 2020. [Online]. Available: https://doi.org/10.1016/j.conbuildmat.2020.118983

[125] N. Jiang, H. Zhang, Z. Chang, E. Schlangen, Z. Ge, and B. Šavija, "Discrete lattice fracture modelling of hydrated cement paste under uniaxial compression at micro-scale," *Construction and Building Materials*, vol. 263, 12 2020. [Online]. Available: https://doi.org/10.1016/j.conbuildmat.2020.120153

[126] D. Liu, B. Šavija, G. E. Smith, P. E. Flewitt, T. Lowe, and E. Schlangen, "Towards understanding the influence of porosity on mechanical and fracture behaviour of quasi-brittle materials: experiments and modelling," *International Journal of Fracture*, vol. 205, pp. 57–72, 5 2017. [Online]. Available: https://doi.org/10.1007/s10704-017-0181-7

[127] B. Šavija, M. Luković, J. Pacheco, and E. Schlangen, "Cracking of the concrete cover due to reinforcement corrosion: A two-dimensional lattice model study," *Construction and Building Materials*, vol. 44, pp. 626–638, 2013. [Online]. Available: https://doi.org/10.1016/j.conbuildmat.2013.03.063

[128] Y. Gan, M. Liang, E. Schlangen, K. van Breugel, and B. Šavija, "Two scale models for fracture behaviours of cementitious materials subjected to static and cyclic loadings," *Construction and Building Materials*, vol. 426, p. 136107, 5 2024. [Online]. Available: https://linkinghub.elsevier.com/retrieve/pii/S0950061824012480

[129] D. Gu, S. Mustafa, J. Pan, and M. Luković, "Reinforcement-concrete bond in discrete modeling of structural concrete," *Computer-Aided Civil and Infrastructure Engineering*, 2022. [Online]. Available: https://doi.org/10.1111/mice.12937

[130] S. Mustafa, S. Singh, D. Hordijk, E. Schlangen, and M. Luković, "Experimental and numerical investigation on the role of interface for crack-width control of hybrid shcc concrete beams," *Engineering Structures*, vol. 251, 1 2022. [Online]. Available: https://doi.org/10.1016/j.engstruct.2021.113378

[131] B. Šavija, J. Pacheco, and E. Schlangen, "Lattice modeling of chloride diffusion in sound and cracked concrete," *Cement and Concrete Composites*, vol. 42, pp. 30–40, 2013. [Online]. Available: http://dx.doi.org/10.1016/j.cemconcomp.2013.05.003

[132] B. Šavija, M. Luković, and E. Schlangen, "Lattice modeling of rapid chloride migration in concrete," *Cement and Concrete Research*, vol. 61-62, pp. 49–63, 2014. [Online]. Available: https://doi.org/10.1016/j.cemconres.2014.04.004

[133] Z. Chang, E. Schlangen, and B. Šavija, "Extended lattice model to simulate the printing process of 3d printed cementitious materials," *RILEM Bookseries*, vol. 28,

pp. 814–823, 2020. [Online]. Available: https://doi.org/10.1007/978-3-030-49916-7_80

[134] Z. Chang, Y. Xu, Y. Chen, Y. Gan, E. Schlangen, and B. Šavija, "A discrete lattice model for assessment of buildability performance of 3d-printed concrete," *Computer-Aided Civil and Infrastructure Engineering*, vol. 36, pp. 638–655, 5 2021. [Online]. Available: https://doi.org/10.1111/mice.12700

[135] Z. Chang, M. Liang, Y. Xu, E. Schlangen, and B. Šavija, "3d concrete printing: Lattice modeling of structural failure considering damage and deformed geometry," *Cement and Concrete Composites*, vol. 133, 10 2022. [Online]. Available: https://doi.org/10.1016/j.cemconcomp.2022.104719

[136] Z. Chang, H. Zhang, M. Liang, E. Schlangen, and B. Šavija, "Numerical simulation of elastic buckling in 3d concrete printing using the lattice model with geometric nonlinearity," *Automation in Construction*, vol. 142, 10 2022. [Online]. Available: https://doi.org/10.1016/j.autcon.2022.104485

[137] G. Lilliu, "3d analysis of fracture processes in concrete," Ph.D. dissertation, Delft University of Technology, 2007. [Online]. Available: https://eburon.nl/product/3d_analysis_of_fracture_processes_in_concrete/

[138] Z. Chang, H. Zhang, E. Schlangen, and B. Šavija, "Lattice fracture model for concrete fracture revisited: Calibration and validation," *Applied Sciences (Switzerland)*, vol. 10, 7 2020. [Online]. Available: https://doi.org/10.3390/app10144822

[139] Y. Xu and B. Šavija, "Development of strain hardening cementitious composite (shcc) reinforced with 3d printed polymeric reinforcement: Mechanical properties," *Composites Part B: Engineering*, vol. 174, 10 2019. [Online]. Available: https://doi.org/10.1016/j.compositesb.2019.107011

[140] B. Šavija, D. Liu, G. Smith, K. R. Hallam, E. Schlangen, and P. E. Flewitt, "Experimentally informed multi-scale modelling of mechanical properties of quasi-brittle nuclear graphite," *Engineering Fracture Mechanics*, vol. 153, pp. 360–377, 3 2016. [Online]. Available: https://doi.org/10.1016/j.engfracmech.2015.10.043

[141] Z. Chang, H. Zhang, E. Schlangen, B. Šavija, and Z. E. Chang, "Lattice model for numerical analysis of fracture process of concrete material under various loading conditions," 2019. [Online]. Available: https://www.researchgate.net/publication/335305423

[142] H. Zhang, "Experimentally validated multi-scale fracture modelling scheme of cementitious materials," Ph.D. dissertation, Delft University of Technology, 2019. [Online]. Available: https://doi.org/10.4233/uuid:9a74f4ee-62e9-4117-bcb0-26c5a1a52cb9

[143] T. Vukasovic, J. F. Vivanco, D. Celentano, and C. García-Herrera, "Characterization of the mechanical response of thermoplastic parts fabricated with 3d printing," *International Journal of Advanced Manufacturing Technology*, vol. 104, pp. 4207–4218, 10 2019. [Online]. Available: https://doi.org/10.1007/s00170-019-04194-z

[144] B. Aadnøy and R. Looyeh, *Stress and Strain Transformation*. Elsevier, 2011, pp. 13–25. [Online]. Available: https://doi.org/10.1016/b978-0-12-385546-6.00002-4

[145] M. Swanbom, "3d stress transformation and principal stresses | derivation & example using casio fx-115es plus," 12 2018. [Online]. Available: https://www.youtube.com/watch?v=YNrhKOsdDlI

[146] M. Lukovic, Y. Yang, E. Schlangen, and D. Hordijk, "On the potential of lattice type model for predicting shear capacity of reinforced concrete and shcc structures," in *fib Symposium*. fib. The International Federation for Structural Concrete, 2018, pp. 804–813. [Online]. Available: https://doi.org/10.1007/978-3-319-59471-2_94

[147] J. Kang, K. Kim, Y. M. Lim, and J. E. Bolander, "Modeling of fiber-reinforced cement composites: Discrete representation of fiber pullout," *International Journal of Solids and Structures*, vol. 51, pp. 1970–1979, 5 2014. [Online]. Available: https://doi.org/10.1016/j.ijsolstr.2014.02.006

[148] Y. Xu, Z. Wan, and B. Šavija, "Elevating mechanical performance of cementitious composites with surface-modified 3d-printed polymeric reinforcements," *Developments in the Built Environment*, vol. 19, 10 2024. [Online]. Available: https://doi.org/10.1016/j.dibe.2024.100522

[149] T. Hyatt, *An Account of Some Experiments with Portland-Cement-Concrete Combined with Iron, as a Building Material*. Chiswick Press, 1877. [Online]. Available: https://books.google.com/books/about/An_Account_of_Some_Experiments_with_Port.html?id=yCZRAAAAYAAJ

[150] D. Abrams, "Tests of bond between concrete and steel," University of Illinois, Tech. Rep., 1913. [Online]. Available: https://www.ideals.illinois.edu/items/5240

[151] M. F. Bado, J. R. Casas, and G. Kaklauskas, "Distributed sensing (dofs) in reinforced concrete members for reinforcement strain monitoring, crack detection and bond-slip calculation," *Engineering Structures*, vol. 226, 1 2021. [Online]. Available: https://doi.org/10.1016/j.engstruct.2020.111385

[152] M. H. Harajli, "Effect of confinement using steel, frc, or frp on the bond stress-slip response of steel bars under cyclic loading," *Materials and Structures/Materiaux et Constructions*, vol. 39, pp. 621–634, 7 2006. [Online]. Available: https://doi.org/10.1617/s11527-005-9054-z

[153] U. Farooq, H. Nakamura, T. Miura, and Y. Yamamoto, "Proposal of bond behavior simulation model by using discretized voronoi mesh for concrete and beam element for reinforcement," *Cement and Concrete Composites*, vol. 110, 7 2020. [Online]. Available: https://doi.org/10.1016/j.cemconcomp.2020.103593

[154] S. M. Mirza and J. Houde, "Study of bond stress-slip relationships in reinforced concrete," *ACI Journal*, vol. 76, pp. 19–46, 1 1979. [Online]. Available: https://doi.org/10.14359/6935

[155] L. A. Lutz and P. Gergely, "Mechanics of bond and slip of deformed bars in concrete," *ACI Journal*, vol. 64, pp. 711–721, 1967. [Online]. Available: https://doi.org/10.14359/7600

[156] ACI-Committee-408, "Bond stress-the state of the art," *Journal of the American Concrete Institute*, vol. 63, pp. 1161–1190, 11 1966. [Online]. Available: https://doi.org/10.14359/7665

[157] ——, "408r-03: Bond and development of straight reinforcing bars in tension," Tech. Rep., 2003. [Online]. Available: https://www.concrete.org/publications/internationalconcreteabstractsportal/m/details/id/12969

[158] G. Xing, C. Zhou, T. Wu, and B. Liu, "Experimental study on bond behavior between plain reinforcing bars and concrete," *Advances in Materials Science and Engineering*, vol. 2015, 2015. [Online]. Available: https://doi.org/10.1155/2015/604280

[159] M. H. Harajli, M. Hout, and W. Jalkh, "Local bond stress-slip behavior of reinforcing bars embedded in plain and fiber concrete," *ACI Journal*, vol. 92, pp. 343–353, 1 1995. [Online]. Available: https://doi.org/10.14359/999

[160] P. Namakiaraghi, A. Sadighi, R. Spragg, A. R. Najafi, and Y. A. Farnam, "Towards development of cement-based composites reinforced with architected 3d-printed polymers," *Construction and Building Materials*, vol. 422, 4 2024. [Online]. Available: https://doi.org/10.1016/j.conbuildmat.2024.135838

[161] R. Eligehausen, E. P. Popov, and V. V. Bertéro, "Local bond stress-slip relationships of deformed bars under generalized excitations," *Proceedings of the 7th European Conference on Earthquake Engineering*, pp. 69–80, 1982. [Online]. Available: https://www.researchgate.net/publication/279507857

[162] M. H. Harajli, "Bond stress-slip model for steel bars in unconfined or steel, frc, or frp confined concrete under cyclic loading," *Journal of Structural Engineering*, vol. 135, pp. 509–518, 5 2009. [Online]. Available: https://doi.org/10.1061/ASCE0733-94452009135:5509

[163] S. Robuschi, J. Sumearll, I. Fernandez, and K. Lundgren, "Bond of naturally corroded, plain reinforcing bars in concrete," *Structure and Infrastructure Engineering*, vol. 17, pp. 792–808, 2021. [Online]. Available: https://doi.org/10.1080/15732479.2020.1768273

[164] A. Delaplace and R. Desmorat, "Discrete 3d model as complimentary numerical testing for anisotropic damage," *International Journal of Fracture*, vol. 148, pp. 115–128, 11 2007. [Online]. Available: https://doi.org/10.1007/s10704-008-9183-9

[165] S. W. Lee, S. B. Kang, K. H. Tan, and E. H. Yang, "Experimental and analytical investigation on bond-slip behaviour of deformed bars embedded in engineered cementitious composites," *Construction and Building Materials*, vol. 127, pp. 494–503, 11 2016. [Online]. Available: https://doi.org/10.1016/j.conbuildmat.2016.10.036

[166] M. Lukovic, E. Schlangen, G. Ye, and B. Šavija, "Impact of surface roughness on the debonding mechanism in concrete repairs," in *VII International Conference on Fracture Mechanics of Concrete and Concrete Structures (FraMCoS-8)*, J. V. Mier, G. Ruiz, C. Andrade, R. Yu, and X. Zhang, Eds., 3 2013. [Online]. Available: https://www.researchgate.net/publication/273796894_Impact_of_surface_roughness_onthe_debonding_mechanism_in_concrete_repairs

[167] X. Li, W. Peng, W. Wu, J. Xiong, and Y. Lu, "Auxetic mechanical metamaterials: from soft to stiff," 12 2023. [Online]. Available: https://doi.org/10.1088/2631-7990/ace668

[168] E. O. Momoh, A. Jayasinghe, M. Hajsadeghi, R. Vinai, K. E. Evans, P. Kripakaran, and J. Orr, "A state-of-the-art review on the application of auxetic materials in cementitious composites," *Thin-Walled Structures*, vol. 196, p. 111447, 3 2024. [Online]. Available: https://linkinghub.elsevier.com/retrieve/pii/S0263823123009254

[169] J. A. Rosewitz, H. A. Choshali, and N. Rahbar, "Bioinspired design of architected cement-polymer composites," *Cement and Concrete Composites*, vol. 96, pp. 252–265, 2 2019. [Online]. Available: https://doi.org/10.1016/j.cemconcomp.2018.12.010

[170] E. Schlangen and J. G. M. V. Mier, "Simple lattice model for numerical simulation of

fracture of concrete materials and structures," *Materials and Structures*, vol. 25, pp. 534–542, 1992. [Online]. Available: https://doi.org/10.1007/BF02472449

[171] H. Zhang, B. Šavija, S. C. Figueiredo, and E. Schlangen, "Experimentally validated multi-scale modelling scheme of deformation and fracture of cement paste," *Cement and Concrete Research*, vol. 102, pp. 175–186, 12 2017. [Online]. Available: https://doi.org/10.1016/j.cemconres.2017.09.011

[172] E. Schlangen and E. J. Garboczi, "Fracture simulations of concrete using lattice models: Computational aspects," Tech. Rep., 1997. [Online]. Available: https://doi.org/10.1016/S0013-7944(97)00010-6

[173] R. Kurihara, Y. Ito, Q. Cai, and N. Chijiwa, "The influence of interlock loss between rebar and concrete on bond performance of rc member," *Applied Sciences (Switzerland)*, vol. 12, 2 2022. [Online]. Available: https://doi.org/10.3390/app12031079

[174] Z. Pan, R. Ma, D. Wang, and A. Chen, "A review of lattice type model in fracture mechanics: theory, applications, and perspectives," *Engineering Fracture Mechanics*, vol. 190, pp. 382–409, 3 2018. [Online]. Available: https://doi.org/10.1016/j.engfracmech.2017.12.037

[175] Y. Xu, Z. Meng, R. J. M. Bol, and B. Šavija, "Spring-like behavior of cementitious composite enabled by auxetic hyperelastic frame," *International Journal of Mechanical Sciences*, vol. 275, 8 2024. [Online]. Available: https://doi.org/10.1016/j.ijmecsci.2024.109364

[176] W. Hao, J. Liu, and H. Kanwal, "Compressive properties of cementitious composites reinforced by 3d printed pa 6 lattice," *Polymer Testing*, vol. 117, 1 2023. [Online]. Available: https://doi.org/10.1016/j.polymertesting.2022.107811

[177] A. Bouteldja, M. A. Louar, L. Hemmouche, L. Gilson, A. Miranda-Vicario, and L. Rabet, "Experimental investigation of the quasi-static and dynamic compressive behavior of polymer-based 3d-printed lattice structures," *International Journal of Impact Engineering*, vol. 180, 10 2023. [Online]. Available: https://doi.org/10.1016/j.ijimpeng.2023.104640

[178] U. A. Dar, H. H. Mian, M. Abid, A. Topa, M. Z. Sheikh, and M. Bilal, "Experimental and numerical investigation of compressive behavior of lattice structures manufactured through projection micro stereolithography," *Materials Today Communications*, vol. 25, 12 2020. [Online]. Available: https://doi.org/10.1016/j.mtcomm.2020.101563

[179] J. Zhang, X. Chen, Y. Sun, Y. Wang, and L. Bai, "Sound-absorption and mechanical properties of multisheet gyroid lattice structures by stereolithography," *Composite Structures*, vol. 325, 12 2023. [Online]. Available: https://doi.org/10.1016/j.compstruct.2023.117589

[180] J. H. Kang, K. Sakthiabirami, K. J. Jang, J. G. Jang, G. J. Oh, C. Park, J. G. Fisher, and S. W. Park, "Mechanical and biological evaluation of lattice structured hydroxyapatite scaffolds produced via stereolithography additive manufacturing," *Materials and Design*, vol. 214, 2 2022. [Online]. Available: https://doi.org/10.1016/j.matdes.2021.110372

[181] R. Raj, M. J. Prajapati, J. T. Tsai, A. Kumar, and J. Y. Jeng, "Design and additive manufacturing of novel hybrid lattice metamaterial for enhanced energy

absorption and structural stability," *Materials and Design*, vol. 245, 9 2024. [Online]. Available: https://doi.org/10.1016/j.matdes.2024.113268

[182] R. Rodríguez-Aparicio, J. M. Alegre, W. M. Verbeeten, M. Lorenzo-Bañuelos, and I. I. Cuesta, "Methodology to predict mechanical properties of pa-12 lattice structures manufactured by powder bed fusion," *Additive Manufacturing*, vol. 78, 9 2023. [Online]. Available: https://doi.org/10.1016/j.addma.2023.103864

[183] S. Li, T. Wang, S. Chen, Y. Li, Y. Zou, B. Cao, J. Hu, X. Tan, and B. Wang, "Compressive properties and biocompatibility of additively manufactured lattice structures by using bioactive materials," *Thin-Walled Structures*, vol. 205, 12 2024. [Online]. Available: https://doi.org/10.1016/j.tws.2024.112469

[184] T. Vitalis, A. Gross, G. Tzortzinis, B. Schagen, and S. Gerasimidis, "Enhancing mortar composite matrices with three-dimensional auxetic truss lattice materials for reinforced concrete structures," *Construction and Building Materials*, vol. 457, 12 2024. [Online]. Available: https://doi.org/10.1016/j.conbuildmat.2024.139165

[185] P. Dong, J. Hu, C. Lin, W. Ding, J. Liu, and Y. Liu, "Topology-optimized lattice enhanced cementitious composites," *Materials and Design*, vol. 244, 8 2024. [Online]. Available: https://doi.org/10.1016/j.matdes.2024.113155

[186] A. Clausen, F. Wang, J. S. Jensen, O. Sigmund, and J. A. Lewis, "Topology optimized architectures with programmable poisson's ratio over large deformations," *Advanced Materials*, vol. 27, pp. 5523–5527, 10 2015. [Online]. Available: https://doi.org/10.1002/adma.201502485

[187] L. Stepinac and J. Galić, "Preliminary investigation of the large-scale sandwich decks with graded 3d printed auxetic core," *Journal of Sandwich Structures & Materials*, vol. 27, pp. 260–278, 1 2025. [Online]. Available: https://journals.sagepub.com/doi/10.1177/10996362241298144

[188] A. Panesar, M. Abdi, D. Hickman, and I. Ashcroft, "Strategies for functionally graded lattice structures derived using topology optimisation for additive manufacturing," *Additive Manufacturing*, vol. 19, pp. 81–94, 1 2018. [Online]. Available: https://doi.org/10.1016/j.addma.2017.11.008

[189] Z. Meng, Y. Xu, J. Xie, W. Zhou, R. J. M. Bol, Q. feng Liu, and B. Šavija, "Unraveling the reinforcing mechanisms for cementitious composites with 3d printed multidirectional auxetic lattices using x-ray computed tomography," *Materials & Design*, vol. 246, p. 113331, 10 2024. [Online]. Available: https://linkinghub.elsevier.com/retrieve/pii/S0264127524007068

[190] G. Zhao, Y. Fan, C. Tang, Y. Wei, and W. Hao, "Preparation and compressive properties of cementitious composites reinforced by 3d printed cellular structures with a negative poisson's ratio," *Developments in the Built Environment*, vol. 17, 3 2024. [Online]. Available: https://doi.org/10.1016/j.dibe.2024.100362

[191] N. K. Choudhry, T. K. Nguyen, V. Nguyen-Van, B. Panda, and P. Tran, "Auxetic lattice reinforcement for tailored mechanical properties in cementitious composite: Experiments and modelling," *Construction and Building Materials*, vol. 438, 8 2024. [Online]. Available: https://doi.org/10.1016/j.conbuildmat.2024.137252

[192] G. Tzortzinis, A. Gross, and S. Gerasimidis, "Auxetic boosting of confinement in mortar by 3d reentrant truss lattices for next generation steel reinforced concrete members," *Extreme Mechanics Letters*, vol. 52, 4 2022. [Online]. Available:

https://doi.org/10.1016/j.eml.2022.101681

[193] M. Chen, Z. Chen, Y. Xuan, T. Zhang, and M. Zhang, "Static and dynamic compressive behaviour of 3d printed auxetic lattice reinforced ultra-high performance concrete," *Cement and Concrete Composites*, vol. 139, 5 2023. [Online]. Available: https://doi.org/10.1016/j.cemconcomp.2023.105046

[194] T. Zahra, M. Asad, and J. Thamboo, "Flexural behaviour of cementitious composites embedded with 3d printed re-entrant chiral auxetic meshes," *Smart Materials and Structures*, vol. 33, 2 2024. [Online]. Available: https://doi.org/10.1088/1361-665X/ad1b24

[195] B. Xie, R. Tian, H. Zhao, T. Ye, Y. Zhang, and N. Hu, "Controlling crack propagation in layered beams with architected lattice-reinforced composite interlayer designs," *Construction and Building Materials*, vol. 426, 5 2024. [Online]. Available: https://doi.org/10.1016/j.conbuildmat.2024.136174

[196] S. Pichandi, "Universidade do minho escola de engenharia development of composite auxetic structures for civil engineering applications," Tech. Rep., 2016. [Online]. Available: https://repositorium.sdum.uminho.pt/bitstream/1822/41500/1/ID4206_Subramani_Pichandi_Full_Thesis.pdf

[197] J. Liu, H. Kanwal, C. Tang, and W. Hao, "Study on flexural properties of 3d printed lattice-reinforced concrete structures using acoustic emission and digital image correlation," *Construction and Building Materials*, vol. 333, 5 2022. [Online]. Available: https://doi.org/10.1016/j.conbuildmat.2022.127418

[198] B. Salazar, P. Aghdasi, I. D. Williams, C. P. Ostertag, and H. K. Taylor, "Polymer lattice-reinforcement for enhancing ductility of concrete," *Materials and Design*, vol. 196, 11 2020. [Online]. Available: https://doi.org/10.1016/j.matdes.2020.109184

[199] B. Xie, X. Li, X. Zhao, and N. Hu, "Tunable properties and responses of architected lattice-reinforced cementitious composite components induced by versatile cell topology and distributions," *Composite Structures*, vol. 312, 5 2023. [Online]. Available: https://doi.org/10.1016/j.compstruct.2023.116850

[200] P. Dong, W. Ding, H. Yuan, and Q. Wang, "3d-printed polymeric lattice-enhanced sustainable municipal solid waste incineration fly ash alkali-activated cementitious composites," *Developments in the Built Environment*, vol. 12, 12 2022. [Online]. Available: https://doi.org/10.1016/j.dibe.2022.100101

[201] W. Zhou, R. J. M. Bol, Y. Zhou, Z. Meng, Y. Xu, J. Xie, and B. Šavija, "Reinforcing mechanism of lattice-reinforced cementitious composites: insights into flexural performance and material interactions," *Materials & Design*, vol. 256, p. 114332, 8 2025. [Online]. Available: https://linkinghub.elsevier.com/retrieve/pii/S026412752500752X

[202] Z. Lu, Q. Wang, X. Li, and Z. Yang, "Elastic properties of two novel auxetic 3d cellular structures," *International Journal of Solids and Structures*, vol. 124, pp. 46–56, 10 2017. [Online]. Available: https://doi.org/10.1016/j.ijsolstr.2017.05.031

[203] F. Wang, O. Sigmund, and J. S. Jensen, "Design of materials with prescribed nonlinear properties," *Journal of the Mechanics and Physics of Solids*, vol. 69, pp. 156–174, 2014. [Online]. Available: https://doi.org/10.1016/j.jmps.2014.05.003

[204] J. B. Mander, M. J. N. Priestley, and R. Park, "Theoretical stress-strain model for confined concrete," *Journal of Structural Engineering*, vol. 114, pp. 1804–1826,

9 1988. [Online]. Available: https://doi.org/10.1061/(ASCE)0733-9445(1988)114:8(1804)

[205] B. Salazar, I. Williams, P. Aghdasi, C. Ostertag, and H. Taylor, "Bending and crack characteristics of polymer lattice-reinforced mortar," in *Int. Congr. Polym. Concr. (ICPIC 2018)*, 2018, pp. 261–266. [Online]. Available: https://doi.org/10.1007/978-3-319-78175-4_32

[206] I. Farina, F. Fabbrocino, G. Carpentieri, M. Modano, A. Amendola, R. Goodall, L. Feo, and F. Fraternali, "On the reinforcement of cement mortars through 3d printed polymeric and metallic fibers," *Composites Part B: Engineering*, vol. 90, pp. 76–85, 4 2016. [Online]. Available: https://doi.org/10.1016/j.compositesb.2015.12.006

[207] J. Versteege, R. J. M. Wolfs, and T. A. M. Salet, "A data-driven view on digital fabrication with concrete: The case of interlayer bond strength," in *Digital Concrete 2024: 4th RILEM International Conference on Concrete and Digital Fabrication*, 2024. [Online]. Available: https://doi.org/10.24355/dbbs.084-202408151209-0

[208] J. Versteege, T. A. Salet, and R. J. Wolfs, "Sensory data mapping and database development for interlayer bond strength: Towards digital shadows in 3d concrete printing," *Additive Manufacturing*, vol. 120, 3 2026. [Online]. Available: https://doi.org/10.1016/j.addma.2026.105105

[209] W. Zhou, W. McGee, H. S. Gökçe, and V. C. Li, "A bio-inspired solution to alleviate anisotropy of 3d printed engineered cementitious composites (3dp-ecc): Knitting/tilting filaments," *Automation in Construction*, vol. 155, 11 2023. [Online]. Available: https://doi.org/10.1016/j.autcon.2023.105051

[210] W. Zhou, Y. Xu, Z. Meng, J. Xie, Y. Zhou, E. Schlangen, and B. Šavija, "Filament stitching: An architected printing strategy to mitigate anisotropy in 3d-printed engineered cementitious composites (ecc)," *Cement and Concrete Composites*, vol. 160, 7 2025. [Online]. Available: https://doi.org/10.1016/j.cemconcomp.2025.106044

[211] S. He, M. Nuri, H. M. Jonkers, M. Luković, and E. Schlangen, "Structural behaviour of reinforced concrete beams with self-healing cover zone as lost formwork," *Developments in the Built Environment*, vol. 18, 4 2024. [Online]. Available: https://doi.org/10.1016/j.dibe.2024.100458

[212] M. E. Hernandez Korner, M. P. Lamban, J. A. Albajez, J. Santolaria, L. d. C. Ng Corrales, and J. Royo, "Cost Model Framework for Pieces Additively Manufactured in Fused Deposition Modeling for Low to Medium Batches," *3D Printing and Additive Manufacturing*, vol. 11, no. 1, pp. 287–298, 2 2024. [Online]. Available: https://doi.org/10.1089/3dp.2022.0044

[213] J. Go, S. N. Schiffres, A. G. Stevens, and A. J. Hart, "Rate limits of additive manufacturing by fused filament fabrication and guidelines for high-throughput system design," *Additive Manufacturing*, vol. 16, pp. 1–11, 8 2017. [Online]. Available: https://doi.org/10.1016/j.addma.2017.03.007

[214] C. M. S. Vicente, M. Sardinha, L. Reis, A. Ribeiro, and M. Leite, "Large-format additive manufacturing of polymer extrusion-based deposition systems: review and applications," *Progress in Additive Manufacturing*, vol. 8, pp. 1257–1280, 12 2023. [Online]. Available: https://doi.org/10.1007/s40964-023-00397-9

ACKNOWLEDGEMENTS

The acknowledgements sections are amongst the most read sections in dissertations, especially by those who are unfamiliar with the scientific content contained in their main bodies of work. At least, this is based on my personal experience and what I hear from colleagues and friends. With theses from colleagues, I have to admit that I typically start reading the acknowledgements section to see if my name is mentioned (and if so, what they say about me), followed by reading the summaries (both in English and Dutch, out of curiosity for the translations), and if I find the topic interesting, I sometimes dive into the table of contents and read little pieces of the work. In the good spirit of the Microlab, where it seems to be some sort of tradition to have very elaborate acknowledgements, I promise I will not let you down - so be prepared!

Looking back at the past four years, I realize that a lot has been going on in my life. While most things were constantly changing, fortunately others remained the same throughout this journey. When I am writing this acknowledgements section, it is almost exactly four years ago that I received the offer for this PhD position by my daily supervisor and promotor, Branko Šavija. It was at a time with a lot of uncertainties in my life: my girlfriend (currently fiancée, more on that later), Renske, had been admitted to the rehabilitation center for the second time. Just a year and a half prior (January 20, 2021 - the longest day of my life), she had a high-risk surgery which took over thirteen hours to remove a large tumor inside the spinal chord of her neck. Afterwards, she was unable to move anything (except for her face), and was diagnosed with a high, incomplete spinal cord injury (C4-5). In the six months that followed, she took on a very intensive rehabilitation trajectory in Rotterdam, where she significantly improved and was discharged. At that time, she was able to walk a few hundred meters with crutches whilst still being wheelchair bound, but she had largely regained her independence. However, after falling backwards with her wheelchair in November 2021, she dramatically relapsed, particularly the right side of her body suffered from additional loss of functioning. For a long time, it was uncertain whether she could recover from this, and it would take until May 2022 for her to be readmitted to the rehabilitation center. During this exact period, I was graduating from my MSc, which I managed to complete in that same month. To paint the full picture: we are from the South of the Netherlands (near Breda), and at that time we did not have our own place, I was driving back and forth to Rotterdam almost every day, and we had no idea what our future would look like. I remember sharing my personal circumstances in an additional meeting with Branko before signing the contract, but he had no concerns at all and gave me all the flexibility I needed to combine my doctoral programme with informal care. To this day, I am deeply grateful for that.

My appointment as a PhD candidate eventually began on September 15, 2022, just a week before Renske was discharged from the rehabilitation center for the second time. Because we did not have our own place (yet), we ended up living at her father's place where the municipality constructed a (temporary) bathroom downstairs. However, we

slept in a bed at the end of the living room behind a room divider for more than a year and a half. During the initial period of my PhD, Renske still had to go to Rotterdam for therapy three times a week. Since Rotterdam is roughly on the route towards Delft, I would drop her off and pick her up at the Westersingel. In these days, I used to start working from home early (approximately from 7 to 9 AM), help her out of bed and with her morning routine, bring her to Rotterdam, drive to Delft, continue working (from about 11 AM to 5 PM), drive to Rotterdam (in peak traffic), and back home (around 7 PM). A major milestone popping up suddenly was the moment we bought our first home together, a newly built house in the village I grew up in: Hoeven. Nonetheless, at some point the situation at her father became untenable, and with us having to wait for over a year before our house was finished, we decided to move to her grandparents' place. This was a tough decision, for which I sought counseling at our executive secretary, Jaap Meijer. As an outsider, and therefore an objective party, he immediately justified our decision to move - exactly the confirmation I needed. Jaap, if you are reading this: thank you so much for taking the time and creating a safe atmosphere for that important conversation. Now that we have landed here, I would also like to thank you for the elaborate conversations we used to have when I was leaving the office (and you stayed, often well beyond 6:30 PM), for which I sometimes got into trouble with my family who were waiting for me to have dinner. Nevertheless, extended family members of Renske (Peter & Edith) kindly offered us from time to time to stay at their holiday home in Westenschouwen, Zeeland, the Netherlands, to have some quality time with the two of us and clear our minds. This proved sometimes necessary, such that we greatly appreciated these little escapes.

Renske's grandparents, Piet & Coby, currently 90 and 86 years old, respectively, were willing to take their granddaughter and 'grandson-in-law' into their home. They had a separate downstairs bedroom with adjacent bathroom, where Piet as a tough (at the time) 88-year old modified the shower to be accessible for Renske by himself. Normally, they were sleeping downstairs, but for us they wanted to live upstairs while we were waiting for our house to be finished. This significantly improved our situation: we finally had our own room! Since Coby did not allow me to cook for us (I guess she wanted the kitchen to herself), we relieved her by having two times a week dinner at my parents (Gido & Hélène) and two times a week dinner at Renske's mother (Thea) and stepdad (Eric). We realize this took a lot of effort from their sides, but we are intensely grateful for their help getting through these days. Actually, it became very cozy to live with the four of us: every day, we had breakfast together, and we ate lunch and made the daily news paper's puzzles together if I worked from home. We even celebrated 'Sinterklaas' together, making rhymes and buying presents for each other. However, over time, the muscles in the back of Renske's neck were no longer able to keep it straight, such that she needed two additional surgeries: one stabilizing the front of her neck, and another one for installing pins running from the top of her neck (C2) until in between her shoulders (T2). This was in November 2023, and just before I submitted my first ever journal paper to *polymers*. On the day of the first surgery, I got mail that the manuscript had been accepted upon minor revisions, and I remember that I was so happy that I made these revisions immediately after the surgery: I was sitting at this small table in the corner of Renske's hospital room, making a final explanatory figure in PowerPoint (for those who are interested, this is Figure 2.3), and writing the response letters to the reviewers. Perhaps this sounds a bit crazy, but

sometimes it feels like that is what it takes to work in academia. In the end, we lived with Piet & Coby for more than a year, for which we will always be indescribably thankful. We finally got the keys to our new home near the end of September 2024, and we moved in on Christmas Eve after three months of work around and inside the house (a huge thanks to my father, Gido, and Renske's stepdad, Eric). Nothing has ever felt more natural than living with the two of us, after all this time. Since our house is fully adapted to Renske's needs, she can do her things and be alone for the day. Nevertheless, she still goes to physiotherapy twice a week to which I accompany her once a week to this day (thanks to our family members (Thea, Hélène, and Eric) for taking her the other day), where I have been working on my notebook in the break room for the better part of two years now. As of May 2026, she started working again, to which I drive her on Tuesdays and Thursdays (until a permanent transportation solution will be arranged). I am incredibly proud of what she has achieved in the past four years, and I am happy with the life we have built given our circumstances.

Perhaps a bit unconventional, but I would like to start with thanking my MSc thesis supervisors from Eindhoven University of Technology, Akke Suiker, Hèrm Hofmeyer, and Payam Poorsolhjouy for their excellent guidance during my graduation. Although I never thought I would ever pursue a PhD, especially Payam encouraged me to do so. Without his enthusiasm about my MSc work, I would have never considered actually taking up a role as doctoral candidate. More specifically, I would like to express my gratitude to Akke and Payam for writing outstanding letters of recommendation (to this day, I am still curious about their contents, because I am pretty sure this is what got me into TU Delft at the first place).

Now the more traditional portion starts, beginning with my daily supervisor and promotor, Branko Šavija. Thank you for believing in me as the right person for this position, for your honorable approachability, incredible flexibility (especially regarding my personal circumstances), and immensely fast responses to my emails (including reviews). You always had the ability to temper my concerns when I felt stuck with my modelling attempts, and together we often came up with alternative solutions. You also gave me the freedom to pursue some other research activities, explore what it is to work in the lab, and encouraged me to attend several international conferences (for which I was a bit hesitant at the beginning). I think you are an amazingly versatile researcher, and a skilled supervisor.

I feel the same way about my other promotor, Erik Schlangen. Although you were more on the background than Branko, you always provided me with mind-changing insights during our meetings. You are also one of the most calm and relaxed academic people I have ever met, which sometimes makes me forget you are a full professor (which I mean completely positively). I remember that in one of my yearly progress meetings you posed the question: 'But what does society gain from this?' This led me to rethink my goals for the PhD to not just answer the research questions or comply with the grant proposal. No, I had to expand my horizons. It was this exact question that caused me to seek for other applications than uniaxial compression for auxetic cementitious composites, because after all, in construction practice we also have floors and beams subjected to bending besides walls and columns in compression. This comment sparked the initiation of the Tailored Poisson's Ratio-reinforced Cementitious Composites (TPRCC) developed in this work, which led to many other endeavors (more on that later).

Along with my two promotors, the independent members of my doctoral committee also reviewed the contents of this dissertation. Thank you for taking the time to read the entire thing, and providing constructive comments that helped improve the quality of it.

Many hours were spent in office 6.08, directly located next to the entrance of the Microlab. I worked here along proficient people with whom I had many insightful conversations, and with some I became friends for life. Some were already finishing upon my arrival, like Yask Kulshreshtha, Albina Kostiuchenko, and Ze Chang. The first long-term resident during my stay was Xiujiao Qiu, one of the most thoughtful people I have ever met. She was always asking about Renske and telling me how much she respected me for being both a doctoral candidate and informal caregiver. I also respect her for the life she has built, together with her husband and lovely dog in Belgium. Although we do not see each other that often, it always feels like those good old days in the office when we meet again. Thank you for our friendship! Later on, Zhaozheng Meng joined our place, my direct experimental colleague-PhD working on Branko's ACC-3D project. He became the master of 3D printing within our lab, having tuned most of our printer settings (including those used throughout this work) for different printers, and always stepped in to guide my students with experiments I was unfamiliar with. Thanks for all these efforts! After Qiu's postdoc ended, her seat was ultimately taken by another ACC-3D colleague: Wen Zhou. You brought an entirely different energy to our office, which often resulted in a lot of fun. I still remember our standard Monday morning chats upon arrival at the office, where I always forgot what I did during the weekend and had to check my agenda to remind myself (just to be clear, we used to have immensely busy weekends). However, I mostly cherish you for taking me under your wing by introducing me to experimental work in the lab without making (too much) fun of me. The Microlab environment really inspired me to learn about experiments, even though my PhD was fundamentally primarily numerical, and I did not really know where to start. Your kind personality and sense of humor got me through these initial steps, making me more confident and shaped the researcher I am today. This led to several publications together, because our collaboration felt like a true synergy. Unfortunately, most of the conferences we had planned together either got canceled (probably because they knew we were attending), or one of us could not make the trip. Nonetheless, I still hope that at some point you can show me around in your city, Beijing. After you left for Singapore, where you are currently an assistant professor at Nanyang Technological University (I am so proud of you, my friend), our office became much more quiet. However, we are still in touch, and I am sure we will continue working together and stay friends. Finally, you fell in love with our kitten (Mup), who will always be by your side in the form of a cat-shaped pillow (including photo-print) I gave you as a farewell present. I am truly grateful that I met you and for the friendship we developed!

Other members of the ACC-3D community were Yading Xu, and later Jinbao Xie. Yading is currently a full professor at Chongqing University in China, and he is one of the originators of ACC-3D (together with Branko). He performed some of the experiments contained in this dissertation, and helped me getting familiar with the Delft lattice model. Jinbao joined us as a postdoc after obtaining his PhD (well done), when he started working on concrete origami (Wen's NWO Open Mind grant). He used to be the *King of Ganbei*, a term introduced during our occasional visit to the student bar (PSOR). According to Gemini, Ganbei is the most common Chinese toast and literally means 'dry cup'. It is

the Chinese translation of ‘cheers’ or ‘bottom-free’. Unlike Western customs, in Chinese culture, after shouting ‘Ganbei’, you are expected to drink your glass completely empty in one go. I leave it to the imagination of the reader which definition we mostly used. Jinbao also had the incredible ability to replenish our cocktail nuts in the blink of an eye, such that he later transitioned into the *King of Nuts*. Thank you for all these unforgettable moments.

This brings me to our valuable technicians of the Microlab: Arjan Thijssen, John van den Berg, and Maiko van Leeuwen. I would like to thank Arjan for his assistance with CT scanning, which helped me understand the damage mechanisms inside the previously discussed TPRCC in this work, and John for this companionship and occasional office chats. Although John and I never conducted any experiments together, we often ran into each other somewhere in the lab, and he was (and still is) a regular PSOR-attendee who is always in for a drink and a nice conversation. For Maiko, please turn to the next page.

Maiko van Leeuwen deserves an entire page dedicated to him. Not only am I actually doing this in view of his involvement with the Microlab, which we therefore often refer to as the *Maikolab*, but also because he once complained to me that for all the work he does around the lab, he often only gets a couple of sentences in the acknowledgements in return (he is also one of those people that only read the acknowledgements sections of dissertations). Since he may frame this page for his *Wall of Fame*, I thought: why not?

Maiko is best described as the *pater familias* of the Microlab (*Maikolab*). He knows how most of the equipment works, does all of the safety instructions for newcomers, assists with mechanical testing, is a concrete genius with a ton of experience, has a great heart for students, organizes food nights, and wants everyone to feel welcome in our community. However, most of all, he is my almost-neighbor. When I started working in Delft as someone from North Brabant (which is about one hour away from Delft), I never expected to have a colleague who lives in the village next to mine. The main follow-up question by people at work after I tell them where I live has always been: 'When do you move to Delft?' Maiko and his family understand why we do not live in Delft, and that this is motivated by our personal reasons. I remember my first day at the office when everyone was talking about 'this guy that was supposed to be my neighbor', and I had no idea what they were talking about. Apparently, Maiko had been happy to finally have someone fun from the good side of the rivers separating the North from the South of the Netherlands (at least, that is what I think happened). When I finally met him, I immediately realized what a great guy he is. He is always joking, while working hard, and trying to bring us academic people together in social events (although most of us have the tendency to be a tad introvert). His main social responsibility is to get as many people to attend the occasional PSOR-evenings at the student bar. I still see him patrolling around all of our offices around 4:30 PM on Thursdays, 'friendly demanding' us to come downstairs to the pub. To be clear, it was never about the drinking - you could decide for yourself to participate in this or not - but his goal was to unite us as a group of bright young people (his words, not mine). Other activities he set up were the Microlab nights to attract students for our master track, including him wearing a suit and putting down a red carpet at the entrance to make them feel like VIPs. Another initiative by him are the Microlab food nights. Since we have a large variety of international people with different cultural backgrounds, he came up with the idea that everyone cooks a meal from their home country and brings it to the office to share and taste each other's dishes at the end of the afternoon. These were always great fun and educational at the same time, learning about food I never heard about.

Before and during my PhD in Delft, he also went through difficult times with his family, such that we could level very well on certain aspects of life. We often sat down in his office to have some serious conversations about our personal circumstances. This really showed me his strength and resilience of taking care of everything and everyone, both at home and at the lab. His sense of responsibility is truly inspirational, and I think many people can learn from him. From our lessons of life, he always told people that 'there is more to life than work'. I think this is the most valuable lesson for someone in academia.

Maiko, you are the true and irreplaceable backbone of the Microlab. I am forever grateful for my friendship with the *Humble Technician*, the carpool rides such that we could have a drink, and for teaching me how to make proper concrete.

It is also Microlab courtesy to thank all of our colleagues that were there along the PhD trajectory. I would rather expand this to our 'TU Delft CEG 6th floor scientific community', and I realize these are a lot of people, and that I will most likely forget someone. Nevertheless, I will give it a try here in random order: Ameya Kamat, Anne Linde van Overmeir, Borcu Aytekin Turkoglu, Boyu Chen, Guilherma da Silva Munhoz, Minfei Liang, Shan He, Stefan Chaves Figueiredo, Zhi Wan, Mayank Gupta, Shizhe Zhang, Aliakbar Ghaderiaram, Farnaz Aghabeyk, Gabriel Mohallem Ferreira, Luiz Miranda de Lima, Max Veeger, Patrick Holthuizen, Xinrui Zhang, Yu Zheng, Henk Jonkers, Mohammad Fotouhi, Oguzhan Copuroglu, Marc Ottele, Guang Ye, Jacqueline Bergenhenegouwen, Sandra Schuchmann-Hagman, Iris Nederhof-van Woggelum, Iris Batterham, Mladena Lukocić, Martin Lesueur, Iuri Rocha, Frans van der Meer, Max Hendriks, Jan Rots, Rita Esposito, Francesco Messali, Tom van Woudenberg, Til Gärtner, Pieter Hofman, Jasmijn van Riggelen, Kelsey (Yi-Cih) Lin, Arpan Adhikari, Tejas Iyer, Chetna Srivastava, Rauf Hassan, Eyüphan Küçükkalfa, Jeroen van Oosten, Anna Alberda van Ekestein, Klaas van Breugel, Bert Sluys, Niels Kostense, Anne Poot, Yopi Prabowo Oktiovan, Leon Riccius, Pedro Rios, Joep Storm, Sakshi Singh, Laura Gómez Jaramillo, Diana Gómez, Winston Lindqwister, and Marija Nedeljković. Thank you for being part of my PhD.

I would also like to thank the students I supervised throughout these years: Dylan, Tahira, Renske, Ka Hao, Wen-Chi, Zhenyu, Amine, Brillian, Herman, Jonathan, Mirthe, Quinten, Ruth, Sybren, Bouwe-Jan, and Koby. It was often very nice to see you growing up in the lab, getting more experienced with the equipment and testing. Especially the planning part related to casting, curing, and testing of cementitious mortar sometimes required an important learning curve. Occasionally, your processes led me to dive deeper into the matter, which increased my knowledge too.

One of the perks of being an academic is the many opportunities to travel to conferences, meeting interesting people, expanding your network, and building new collaborations. I had the pleasure of attending several major conferences: ConCreep12 (Delft, the Netherlands), SSCS-AUXETICON 2025 (Rotterdam, the Netherlands), RILEM Spring Convention 2026 (Ghent, Belgium), FRaMCoS-XII (Vienna, Austria), EURO-C 2026 (Seefeld in Tirol, Austria), and EMI 2025 (Anaheim, California, USA). Here, I must give credits to my lovely sister-in-law, Nienke, for helping Renske when I was travelling to these places. Without her, I would not have been able to do this, spread my research findings globally, and establishing a scientific network. I cherish the most beautiful memories of my furthest trip ever to EMI 2025 in the USA. Erik and Branko asked me if I was willing to present my TRPCC work over there, an opportunity I could not turn down. Back then, Renske was not working yet, and people told us that the USA is incredibly wheelchair accessible, so we turned this adventure into our first overseas holiday since she got into a wheelchair. Our first flight including medical equipment was exciting, but everything turned out fine. I recall that I was the second speaker of the first session on the first day. We were sitting in the room with the chairman, the first speaker, and myself at 9 AM sharp, and I thought: nobody is going to see my presentation. After the first speaker had started, people from various rooms began to trickle in. At the time it was my turn to present, the room was about half full - thankfully. The presentation felt good, and I was happy with how I did. During questioning, there was this one woman who seemed very interested in my work, so that she asked several questions until the chairman cut us off.

At the end of the session, she came up to me and started speaking entirely in Flemish. I was bewildered to speak in my native language at the other side of the planet, but it was a great conversation wherein she introduced me to one of her PhD students, Isabel Moreira de Oliveira. We discovered some potential overlaps between our studies, which we are currently still exploring. It turned out that this woman was Sigrid Adriaenssens, a professor at the Form Finding Lab of Princeton University, which I only found out a day later when she gave a truly inspiring keynote lecture on large scale extraordinary mechanics. Unexpectedly enough, I also met my old MSc supervisor, Payam, there. After the conference, Renske and I rented a campervan to make the most beautiful four-week road trip of our lives, all across the West of the USA. We drove more than 10.000 km along the states of California, Arizona, Utah, Wyoming, Montana, Idaho, Washington, Oregon, and Nevada. We visited a majority of National Parks (Joshua Tree, Grand Canyon, Zion, Bryce Canyon, Canyonlands, Arches, Capitol Reef, Grand Teton, Yellowstone, Glacier, Mount Rainier, Crater Lake, Redwood, Yosemite, Sequoia, and King's Canyon), and several State Parks (Gooseneck, Dead Horse, Smith Rock, and Redwood), among others. Ultimately, I proposed to Renske on the valley floor in front of the highest waterfall in North America at the most beautiful place on Earth: Yosemite National Park (to be specific, at the pullout of Cook's Meadow Loop (37.744003, -119.591844) of Yosemite Valley, facing Yosemite Falls). While she is currently still my fiancée, I am already proud to call her my wife after the 21st of May, 2027. This indescribable road trip will forever be etched into our memories, and I am extremely grateful to Erik and Branko for providing me with this opportunity. It sparked the onsets of both a new chapter in our lives, as well as a potential new research direction for my professional career.

Finally, I would like to thank my brother, Riffy, grandmother, Cor, the rest of my family, and close friends for their unconditional support throughout this period, especially my mother, Hélène. A special thanks goes to my fiancée, Renske, who has always been my biggest supporter. In addition to that, I would like to thank my friend Louise van den Wildenberg for creating the beautiful cover of this dissertation.

Credits to you if you made it until here. I realize this is a very elaborate acknowledgements section, even for a member of the Microlab. However, it feels justified given the rollercoaster the past four years have been. I hope the kind words provided here do (a little) justice to all the help Renske and I received in these difficult times; from houses to live in, dinners to eat, help around the house, to a strong social network to rely on. We could not have done it without you. Please be aware that without the people addressed in this section, especially my fiancée and our families, this dissertation would not have existed.

Rowin J.M. Bol



Delft, June 2026

A

Appendices

The appendices contain supplementary information that supports and clarifies the primary content of the thesis.

A

A.1. VARIABILITY INFLUENCE ON NUMERICAL OUTPUT

To check the influence of the variability in the material scale dog bone specimens results as shown in Figure 3.7 in Chapter 3, additional auxetic structure scale simulations are carried out. For each of the two auxetic designs, RE and RS, the 3 main directions models are simulated for Seed = 0 given the following properties: all local strength inputs raised by their corresponding standard deviation values in all directions (Upper Bound in Figure A.1), and all local strengths lowered by their corresponding standard deviation values in all directions (Lower Bound in Figure A.1). When comparing the numerically obtained force displacement curves to the experimental results in Figure A.1, these show upper and lower bounds for their input. The resulting load responses for RE (Figure A.1(a)) yield percentage differences of about 6.5 % and 9.3 % for the upper and lower bounds, respectively. Similar to its comparison with the 7 RVE directions and 3 main directions models, RS returns a more protruding percentage difference around 20 % for the upper bound while the lower bound is close to only 1.8 %. Even though the force displacement output of the numerical analyses is influenced by the standard deviations in Figure 3.7(d), all failure mechanisms remained the same.

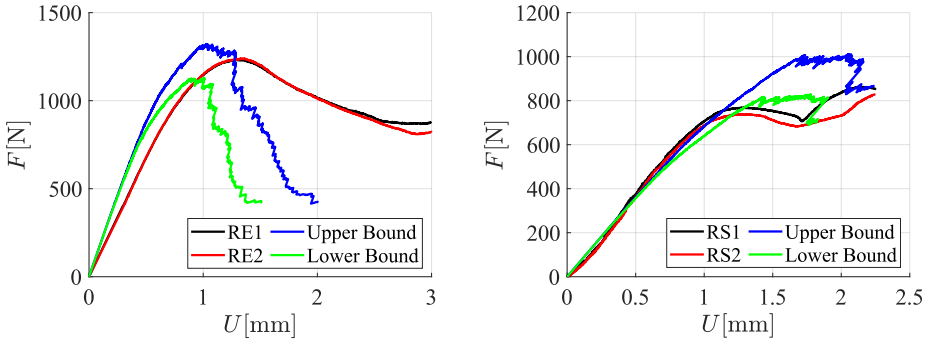

(a) Re-Entrant (RE)

(b) Rotating Square (RS)

Figure A.1: Variability influence on numerical output of (a) Re-Entrant (RE), and (b) Rotating Square (RS) architectures

A.2. 2D FINITE ELEMENT METHOD SIMULATIONS OF ACCS

Xu & Šavija [110] considered the same ACCs as discussed in Chapter 5, with the only difference being the printing parameters which were updated in this chapter. The printing parameters used in [110] are provided in Table A.1, where it can be seen that the printing temperature and printing speed are different.

Table A.1: Previous printing parameters [110]

Printing parameters	**Configurations**
Printing temperature (°C)	250
Printing speed ($mm\,s^{-1}$)	40
Nozzle size (mm)	0.6
Layer thickness (mm)	0.15

The same 3D printed ABS auxetic reinforcement geometries and ACC specimens were modelled by means of a 2D Finite Element Method (FEM) in the commercial software ABAQUS/Explicit. The ABS received a plastic material description (see Table A.2), whilst the cementitious matrix was described by a Concrete Damaged Plasticity Model (CDPM) (see Tables A.3, A.4, and A.5) [110]. The ABS was modeled with a density of $1.07 \times 10^{-9}\,t\,mm^{-3}$, a Young's modulus of 1590 MPa, and a Poisson's ratio of 0.2. The matrix was modeled with a density of $1.87 \times 10^{-9}\,t\,mm^{-3}$, a Young's modulus of 10 105 MPa, and a Poisson's ratio of 0.2. The bond relationship among Acrylonitrile Butadiene Styrene (ABS) and cementitious mortar was assumed by an arbitrary friction coefficient equal to 1.0.

Table A.2: Plastic material description for the ABS polymer [110]

Yield Stress (MPa)	Plastic Strain
38	0
40	0.6
32	0.7
15	1.0
1	1.2

Table A.3: Concrete Damaged Plasticity [110]

Dilatation angle	Eccentricity	f_{b0}/f_{c0}	K	Viscosity parameter
35	0.1	1.16	0.667	0.001

For comparison with the Lattice Beam Model (LBM) developed in this work and to give the reader a complete overview of our previous results obtained through 2D FEM, the experimental and numerical stress strain curves of ACC RE and ACC RS from [110] are given in Figures A.2 and A.3, respectively. A comparison of the previously

A

Table A.4: Concrete Compression Damage [110]

Yield Stress (MPa)	Inelastic Strain	Damage Parameter
12	0	0
24	0.0070	0
20	0.0526	0.20
12	0.0576	0.52
10	0.0586	0.60
8	0.0616	0.68
6	0.0636	0.76
3	0.0866	0.88
3	0.2066	0.88

Table A.5: Concrete Tension Damage [110]

Yield Stress (MPa)	Inelastic Strain	Damage Parameter
3.5	0	0
1	0.0014	0.71
0.5	0.0019	0.86
0.3	0.0025	0.91

obtained compressive strengths and toughness values is shown in Figure A.4 and Table A.6. The simulated stress strain curves of both ACC RE (Figure A.2) and ACC RS (Figure A.3) matched well in terms of compressive strength, with only minor deviations compared to the experiments (see Figure A.4(a)). However, as observed in Figure A.4(b), there is a notable overestimation in toughness due to the previous simulation's lack of capturing the post-peak softening response, which instead maintained a plateau near their compressive strength value. It is also evident that, due to the difference in printing parameters, the shaded bands representing the spread observed in parallel measurements in Figures A.2 and A.3 are significantly larger compared to the experimental results in Figures 5.7(a) and 5.14(a), especially in the post-peak regimes. This is further emphasized by the higher standard deviations in Table A.6 compared to those in Tables 5.4 and 5.5.

Table A.6: Mechanical properties of previous ACCs [110]

ACC	**Load Capacity** (kN)	**Toughness** (J)
RE (EXP)	19.9 ± 2.4	31.6 ± 7.0
RE (FEM)	19.4	45.1
RS (EXP)	20.7 ± 1.3	29.8 ± 4.2
RS (FEM)	18.3	42.8

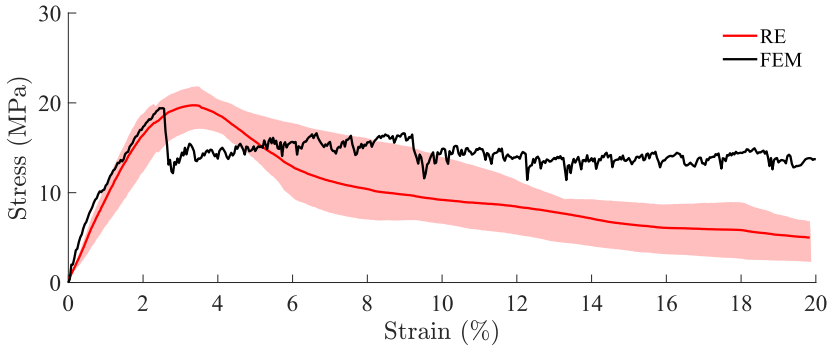

Figure A.2: Comparison of experimental and numerical stress strain curves for uniaxial compression of ACC RE from previous work [110]. For experimental data, the shaded bands reflect the spread observed in parallel measurements, and the solid lines denote the mean outcomes.

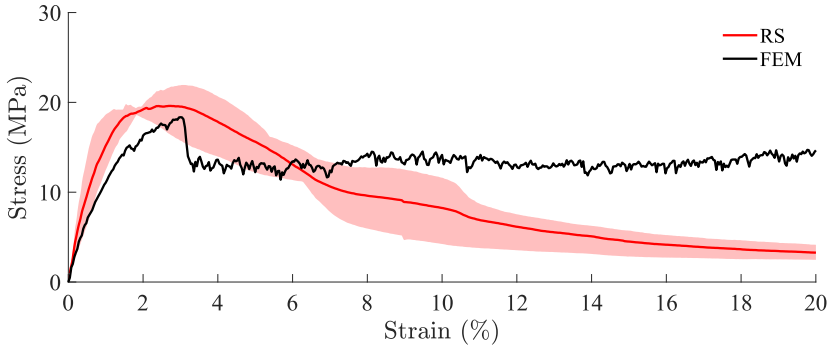

Figure A.3: Comparison of experimental and numerical stress strain curves for uniaxial compression of ACC RS from previous work [110]. For experimental data, the shaded bands reflect the spread observed in parallel measurements, and the solid lines denote the mean outcomes.

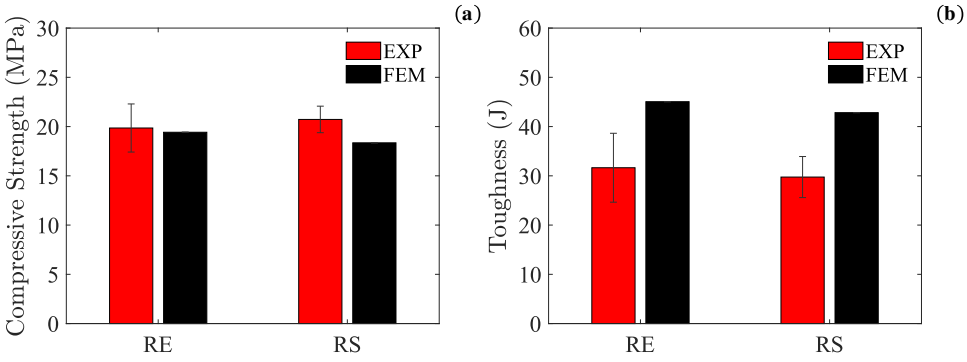

Figure A.4: Comparison of experimental and numerical mechanical properties for uniaxial compression of ACCs from previous work [110]: (a) Compressive strengths, and (b) toughness values.

A

A.3. LBM SIMULATIONS OF TPR AND TPRCC USING ISOTROPIC PROPERTIES

To illustrate the importance of incorporating printing path-dependent anisotropy in numerical simulations of the Fused Deposition Modeling (FDM) 3D-printed Tailored Poisson's Ratio-reinforcement (TPR) and Tailored Poisson's Ratio-reinforced Cementitious Composites (TPRCC) from Chapter 7, additional simulations were performed wherein the reinforcement only received isotropic material properties corresponding to the bead direction (n_i in Figure 7.2). All other properties remained the same as discussed in Section 7.2.1. Similar to the experimental and numerical descriptions in the main text of this work, first the flexural behaviour of the isotropic Tailored Poisson's Ratio-reinforcement (TPR) simulations are considered here. Comparisons of the load-displacement curves, deformation and fracture patterns from the experiments and isotropic simulations are shown in Figure A.5.

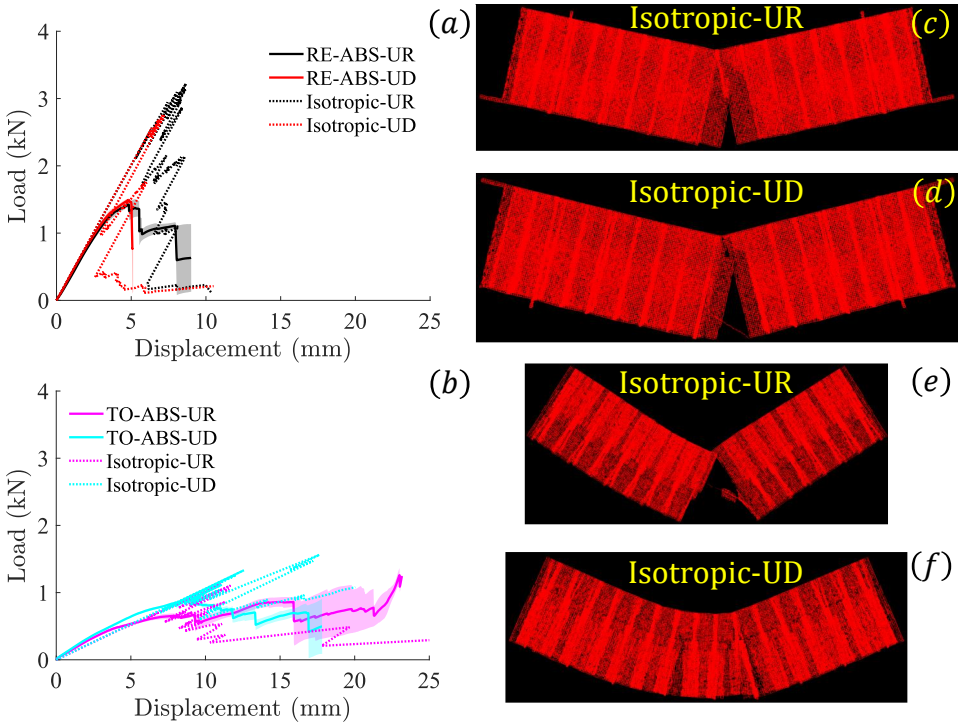

Figure A.5: Flexural behaviour of isotropic TPR simulations: (a,b) Load-displacement curves, (c-f) deformation and fracture patterns. Note: (c,e) UR, (d,f) UD.

The resulting load-displacement curves in Figures A.5(a) and (b) for RE and TO, respectively, provide significant strength overestimation for both UR and UD configurations. The experimental and isotropic load capacity comparison is graphically illustrated in Figure A.6 and quantified in Table A.7. Moreover, Figures A.5(c-f) demonstrate completely different numerical fracture patterns compared to those obtained experimentally (Figures

7.4(c-f) and 7.5(c-f)), which agrees with observations in Chapter 3. Whereas the experiments showed a combination of vertical cracking and inter-layer horizontal delamination, the isotropic simulations only display straight vertical cracks.

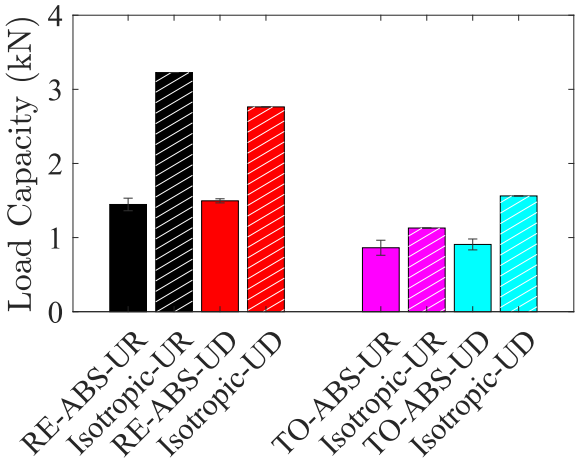

Figure A.6: Comparison of experimental and isotropic TPR simulation load capacities.

Table A.7: Load capacities of experiments and isotropic TPR simulations

TPR	**Load Capacity** (kN)
RE-ABS-UR	1.45 ± 0.08
Isotropic-UR	3.23
RE-ABS-UD	1.50 ± 0.03
Isotropic-UD	2.76
TO-ABS-UR	0.86 ± 0.10
Isotropic-UR	1.13
TO-ABS-UD	0.91 ± 0.07
Isotropic-UD	1.56

Comparisons of the experimental and isotropic load-displacement curves and fracture patterns of the Tailored Poisson's Ratio-reinforced Cementitious Composite (TPRCC) layouts are illustrated in Figure A.7. Due to the isotropic material properties assigned throughout the reinforcement, all simulations reach significantly higher load capacities compared to the tests and simulations including anisotropy (Figures 7.7(a,b) and 7.8(a,b)). The experimental and isotropic load capacity comparison is graphically illustrated in Figure A.8 and quantified in Table A.8. From Figures A.7(a) and A.8 it can be seen that Iso.-UR still maintains the highest load capacity, although the difference with Iso.-UD is smaller compared to RE-UR versus RE-UD. Analogous to the experimental results, RE-UR is able to sustain a higher secondary stiffness over a longer deformation range after the

A

onset of matrix cracking (near 2 kN), whilst the secondary stiffness of RE-UD deteriorates faster. The same trend is observed in Figures A.7(b) where Iso.-UR closely follows the greater secondary stiffness exhibited by TO-UR, whereas Iso.-UD and TO-UD trace a substantially smaller secondary stiffness. Nonetheless, near 6 mm displacement, Iso.-UD surpasses the maximum load capacity reached by Iso.-UR as a result of its continuous strain hardening response. Figures A.7(c-f) show increased multiple cracking for all isotropic simulations compared to the experiments and anisotropic models (Figures 7.7(c-f) and 7.8(c-f)). This is obviously caused by the larger displacements at which the peak loads for the isotropic cases are reached.

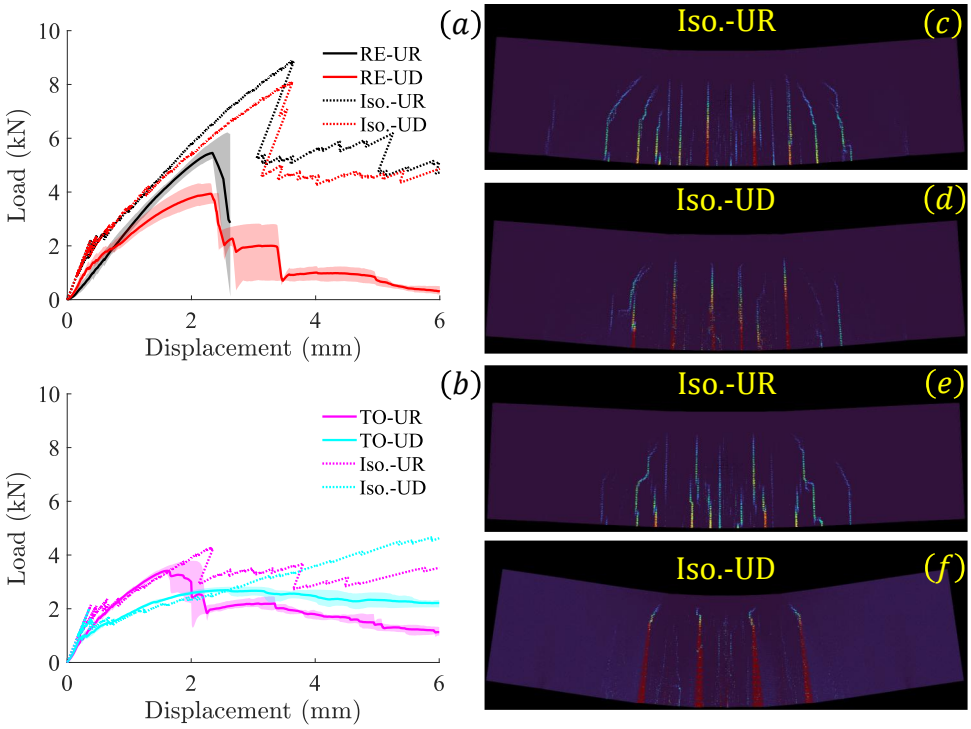

Figure A.7: Flexural behaviour of TPRCC simulations with isotropic TPR: (a,b) Load-displacement curves, (c-f) numerical cracks recorded by LBM prior to reaching peak load. Note: (c,e) UR, (d,f) UD.

Regarding the internal lateral confinement mechanism, a similar response as in the printing path-dependent simulations is obtained for the isotropic input, but enhanced due to the larger deformations. Figure A.9 illustrates the lateral stress (S_y) in the cementitious matrix phase near the peak load of the isotropic (a) RE-UR and (b) RE-UD bottom chords. In RE-UR (Figure A.9(a)), larger negative lateral stress concentrations in the centers of the TPR unit cells occur compared to those observed in Figure 7.11(a). Larger displacements cause larger longitudinal strains, which in turn accommodate larger lateral contraction of the reinforcement, leading to increased confinement. As a result, it is also noteworthy that the affected cementitious mortar cells experiencing lateral confinement

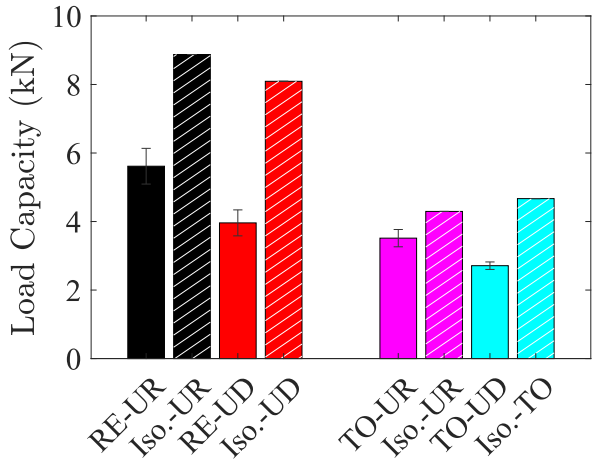

Figure A.8: Comparison of experimental and isotropic TPRCC simulation load capacities.

Table A.8: Load capacities of experiments and isotropic TPRCC simulations

TPRCC	**Load Capacity** (kN)
RE-UR	5.61 ± 0.52
Iso.-UR	8.87
RE-UD	3.96 ± 0.38
Iso.-UD	8.09
TO-UR	3.52 ± 0.25
Iso.-UR	4.30
TO-UD	2.71 ± 0.11
Iso.-UD	4.67

have increased from the three central units in Figure 7.11(a) to five units in Figure A.9(a). Similarly, the outer regions of the mortar in the unit cells are still under minor positive lateral stress. On the other hand, RE-UD (Figure A.9(b)) depicts near zero lateral stress values in the middle of the central unit cells. The outer regions of the mortar are again in compression, exactly opposite to the stress state in RE-UR.

Figure A.10 shows the internal stress (S_y) in the mortar bottom chords of (a) TO-UR and (b) TO-UD. TO-UR (Figure A.10(a)) displays the same, but larger negative lateral stress concentrations inside the TPR unit cells around the center of the beam compared to Figure 7.13(a). Identical to Figure A.9, the affected matrix regions subjected to lateral confinement have spread from three (Figure 7.13(a)) to five (Figure A.10(a)). Similar to Figure 7.13(b), the isotropic TO-UD (Figure A.10(b)) also exhibits negative lateral stress concentrations in the alternating unit cells: the lateral hourglass-shaped cells experience the largest stress concentrations, whilst the longitudinal ones show near zero or minor tensile stress.

A

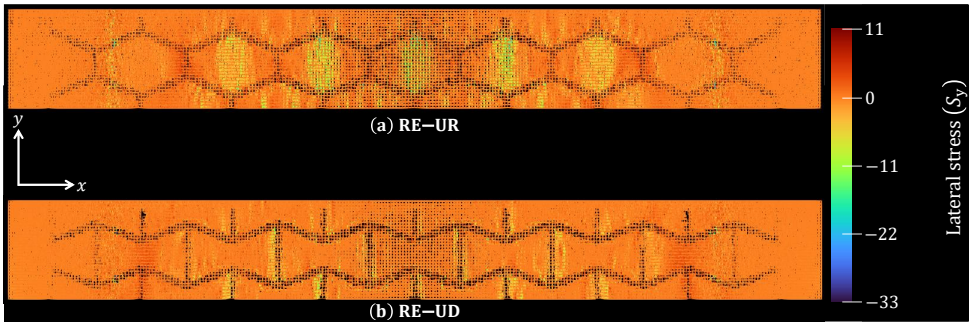

Figure A.9: Internal lateral stress (S_y) in cementitious matrix phase near peak load of isotropic (a) RE-UR and (b) RE-UD bottom chords (unit: MPa).

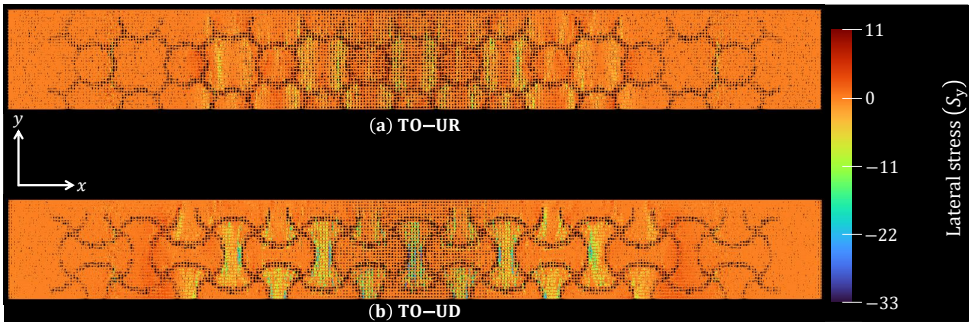

Figure A.10: Internal lateral stress (S_y) in cementitious matrix phase near peak load of isotropic (a) TO-UR and (b) TO-UD bottom chords (unit: MPa).

Visualizations of the internal cracking patterns at the Region Of Interest (ROI) shown in Figure 7.16 are displayed for the TPRCC simulations with isotropic TPR in Figure A.11. Figures A.11(a) and (c) show the numerical crack widths of RE-UR and RE-UR, respectively, obtained by isotropic LBM simulations. In RE-UR (Figure A.11(a)) multiple vertical cracks are present, where those with the largest crack widths run along the TPR as seen before in Figure 6.22(c) for a single crack. Analogous to the reconstructed μ-CT images in Figures 6.22(a,b), debonding seems to be the primary cause of the observed fracture patterns. When looking at RE-UD (Figure A.11(c)), significantly more and larger crack widths are recorded in the cementitious matrix. This aligns well with the experimental findings in Chapter 6 and the anisotropic simulations here that RE-UR more effectively mitigates internal damage compared to RE-UD.

Similarly, Figures A.11(b) and (d) depict the isotropic numerical crack widths of TO-UR and TO-UD, respectively. The same behaviour is found as for TPRCC-RE. For TO-UR (Figure A.11(b)), the internal fracture analysis shows multiple smaller cracks that are mainly aligned with the organic reinforcement shape. On the other hand, Figure A.11(d) for TO-UD displays substantially more and larger crack widths, as well as multiple internal cracks initiated at different locations. This also evidences that TO-UR is better in alleviating internal mortar fracture compared to TO-UD.

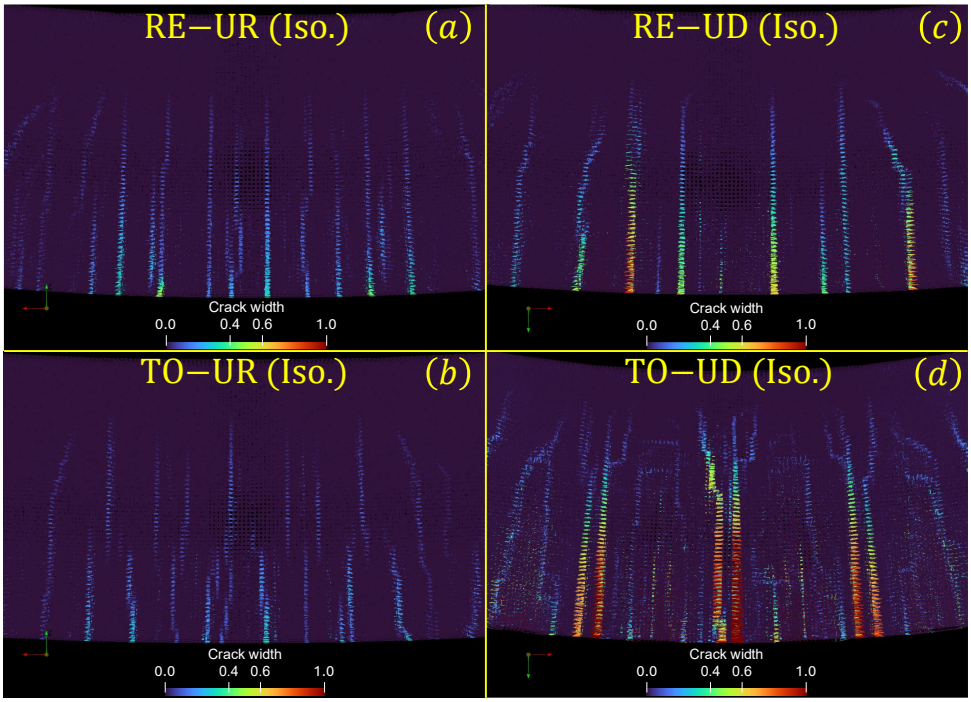

Figure A.11: Internal fracture at ROI in TPRCC simulations with isotropic TPR: (a) numerical crack width of RE-UR, (b) numerical crack width of TO-UR, (c) numerical crack width of RE-UD, and (d) numerical crack width of TO-UD (unit: mm).

CURRICULUM VITÆ

Rowin Johannes Marinus BOL

25-09-1997 Born in Halderberge, the Netherlands.

EDUCATION

2022–2026 PhD. Civil Engineering & Geosciences | Experimental Micromechanics
Delft University of Technology (TUD), Materials & Environment, Microlab
Delft, the Netherlands
Thesis: Squeezing Concrete:
A Numerical and Experimental Study on the Mechanisms within Auxetic Cementitious Composites
Promotors: Dr. B. Šavija
Prof. dr. ir. E. Schlangen

2019–2022 MSc. Architecture, Building & Planning | Structural Engineering & Design
Eindhoven University of Technology (TU/e), Chair of Applied Mechanics
Eindhoven, the Netherlands
Thesis: Multi-Scale Material Modelling:
Application in Topology Optimization of Structures
Supervisors: Dr. P. Poorsolhjouy
Dr. ir. H. Hofmeyer
Prof. dr. ir. A.S.J. Suiker

2017–2019 BEd. Physics
Eindhoven University of Technology (TU/e)
Eindhoven School of Education (ESoE)
Eindhoven, the Netherlands

2016–2019 BSc. Architecture, Urbanism & Building Sciences | Structural Design
Eindhoven University of Technology (TU/e)
Eindhoven, the Netherlands

EXPERIENCE

2026–2027	Postdoctoral Researcher 3D Concrete Printing Digital Fabrication with Concrete Eindhoven University of Technology (TU/e) Eindhoven, the Netherlands
2022–2026	PhD. Civil Engineering & Geosciences | Experimental Micromechanics Delft University of Technology (TUD) Delft, the Netherlands *Thesis:* Squeezing Concrete: A Numerical and Experimental Study on the Mechanisms within Auxetic Cementitious Composites *Promotors:* Dr. B. Šavija Prof. dr. ir. E. Schlangen
2020–2021	Structural Engineer A.V.S. Engineering B.V. Etten-Leur, the Netherlands
2018–2021	Constructive Engineering Advisor Handel Bouw Advies B.V. Etten-Leur, the Netherlands
2015–2020	STEM Tutor Huiswerkbegeleiding Etten-Leur & Prinsenbeek Etten-Leur, the Netherlands & Prinsenbeek, the Netherlands
2019	Trainee-Teacher in Phyisics Sint Oelbert Gymnasium Oosterhout, the Netherlands
2018	Trainee- & Summer School Teacher in Physics Katholieke Scholengemeenschap Etten-Leur (KSE) Etten-Leur, the Netherlands
2017–2018	Tutor Applied Physics (TA) Eindhoven University of Technology (TU/e) Eindhoven, the Netherlands

AWARDS, FUNDING & GRANTS

2025	Security & Resilience for Society. Kirigami as Reinforcement for Safer and More Resilient Concrete Structures. **TUD Safety and Security Institute Seed funding**
2023	Audience Award MSc thesis **TU/e Academic Awards**
2023	Best MSc Thesis of the Department of the Built Environment **TU/e Academic Awards**

List of Publications

Journal publications:

12. **R.J.M. Bol**, H. Hofmeyer, P. Poorsolhjouy, *Micromechanics-Informed Proportional Topology Optimization of Granular Structures with Asymmetric Stiffness and Strength*, under review.

11. **R.J.M. Bol**, W. Zhou, Z. Meng, E. Schlangen, B. Šavija, *Revealing lateral confinement mechanisms in tailored Poisson's ratio-reinforced cementitious composites using lattice models*, under review.

10. Z. Meng, M. Liang, Y. Zhang, J. Xie, **R.J.M. Bol**, E. Schlangen, B. Šavija, *Programming elasto-plastic lattice metamaterials via conditional generative modeling*, under review.

9. **R.J.M. Bol**, Y. Xu, Z. Meng, J. Xie, B. Šavija, *Multi-Scale Lattice Modelling of Deformation and Fracture in Auxetic Cementitious Composites Subjected to Uniaxial Compression*, under review.

8. Z. Meng, Y. Xu, W. Zhou, **R.J.M. Bol**, J. Xie, B. Šavija, *Confinement mechanisms governed by stiffness contrasts in auxetic cementitious composites*, International Journal of Mechanical Sciences **318**, 111546 (2026).

7. **R.J.M. Bol**, W. Zhou, Z. Meng, E. Schlangen, B. Šavija, *Tailored Poisson's Ratio-reinforced Cementitious Composites for flexural applications*, Cement and Concrete Composites **168**, 106485 (2026).

6. W. Zhou, **R.J.M. Bol**, Y. Zhou, Z. Meng, Y. Xu, J. Xie, B. Šavija, *Reinforcing mechanisms of lattice-reinforced cementitious composites: insight into flexural performance and material interactions*, Materials & Design **256**, 114332 (2025).

5. **R.J.M. Bol**, Y. Xu, M. Luković, B. Šavija, *Does printing direction influence the bond between 3D printed polymeric reinforcement and cementitious matrix?*, Engineering Failure Analysis **174**, 109471 (2025).

4. Z. Meng, Y. Xu, J. Xie, W. Zhou, **R.J.M. Bol**, Q. Liu, B. Šavija, *Unraveling the reinforcing mechanisms for cementitious composites with 3D printed multidirectional auxetic lattices using X-ray computed tomography*, Materials & Design **246**, 113331 (2024).

3. **R.J.M. Bol**, Y. Xu, B. Šavija, *Printing path-dependent two-scale models for 3D printed planar auxetics by material extrusion*, Additive Manufacturing **89**, 104293 (2024).

2. Y. Xu, Z. Meng, **R.J.M. Bol**, B. Šavija, *Spring-like behaviour of cementitious composite enabled by auxetic hyperelastic frame*, International Journal of Mechanical Sciences **275**, 109364 (2024).

1. **R.J.M. Bol**, B. Šavija, *Micromechanical Models for FDM 3D-Printed Polymers: A Review*, *Polymers* **2023**, 15(23), 4497.

Proceedings:

3. **R.J.M. Bol**, W. Zhou, Z. Meng, E. Schlangen, B. Šavija, *Tailored Poisson's Ratio-reinforced Cementitious Composites for Flexural Applications*, RILEM Spring Convention & Conference on Innovative Construction Materials and Processes for Sustainable Buildings and Infrastructure, Ghent, Belgium, April 13-17, 2026.
2. **R.J.M. Bol**, E. Schlangen, B. Šavija, *Towards lattice modelling of additively manufactured cement-based composites with tailored Poisson's ratio-reinforcement*, Computational Modelling of Concrete and Concrete Structures (EURO-C 2026), pp. 767-774, Seefeld in Tirol, Austria, March 9-12, 2026.
1. **R.J.M. Bol**, Y. Xu, M. Luković, B. Šavija, *Does printing direction influence the bond between 3D printed polymeric reinforcement and cementitious matrix?*, 12th International Conference on Fracture Mechanics of Concrete and Concrete Structures (FraMCoS-12), Vienna, Austria, April 23-25, 2025.

Conferences:

8. **R.J.M. Bol**, W. Zhou, Z. Meng, E. Schlangen, B. Šavija, *Tailored Poisson's Ratio-reinforced Cementitious Composites for Flexural Applications*, RILEM Spring Convention & Conference on Innovative Construction Materials and Processes for Sustainable Buildings and Infrastructure, Ghent, Belgium, April 13-17, 2026.
7. **R.J.M. Bol**, E. Schlangen, B. Šavija, *Towards lattice modelling of additively manufactured cement-based composites with tailored Poisson's ratio-reinforcement*, Computational Modelling of Concrete and Concrete Structures (EURO-C 2026), pp. 767-774, Seefeld in Tirol, Austria, March 9-12, 2026.
6. **R.J.M. Bol**, W. Zhou, Z. Meng, E. Schlangen, B. Šavija, *Tailored Poisson's Ratio-reinforced Cementitious Composites for Flexural Applications*, 28th Engineering Mechanics Symposium, Arnhem, The Netherlands, October 30-31, 2025.
5. **R.J.M. Bol**, W. Zhou, Z. Meng, E. Schlangen, B. Šavija, *Tailored Poisson's Ratio-reinforced Cementitious Composites for Flexural Applications*, Numerical Modelling Strategies for Sustainable Concrete Structures (SSCS 2025) & 1st International Conference on Auxetics in Construction (AUXETICON 2025), Rotterdam, The Netherlands, July 7-9, 2025.
4. **R.J.M. Bol**, Y. Xu, M. Luković, B. Šavija, *Does printing direction influence the bond between 3D printed polymeric reinforcement and cementitious matrix?*, Numerical Modelling Strategies for Sustainable Concrete Structures (SSCS 2025) & 1st International Conference on Auxetics in Construction (AUXETICON 2025), Rotterdam, The Netherlands, July 7-9, 2025.
3. **R.J.M. Bol**, W. Zhou, Z. Meng, E. Schlangen, B. Šavija, *Tailored Poisson's Ratio-reinforced Cementitious Composites for Flexural Applications*, Engineering Mechanics Institute Conference (EMI 2025), Anaheim, United States of America, May 27-30, 2025.
2. **R.J.M. Bol**, Y. Xu, M. Luković, B. Šavija, *Does printing direction influence the bond between 3D printed polymeric reinforcement and cementitious matrix?*, 12th International Conference on Fracture Mechanics of Concrete and Concrete Structures (FraMCoS-12), Vienna, Austria, April 23-25, 2025.
1. **R.J.M. Bol**, Y. Xu, B. Šavija, *Printing path-dependent two-scale models for 3D printed planar auxetics by material extrusion*, 27th Engineering Mechanics Symposium, Arnhem, The Netherlands, October 22-23, 2024.

TU Delft

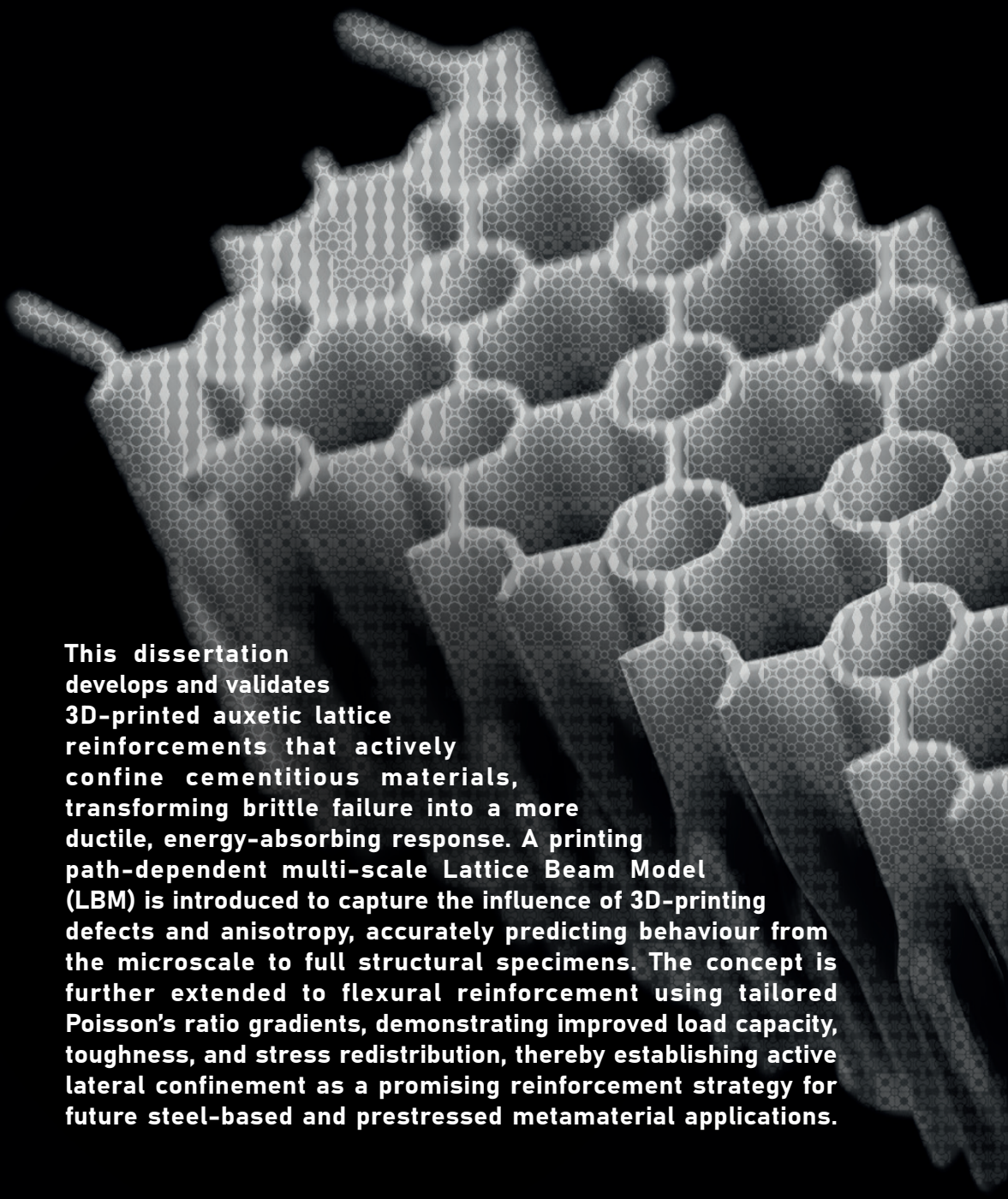

This dissertation develops and validates 3D-printed auxetic lattice reinforcements that actively confine cementitious materials, transforming brittle failure into a more ductile, energy-absorbing response. A printing path-dependent multi-scale Lattice Beam Model (LBM) is introduced to capture the influence of 3D-printing defects and anisotropy, accurately predicting behaviour from the microscale to full structural specimens. The concept is further extended to flexural reinforcement using tailored Poisson's ratio gradients, demonstrating improved load capacity, toughness, and stress redistribution, thereby establishing active lateral confinement as a promising reinforcement strategy for future steel-based and prestressed metamaterial applications.